

Figure 503.49: Simulated Acceleration Time Series, Turkey Kocaeli 1999, Yarimca, Comparison of Two Cases (Structure Bent 1)

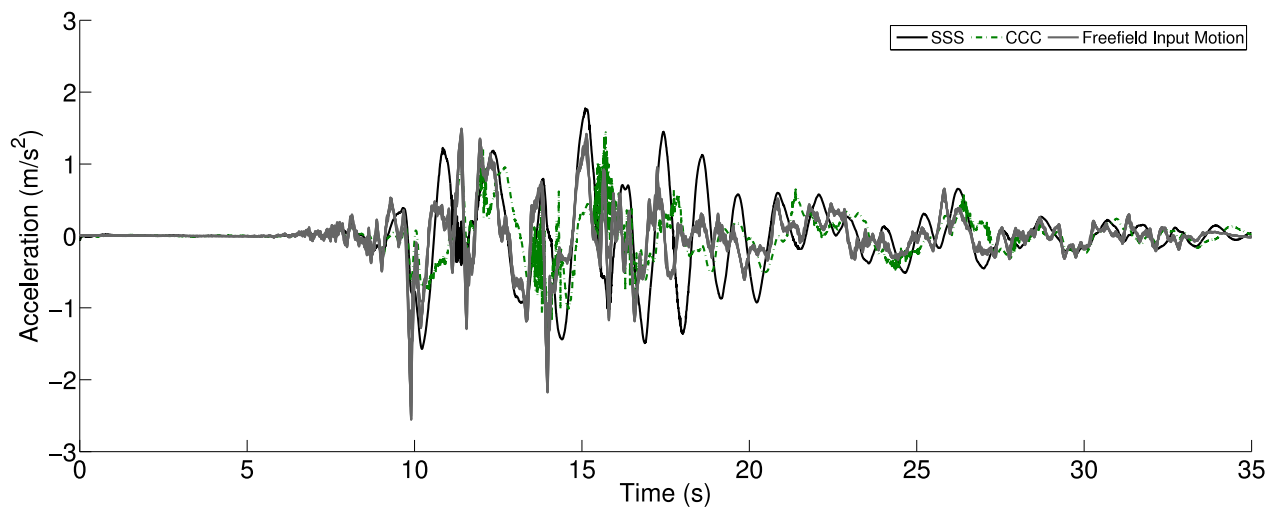


Figure 503.50: Simulated Acceleration Time Series, Turkey Kocaeli 1999, Yarimca, Comparison of Two Cases with Free Field Motions (Soil Block 2)

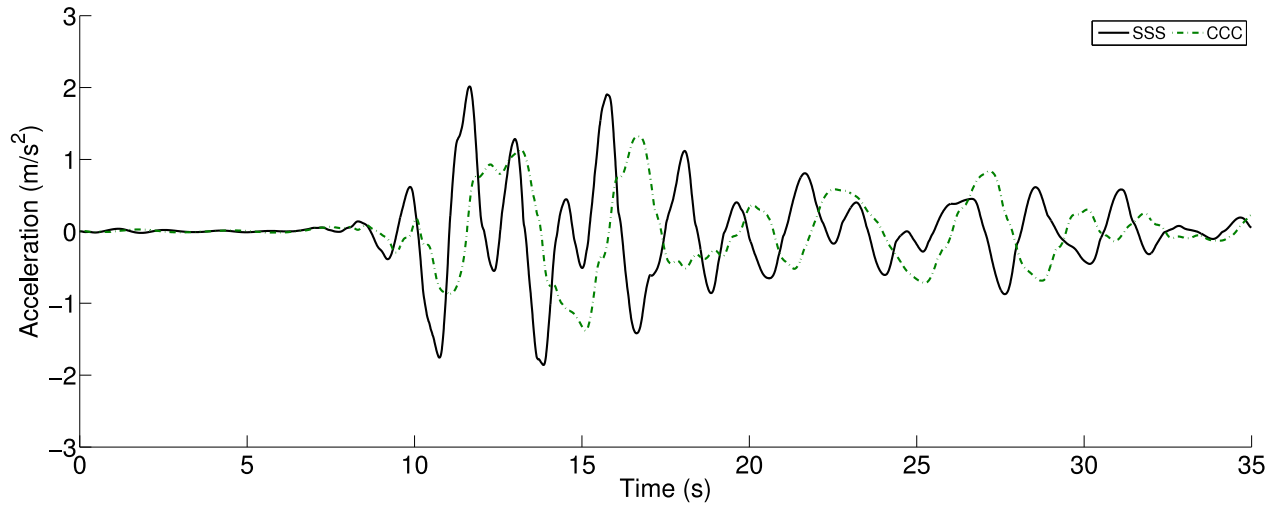


Figure 503.51: Simulated Acceleration Time Series, Turkey Kocaeli 1999, Yarimca, Comparison of Two Cases (Structure Bent 2)

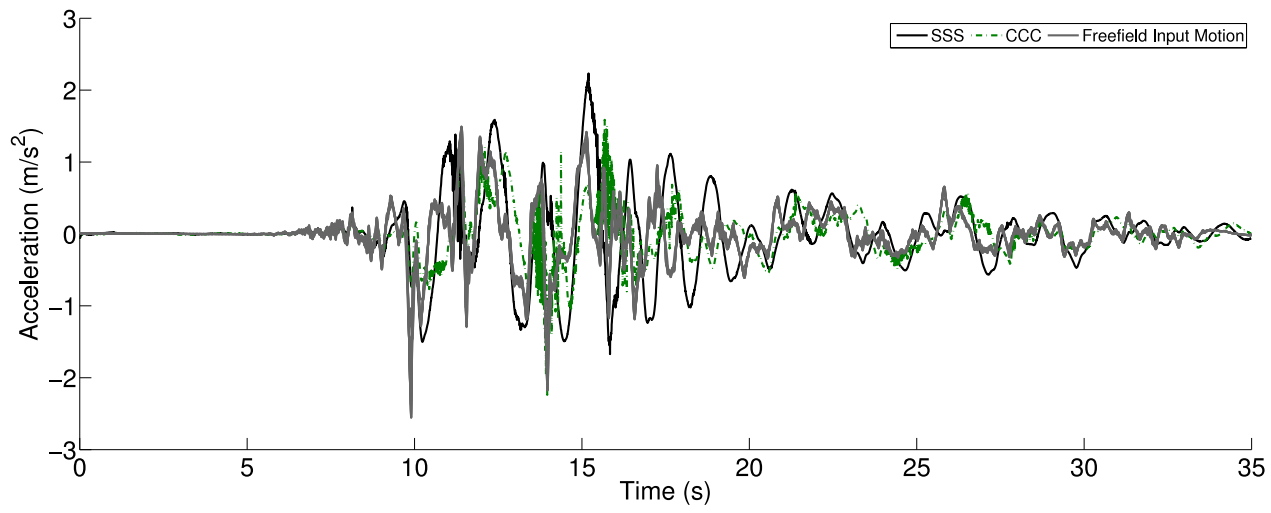


Figure 503.52: Simulated Acceleration Time Series, Turkey Kocaeli 1999, Yarimca, Comparison of Two Cases with Free Field Motions (Soil Block 3)

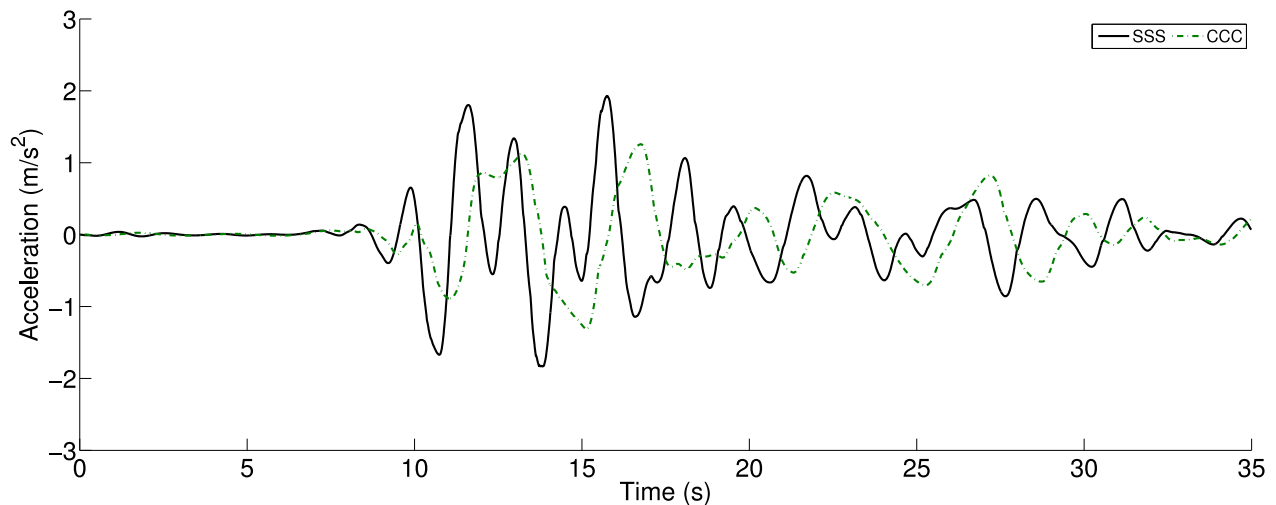


Figure 503.53: Simulated Acceleration Time Series, Turkey Kocaeli 1999, Yarimca, Comparison of Two Cases (Structure Bent 3)

503.2.3.3 Displacement Response Spectra

The response spectra are useful tools to look deep into the frequency domain. As we explained before, the Turkey Kocaeli shaking was picked for this study because it contains much longer period contents that were not present in the 1999 Northridge earthquake. In this section, we can clearly see how the soil foundation can affect the structures on top of it. Firstly, structures supported by stiff soil will only see amplification from those low period, high frequency components. Correspondingly, structures supported by soft soil tend to respond much more to long period, low frequency components of the shaking motion. Secondly, this plots exactly show how important the SFSI analysis is. It will not make much sense if one wants to analyze the structure without acknowledging the characteristics of the underlying soil foudation and the input motion. How the structure behaves is the combination of answers to many questions such as the stiffness of soil and the frequency contents of the motions.

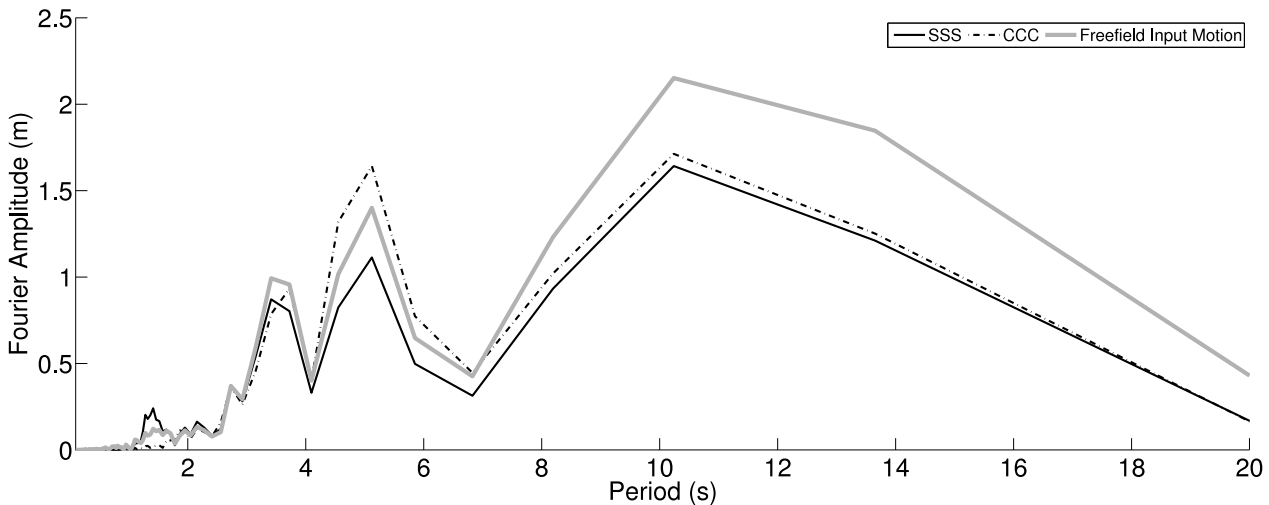


Figure 503.54: Simulated Displacement Response Spectra, Turkey Kocaeli 1999, Yarimca, Comparison of Two Cases with Free Field Motions (Soil Block 1)

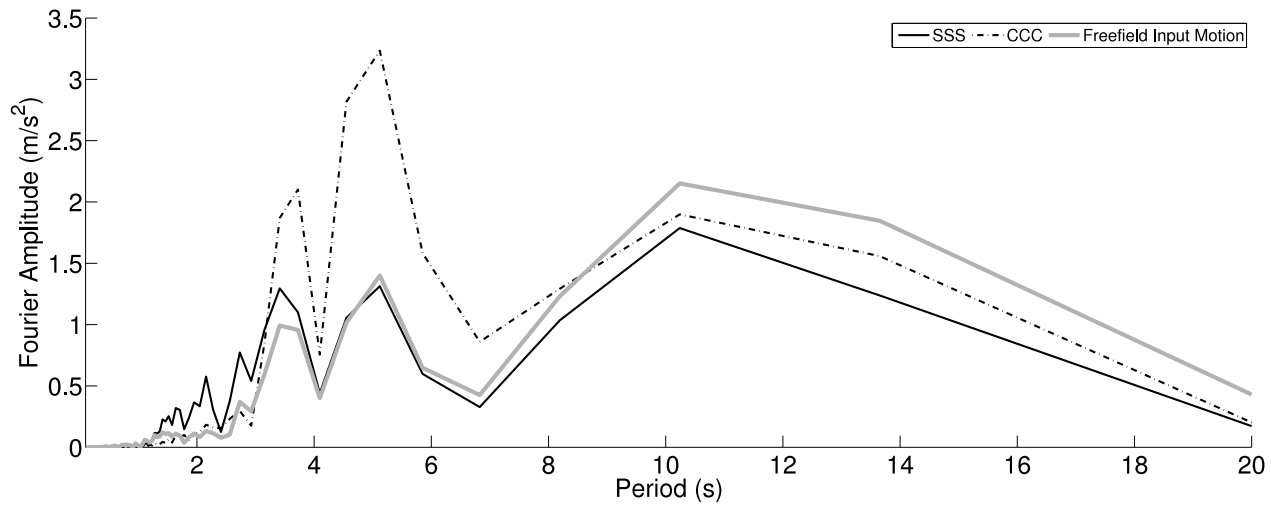


Figure 503.55: Simulated Displacement Response Spectra, Turkey Kocaeli 1999, Yarimca, Comparison of Two Cases (Structure Bent 1)

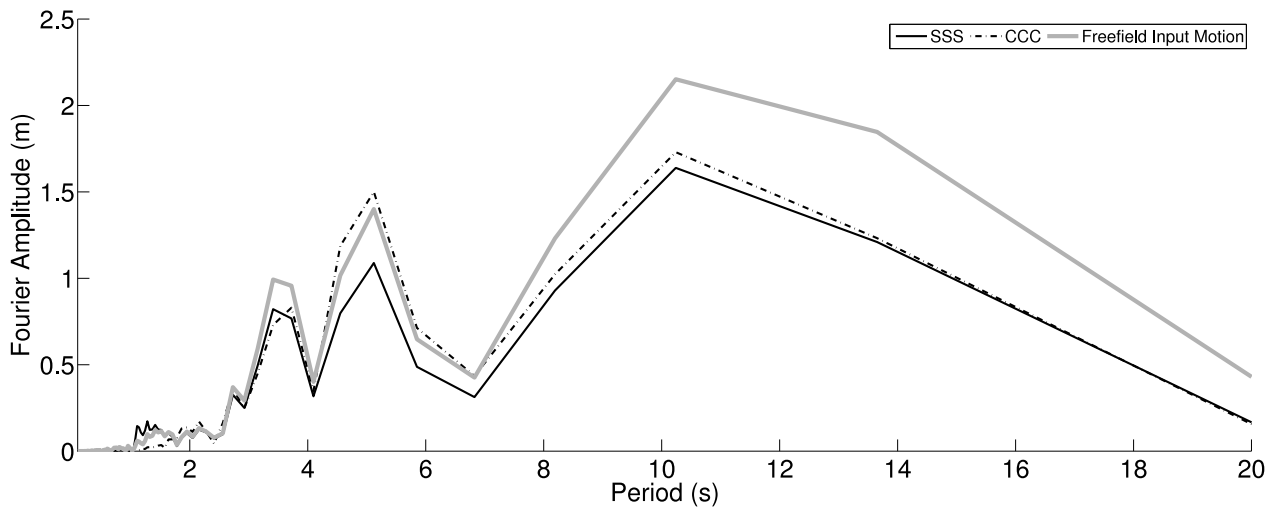


Figure 503.56: Simulated Displacement Response Spectra, Turkey Kocaeli 1999, Yarimca, Comparison of Two Cases with Free Field Motions (Soil Block 2)

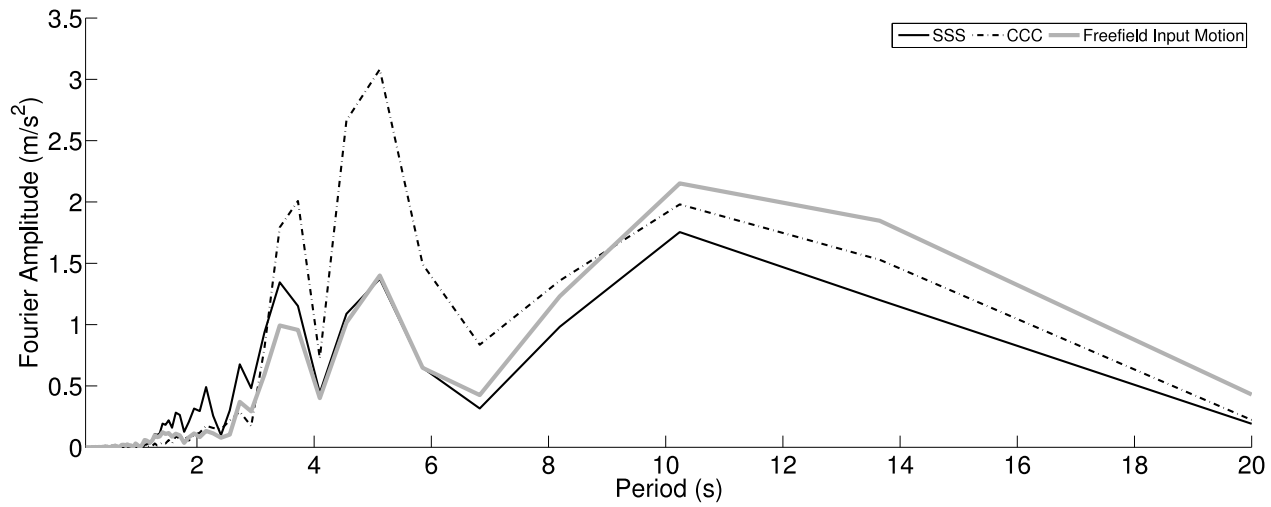


Figure 503.57: Simulated Displacement Response Spectra, Turkey Kocaeli 1999, Yarimca, Comparison of Two Cases (Structure Bent 2)

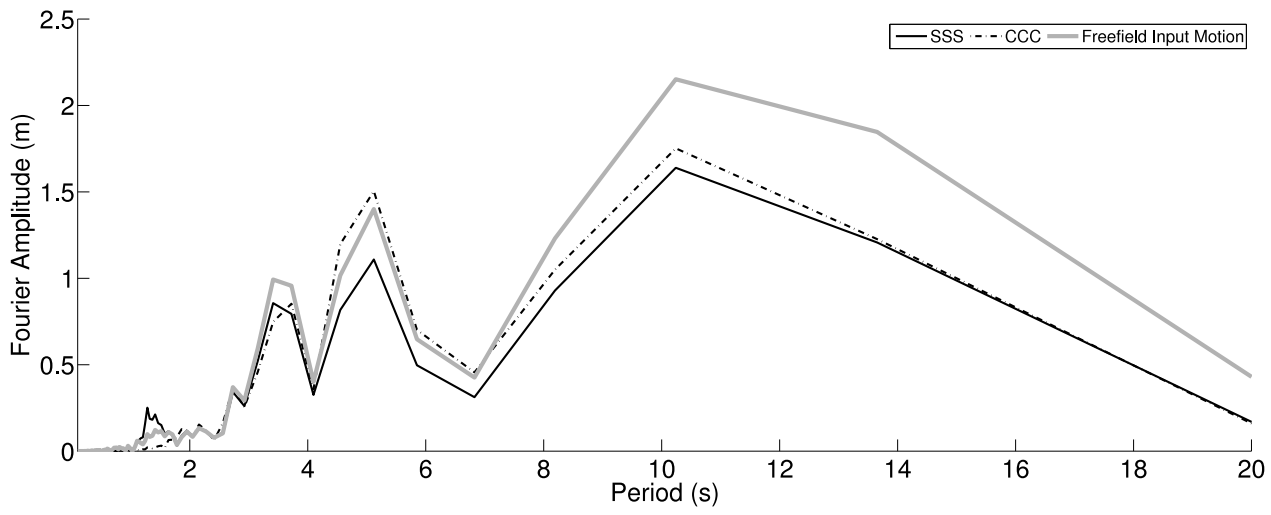


Figure 503.58: Simulated Displacement Response Spectra, Turkey Kocaeli 1999, Yarimca, Comparison of Two Cases with Free Field Motions (Soil Block 3)

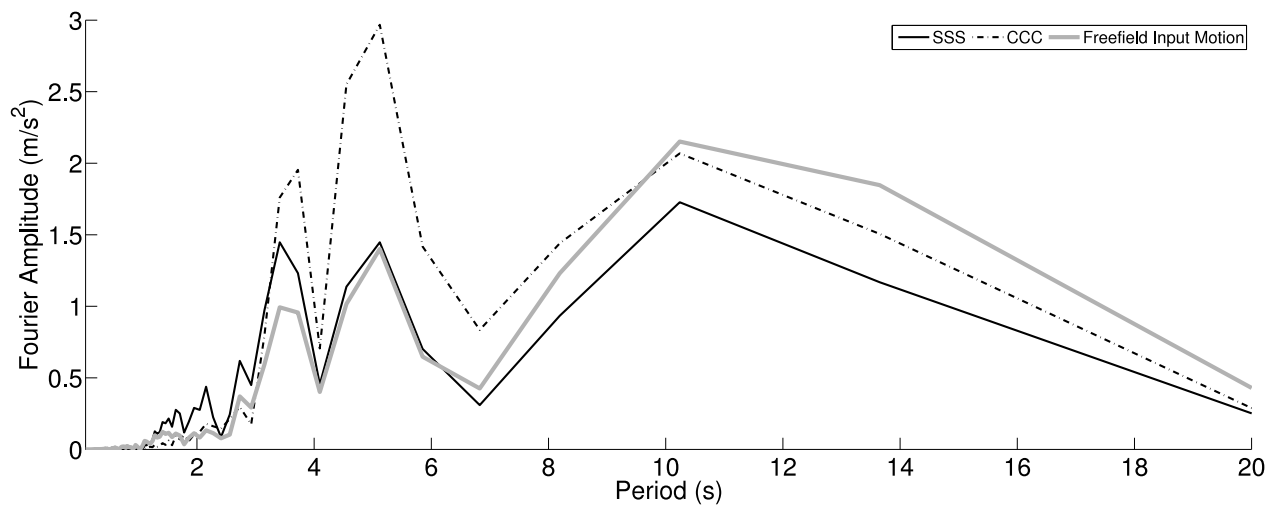


Figure 503.59: Simulated Displacement Response Spectra, Turkey Kocaeli 1999, Yarimca, Comparison of Two Cases (Structure Bent 3)

503.2.3.4 Acceleration Response Spectra

As we discussed before, the acceleration response shows much focused content to the high frequency (low period) side as acceleration is the derivative of displacement. But it is still clearly shows the difference between the structures supported by stiff soil and those supported by soft soil. SFSI is crucial in the sense that the structure response must be determined by both short period and long period components. The overall response is determined by the primary periods of both underlying soil and the input motion.

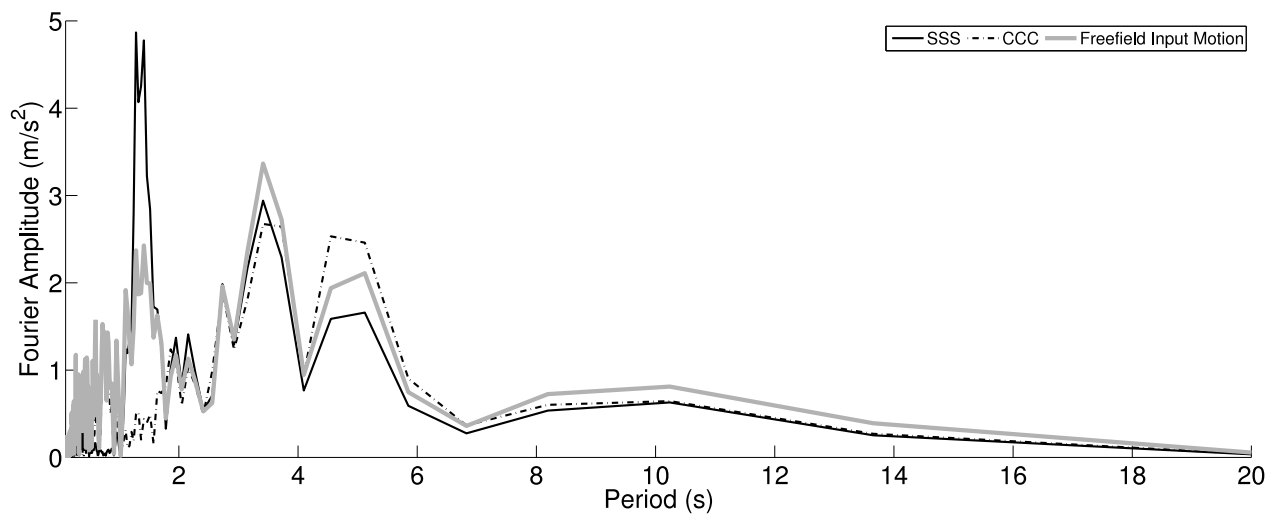


Figure 503.60: Simulated Acceleration Response Spectra, Turkey Kocaeli 1999, Yarimca, Comparison of Two Cases with Free Field Motions (Soil Block 1)

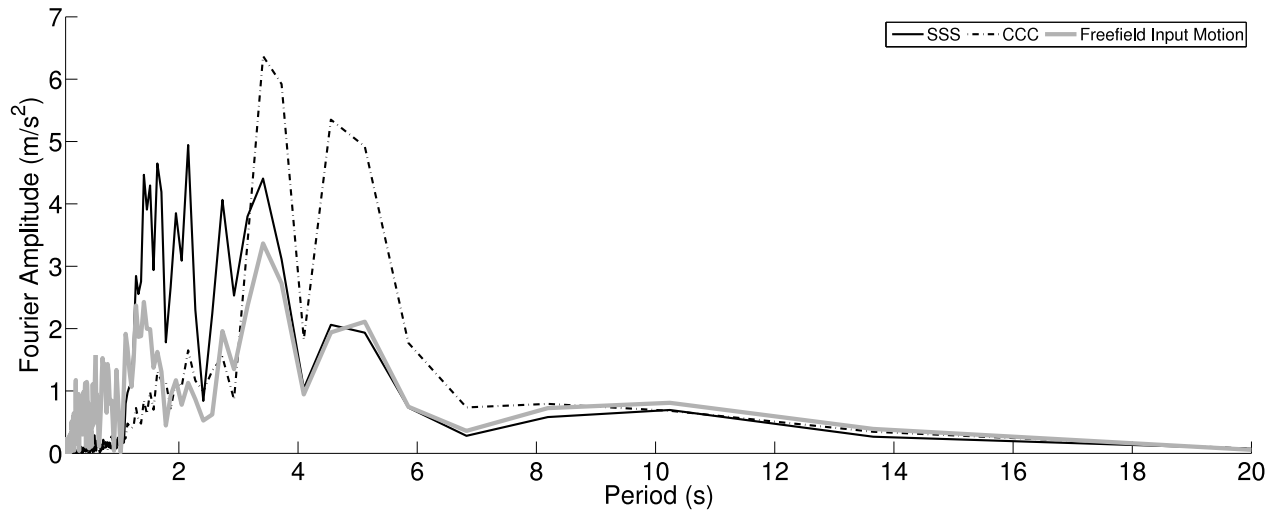


Figure 503.61: Simulated Acceleration Response Spectra, Turkey Kocaeli 1999, Yarimca, Comparison of Two Cases (Structure Bent 1)

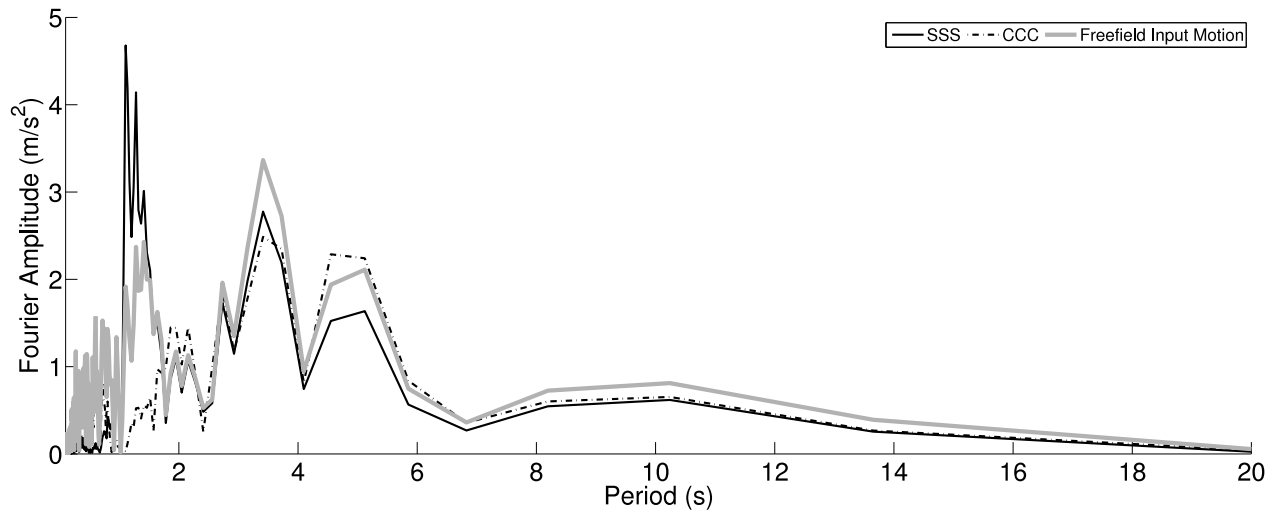


Figure 503.62: Simulated Acceleration Response Spectra, Turkey Kocaeli 1999, Yarimca, Comparison of Two Cases with Free Field Motions (Soil Block 2)

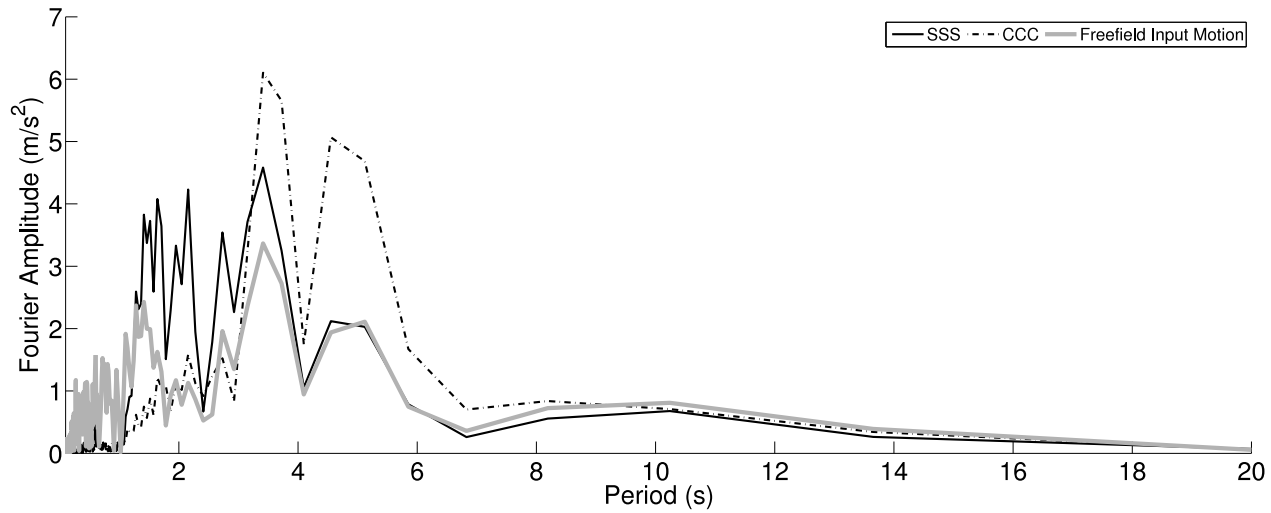


Figure 503.63: Simulated Acceleration Response Spectra, Turkey Kocaeli 1999, Yarimca, Comparison of Two Cases (Structure Bent 2)

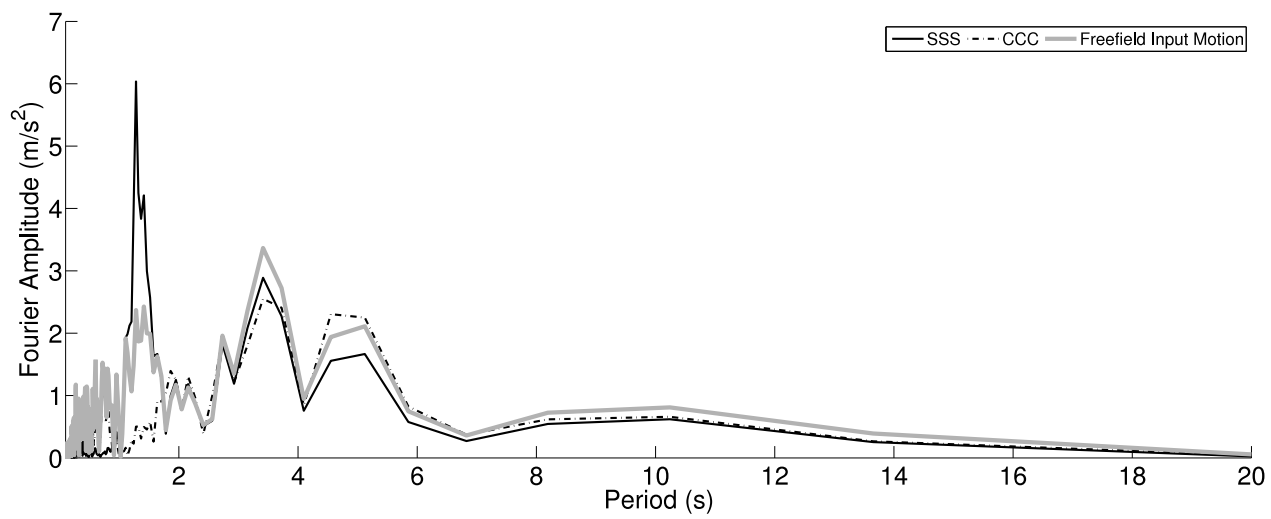


Figure 503.64: Simulated Acceleration Response Spectra, Turkey Kocaeli 1999, Yarimca, Comparison of Two Cases with Free Field Motions (Soil Block 3)

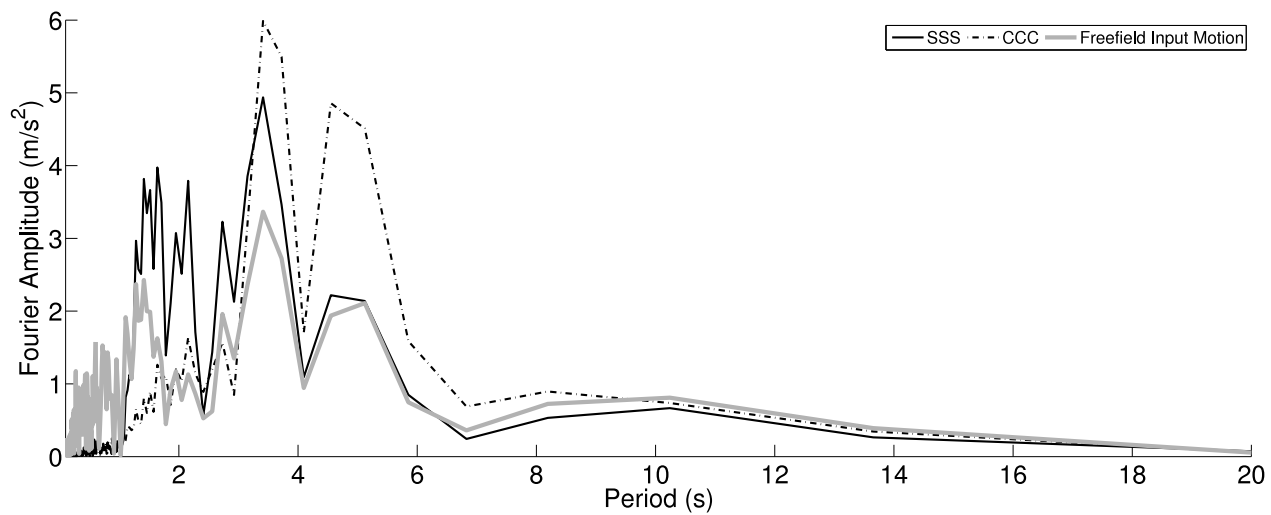


Figure 503.65: Simulated Acceleration Response Spectra, Turkey Kocaeli 1999, Yarimca, Comparison of Two Cases (Structure Bent 3)

503.2.3.5 Structural Response

The structure response now directly shows how differently the structure can react to the same input motion, given different soil conditions. We can again see the structure on top of soft soil exhibits much response to long period content especially for the fact that the structure on top of the soft soil reaches maximum moment for about 3 seconds, which is not present in the stiff soil case. This is also consistent with the observation that the displacement of the structure supported by soft soil is much larger due to the much longer time for plastic slip when the plastic moment is reached.

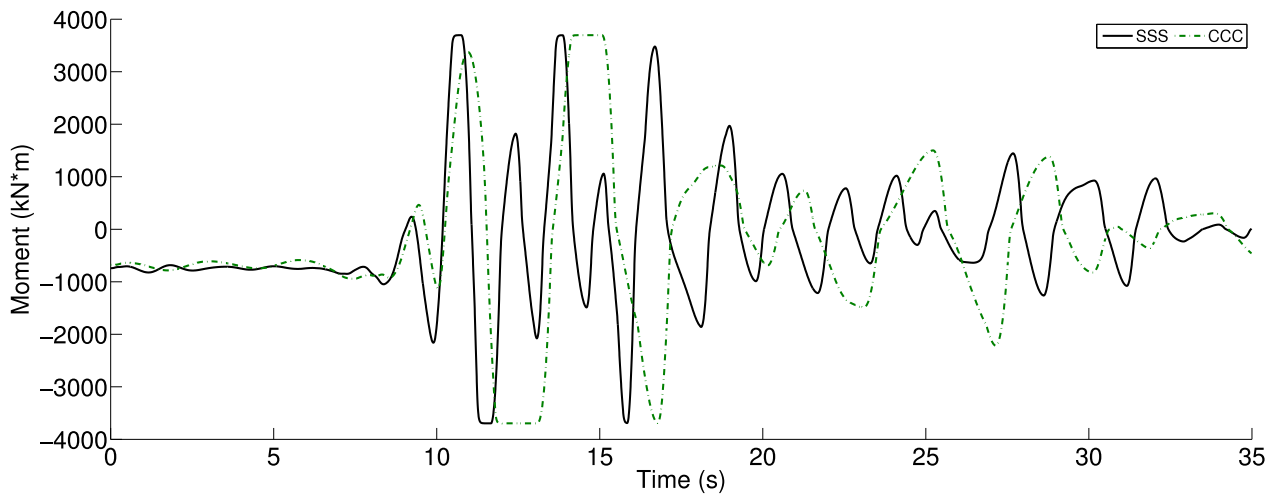


Figure 503.66: Simulated Maximum Moment Time Series, Turkey Kocaeli 1999, Yarimca, Comparison of Two Cases (Structure Bent 1 Pile 1)

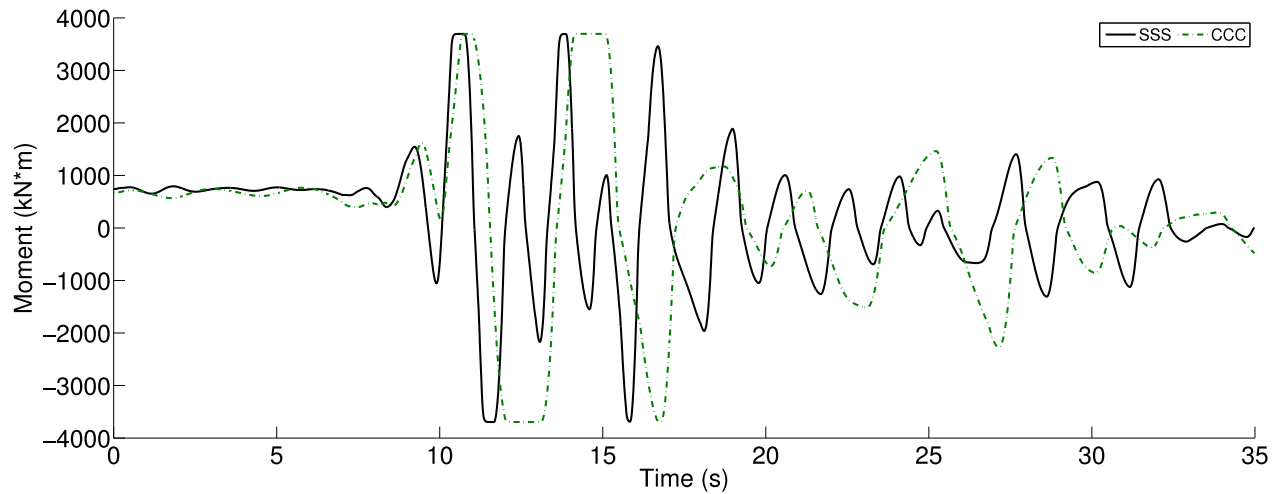


Figure 503.67: Simulated Maximum Moment Time Series, Turkey Kocaeli 1999, Yarimca, Comparison of Two Cases (Structure Bent 1 Pile 2)

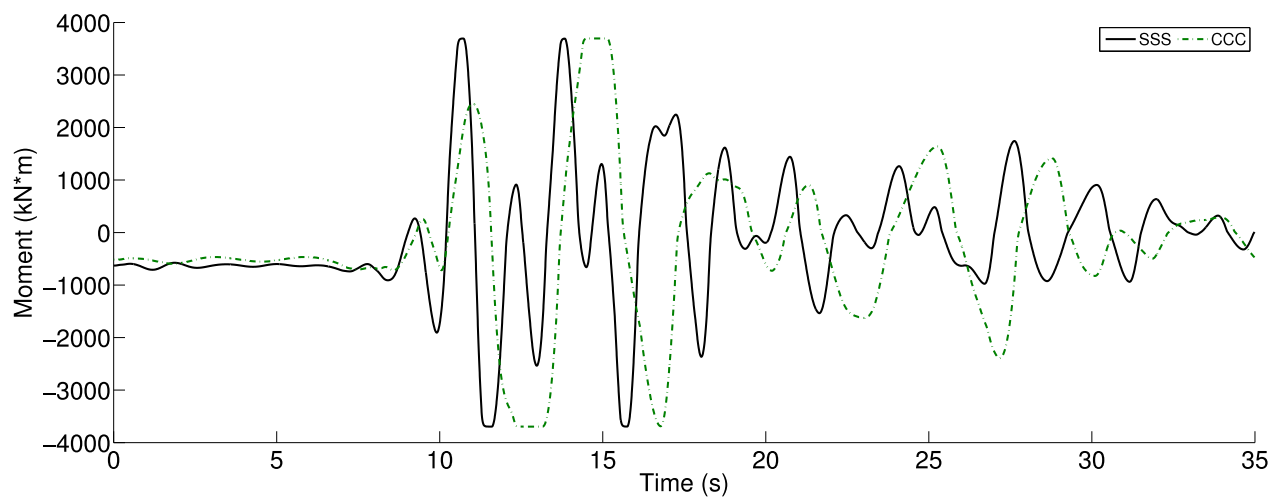


Figure 503.68: Simulated Maximum Moment Time Series, Turkey Kocaeli 1999, Yarimca, Comparison of Two Cases (Structure Bent 2 Pile 1)

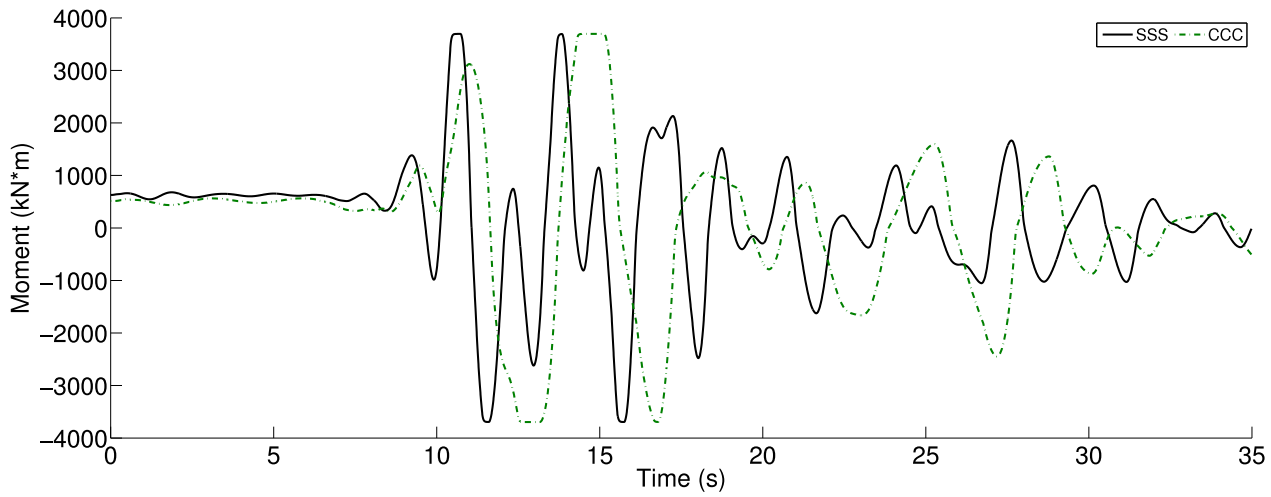


Figure 503.69: Simulated Maximum Moment Time Series, Turkey Kocaeli 1999, Yarimca, Comparison of Two Cases (Structure Bent 2 Pile 2)

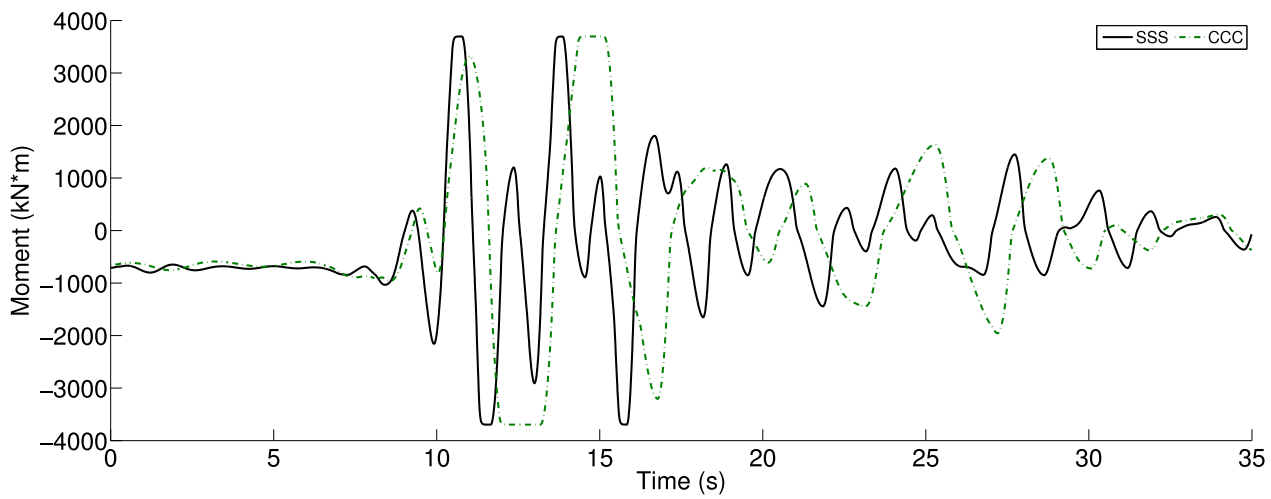


Figure 503.70: Simulated Maximum Moment Time Series, Turkey Kocaeli 1999, Yarimca, Comparison of Two Cases (Structure Bent 3 Pile 1)

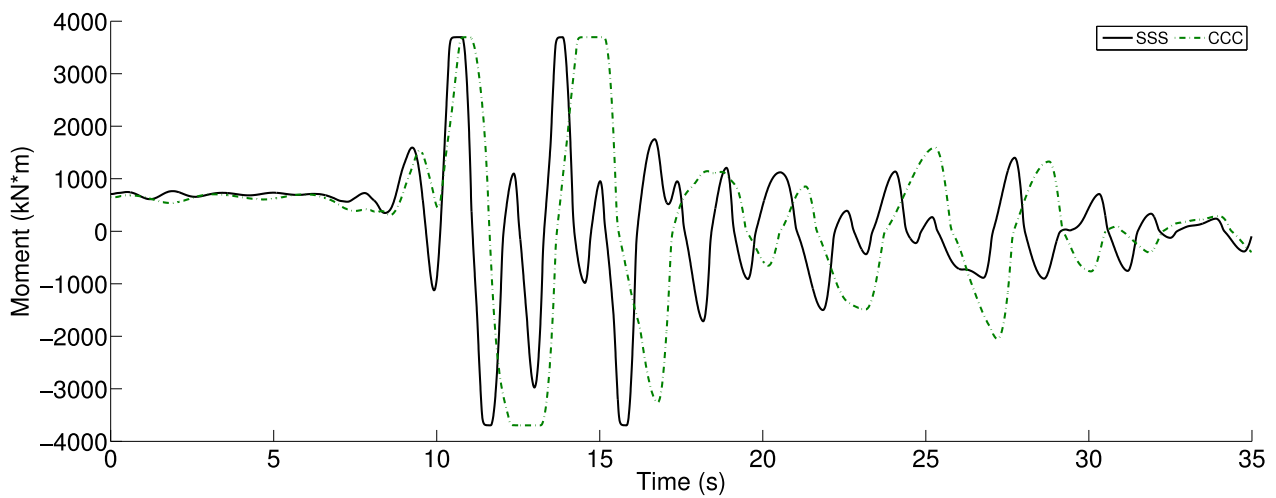


Figure 503.71: Simulated Maximum Moment Time Series, Turkey Kocaeli 1999, Yarimca, Comparison of Two Cases (Structure Bent 3 Pile 2)

Table 503.5: Simulation Scenarios for Prototype ESSI Studies

Simulation Cases	Soil Block 1	Soil Block 2	Soil Block 3
Case 1	Stiff Sand	Stiff Sand	Stiff Sand
Case 8	Soft Clay	Soft Clay	Soft Clay

503.2.4 Earthquake Soil Structure Interaction Effects

In the following sections we analyze various Earthquake Soil Structure Interaction (ESSI) effects.

503.2.4.1 How Strength of Soil Foundations Affects ESSI

It has been well known that stiffer soil layer will provide higher bearing capacity of structures so site improvements will always be preferred in engineering practice when one talks about foundation design.

While for dynamic cases, this widely-held impression will not be valid anymore. In order to see how stiffness of soil can affect the response of the whole ESSI system during earthquake shaking, two distinct scenarios listed in Table 503.5, Case 1 with all stiff soil foundations, and Case 8 with all soft soil foundations have been extracted to show the dynamic system response.

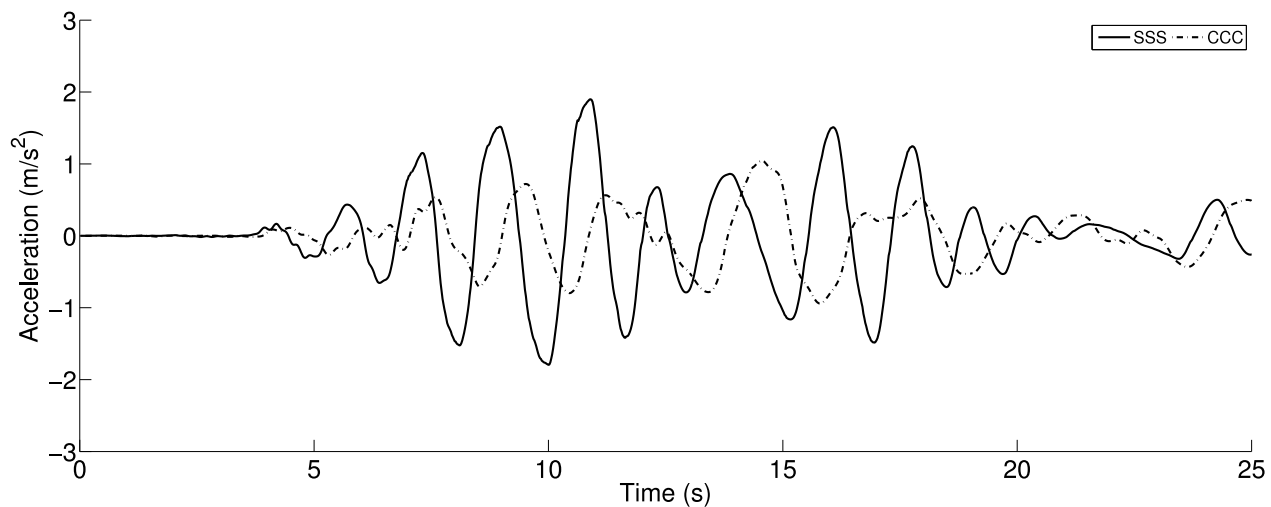


Figure 503.72: Simulated Acceleration Time Series, Northridge 1994, Century City, Comparison of Two Cases - First 25s (Structure Bent 1)

Case 1 and Case 8

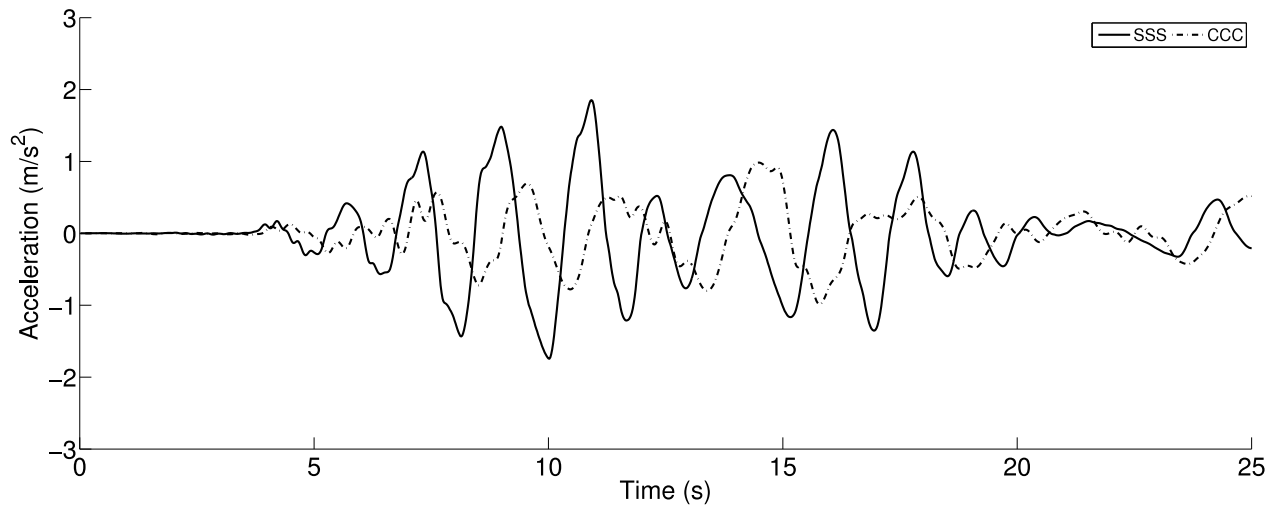


Figure 503.73: Simulated Acceleration Time Series, Northridge 1994, Century City, Comparison of Two Cases - First 25s (Structure Bent 2)

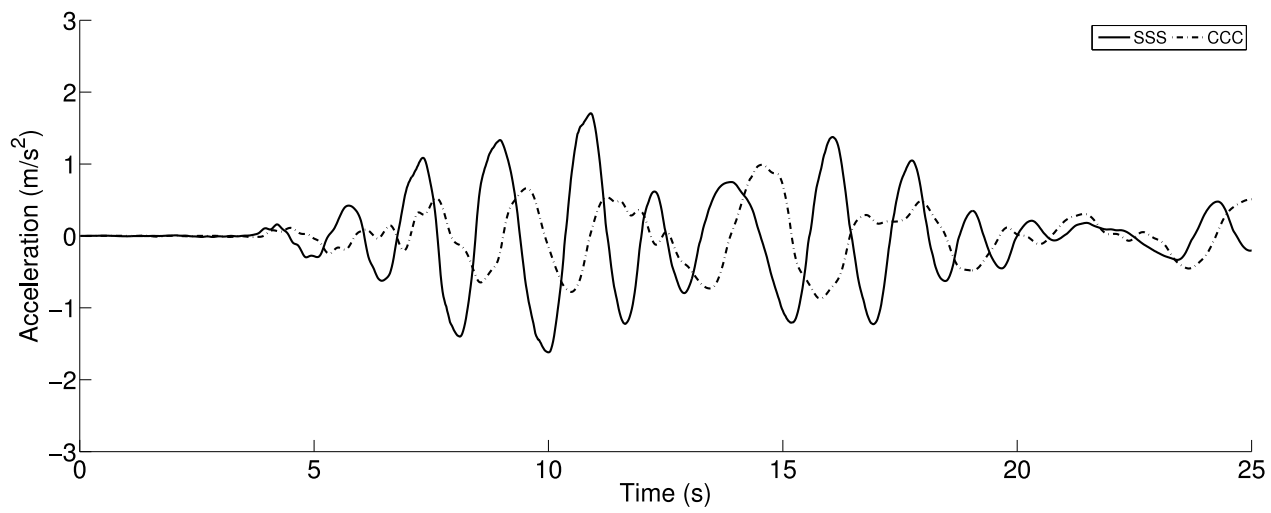


Figure 503.74: Simulated Acceleration Time Series, Northridge 1994, Century City, Comparison of Two Cases - First 25s (Structure Bent 3)

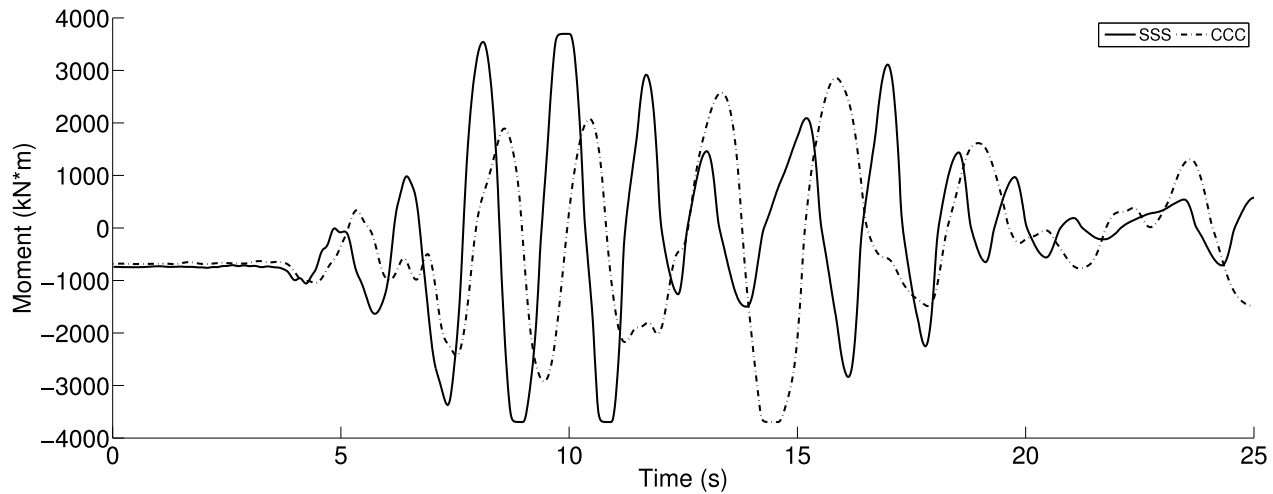


Figure 503.75: Simulated Maximum Moment Time Series, Northridge 1994, Century City, Comparison of Two Cases - First 25s (Structure Bent 1)

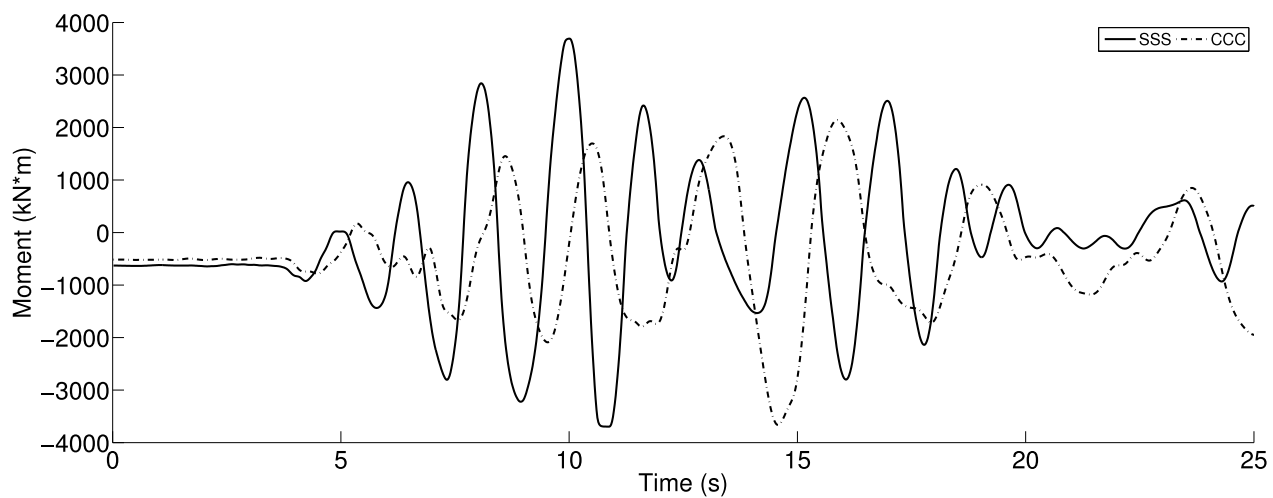


Figure 503.76: Simulated Maximum Moment Time Series, Northridge 1994, Century City, Comparison of Two Cases - First 25s (Structure Bent 2)

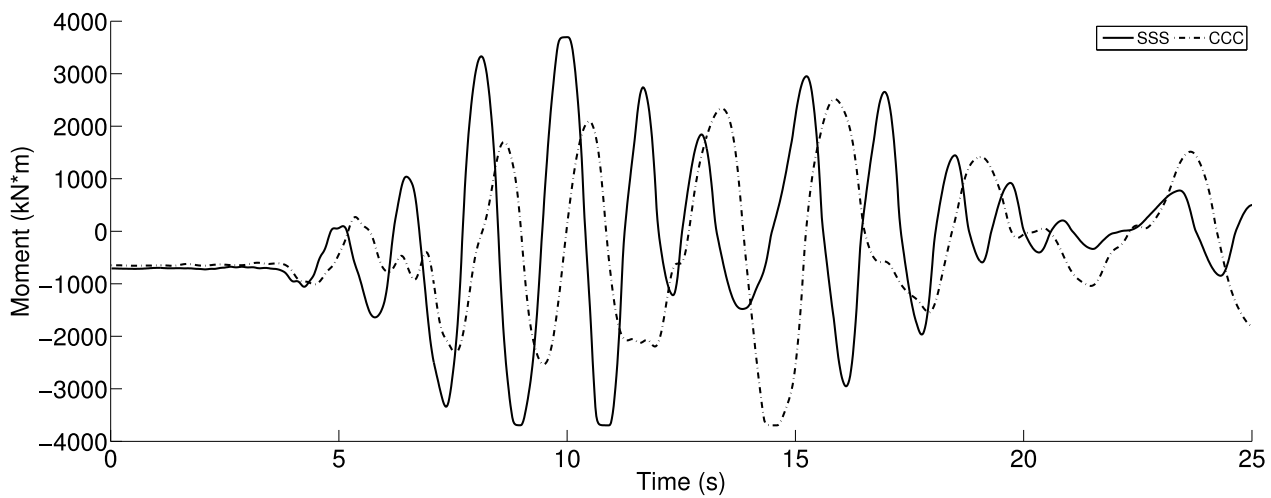


Figure 503.77: Simulated Maximum Moment Time Series, Northridge 1994, Century City, Comparison of Two Cases - First 25s (Structure Bent 3)

It has been shown in this research that if the soil layer is stiffer, structures will see much more amplification from earthquake shaking. Figures 503.72 to 503.74 show the acceleration response from ESSI systems with stiff sand and soft clay, which clearly shows that stiff sand delivers much stronger energy input to superstructures. The superstructures on top of stiffer soil also yield sooner than softer soil layers as shown in maximum moment time series Figures 503.75 to 503.77. This observation proves one interesting point that in order to improve structural stability, site improvement is not necessarily improving the dynamic resistance of the ESSI system. In later section of this work, further observation will be made to correlate this conclusion with the characteristics of the input motion.

As for the soil side, near-structure soil motion will be also affected by ESSI. So the traditional way of assuming that recorded ground motion can be used as input motion to ESSI analysis should be revisited. According to Figures 503.78 503.79 503.80, we can see that stiff soil also shows stronger surface motion records during earthquake shaking.

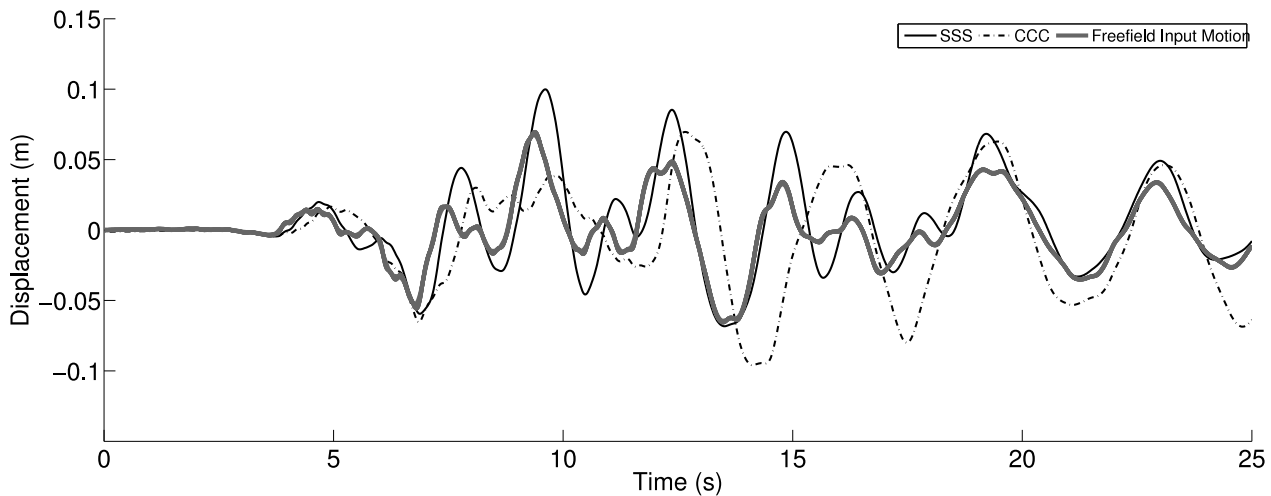
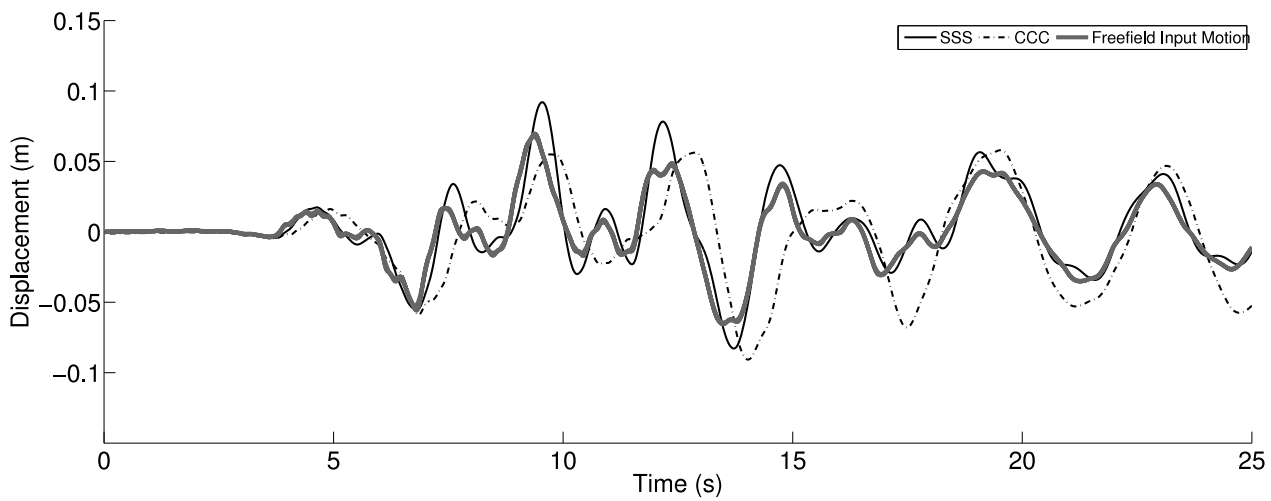


Figure 503.78: Simulated Displacement Time Series, Northridge 1994, Century City, Comparison of Two Cases - First 25s (Soil Block 1)



Jeremić et al., Real-ESSI

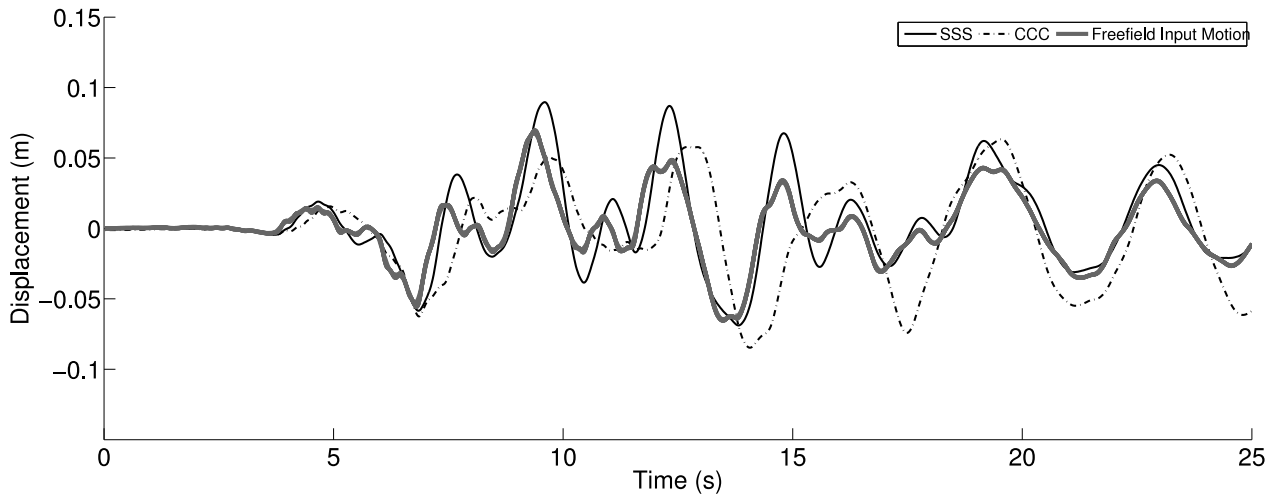


Table 503.6: Simulation Scenarios for Prototype ESSI Studies

Simulation Cases	Soil Block 1	Soil Block 2	Soil Block 3
Case 3	Stiff Sand	Soft Clay	Stiff Sand

503.2.4.2 How Site Non-Uniformity Affects ESSI

Bridge is always constructed over gulfs or bays. It is a common case that for multi-span bridge, different bents will inevitably sit on soil foundations with totally different strength. This site nonuniformity complicates design because individual structure response might be largely varied.

In order to study the effects of site non-uniformity on the dynamic response of ESSI system, Case 3 listed in Table 503.6 has been selected as the test bed of our simulation. This scenario corresponds to the case that a 4-span bridge sits on solid abutments but with much softer bay-mud type foundation in the middle of a bay.

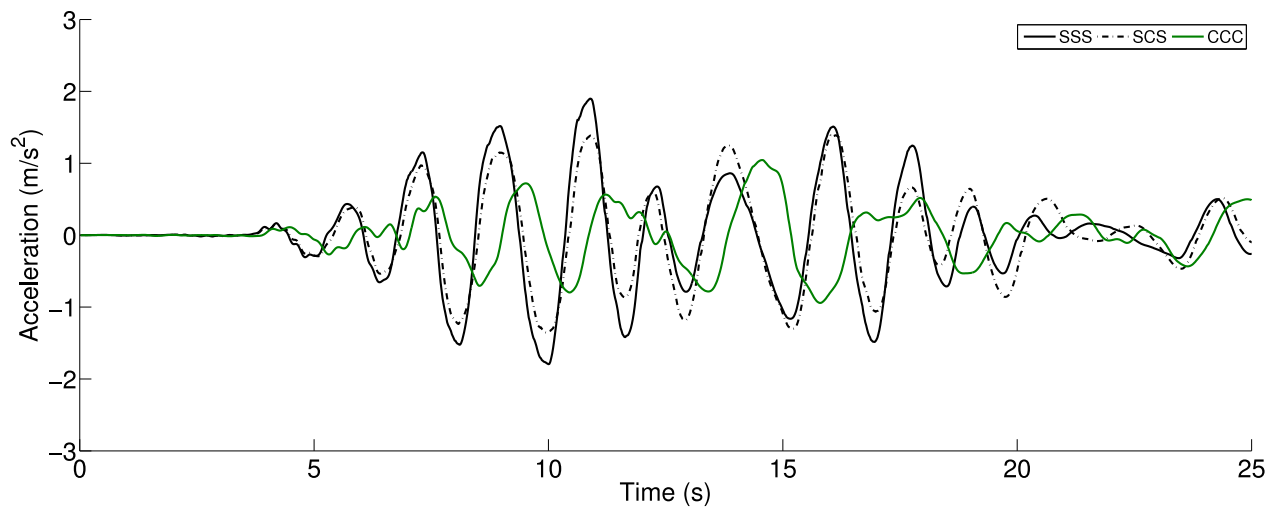


Figure 503.81: Simulated Acceleration Time Series, Northridge 1994, Century City, Comparison of Three Cases - First 25s (Structure Bent 1)

Case 3

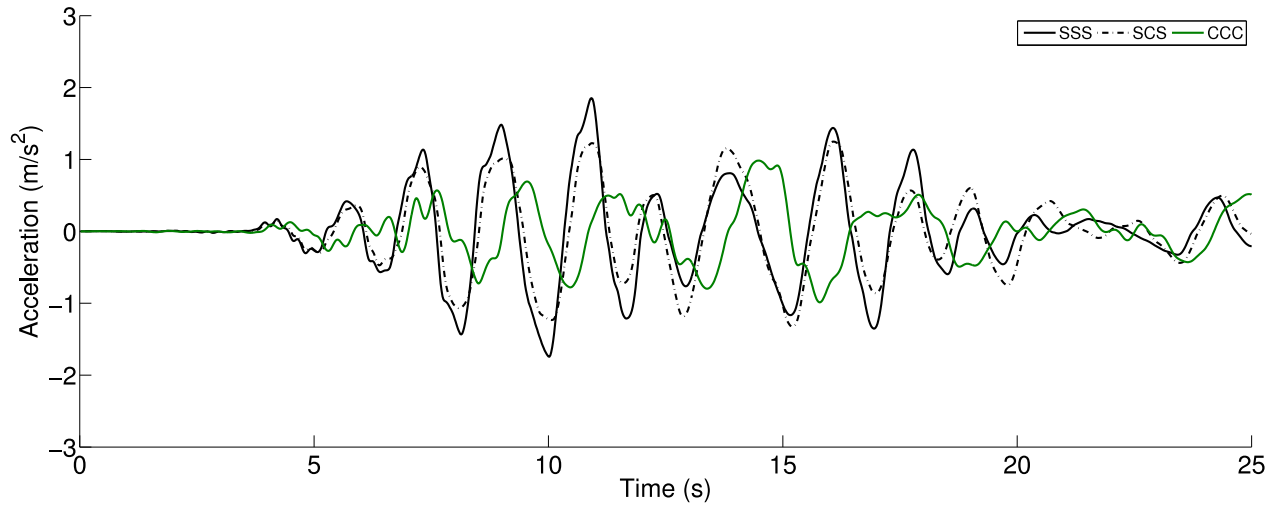


Figure 503.82: Simulated Acceleration Time Series, Northridge 1994, Century City, Comparison of Three Cases - First 25s (Structure Bent 2)

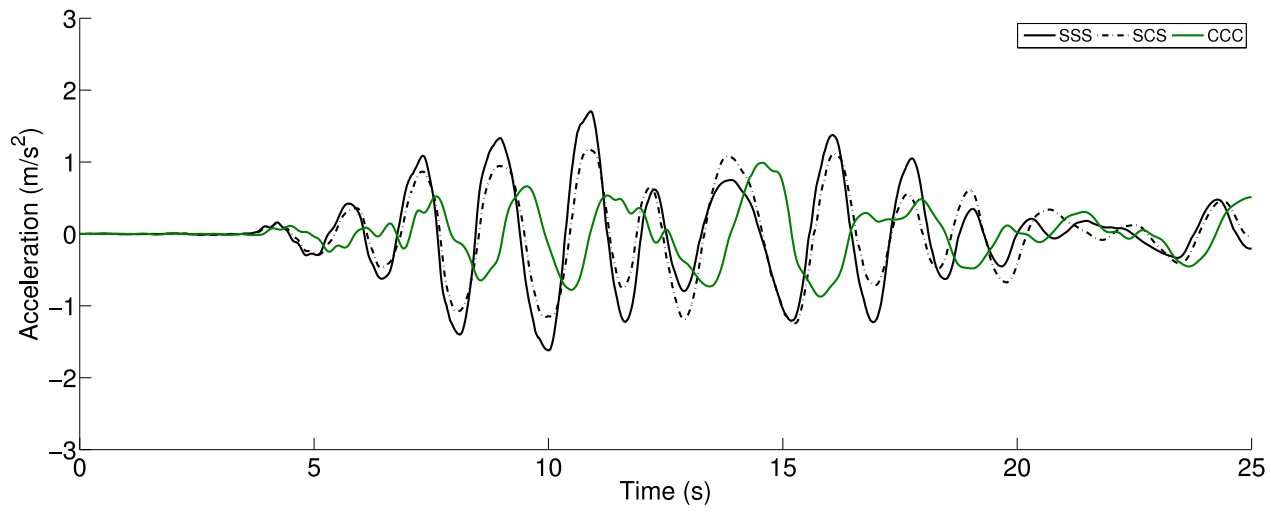


Figure 503.83: Simulated Acceleration Time Series, Northridge 1994, Century City, Comparison of Three Cases - First 25s (Structure Bent 3)

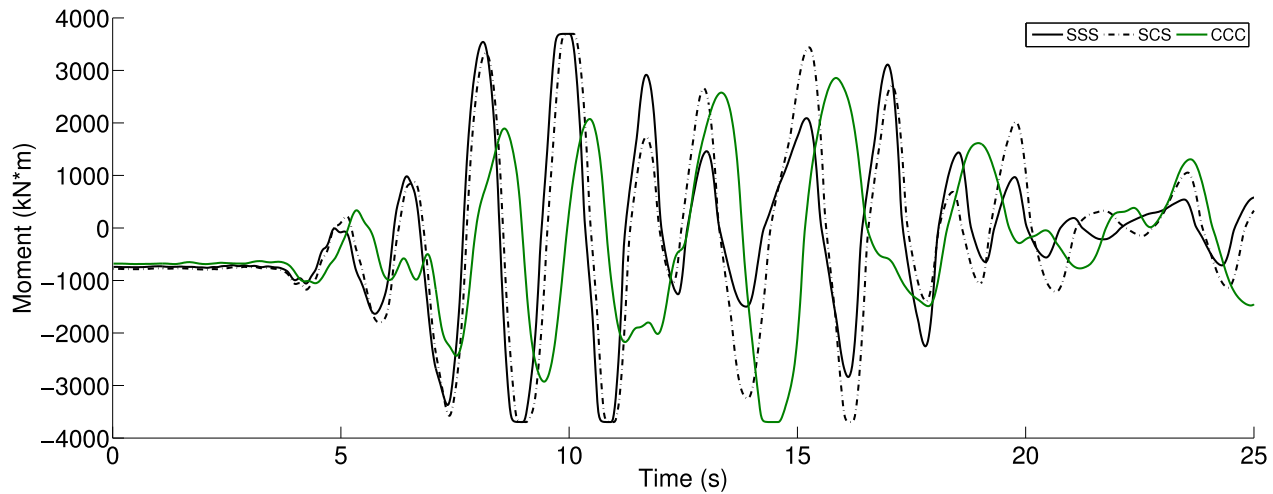


Figure 503.84: Simulated Maximum Moment Time Series, Northridge 1994, Century City, Comparison of Three Cases - First 25s (Structure Bent 1)

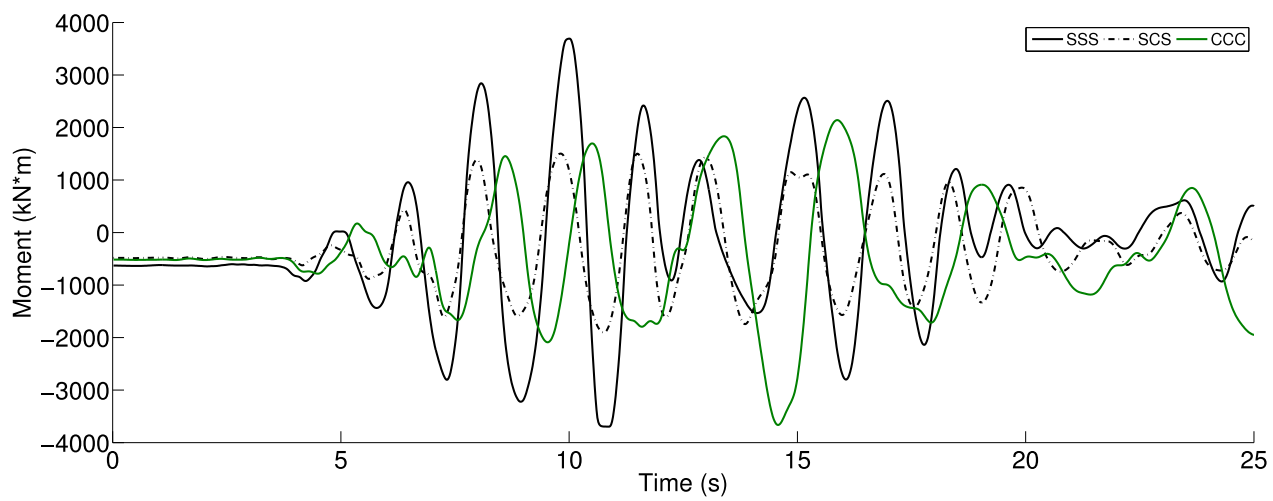


Figure 503.85: Simulated Maximum Moment Time Series, Northridge 1994, Century City, Comparison of Three Cases - First 25s (Structure Bent 2)

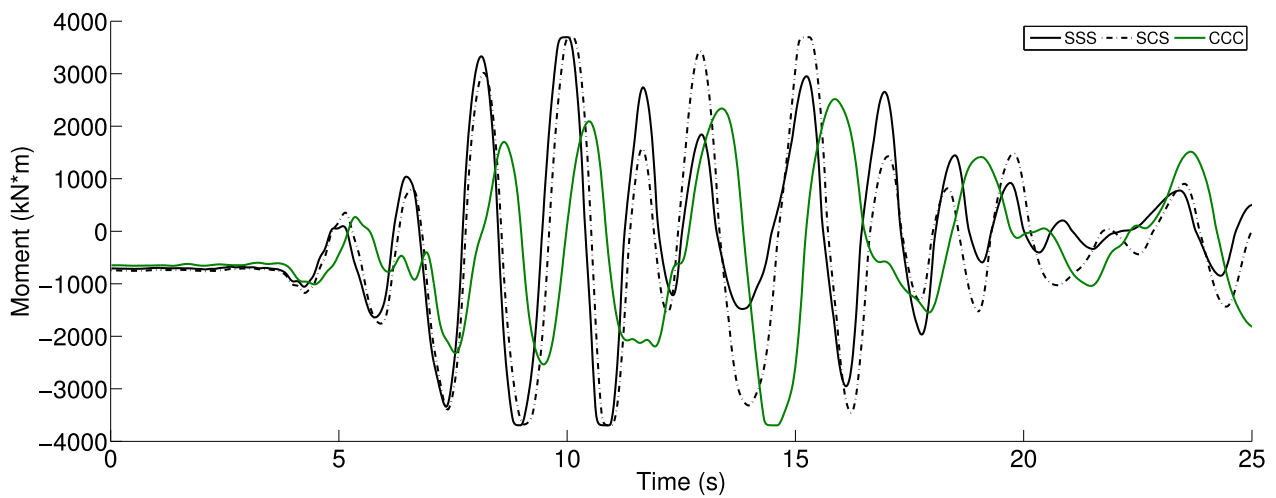


Figure 503.86: Simulated Maximum Moment Time Series, Northridge 1994, Century City, Comparison of Three Cases - First 25s (Structure Bent 3)

Table 503.7: Simulation Scenarios for Prototype ESSI Studies

Simulation Cases	Soil Block 1	Soil Block 2	Soil Block 3
Case 2	Stiff Sand	Stiff Sand	Soft Clay
Case 5	Soft Clay	Stiff Sand	Stiff Sand

From acceleration Figures 503.81, 503.82, 503.83, and moment Figures 503.84, 503.85 and 503.86, we can clearly see that due to the presence of a soft soil block, all structures show smaller magnitude in response. This is especially true for the superstructure that directly sits on top of the softer soil foundation. For Case 3 listed in Table 503.6, the superstructure (bent 2) gets much smaller response because it is right on top of clay (bay mud) foundation. As a matter of fact, the middle bent (bent 2) does not yield at all.

We want to extend this observation to other cases as listed in Table 503.7. Case 2 shows the scenario that the soil foundation supporting bent 3 is soft bay mud, while Case 5 shows it for bent 1.

The same reasoning can be applied to these similar cases. Figures 503.87 to 503.92 show the results of Case 2 and Figures 503.93 to 503.98 for Case 5.

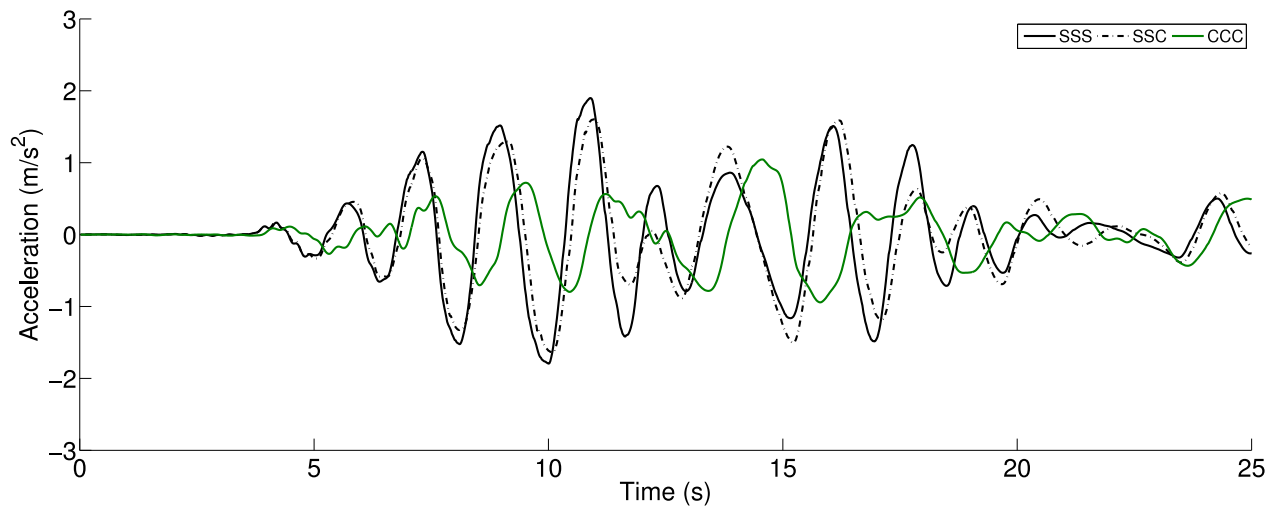


Figure 503.87: Simulated Acceleration Time Series, Northridge 1994, Century City, Comparison of Three Cases - First 25s (Structure Bent 1)

Case 2

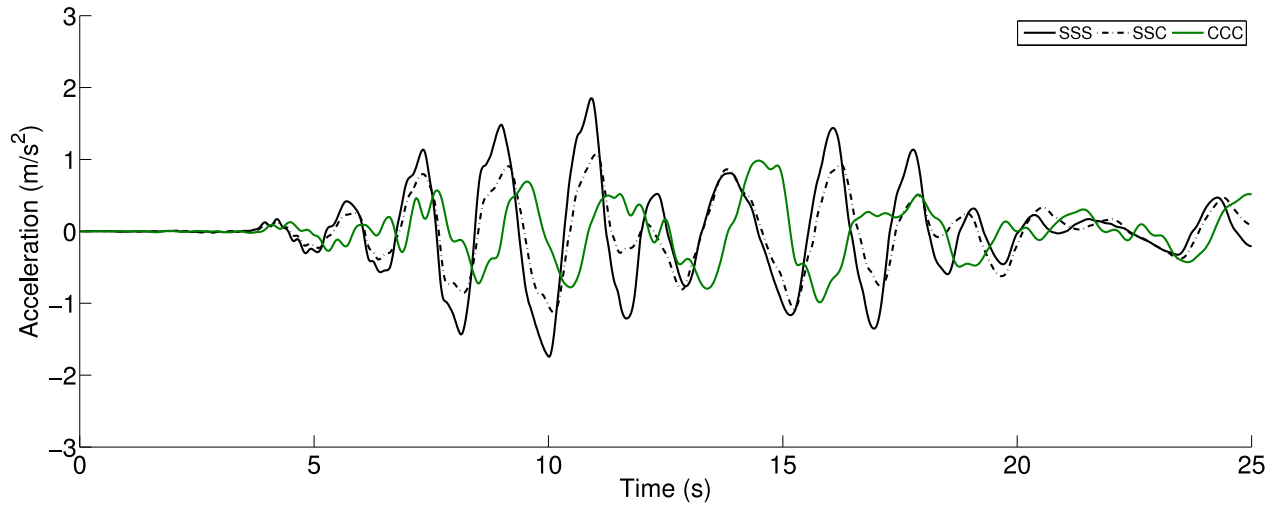


Figure 503.88: Simulated Acceleration Time Series, Northridge 1994, Century City, Comparison of Three Cases - First 25s (Structure Bent 2)

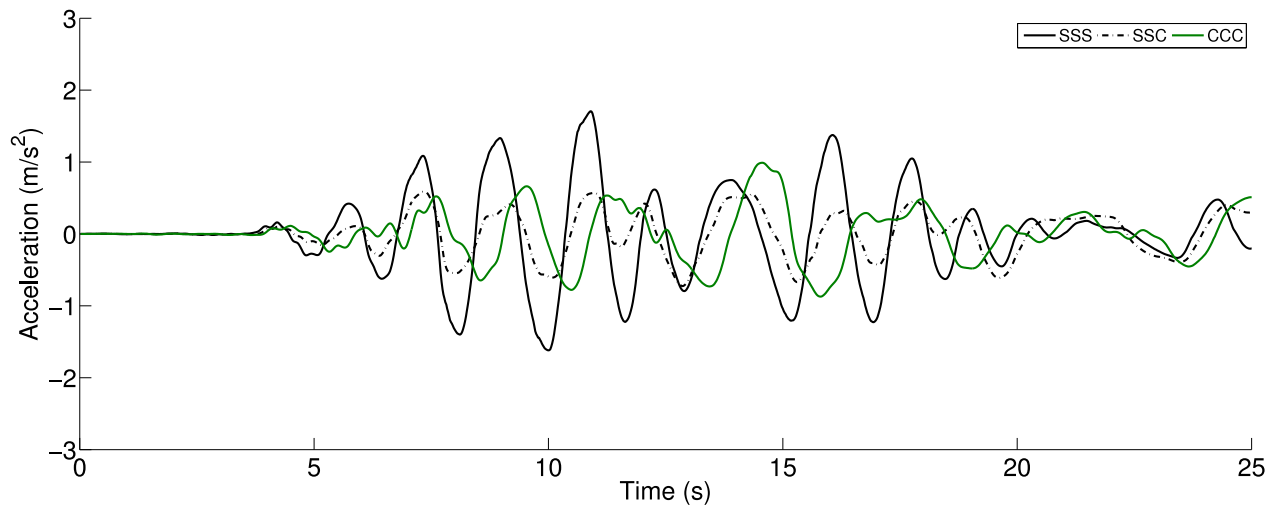


Figure 503.89: Simulated Acceleration Time Series, Northridge 1994, Century City, Comparison of Three Cases - First 25s (Structure Bent 3)

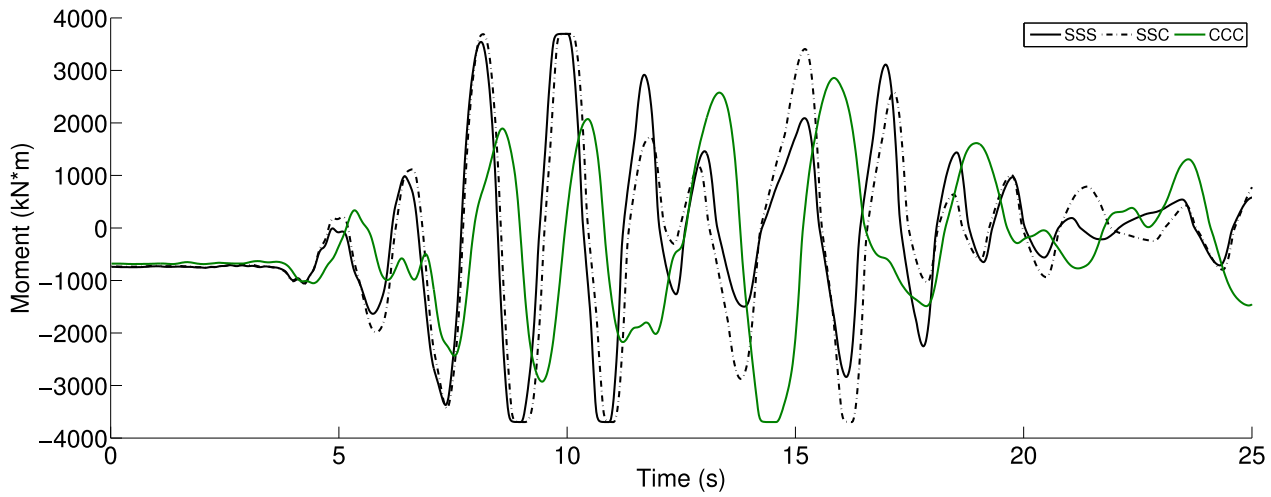


Figure 503.90: Simulated Maximum Moment Time Series, Northridge 1994, Century City, Comparison of Three Cases - First 25s (Structure Bent 1)

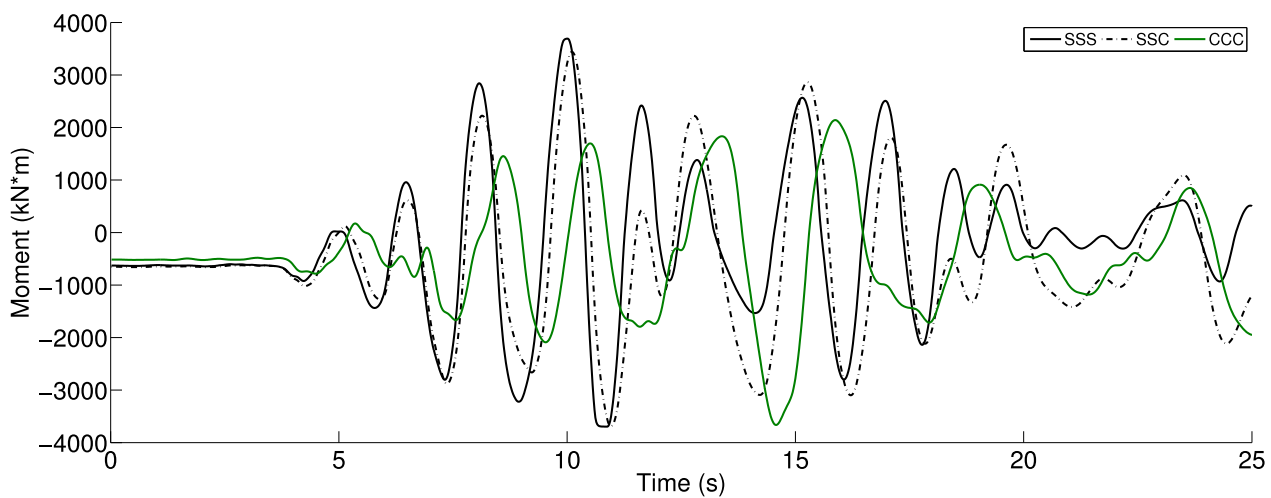


Figure 503.91: Simulated Maximum Moment Time Series, Northridge 1994, Century City, Comparison of Three Cases - First 25s (Structure Bent 2)

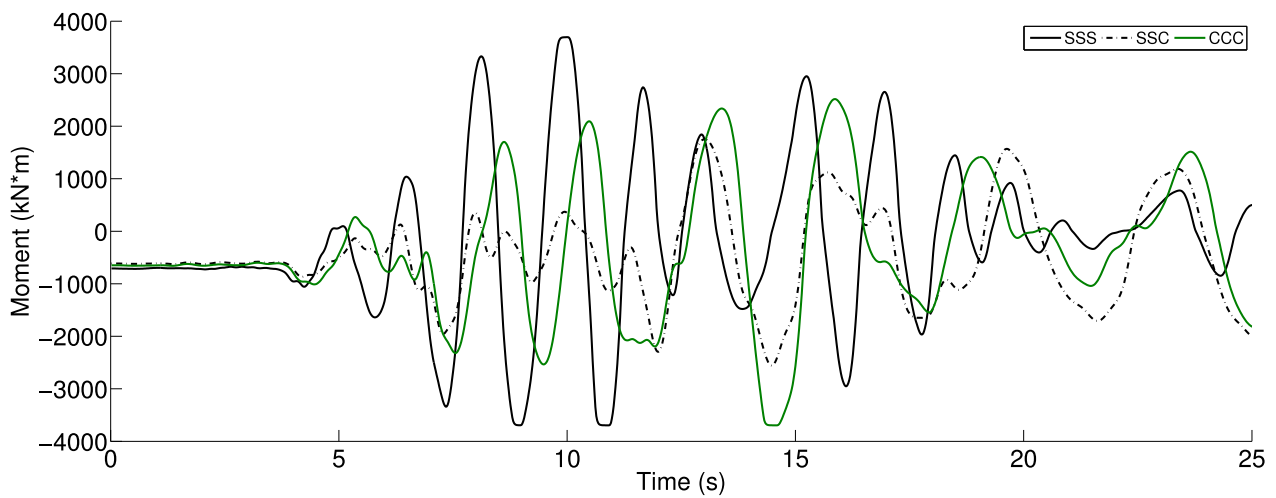


Figure 503.92: Simulated Maximum Moment Time Series, Northridge 1994, Century City, Comparison of Three Cases - First 25s (Structure Bent 3)

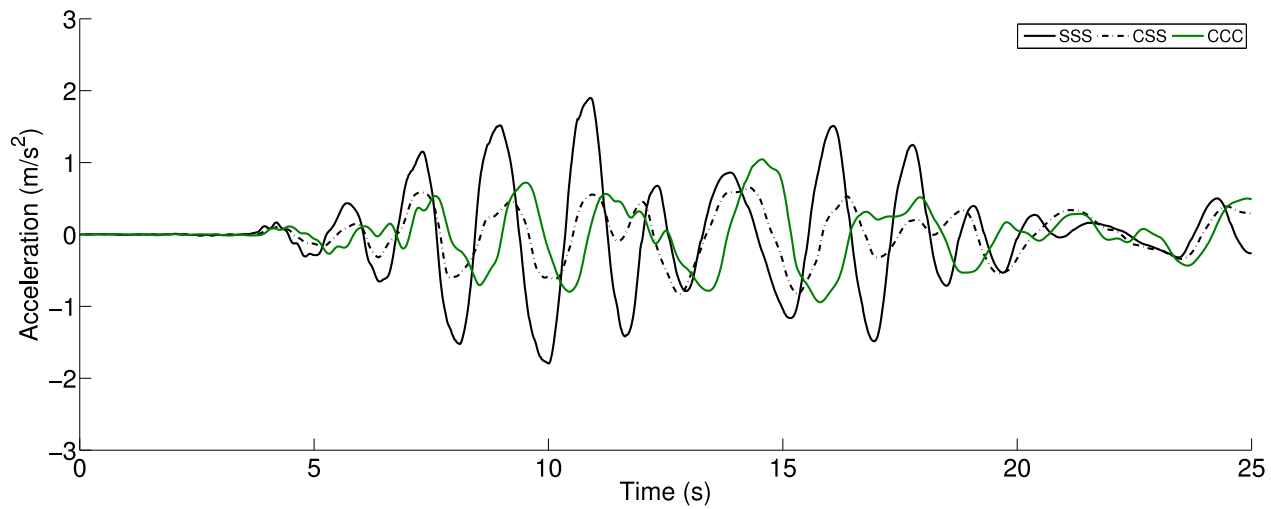


Figure 503.93: Simulated Acceleration Time Series, Northridge 1994, Century City, Comparison of Three Cases - First 25s (Structure Bent 1)

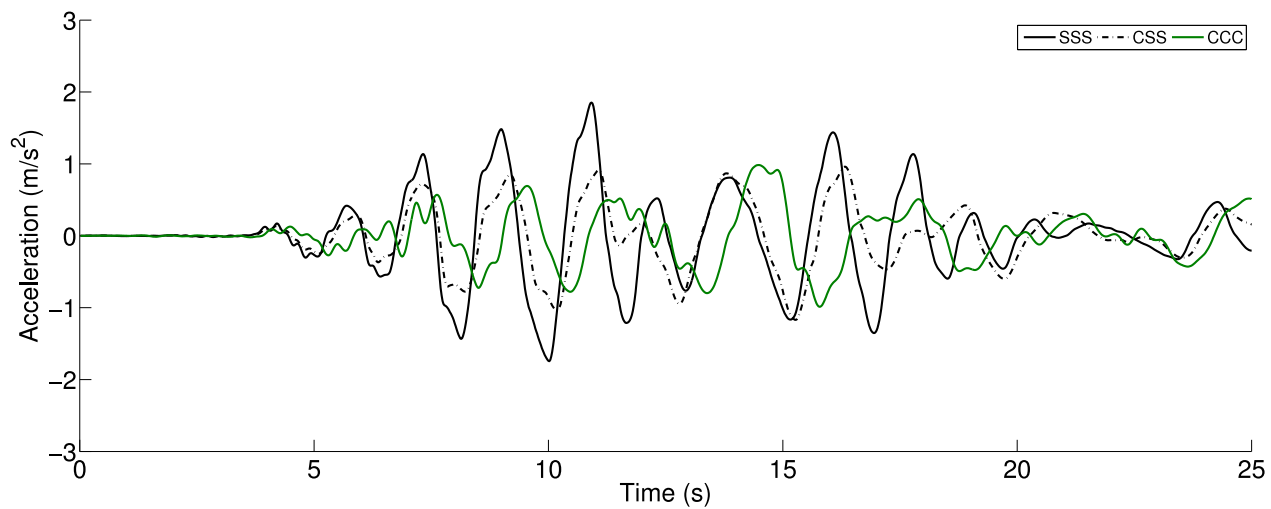


Figure 503.94: Simulated Acceleration Time Series, Northridge 1994, Century City, Comparison of Three Cases - First 25s (Structure Bent 2)

Case 5

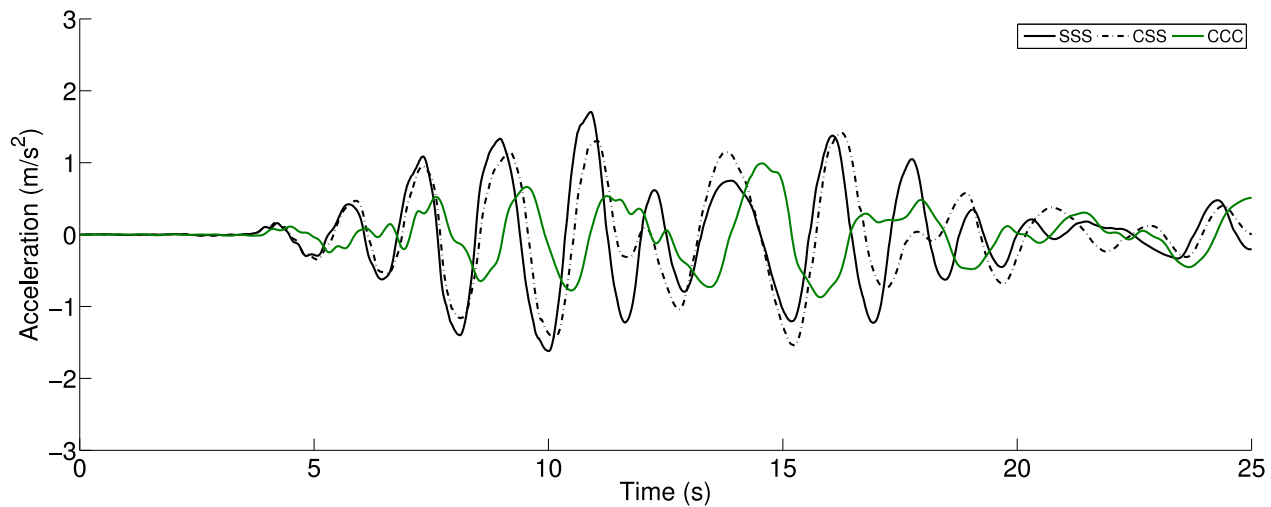


Figure 503.95: Simulated Acceleration Time Series, Northridge 1994, Century City, Comparison of Three Cases - First 25s (Structure Bent 3)

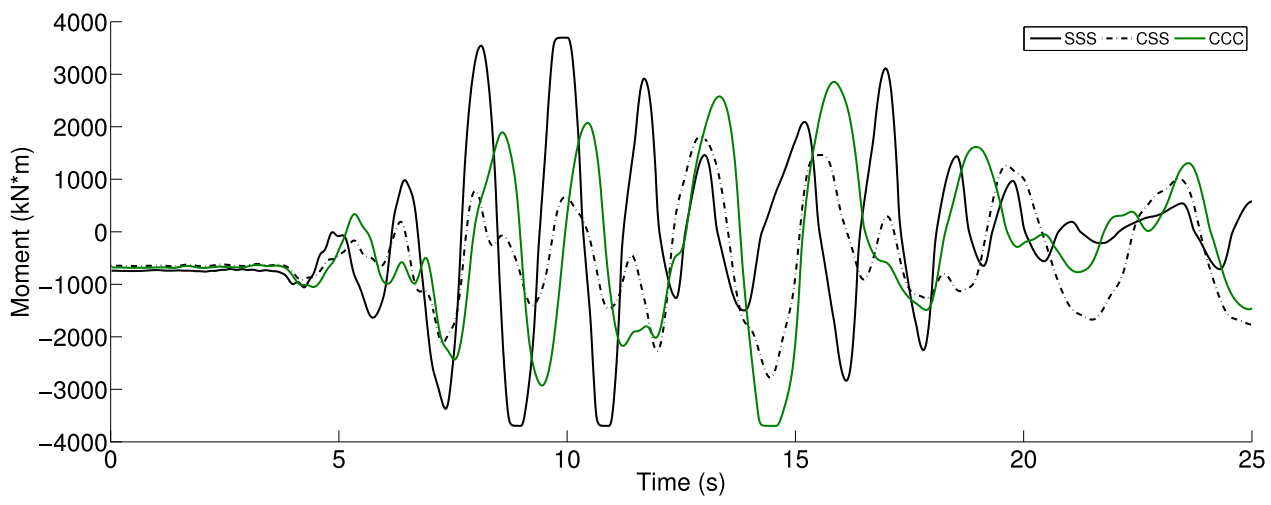


Figure 503.96: Simulated Maximum Moment Time Series, Northridge 1994, Century City, Comparison of Three Cases - First 25s (Structure Bent 1)

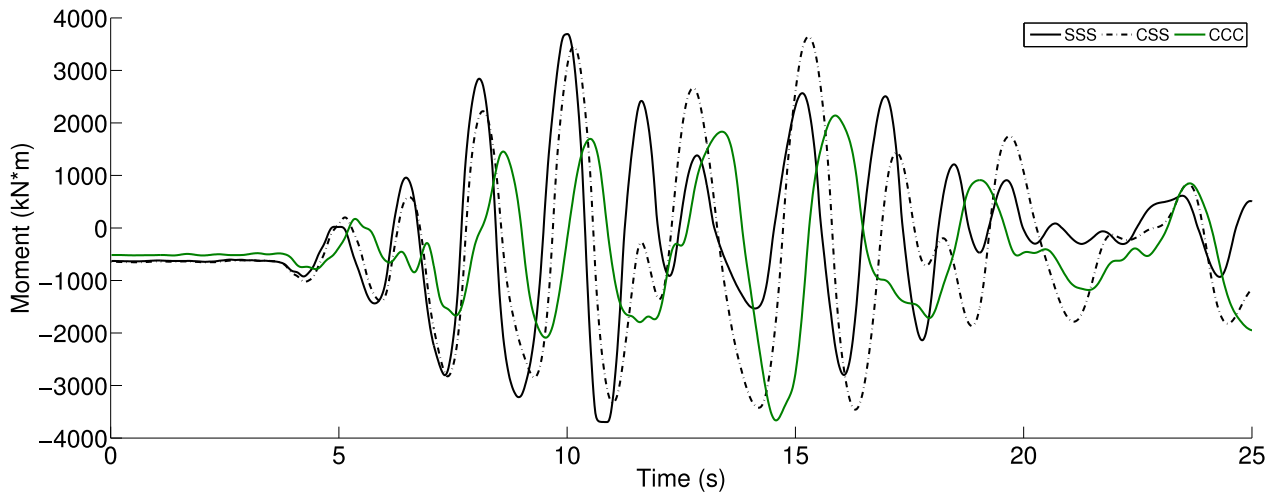


Figure 503.97: Simulated Maximum Moment Time Series, Northridge 1994, Century City, Comparison of Three Cases - First 25s (Structure Bent 2)

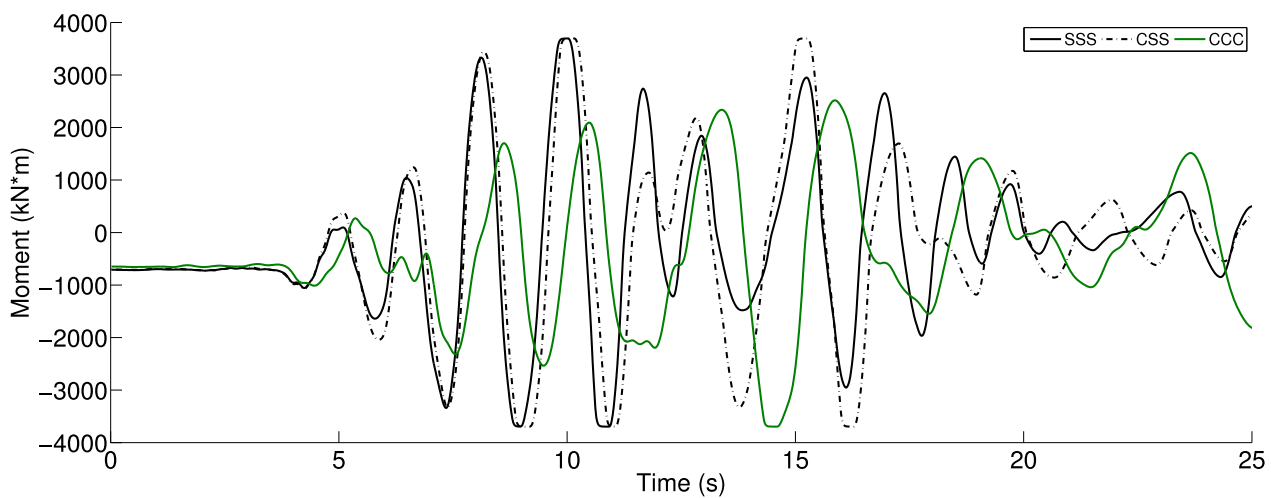


Figure 503.98: Simulated Maximum Moment Time Series, Northridge 1994, Century City, Comparison of Three Cases - First 25s (Structure Bent 3)

Table 503.8: Simulation Scenarios for Prototype ESSI Studies

Simulation Cases	Soil Block 1	Soil Block 2	Soil Block 3
Case 4	Stiff Sand	Soft Clay	Soft Clay
Case 6	Soft Clay	Stiff Sand	Soft Clay
Case 7	Soft Clay	Soft Clay	Stiff Sand

As a final conclusion, if there exists one substantially weaker soil layer for the ESSI system, the dynamic response for the whole ESSI system will be attenuated. The structure that directly sits on top of the soft soil block will receive significantly smaller excitation during earthquake shakings.

The other side of story can be also formulated using results obtained in this work. What if there is a substantially stronger soil foundation in the ESSI system? It would be worthwhile exploring the other side of reasoning. In this work, three other cases have been used to observe how the ESSI system will behave for the cases that one soil block is much stronger than the other blocks as listed in Table 503.8.

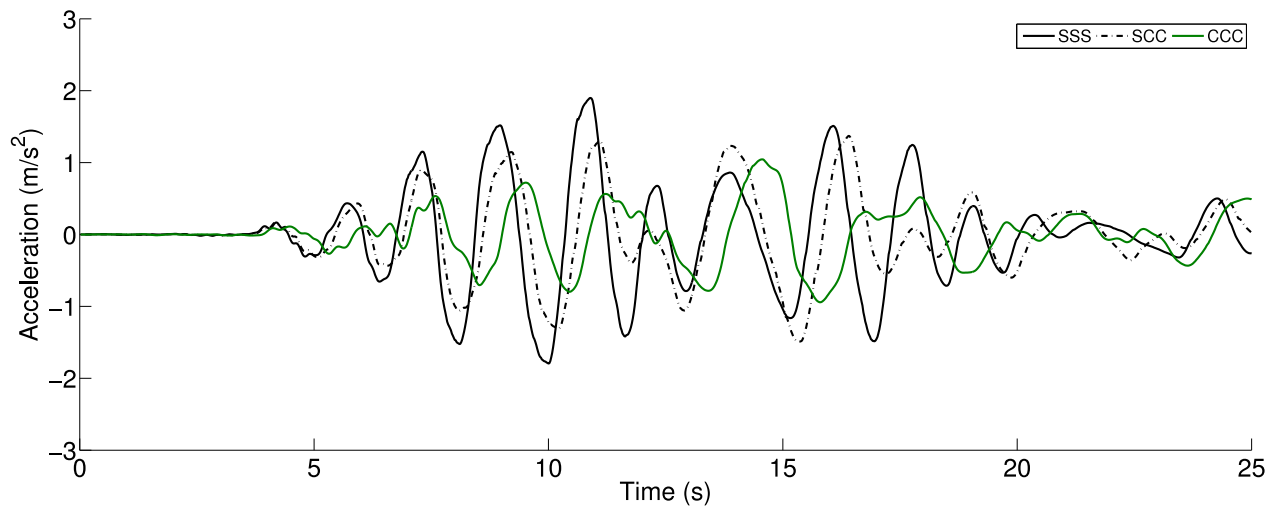


Figure 503.99: Simulated Acceleration Time Series, Northridge 1994, Century City, Comparison of Three Cases - First 25s (Structure Bent 1)

Case 4

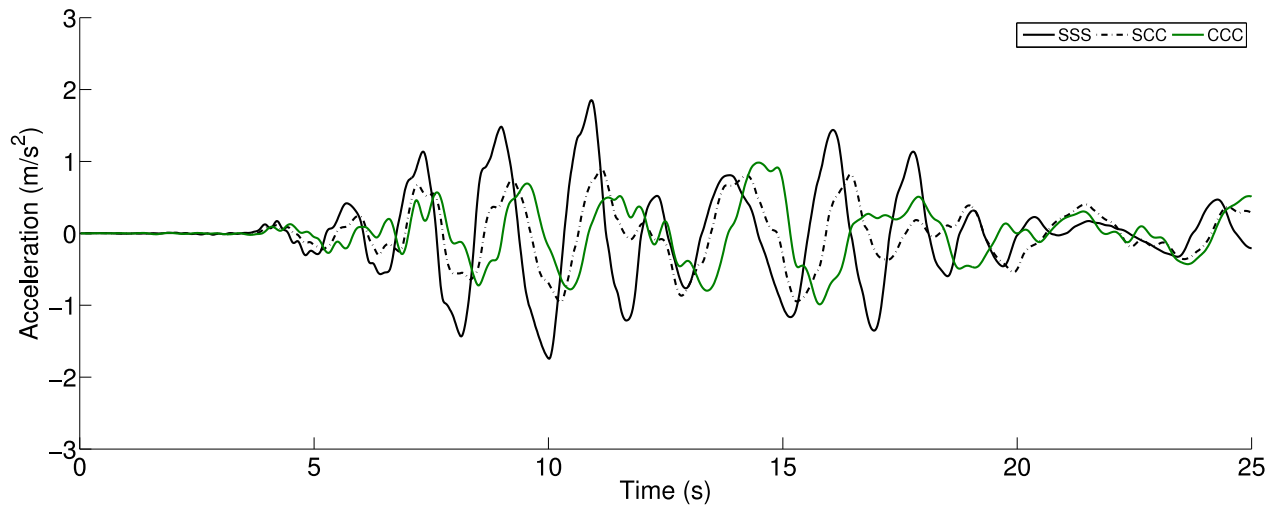


Figure 503.100: Simulated Acceleration Time Series, Northridge 1994, Century City, Comparison of Three Cases - First 25s (Structure Bent 2)

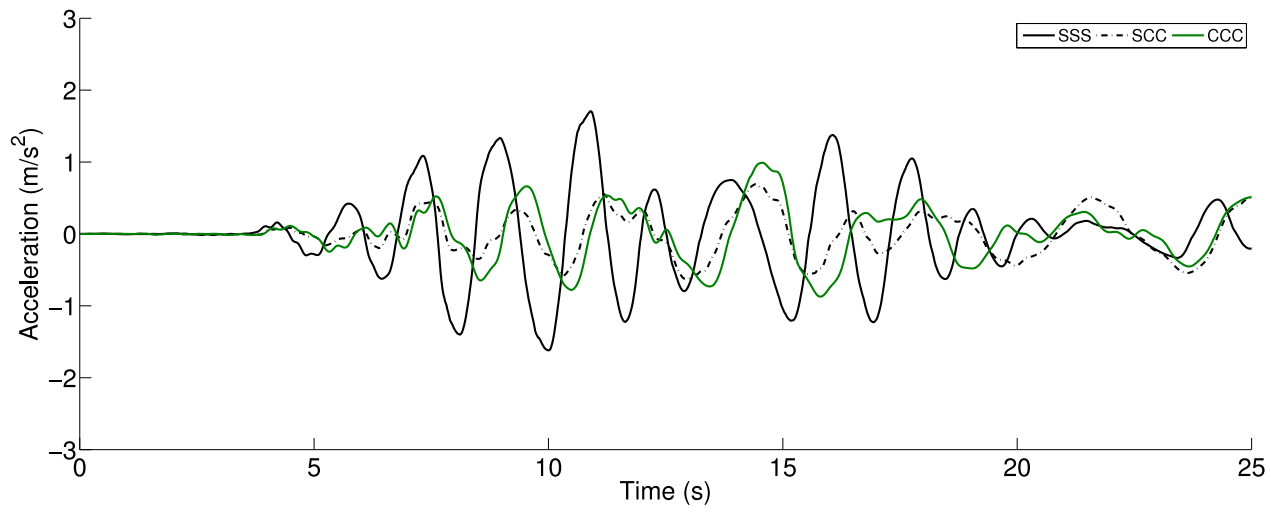


Figure 503.101: Simulated Acceleration Time Series, Northridge 1994, Century City, Comparison of Three Cases - First 25s (Structure Bent 3)

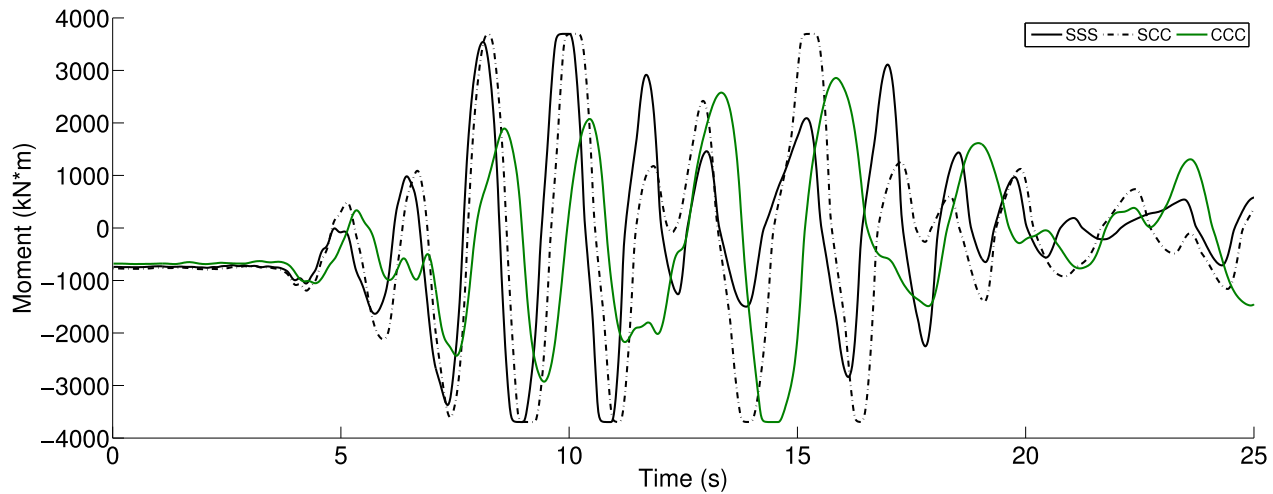


Figure 503.102: Simulated Maximum Moment Time Series, Northridge 1994, Century City, Comparison of Three Cases - First 25s (Structure Bent 1)

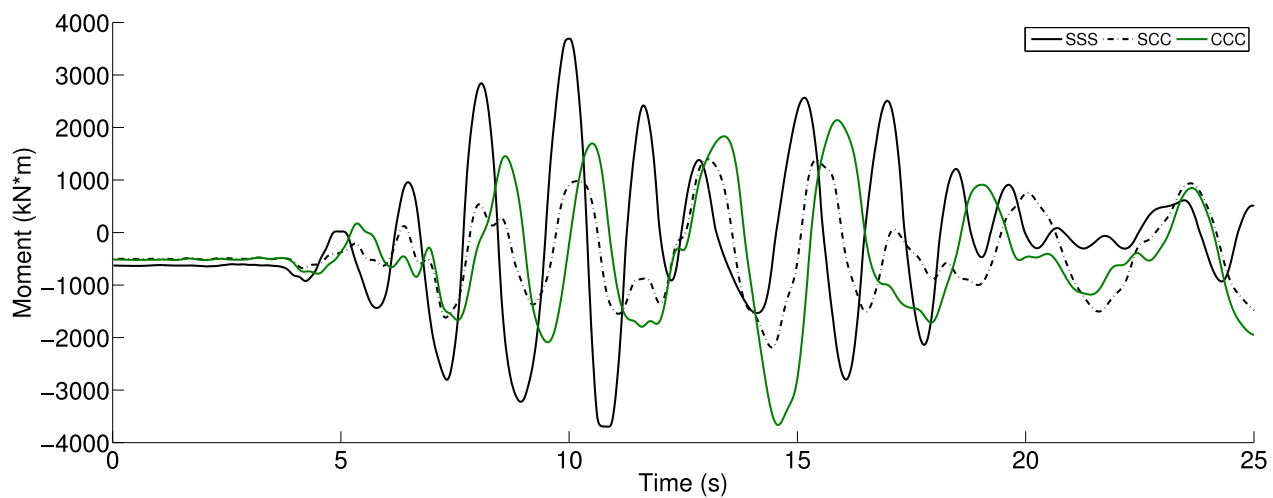


Figure 503.103: Simulated Maximum Moment Time Series, Northridge 1994, Century City, Comparison of Three Cases - First 25s (Structure Bent 2)

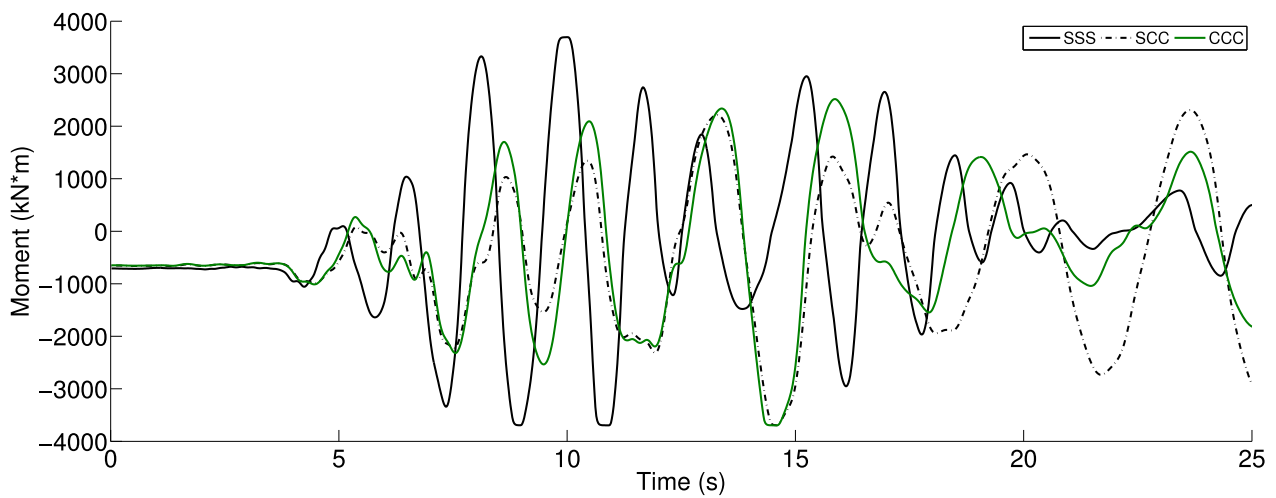


Figure 503.104: Simulated Maximum Moment Time Series, Northridge 1994, Century City, Comparison of Three Cases - First 25s (Structure Bent 3)

It can easily be seen from Figures 503.99 to 503.104 that the structure on top of the strong soil block will exhibit much bigger response and while the other structures sitting on weaker soil blocks will not get much shaking at all.

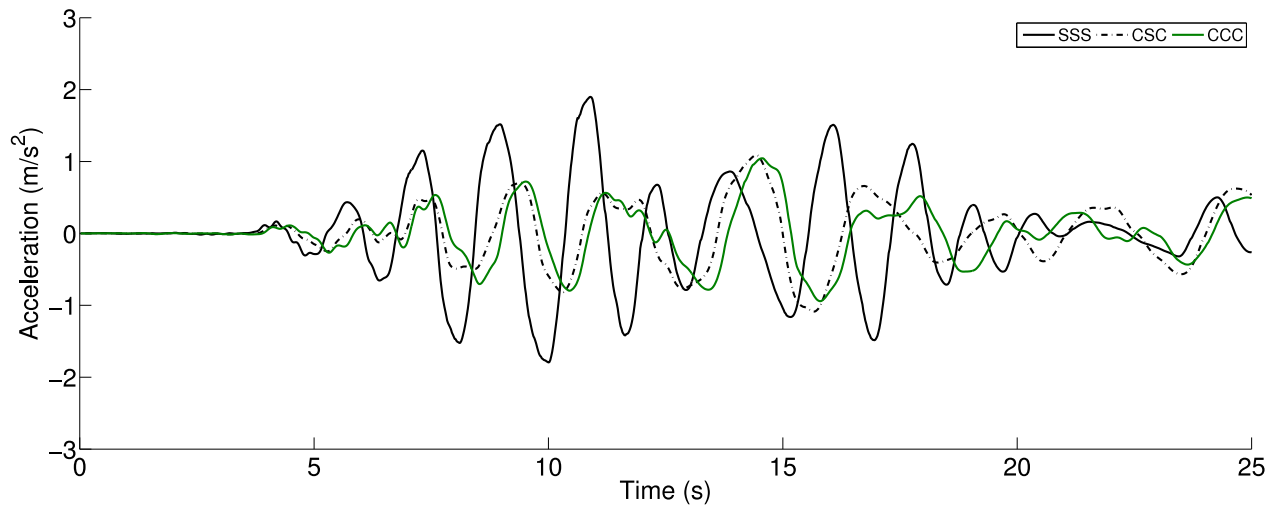


Figure 503.105: Simulated Acceleration Time Series, Northridge 1994, Century City, Comparison of Three Cases - First 25s (Structure Bent 1)

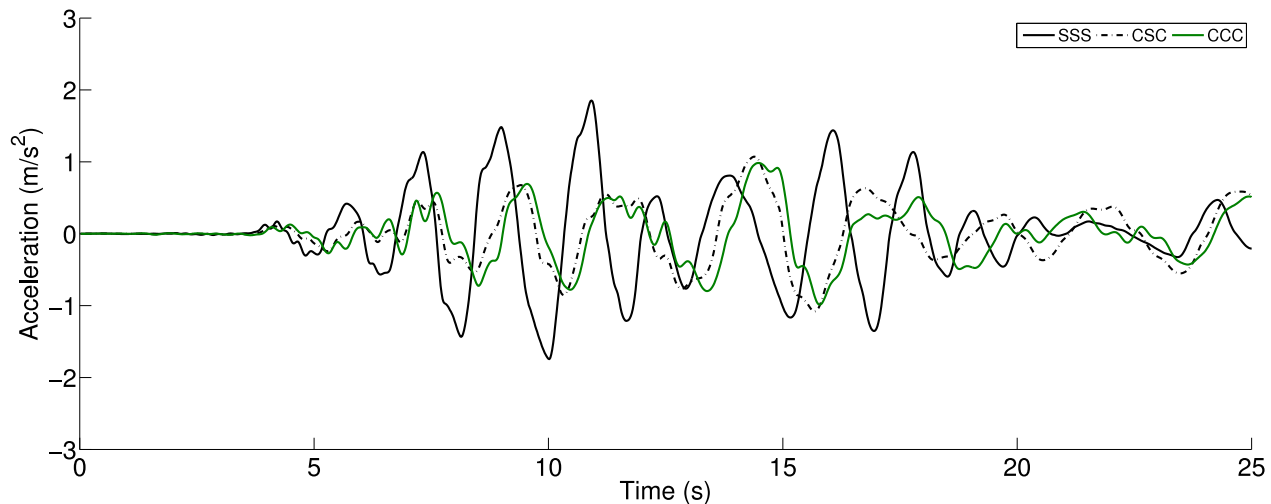


Figure 503.106: Simulated Acceleration Time Series, Northridge 1994, Century City, Comparison of Three Cases - First 25s (Structure Bent 2)

Case 6

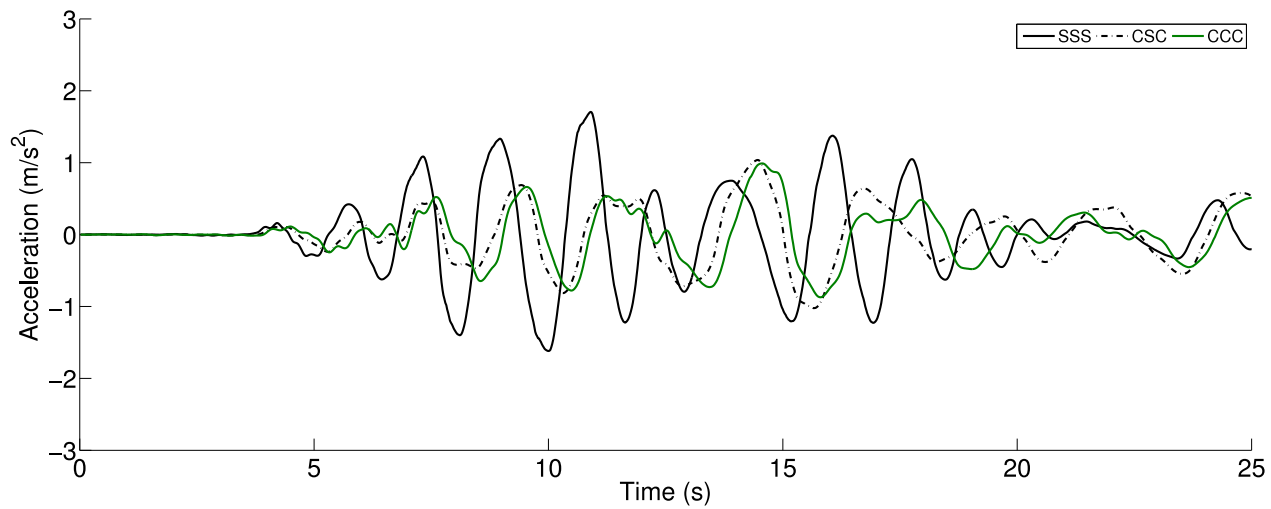


Figure 503.107: Simulated Acceleration Time Series, Northridge 1994, Century City, Comparison of Three Cases - First 25s (Structure Bent 3)

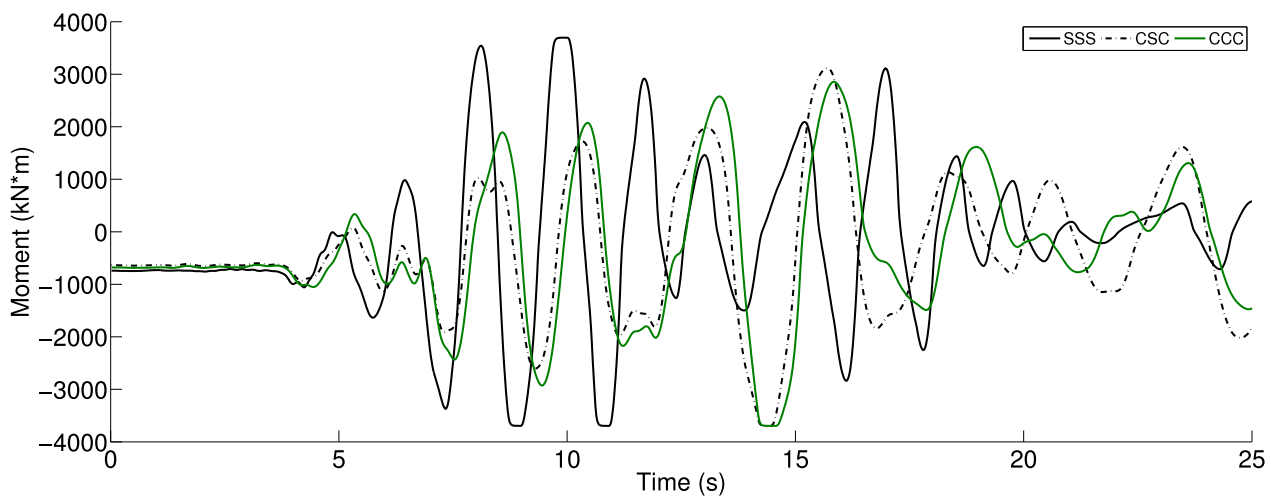


Figure 503.108: Simulated Maximum Moment Time Series, Northridge 1994, Century City, Comparison of Three Cases - First 25s (Structure Bent 1)

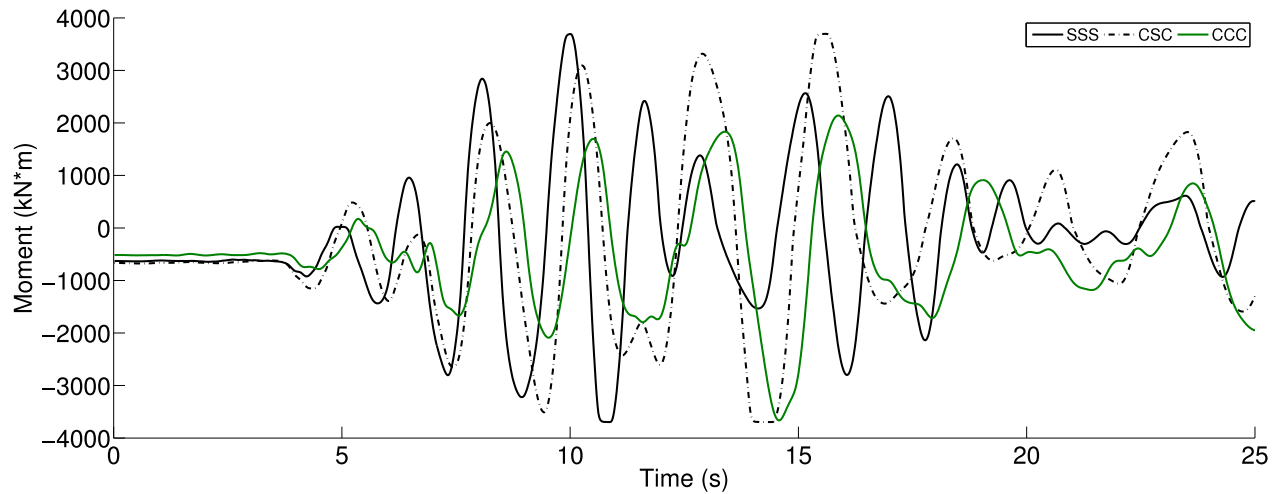


Figure 503.109: Simulated Maximum Moment Time Series, Northridge 1994, Century City, Comparison of Three Cases - First 25s (Structure Bent 2)

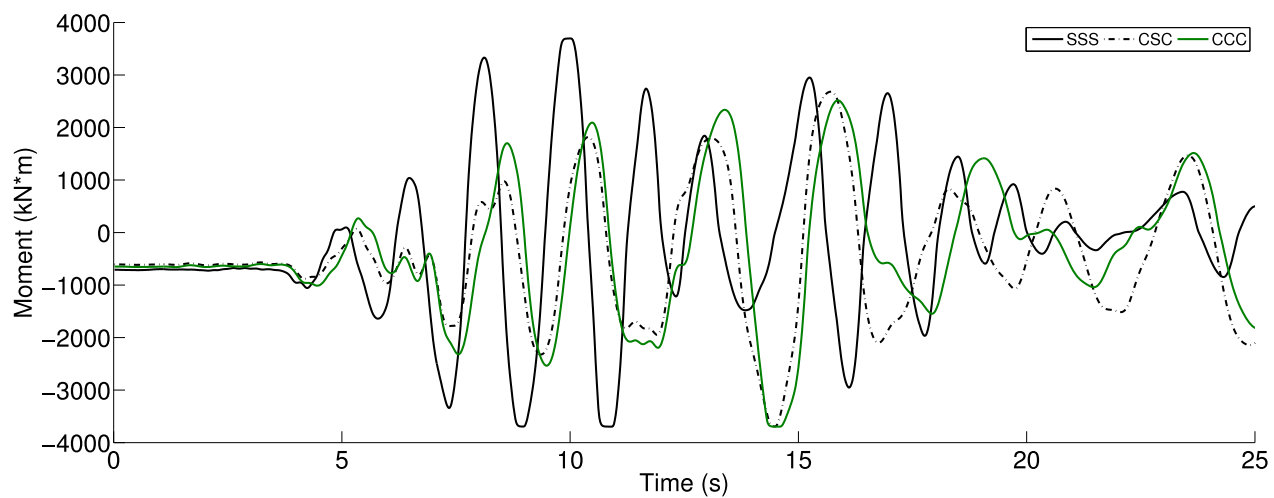


Figure 503.110: Simulated Maximum Moment Time Series, Northridge 1994, Century City, Comparison of Three Cases - First 25s (Structure Bent 3)

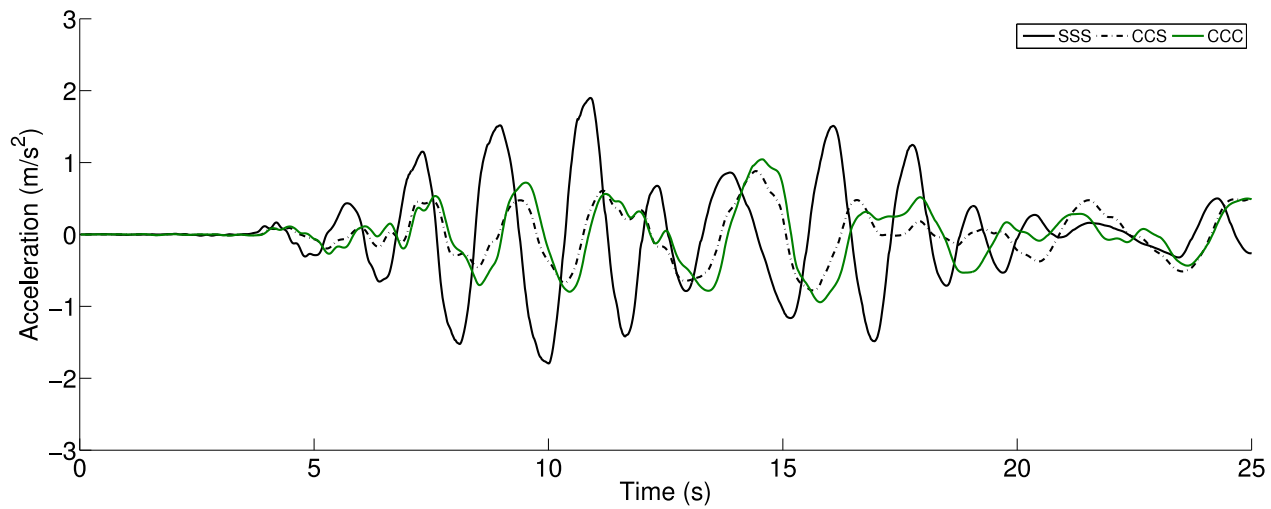


Figure 503.111: Simulated Acceleration Time Series, Northridge 1994, Century City, Comparison of Three Cases - First 25s (Structure Bent 1)

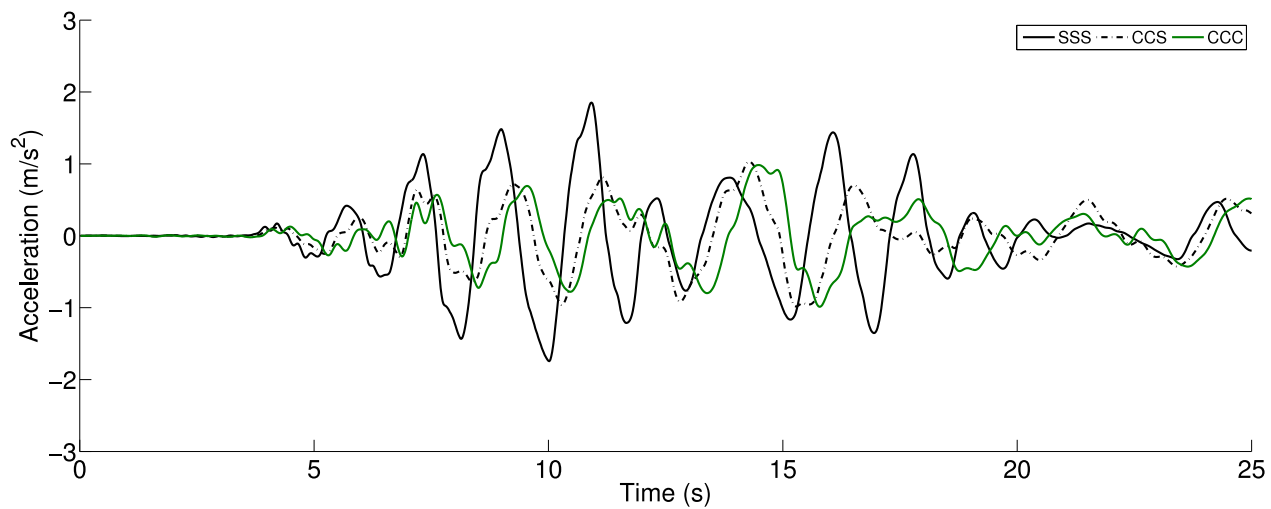


Figure 503.112: Simulated Acceleration Time Series, Northridge 1994, Century City, Comparison of Three Cases - First 25s (Structure Bent 2)

Case 7

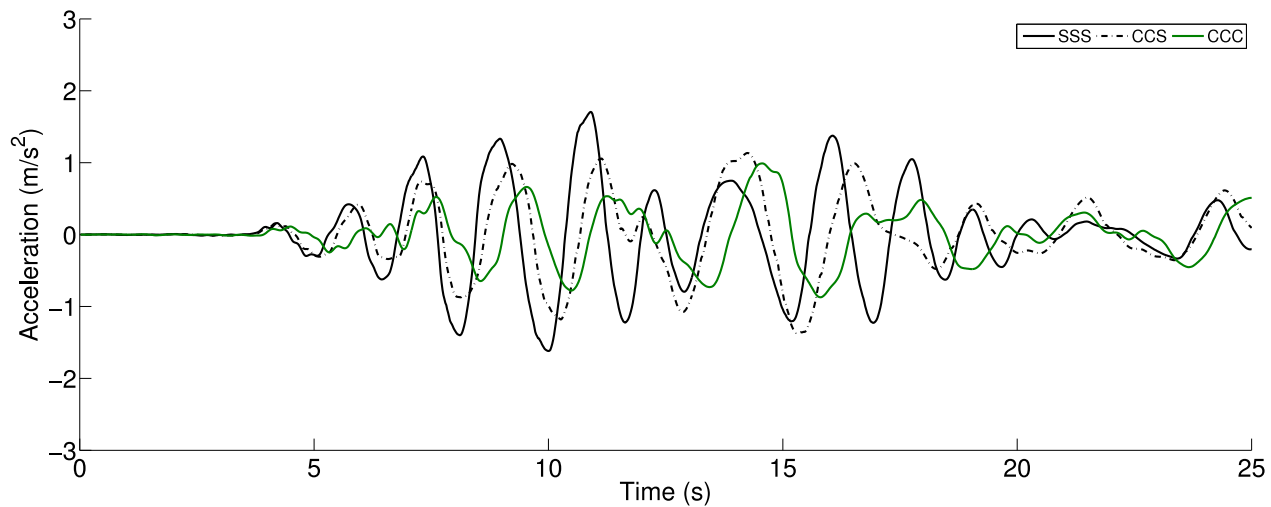


Figure 503.113: Simulated Acceleration Time Series, Northridge 1994, Century City, Comparison of Three Cases - First 25s (Structure Bent 3)

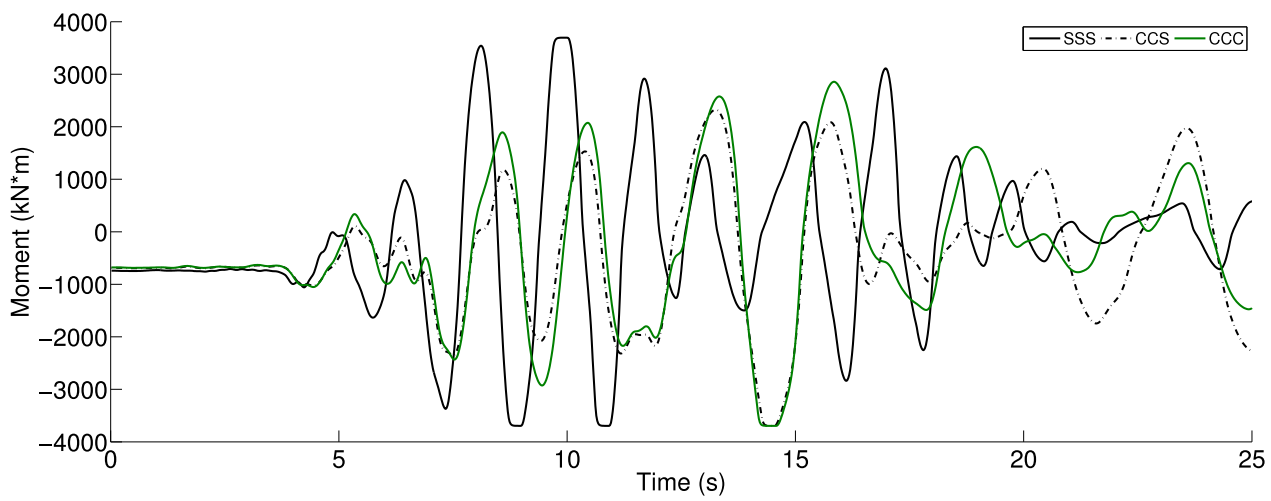


Figure 503.114: Simulated Maximum Moment Time Series, Northridge 1994, Century City, Comparison of Three Cases - First 25s (Structure Bent 1)

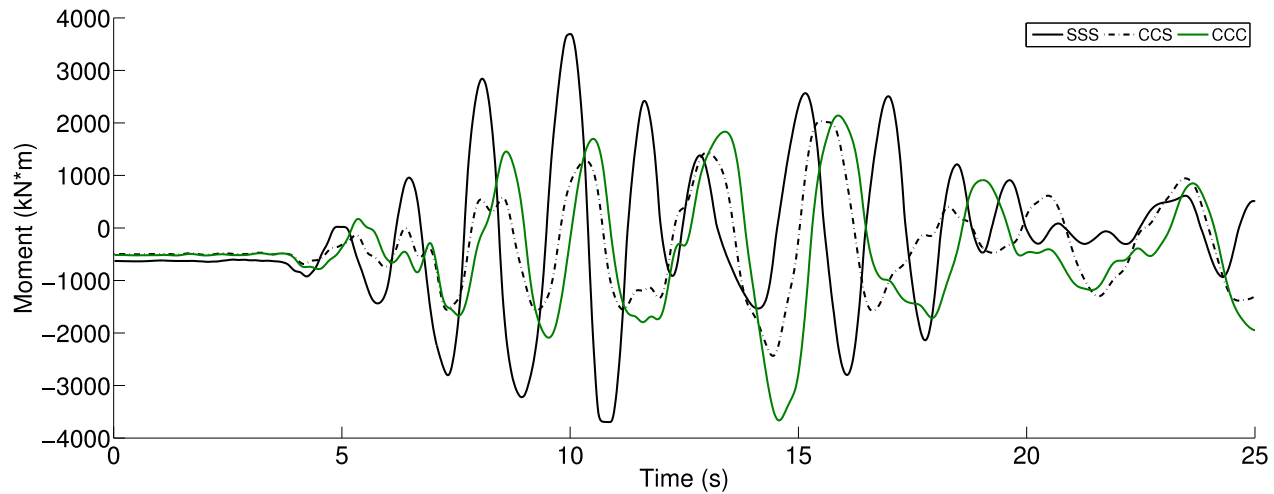


Figure 503.115: Simulated Maximum Moment Time Series, Northridge 1994, Century City, Comparison of Three Cases - First 25s (Structure Bent 2)

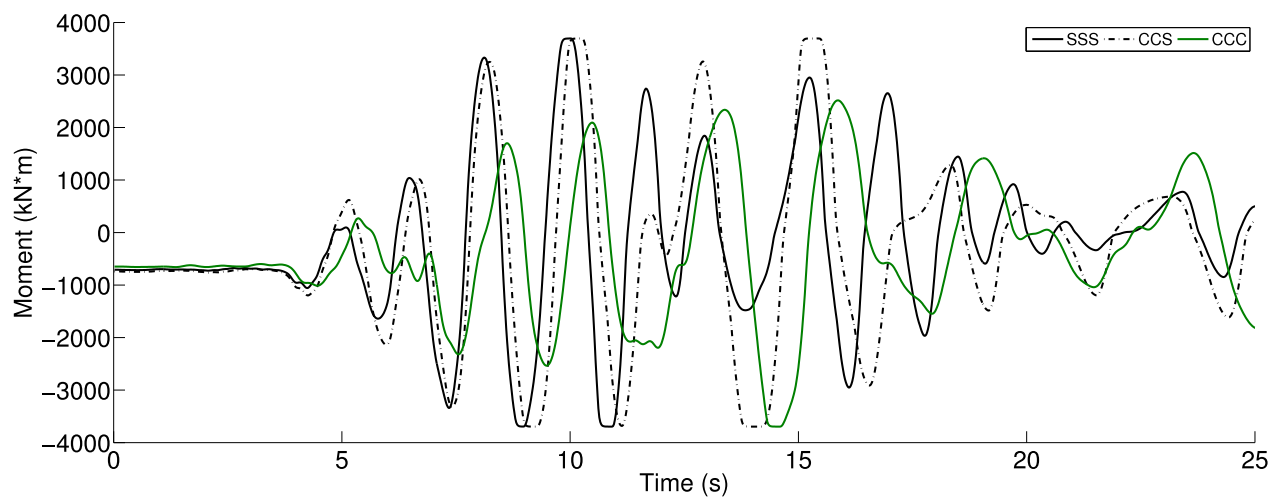


Figure 503.116: Simulated Maximum Moment Time Series, Northridge 1994, Century City, Comparison of Three Cases - First 25s (Structure Bent 3)

As a conclusion, dynamic behaviors of the ESSI system on non-uniform sites can be much more complicated than the uniform case. Generally speaking, the existence of soft soil foundation will attenuate the dynamic response of the whole ESSI system. The structure supported by soft soil block will see far less shakings than the ones supported by stiff soil. From the design perspective, the structure on top of strong soil foundations should be designed to higher safety with larger margin.

503.2.4.3 How Input Motion Affects ESSI

All the results have been shown in previous section, the purpose is to investigate how the whole ESSI system will respond to excitations with different predominant frequency.

From Figure 503.117 and 503.118, we can clearly see the difference in frequency contents of the two ground motions studied. The 1999 Turkey Kocaeli earthquake contains more long period components that are not present at the 1994 Northridge site.

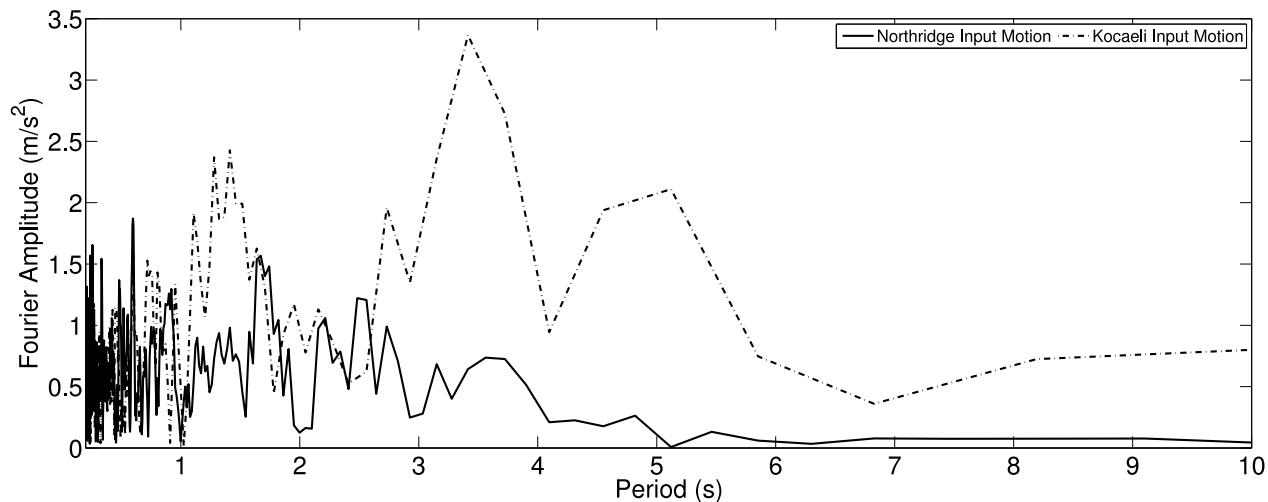


Figure 503.117: Frequency Contents of Ground Motions - Acceleration Time Series

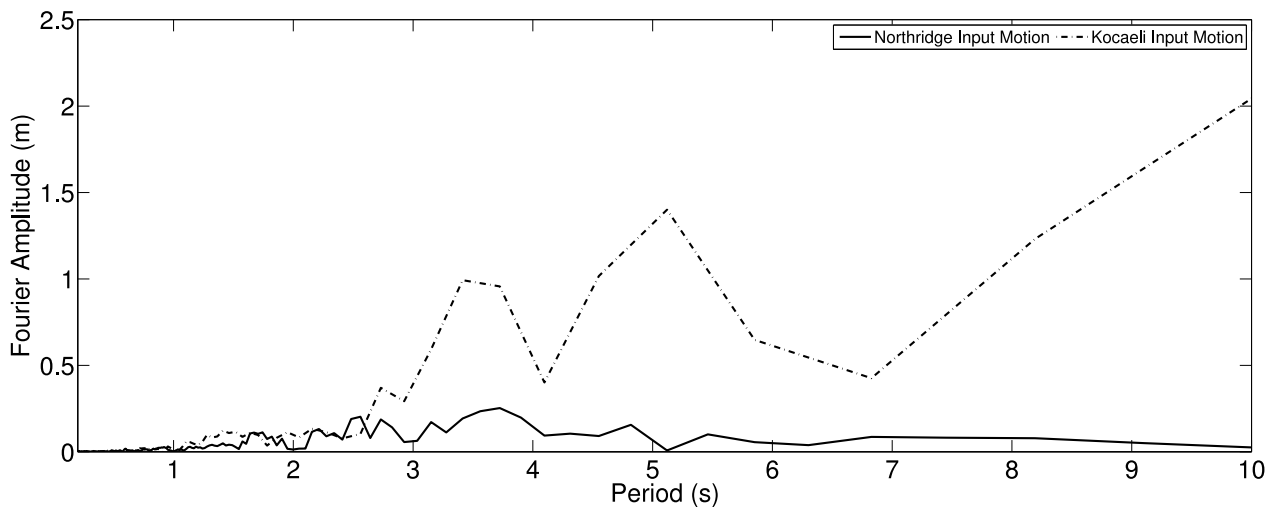


Figure 503.118: Frequency Contents of Ground Motions - Displacement Time Series

Depending on different site conditions, ESSI system will exhibit varied response to excitations with different predominant frequencies. As we can see from Figure 503.42 to Figure 503.47, the structure sitting on softer soil foundations now exhibits much larger structural response when it is subject to long period excitations. This conclusion has been supported by every single plot that records the response spectra of structures such as Figure 503.61, Figure 503.63 and Figure 503.65. For the long predominant periods present in the Kocaeli earthquake, the structures supported by soft clays exhibit much larger amplification than those supported by stiff soils.

It is also worthwhile to look deeper into the transfer function that tells some other aspects of the simulation scenarios. We can see from Figure 503.119 to Figure 503.130 that in terms of transfer function, which defines the amplification from soil surface to top of the structure, the structure is able to pick up much high frequency content that is not present within the soil layers. The visual representation of this is that the transfer function has much larger value at the high frequency end (low period end). This can be explained that typically people construct pile foundation inside the stiff soil (or bedrock). In our simulation, we also have a very stiff sustaining layer to provide pile tip resistance. The results shown in transfer functions make sense and also verifies our numerical model. Acceleration results are also shown as following.

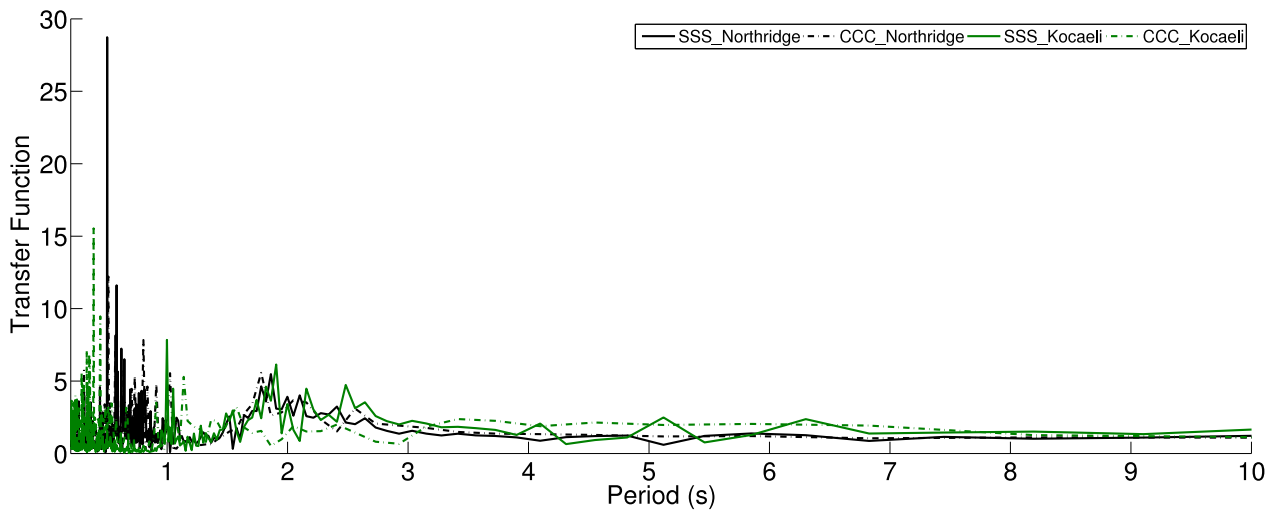


Figure 503.119: Transfer Function of Simulated Displacement Time Series for Both Long Period and Short Period Motions (Structure Bent 1, from Soil Surface to Top of Bent)

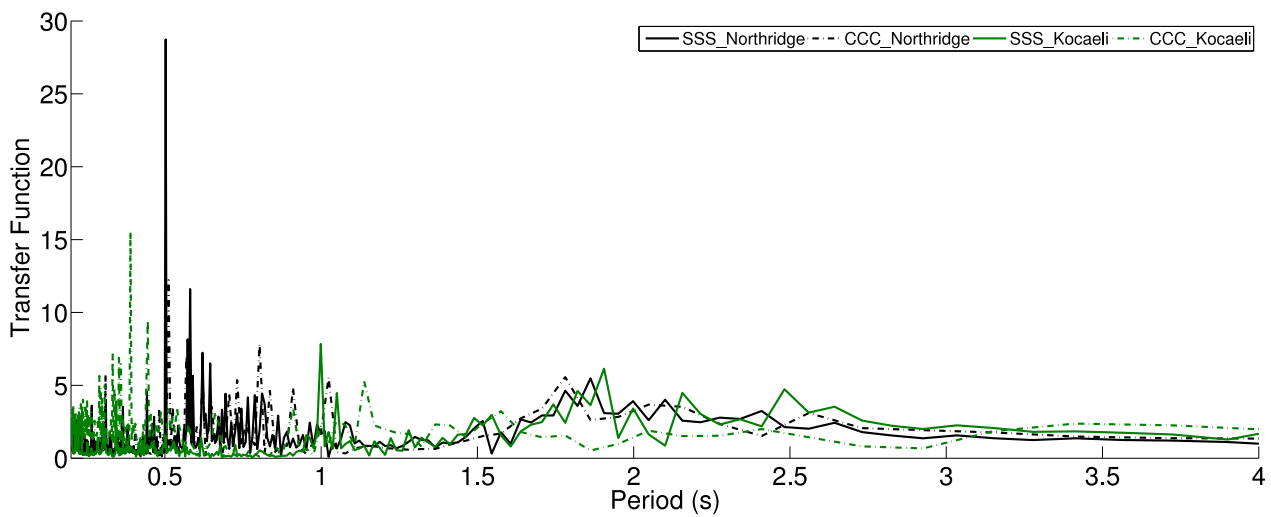


Figure 503.120: Zoomed View: Transfer Function of Simulated Displacement Time Series for Both Long Period and Short Period Motions (Structure Bent 1, from Soil Surface to Top of Bent)

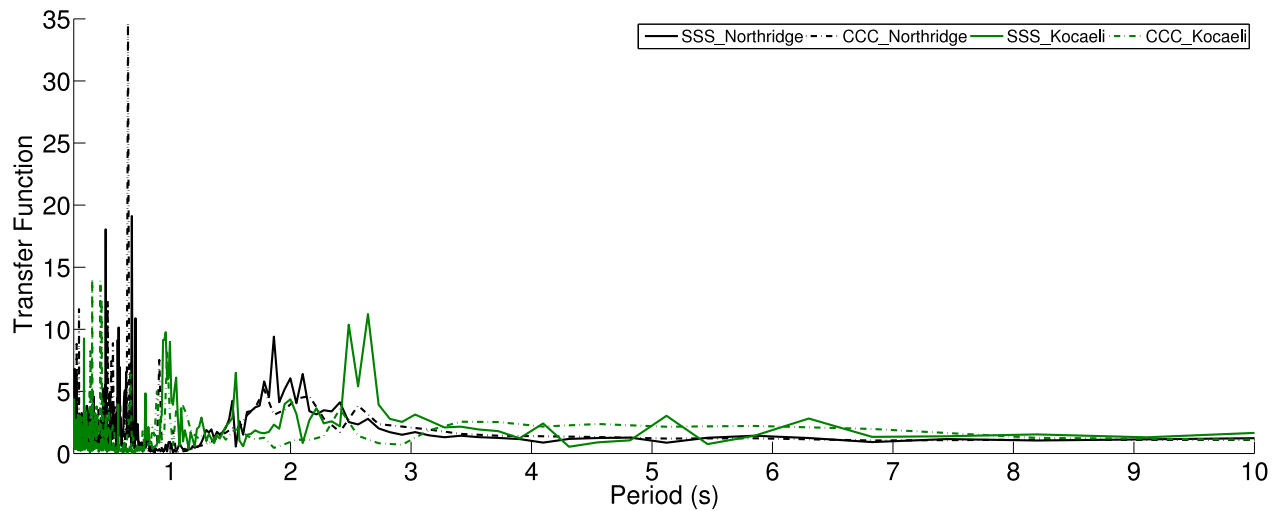


Figure 503.121: Transfer Function of Simulated Displacement Time Series for Both Long Period and Short Period Motions (Structure Bent 2, from Soil Surface to Top of Bent)

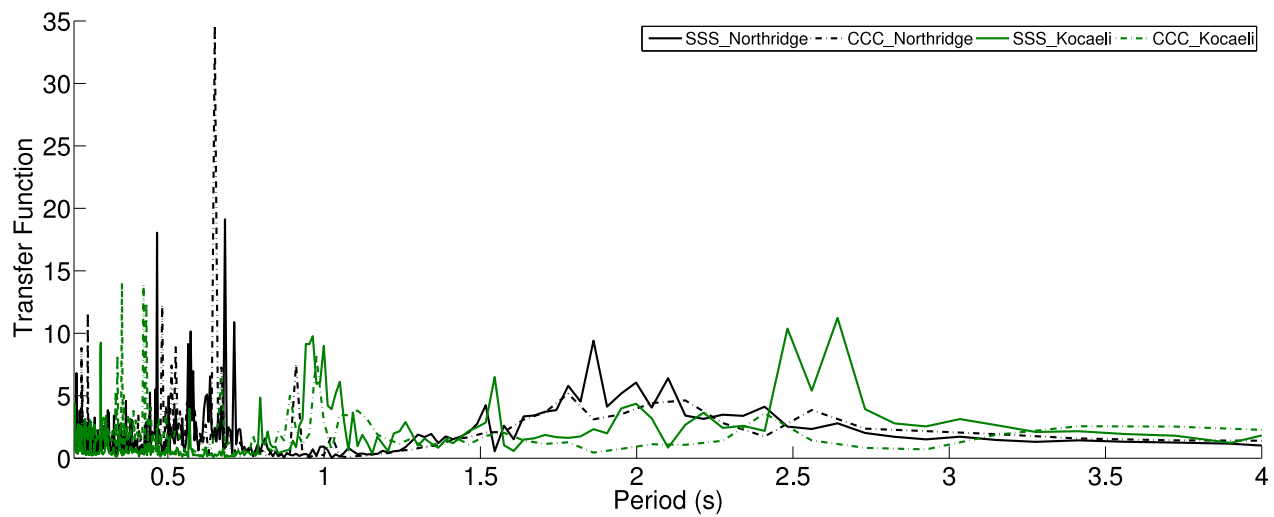


Figure 503.122: Zoomed View: Transfer Function of Simulated Displacement Time Series for Both Long Period and Short Period Motions (Structure Bent 2, from Soil Surface to Top of Bent)

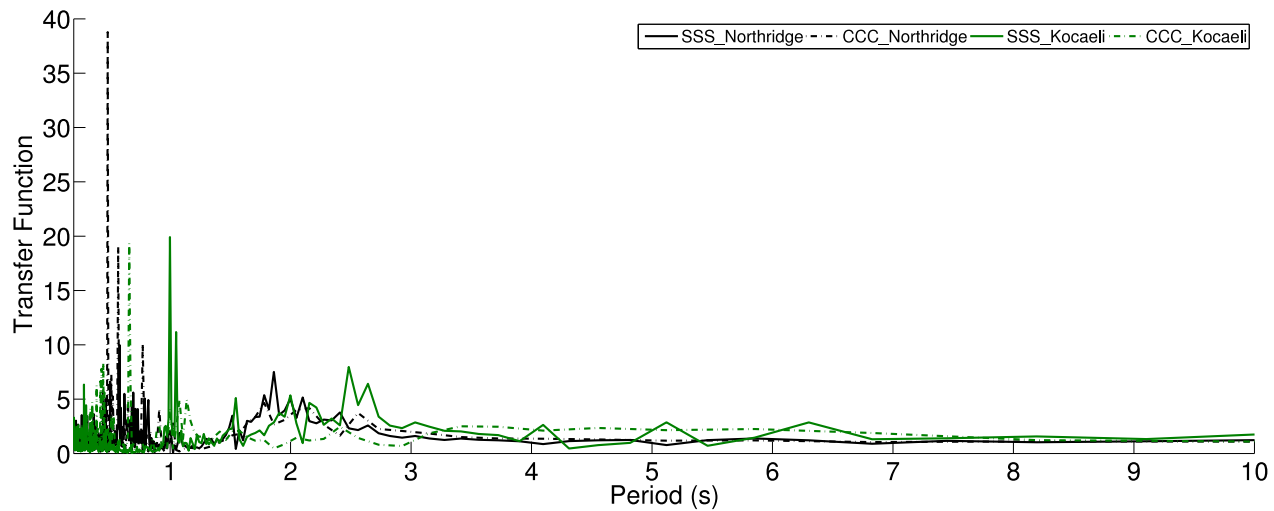


Figure 503.123: Transfer Function of Simulated Displacement Time Series for Both Long Period and Short Period Motions (Structure Bent 3, from Soil Surface to Top of Bent)

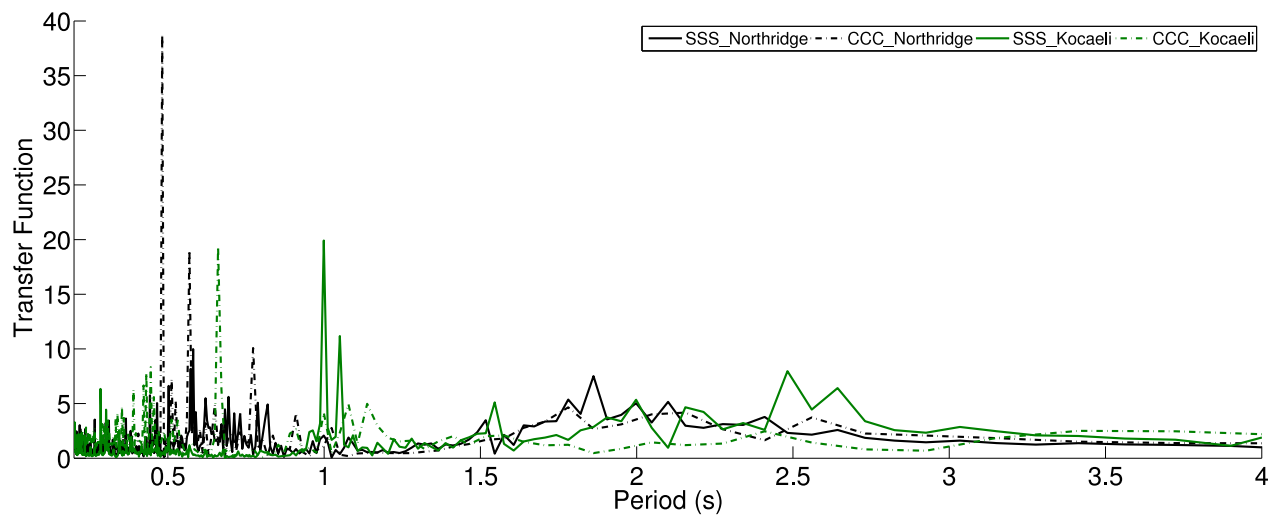


Figure 503.124: Zoomed View: Transfer Function of Simulated Displacement Time Series for Both Long Period and Short Period Motions (Structure Bent 3, from Soil Surface to Top of Bent)

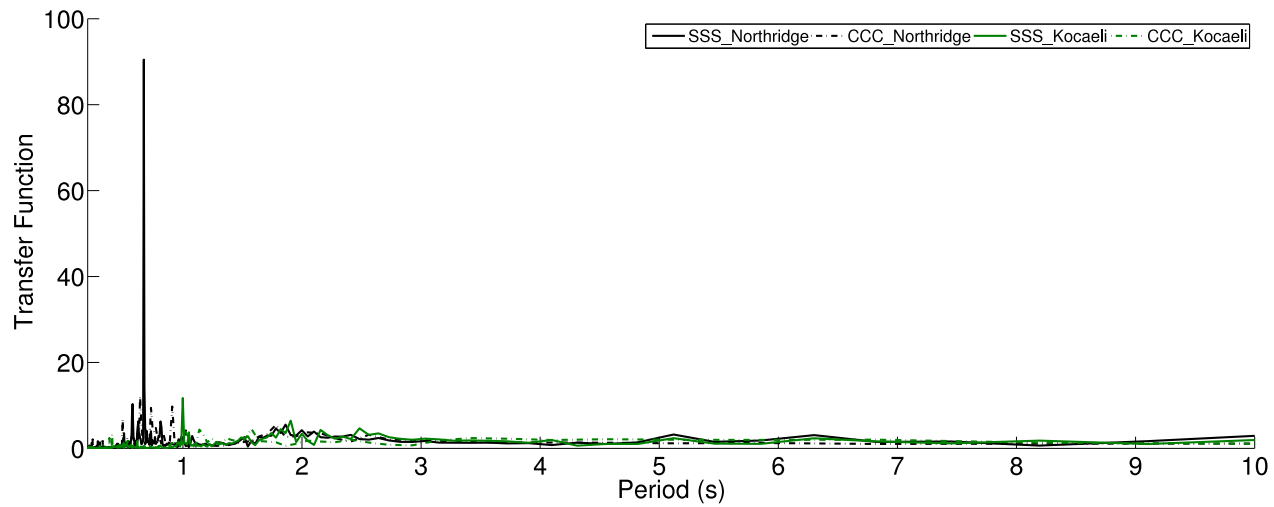


Figure 503.125: Transfer Function of Simulated Acceleration Time Series for Both Long Period and Short Period Motions (Structure Bent 1, from Soil Surface to Top of Bent)

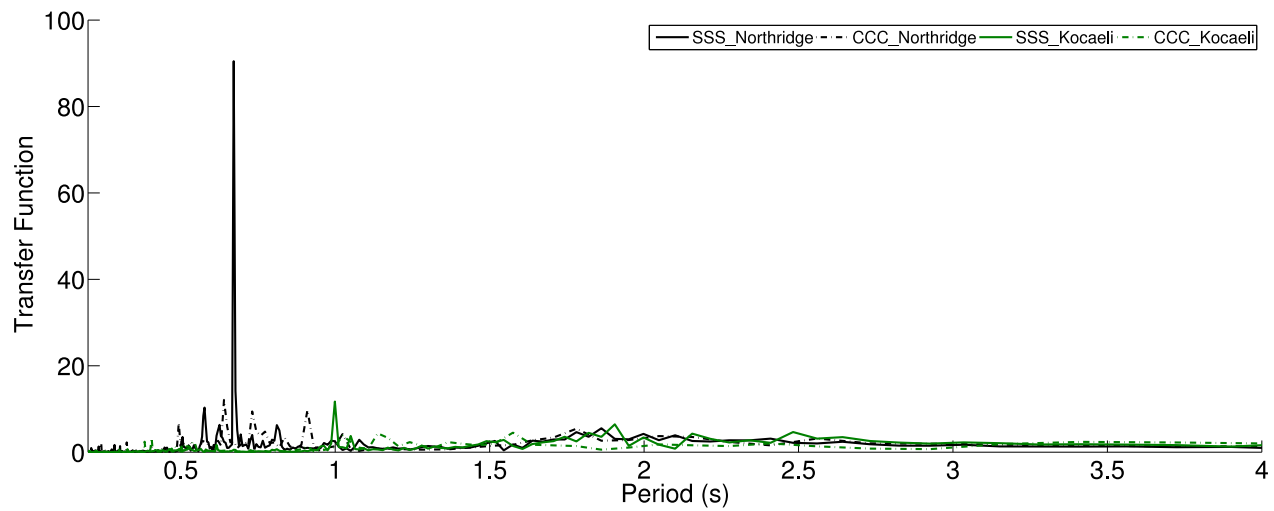


Figure 503.126: Zoomed View: Transfer Function of Simulated Acceleration Time Series for Both Long Period and Short Period Motions (Structure Bent 1, from Soil Surface to Top of Bent)

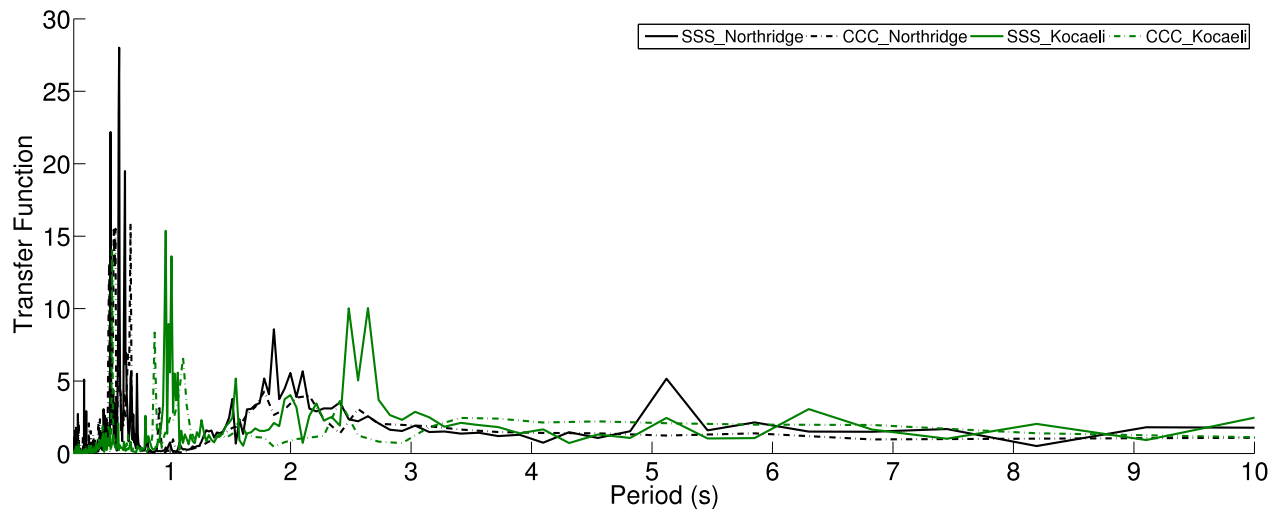


Figure 503.127: Transfer Function of Simulated Acceleration Time Series for Both Long Period and Short Period Motions (Structure Bent 2, from Soil Surface to Top of Bent)

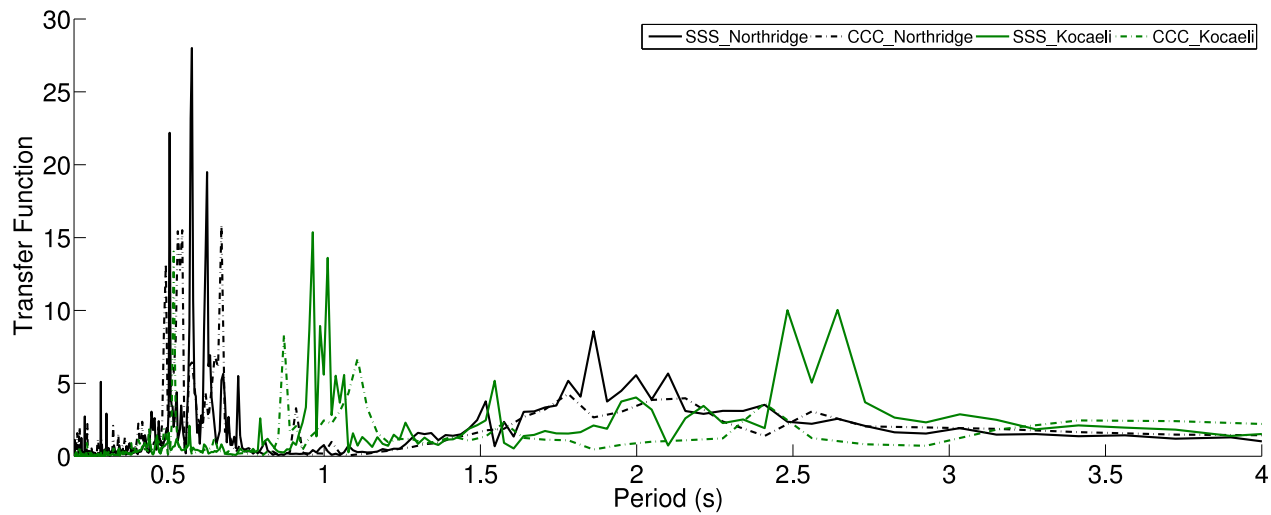


Figure 503.128: Zoomed View: Transfer Function of Simulated Acceleration Time Series for Both Long Period and Short Period Motions (Structure Bent 2, from Soil Surface to Top of Bent)

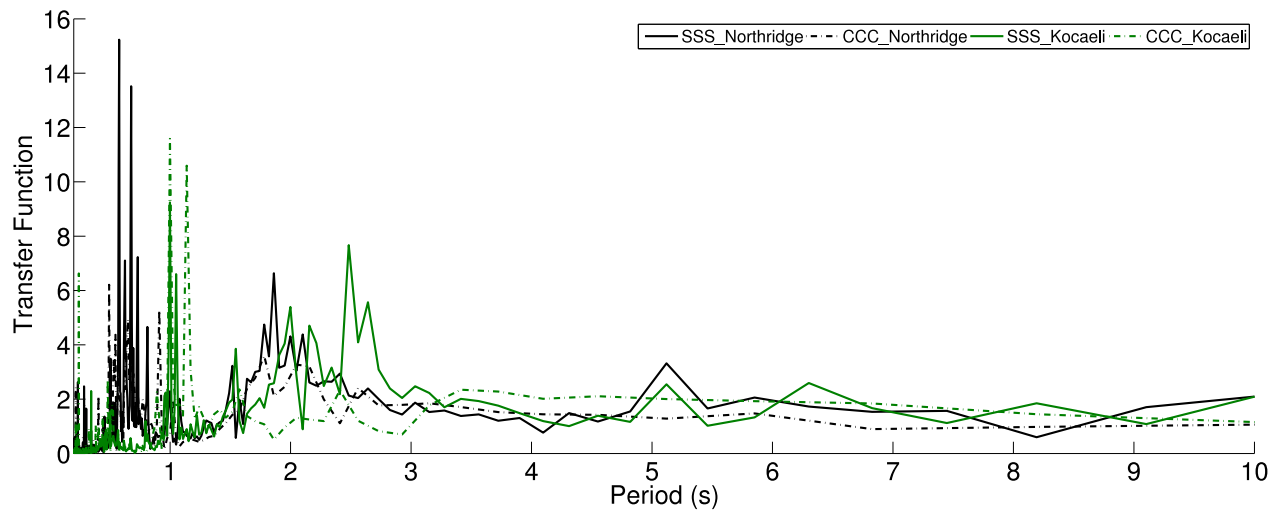


Figure 503.129: Transfer Function of Simulated Acceleration Time Series for Both Long Period and Short Period Motions (Structure Bent 3, from Soil Surface to Top of Bent)

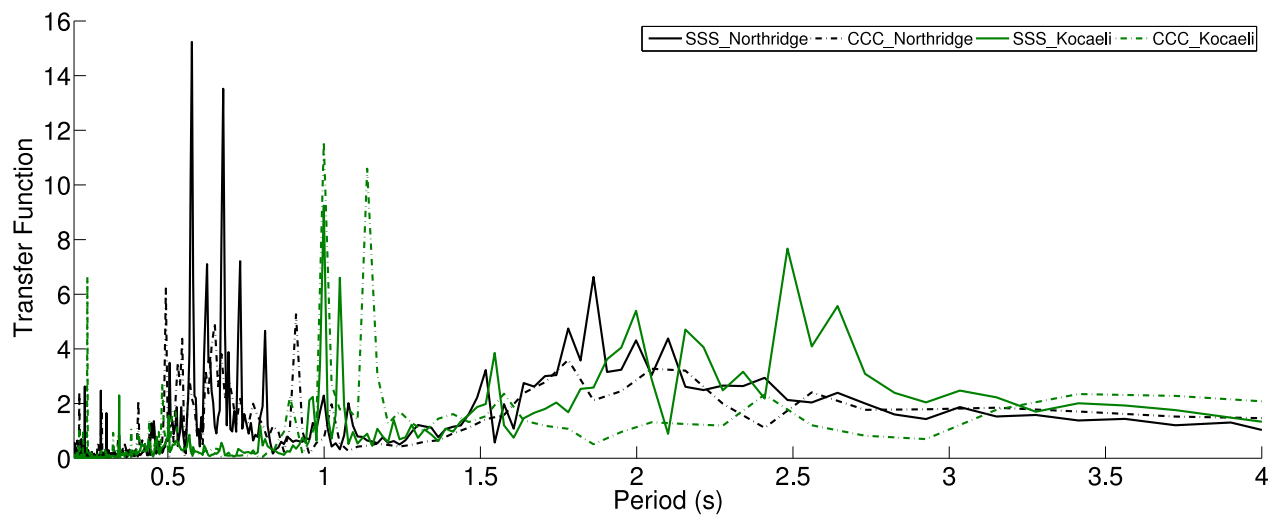


Figure 503.130: Zoomed View: Transfer Function of Simulated Acceleration Time Series for Both Long Period and Short Period Motions (Structure Bent 3, from Soil Surface to Top of Bent)

Chapter 504

Earthquake-Soil-Structure Interaction, Nuclear Power Plants

(2010-2011-2012-2017-2018-2019-2020-2021-2023-)

(In collaboration with Dr. Nima Tafazzoli, Prof. José Abell, Dr. Yuan Feng, Prof. Sumeet Kumar Sinha, Prof. Han Yang and Dr. Hexiang Wang, Dr. Katarzyna Staszewska)

504.1 Stick/Solid Finite Element Model

The 3D finite element model is shown in Figure (504.1). The finite element model is created using both 8 node brick elements for modeling the soil part and 27 node brick elements for modeling the foundation part, and displacement beam element for structural components.

The size of the model is 140m along the X and Y directions, and 50m along the Z direction (the height of the soil layer). Shear wave velocity of the soil is considered to be 700m/s with density of 2200kg/m³. Foundation has the height of 5m embedded in the soil layer, with size of 90m in each horizontal direction. Concrete is chosen to have shear wave velocity of 2000m/s with density of 2400kg/m³. The size of the elements are 5m in each direction for both foundation and soil elements. Structural beam is composed of 12 displacement beam elements attached to each other with different stiffness and mass properties. Domain Reduction Method is used to apply the input effective forces. Both 1C and 3C wave propagation cases are using the same finite element model for second stage of DRM analysis.

Frictional contact/interface elements are placed at the interface of foundation and soil layer. The contact/interface element used here has the same normal and tangential stiffness with magnitude of 10⁸N/m. Friction ratio and cohesion of the contact/interface element are $\mu = 0.4$ and $c = 0.0$ respectively. Contact elements are oriented along the Z axis of global model.

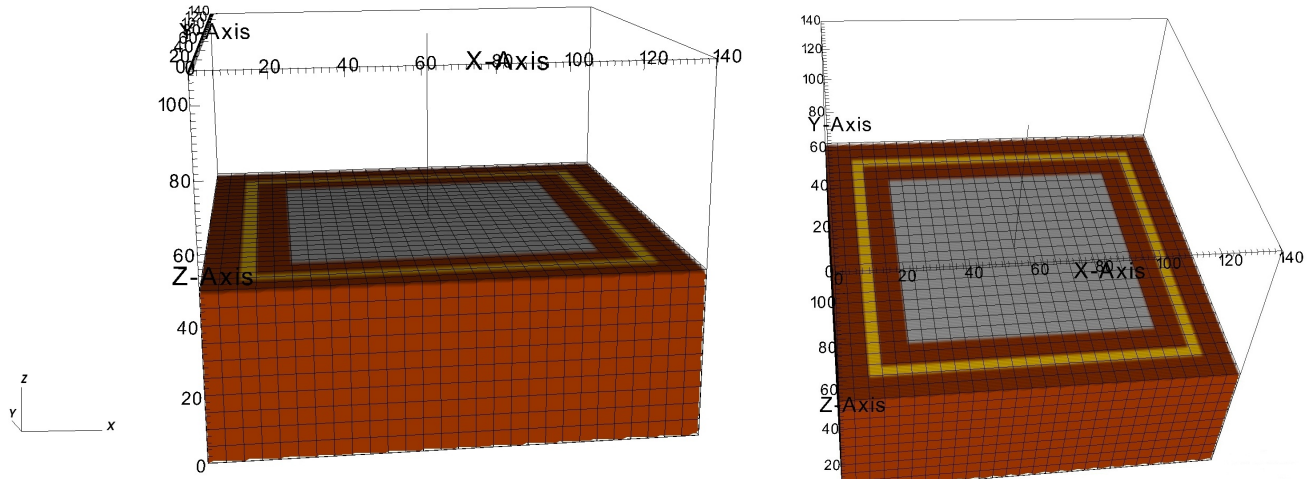


Figure 504.1: 3D finite element SFSI model considering slipping behavior at the interface of foundation and soil layer

In general it is accepted that in order to represent a traveling wave of a given frequency, the size of the finite elements have to have about 10 nodes per wavelength λ ([Hughes \(1987\)](#); [Argyris and Mlejnek](#)

(1991)). Using fewer than 10 nodes per wave length λ specially for linear elements leads to numerical damping of higher frequencies as such element discretization misses certain frequencies of the wave. In order to satisfy this requirement, the size of the mesh should satisfy Equation (504.1) which is a function of the maximum frequency (f_{max}) of the input motion and also the shear wave velocity of the media $V_s = \sqrt{G/\rho}$ where G is the shear modulus and ρ is density of the soil.

$$\Delta h \leq \lambda/10 = V_s/(10f_{max}) \quad (504.1)$$

In this model, the size of the elements are chosen to be 5m in each direction. Considering that the shear wave velocity of the soil is 700m/s, the maximum frequency able to be propagated through this model is 14Hz.

504.1.1 Slipping behavior of SFSI models by considering 1C wave propagation

In this section, slipping behavior of SFSI systems is studied under 1C seismic wave propagation assumption to come up with the input motion to be used for the model prepared for second stage of DRM. Morgan Hill earthquake and Ricker wavelets are used as the source of motion.

Domain Reduction Method is used to apply the input effective forces. In order to obtain the displacement and acceleration time histories used for calculating the DRM layer effective forces, a finite element soil column with shear behavior is considered representing the 1C wave propagation. The motions are applied at the base of the 1C finite element model and propagated through the soil column using multiple support excitation pattern.

504.1.1.1 Morgan Hill earthquake

Figures (504.2) to (504.3) show the acceleration and displacement time histories and FFT of the Morgan Hill earthquake at the base of the 1D model. Figure (504.4) shows the acceleration time histories recorded at the bottom and top of the structure in X and Z directions.

As it is observed, the acceleration time history of slipping and no-slipping model has differences in amplitude and the phase in X direction of the model. However, the differences in phases of the recorded motions seems to be more along the Z direction. It shows that considering the slipping behavior has caused a lag in phase of the response. Comparison of displacement time histories of the same models is shown in Figure (504.5) along X and Z directions. As it is shown, displacement time histories along X direction are quite similar in this case while along Z direction they have different amplitudes due to initial settlement and different phases. FFT of the accelerations do not have much of a difference in terms of frequency content (shown in Figure (504.6) but they are different in amplitude which has been observed in acceleration time histories as well. In general it is observed that in this earthquake the magnitude of accelerations and displacements are less at top of the structure comparing to the ones recorded at the bottom of the structure for both slipping and no-slipping behavior cases.

Figure (504.7) shows the distribution of sliding at the interface of foundation and the soil layer at 9 different time steps of analysis from 0.5 to 1.3 seconds. As it is observed, location of maximum sliding is changed along the foundation in time while magnitude and direction of the applied motion changes. Slipping happens at the specific steps and parts of the interface zone in which the applied force is more than the resistant one.

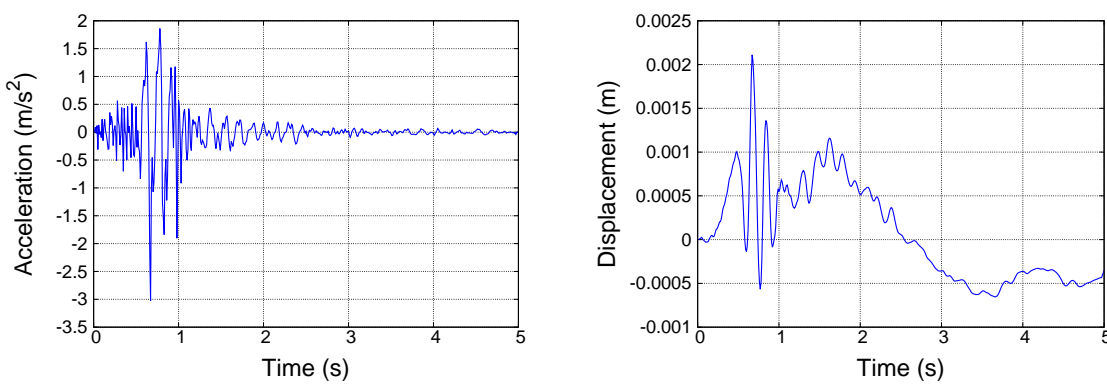


Figure 504.2: Acceleration and displacement time histories of Morgan Hill earthquake

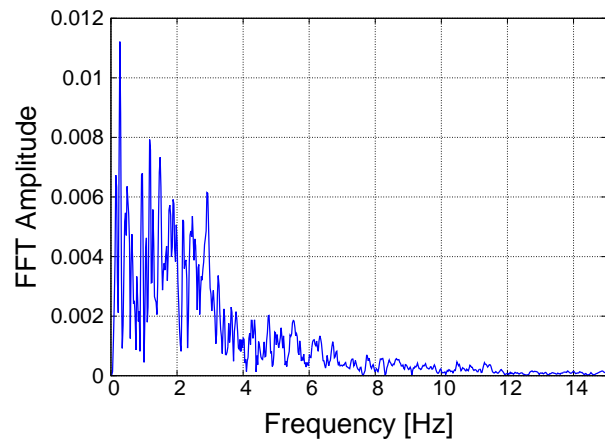


Figure 504.3: FFT of Morgan Hill earthquake

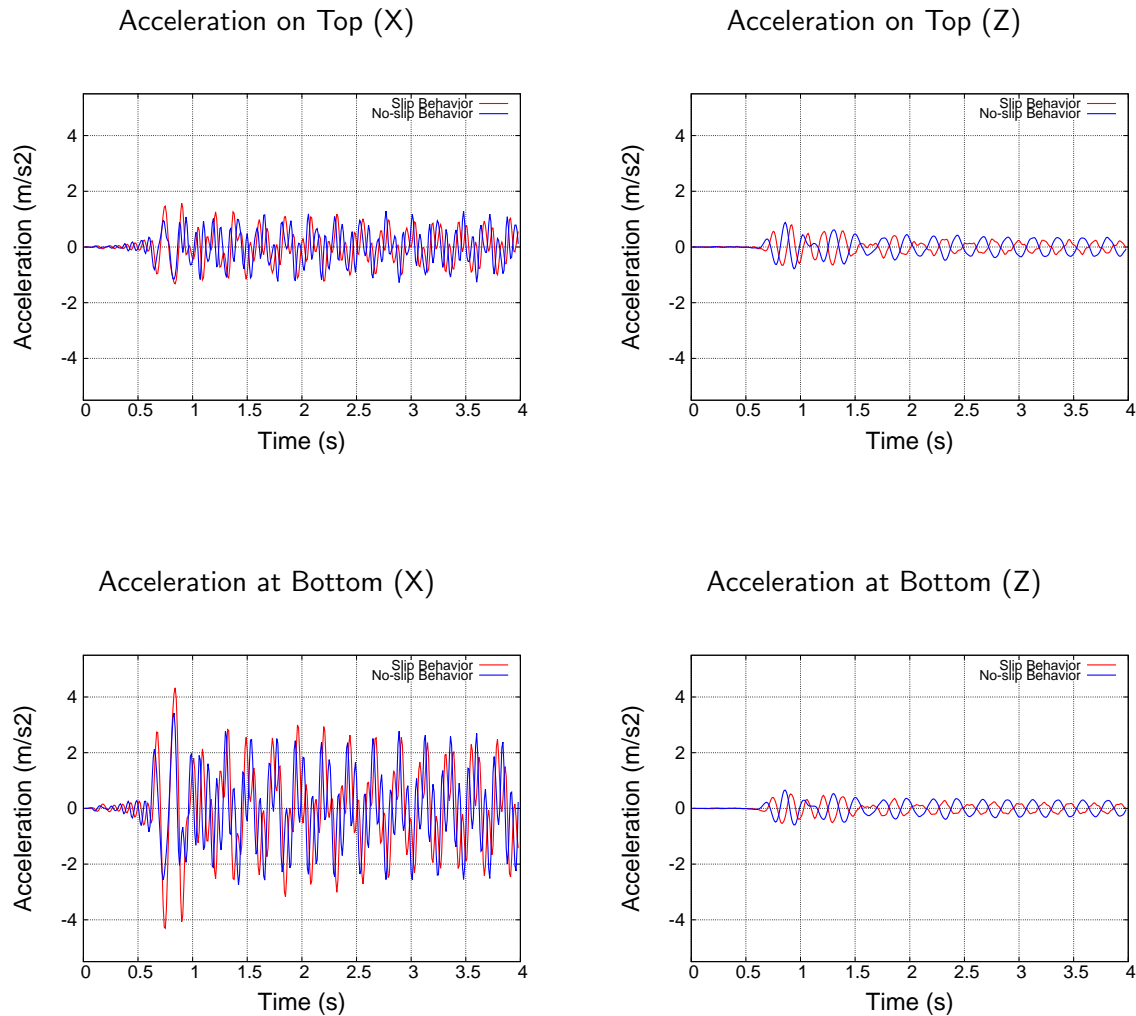


Figure 504.4: Comparison of acceleration time histories of the structure between slipping and no-slipping models for Morgan Hill earthquake

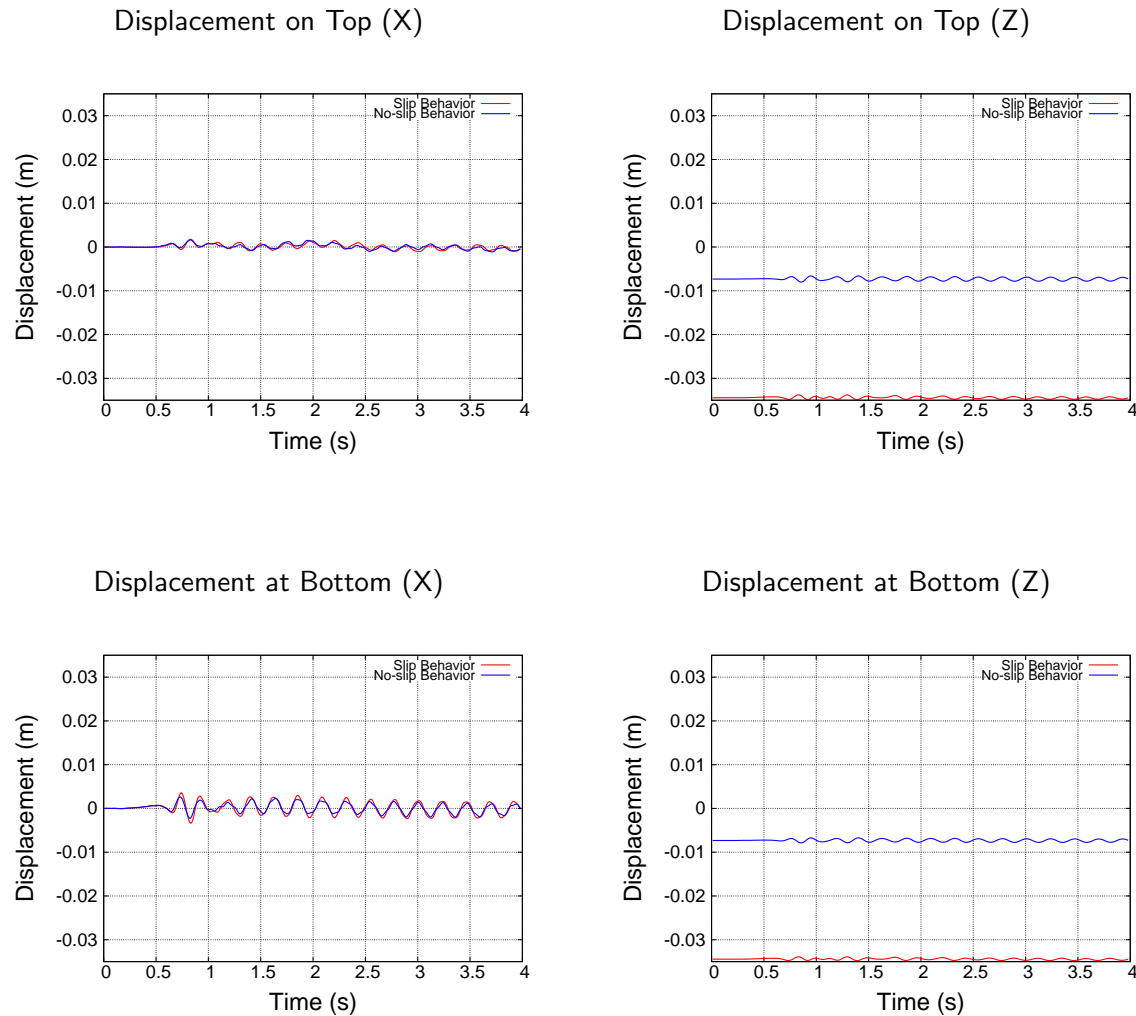


Figure 504.5: Comparison of displacement time histories of the structure between slipping and no-slipping models for Morgan Hill earthquake

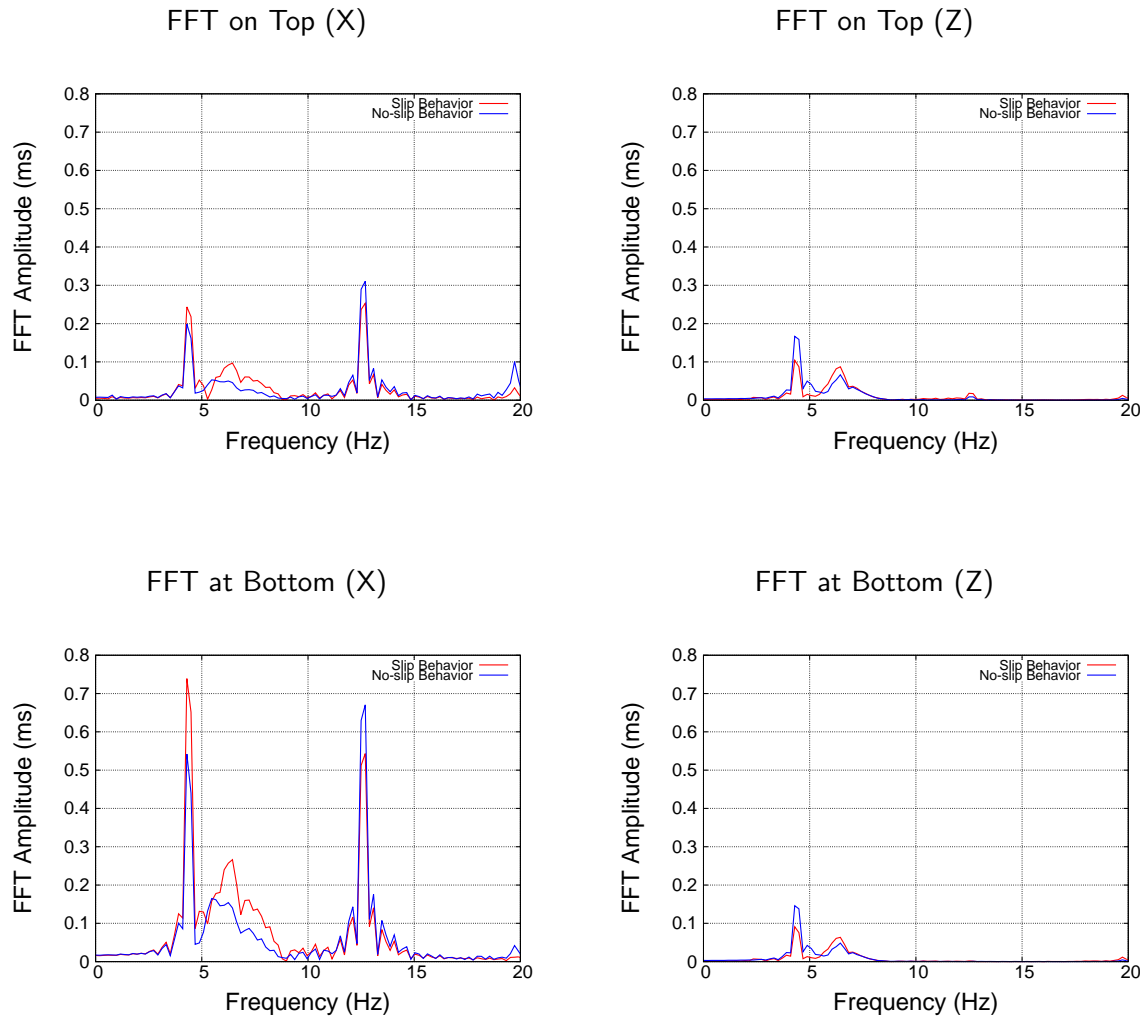


Figure 504.6: Comparison of FFT of the acceleration of the structure between slipping and no-slipping models for Morgan Hill earthquake

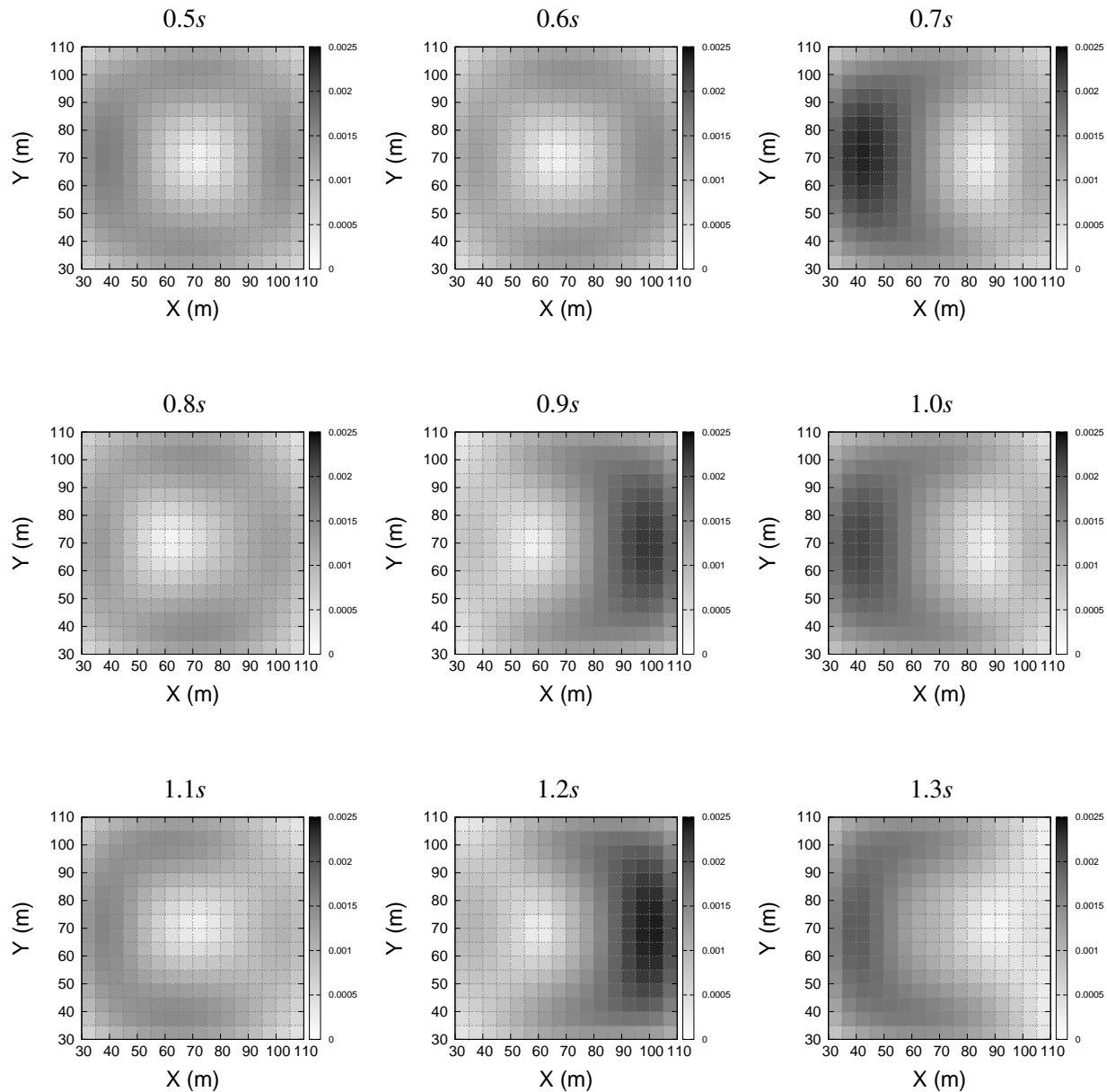


Figure 504.7: Distribution of sliding along the contact/interface for Morgan Hill earthquake (gray scale given in meters)

504.1.1.2 Ricker wave

In order to investigate more, the Ricker wave with dominant frequency of 1Hz is used for analysis of the same model. The maximum of this function happens at 1 second. Figures (504.8) and (504.9) show the acceleration and displacement time histories as well as the FFT of the Ricker wave respectively.

As shown in Figure (504.10), displacement time history of top of the structure along X direction is higher when slipping behavior is not considered, while along Z direction it is higher considering the slipping behavior. Since structural components have rotational degrees of freedom, the slipping behavior and gaps in the model will lead to have more rotational movement and rocking of the foundation. There is also a phase lag in response of the structure in slipping behavior model. The displacement time histories at the bottom of the structure are slightly different in X direction. It can also be observed that along Z direction, the response of the structure in slipping model is higher comparing to the no-slipping one.

In this analysis slipping behavior make the movement to be less along the X direction. This might be due to the fact that while the foundation and structure are moving, there are gaps created at some parts of the interface which will affect the rocking movement of the foundation.

Figure (504.11) shows the FFT of the acceleration at the bottom and top of the structure. As it is observed, there is a slight shift in predominant frequency of the response between the slipping and no-slipping behavior. By considering the slipping behavior, the dominant frequency of the motion is decreased along the X direction while is increased along the Z direction. This means that the system gets softer along X direction and stiffer along Z direction. This is due to the gap openings and slidings at the foundation and soil layer interface. Since sliding happens along the X direction, and also considering the gap openings occur along the Z direction which can lead to the rocking of the foundation, it makes the system softer along the X direction. In general this shows the fact that the natural frequency of the system can be changed due to the slipping behavior.

Figures (504.12) and (504.13) show the distribution of gap openings and slidings at the interface of foundation and the soil layer at 9 different time steps of analysis from 0.5 to 1.3 seconds. It can be observed from Figure (504.12) how the location of gap openings are changed on different parts of the contact/interface as the dynamic motion is applied. The location of gap openings are changed from one side to the other while the magnitude and direction of the applied motion changes. The maximum of the gap openings at these time steps happen at 1.3 second with maximum amount of 0.1m on the right side of the interface. Maximum sliding at the shown range of time steps happens at 1.0 second with maximum value of 0.07m on the left side of the interface.

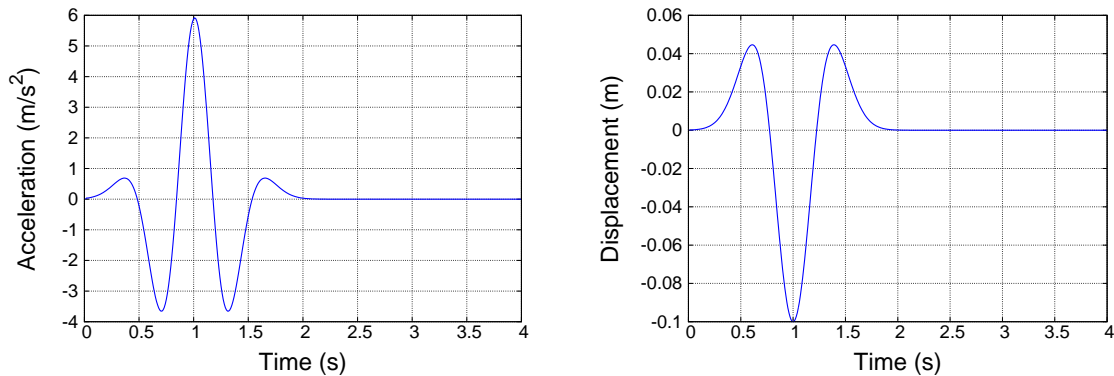


Figure 504.8: Acceleration and displacement time histories of Ricker wave with dominant frequency of 1Hz

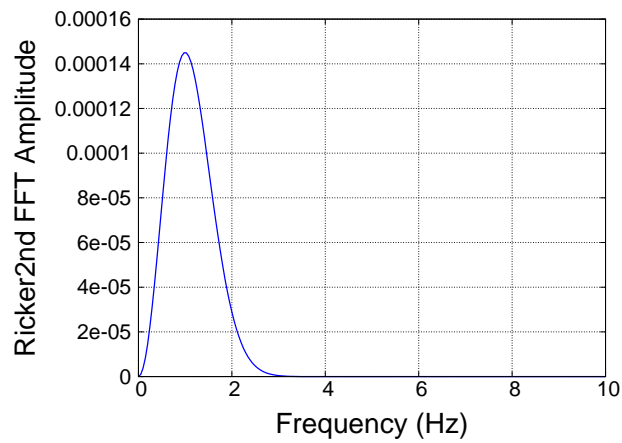


Figure 504.9: FFT of Ricker wave with dominant frequency of 1Hz

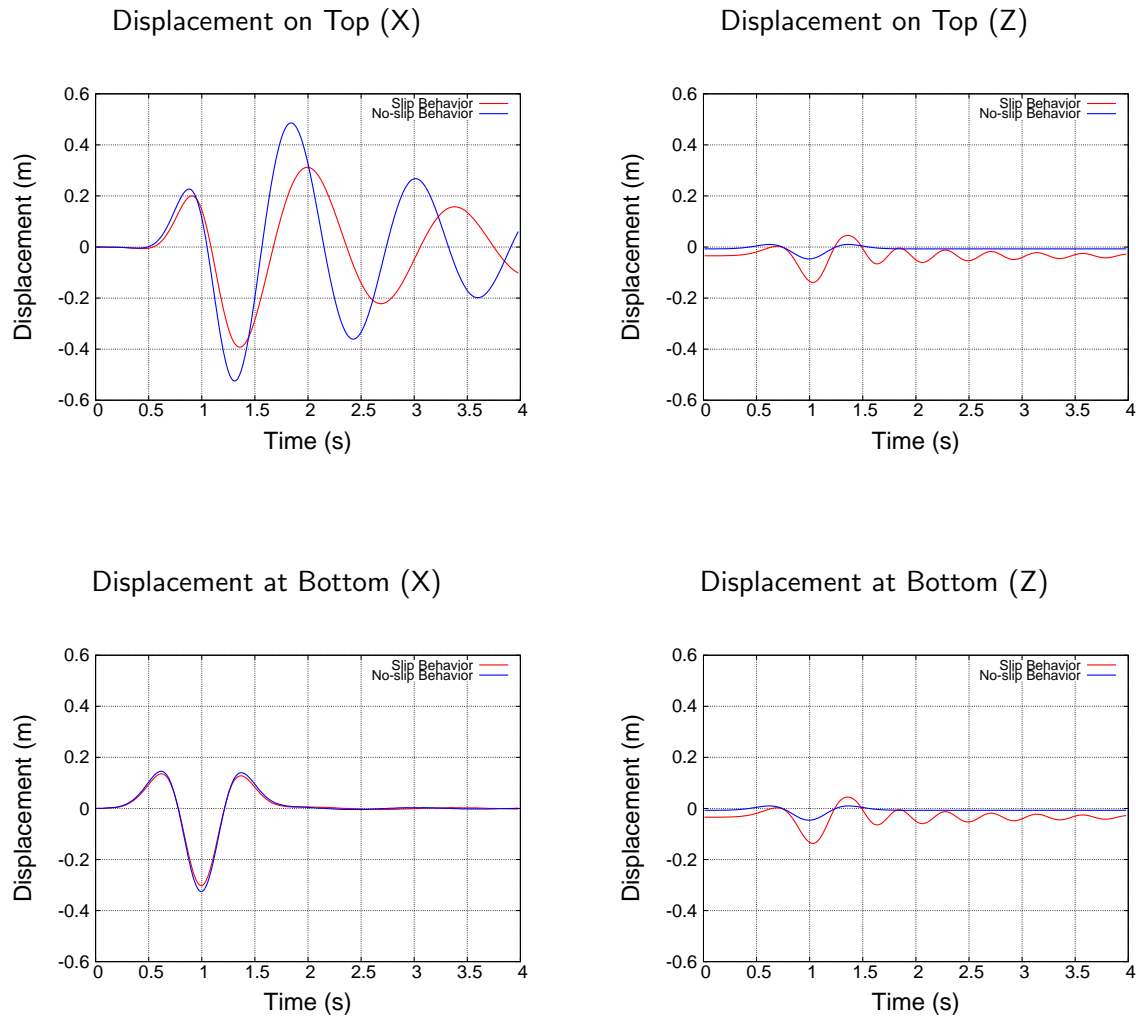


Figure 504.10: Comparison of displacement time histories of the structure between slipping and no-slipping models for Ricker wave

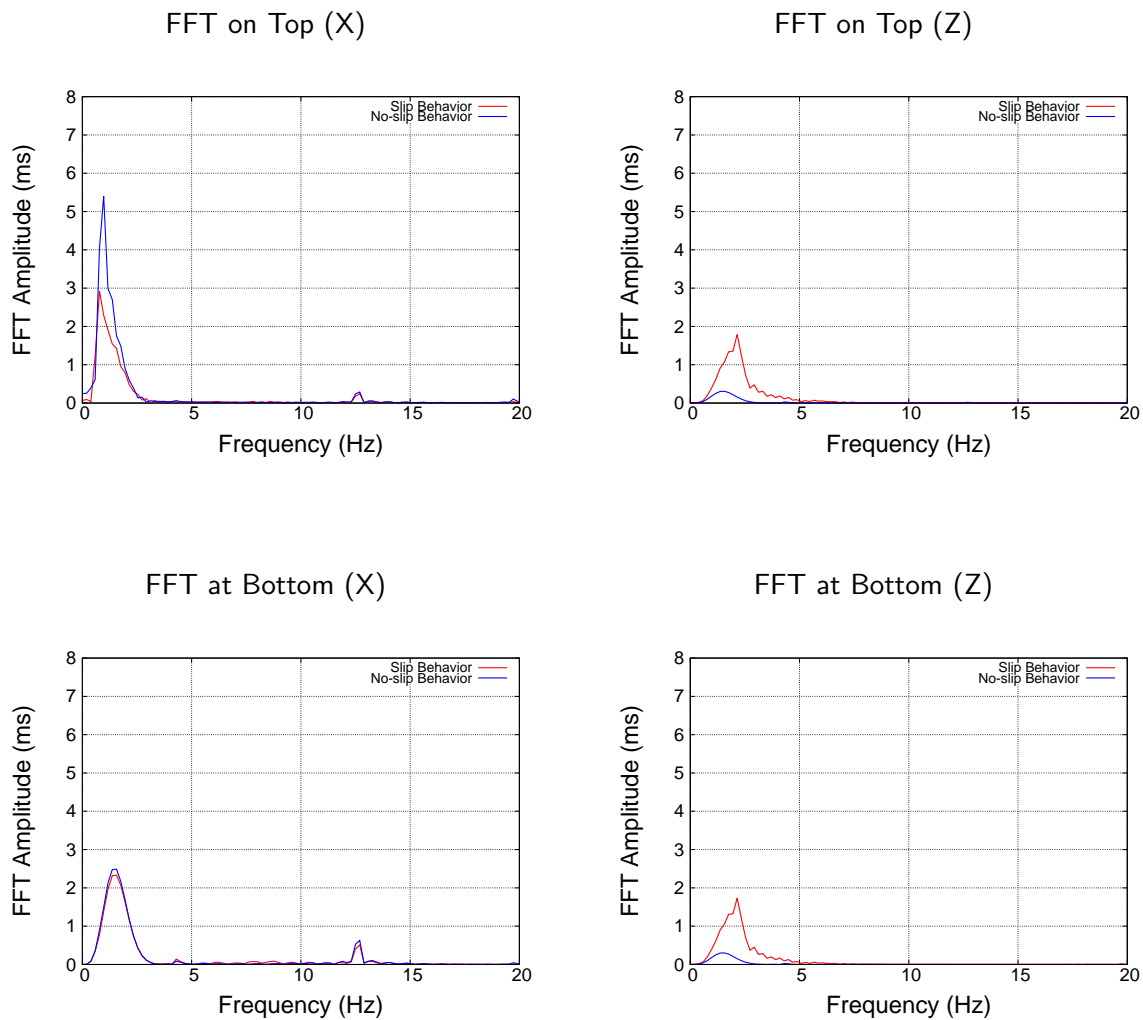


Figure 504.11: Comparison of FFT of the acceleration of the structure between slipping and no-slipping models for Ricker wave

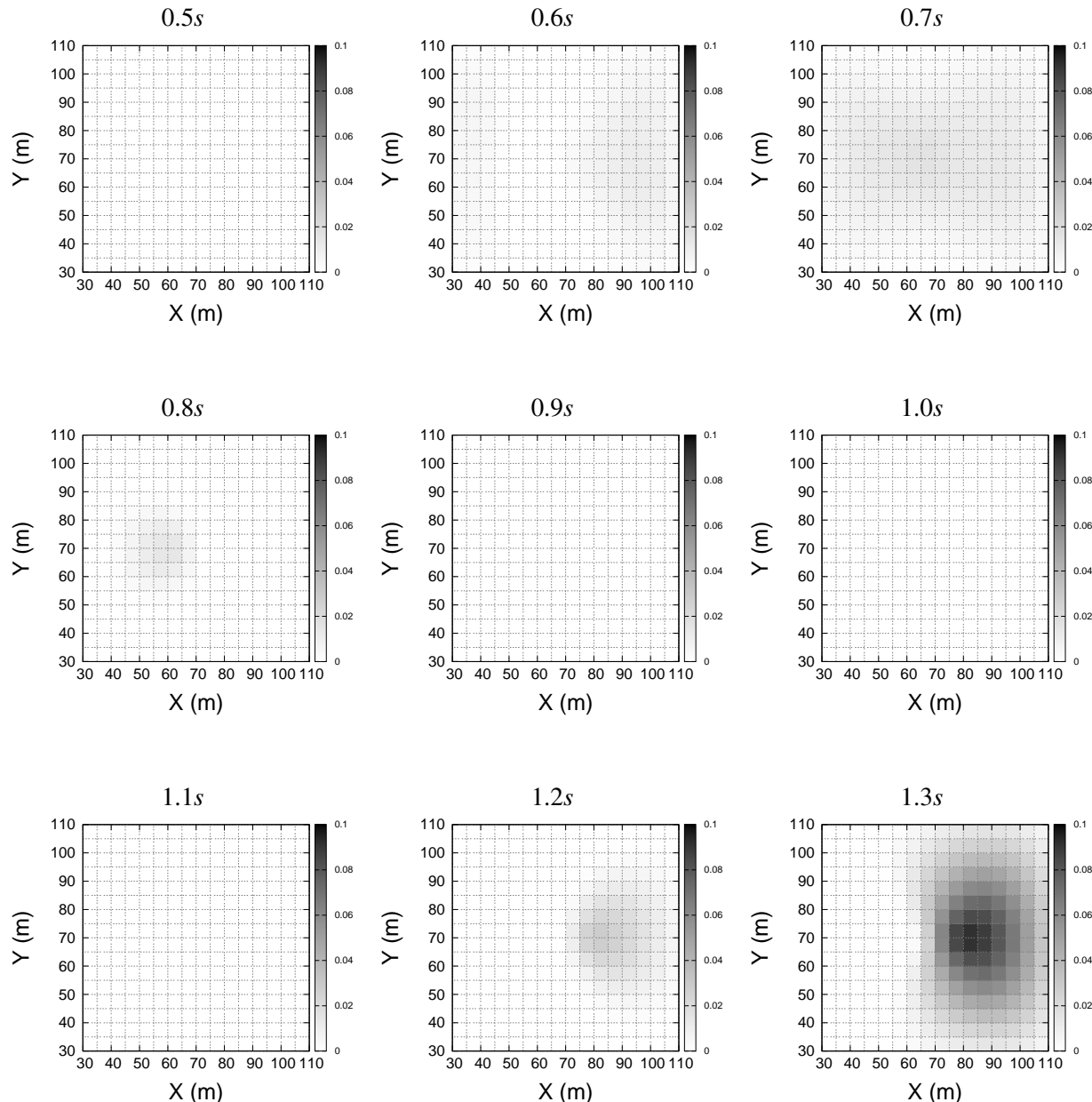


Figure 504.12: Distribution of gap openings along the contact/interface for Ricker wave (gray scale given in meters)

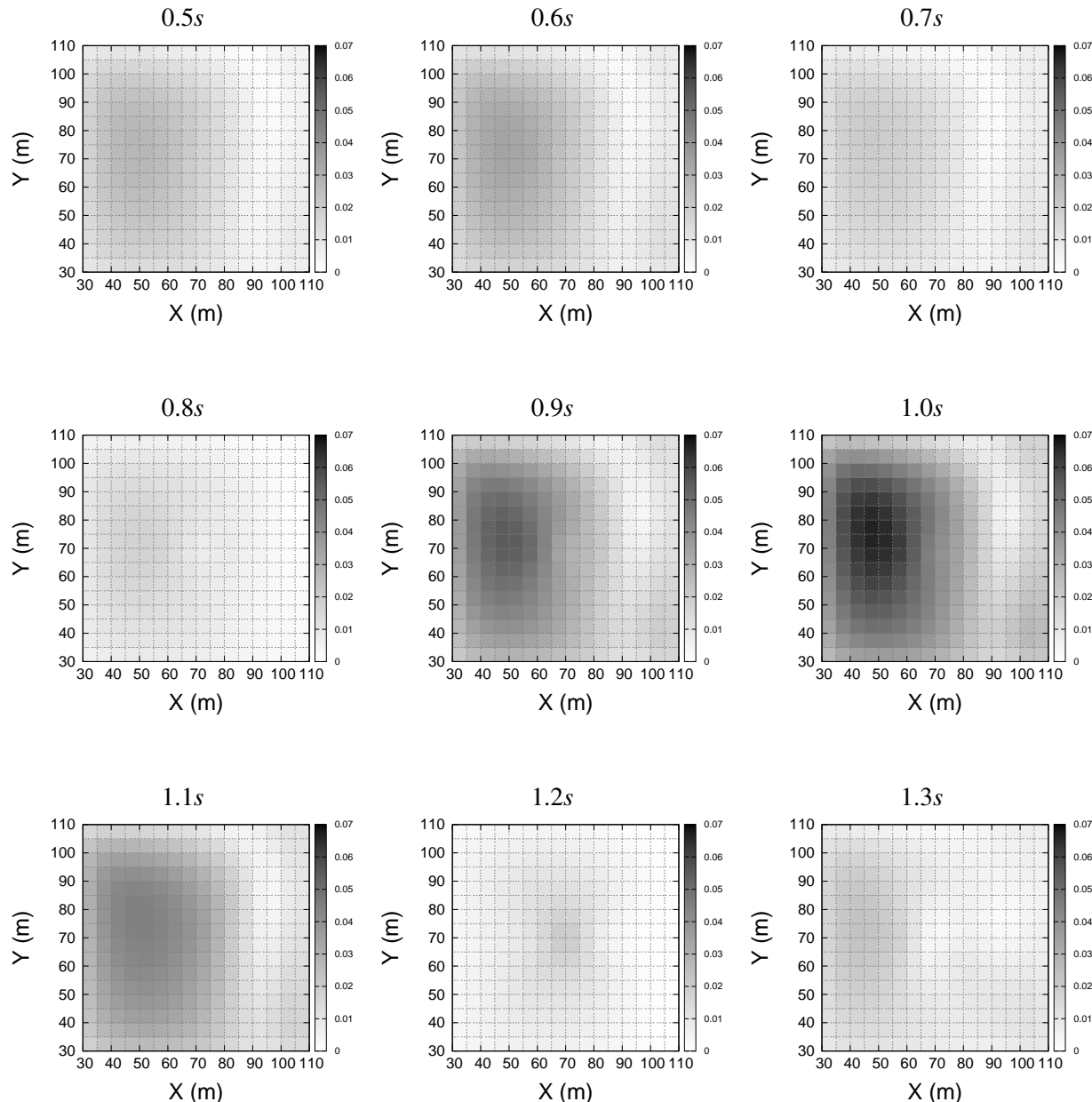


Figure 504.13: Distribution of sliding along the contact/interface for Ricker wave (gray scale given in meters)

504.1.2 Slipping behavior of SFSI models by considering 3C wave propagation

In this section, the same finite element SFSI model as previous section is used with 3C wave propagated motions as input motions for simulations. The input motion used here is Ricker wave (as shown in Figure (504.8)).

In order to study the slipping behavior of SFSI considering 3C wave propagation for first stage of DRM simulation, a finite element model with dimensions of $10000m \times 50m \times 5000m$ is considered. Two cases are studied here with the source of motion (fault) to be located at $(x = 3000m, y = 0, z = 3000m)$ and $(x = 3000m, y = 0, z = 3000m)$. Figures (504.14) and (504.15) show these two cases respectively.

The size of the elements is chosen to be $50m$ in all directions for both cases in order to reduce the computational time. The soil parameters are: shear wave velocity of $700m/s$ and density of $2200kg/m^3$. Analyses for the fault slip model are done by applying the motion at the nodes of one element. This is done in order to represent the the wave propagation starting from the fault using multiple support excitation pattern. This is representing the first stage of analysis of DRM in which a big model including the fault is considered for free field case in order to obtain the required motions for DRM layer.

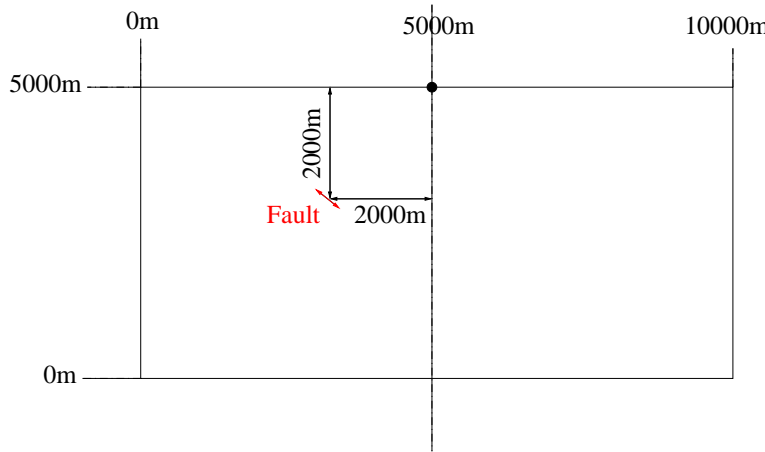


Figure 504.14: Domain to be analyzed for the 1st stage of DRM with fault located at an angle of 45° with respect to the top middle point of the model

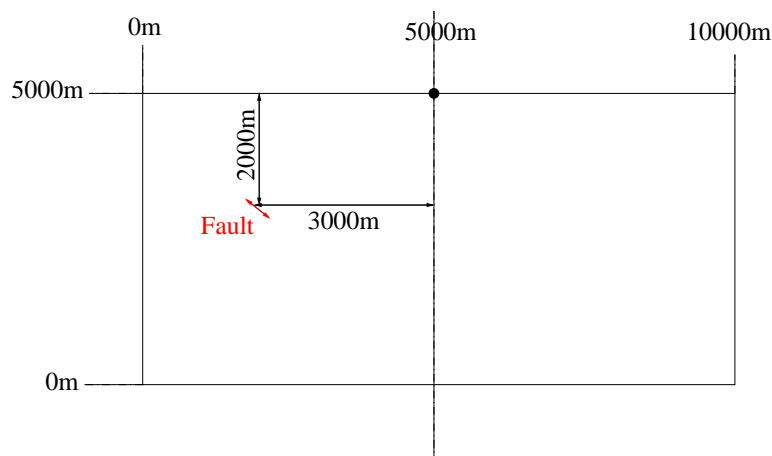


Figure 504.15: Domain to be analyzed for the 1st stage of DRM with fault located at an angle of 34° with respect to the top middle point of the model

504.1.2.1 Ricker wave, with fault located at 45° towards the top middle point of the model

For the first case to be studied here, Ricker wavelet is considered as an input motion with dominant frequency of 1Hz. The fault is located with angle of 45° toward the top middle point of the model (Figure (504.14)).

Displacement time histories of the structure along X and Z directions are shown in Figure (504.16). It is observed that along the X direction, the amplitude of displacement is little less at the beginning of the shaking of the slipping behavior model and a slight phase lag can be observed as well. However, when the actual pick of the motion is gone, it is shown that the motion for no-slipping model will damp out sooner. So the magnitude of displacements are higher at this time range for slipping model which could be because of the gap/sliding at the interface zone. The displacement time histories do not have a significant difference at the bottom of the structure. Displacement time histories observed along the Z direction shows the fact that magnitude of displacements for slipping model is higher and will damp out later comparing to the no-slipping model.

Acceleration time histories along X and Z directions at the bottom and top of the structure are shown in Figure (504.17). It is observed that along the X direction the amplitude of acceleration is less considering the slipping behavior and also there is a phase lag in the observed motion. However, the amplitude of the acceleration along Z direction is much higher in case of considering the slipping case. This is the same behavior observed in 1C wave propagation as well but with higher difference in time histories amplitudes.

As shown in Figure (504.18), the dominant frequency of the response in case of slipping is less than the one observed in no-slipping case along X direction while it is higher along Z direction.

Figures (504.19) and (504.20) show the distribution of sliding at the interface of foundation and the soil layer at 9 different time steps of analysis from 4.5 to 5.3 seconds. It can be observed from Figure (504.19) that maximum gap opening of 0.12m is occurred at 4.7 seconds while the location of the openings are changed during the analysis. In addition, maximum sliding at the interface zone in this case happens at 4.8 seconds with magnitude of 0.03m. In both gap and slide distribution plots, it can be observed that the place of maximum is close to the middle of the foundation which is where the structure is located.

Distribution of cumulative dissipated energy due to sliding of the foundation and soil layer contact/interface zone is shown in Figure (504.21). By modeling the slipping behavior at the interface zone, part of the seismic energy is dissipated through the sliding and rocking of the foundation and therefore, less amount will be transferred to the structural components. Figure (504.22) shows how energy can be dissipated during the analysis for the point at the middle of the interface zone (location of the structure).

When sliding happens, some part of the energy is dissipated as shown while there will be no change in dissipated energy if the foundation and soil are sticking to each other.

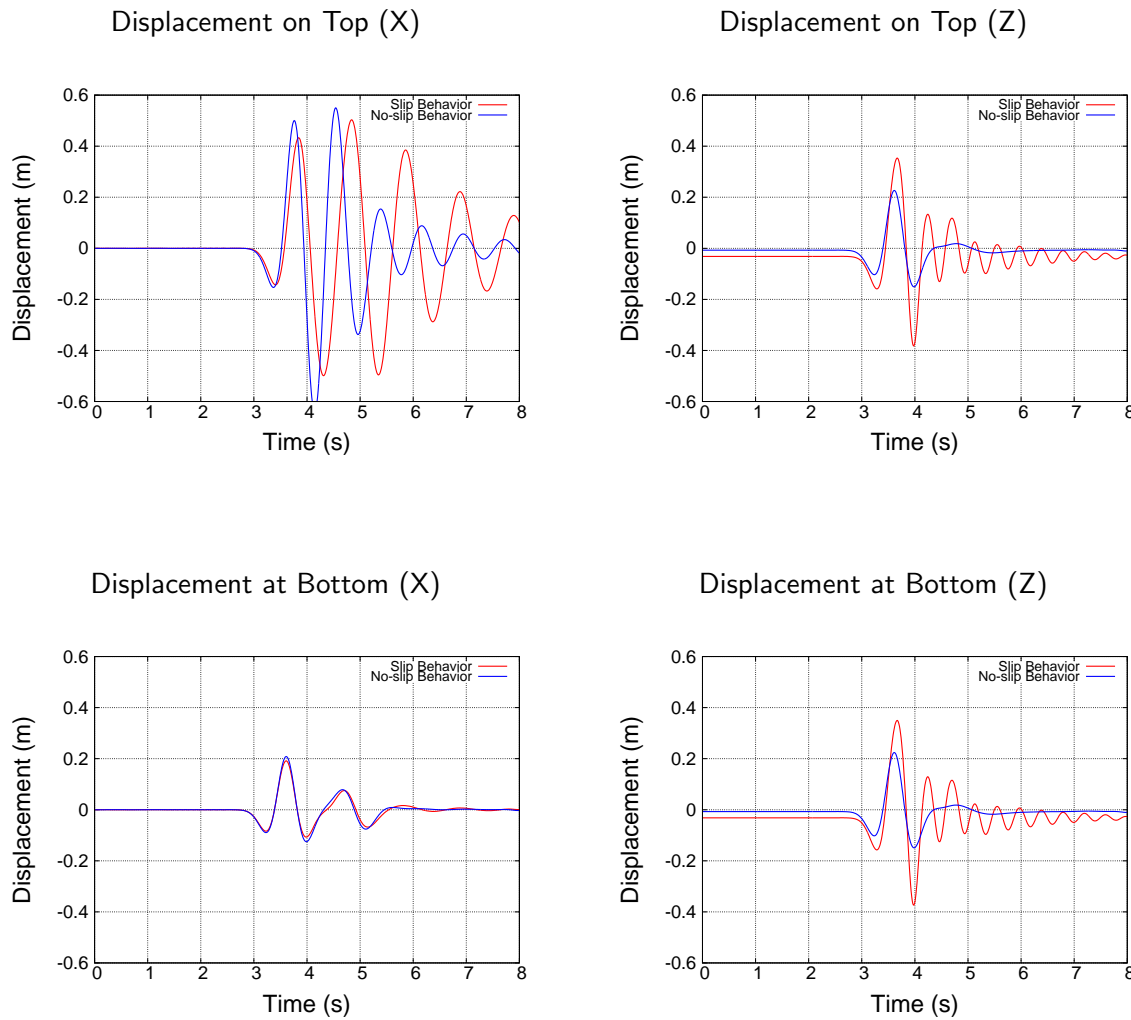


Figure 504.16: Comparison of displacement time histories of the structure between slipping and no-slipping models for Ricker wave

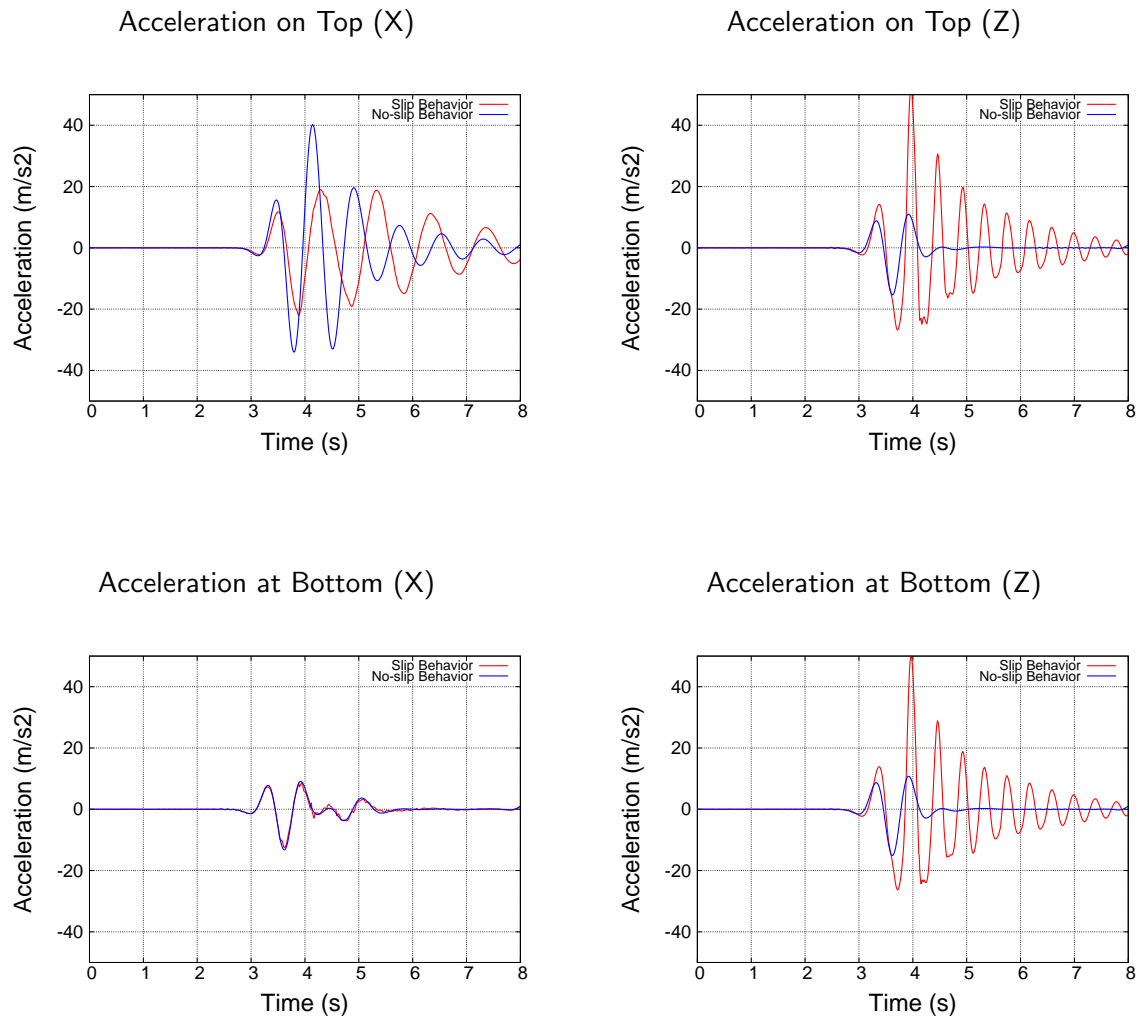


Figure 504.17: Comparison of acceleration time histories of the structure between slipping and no-slipping models for Ricker wave

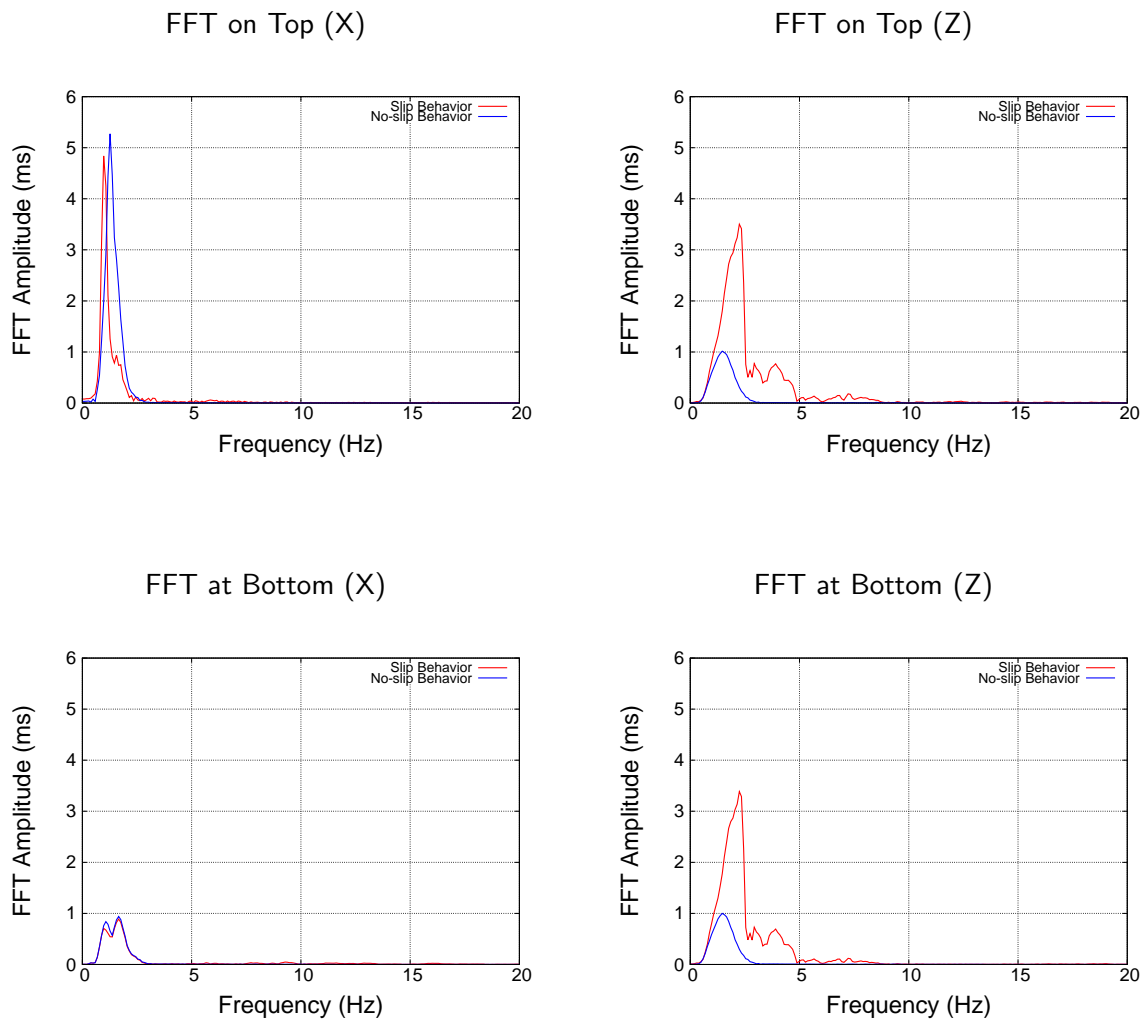


Figure 504.18: Comparison of FFT of the acceleration of the structure between slipping and no-slipping models for Ricker wave

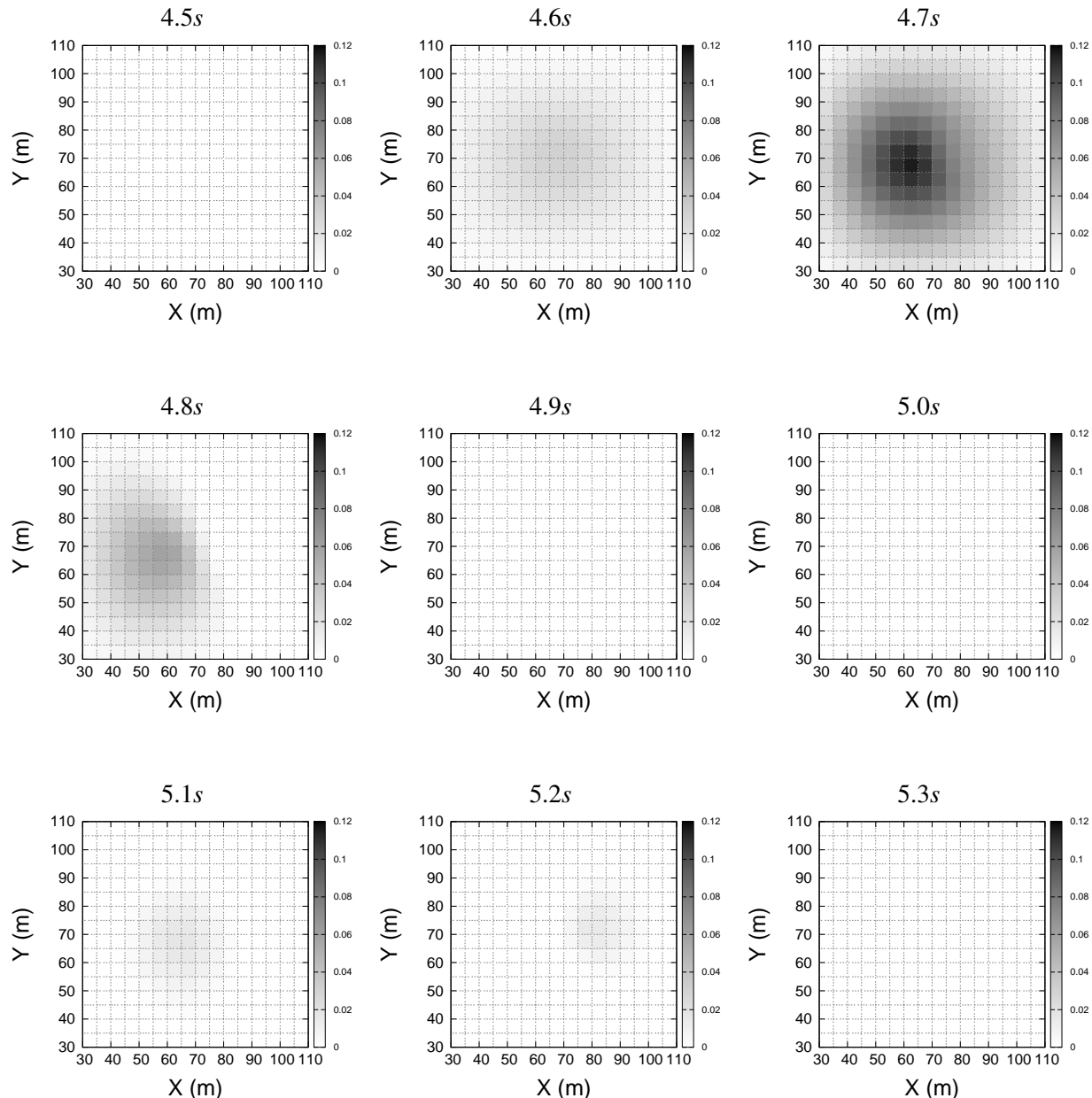


Figure 504.19: Distribution of gap openings along the contact/interface interface for Ricker wave (gray scale given in meters).

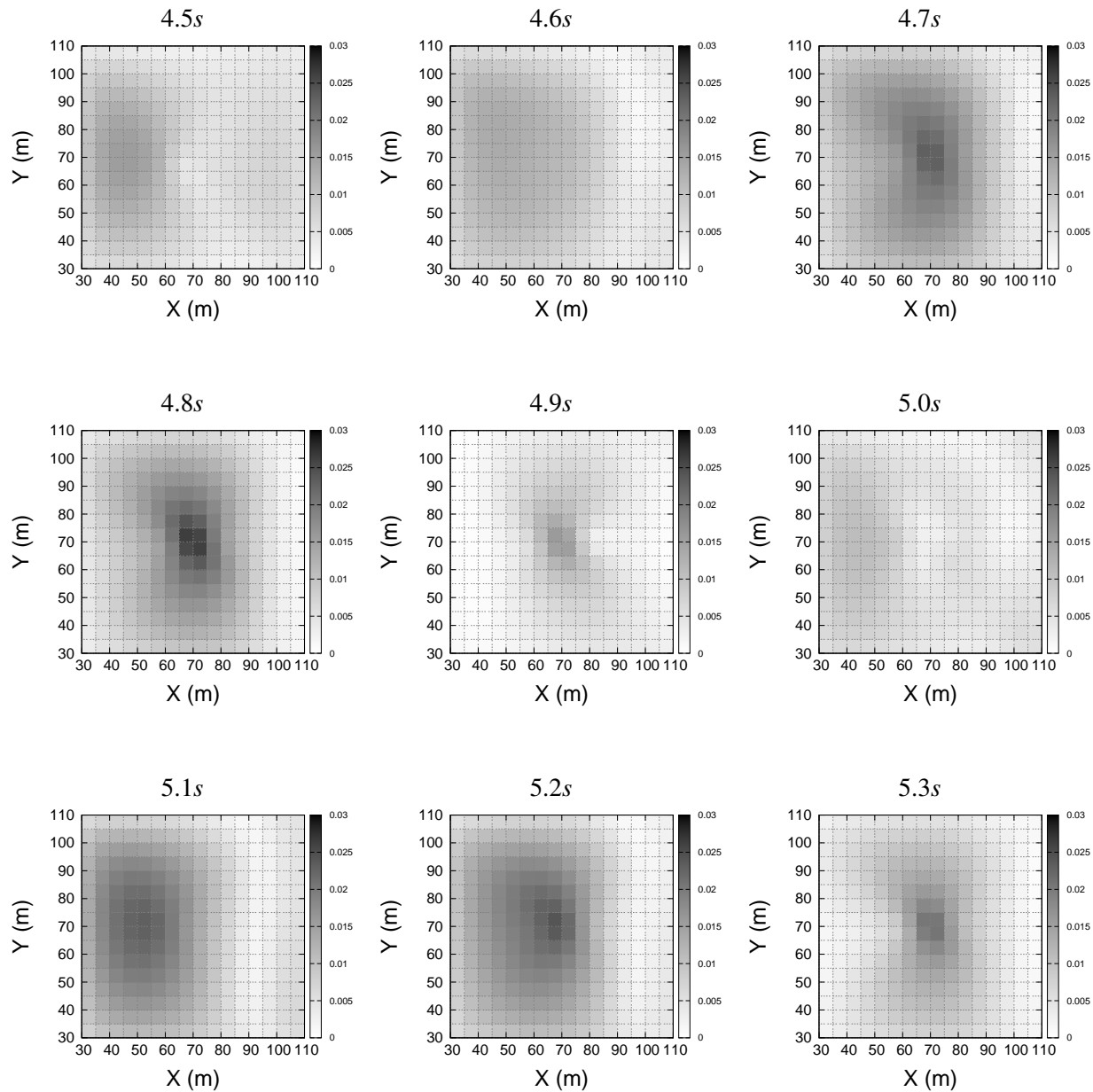


Figure 504.20: Distribution of sliding along the contact/interface for Ricker wave (gray scale given in meters).

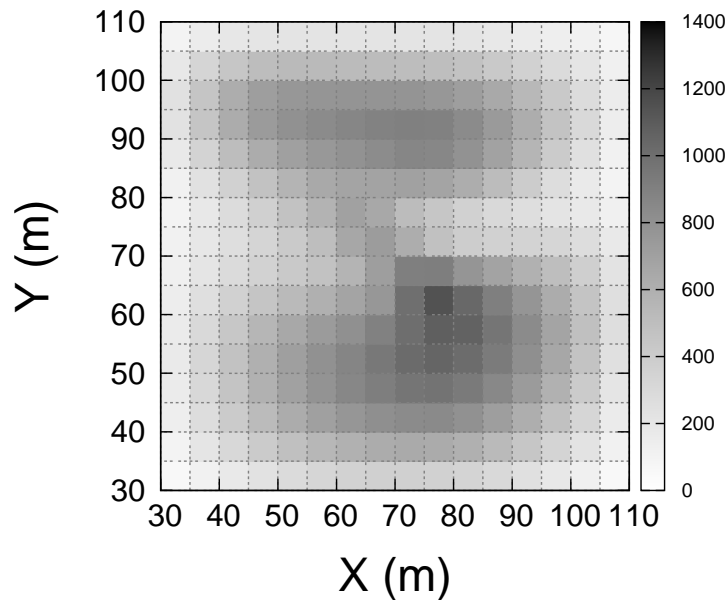


Figure 504.21: Distribution of cumulative dissipated energy due to sliding along the contact/interface for Ricker wave (gray scale given in kJ).

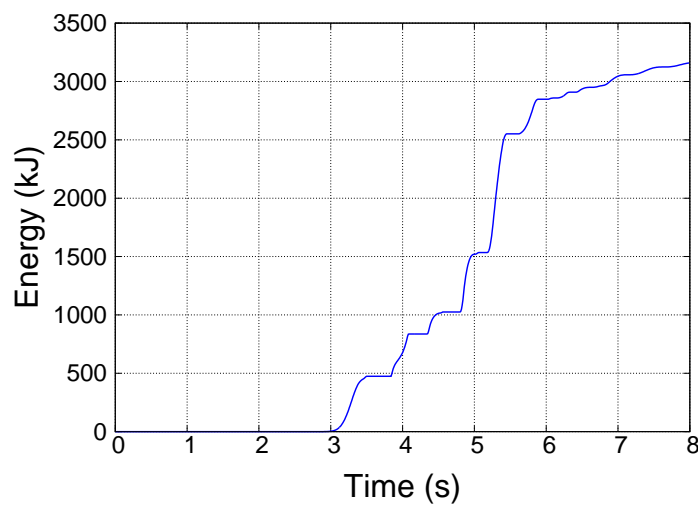


Figure 504.22: Cumulative dissipated energy time history due to sliding at the mid-center of the contact/interface for Ricker wave (gray scale given in kJ).

504.1.2.2 Ricker wave, with fault located at 34° towards the top middle point of the model

The last simulation to be studied here is the case which the location of the fault has an angle of 34° with respect to the top middle point of the model (Figure (504.15)). Same Ricker wave is used as an input motion to be propagated through the model built for first stage of DRM analysis. In this case, since the source of the motion is farther from the interested domain (comparing to previous case with the angle of 45°), motions will arrive later at the interface zone, and structure start shaking later.

Displacement time histories at the bottom and top of the structure are recorded and shown in Figure (504.23) along X and Z directions. Comparing to the previous case along X direction, at the beginning of the shaking the magnitude of the displacement for slipping behavior model is a bit smaller while it damps out sooner as well. Along the X direction, the trend of the displacement time histories are pretty much the same with a slight difference in magnitudes in time.

Acceleration time histories of the structure are shown in Figure (504.24) along X and Z directions. The same behavior is observed here as previous case such that the amplitude of the acceleration is significantly higher for case of no-slipping along the X direction while it is less along the Z direction. The seismic wave damps out sooner along X direction in case of considering the slipping behavior.

The frequency content change is shown in Figure (504.25) by comparing the FFT of the accelerations obtained from the model considering the slipping behavior and the one with no-slipping behavior. It can be observed that there is a slight change in frequency content and predominant frequencies along both X and Z directions.

Figure (504.26) shows the distribution of gap openings along the soil-foundation contact/interface zone for 9 time steps from 4.5 to 5.3 seconds. The maximum gap opening happens at 4.5 seconds with magnitude of $0.12m$. On the other hand, the sliding at the contact/interface zone is shown in Figure (504.27) with maximum magnitude of $0.0035m$ happening at 4.5 seconds. In this case, the maximum sliding happens around the location of the structure.

Figures (504.28) and (504.29) show the distribution of the dissipated seismic energy at the interface zone and dissipated energy time history at the middle of the contact/interface zone respectively.

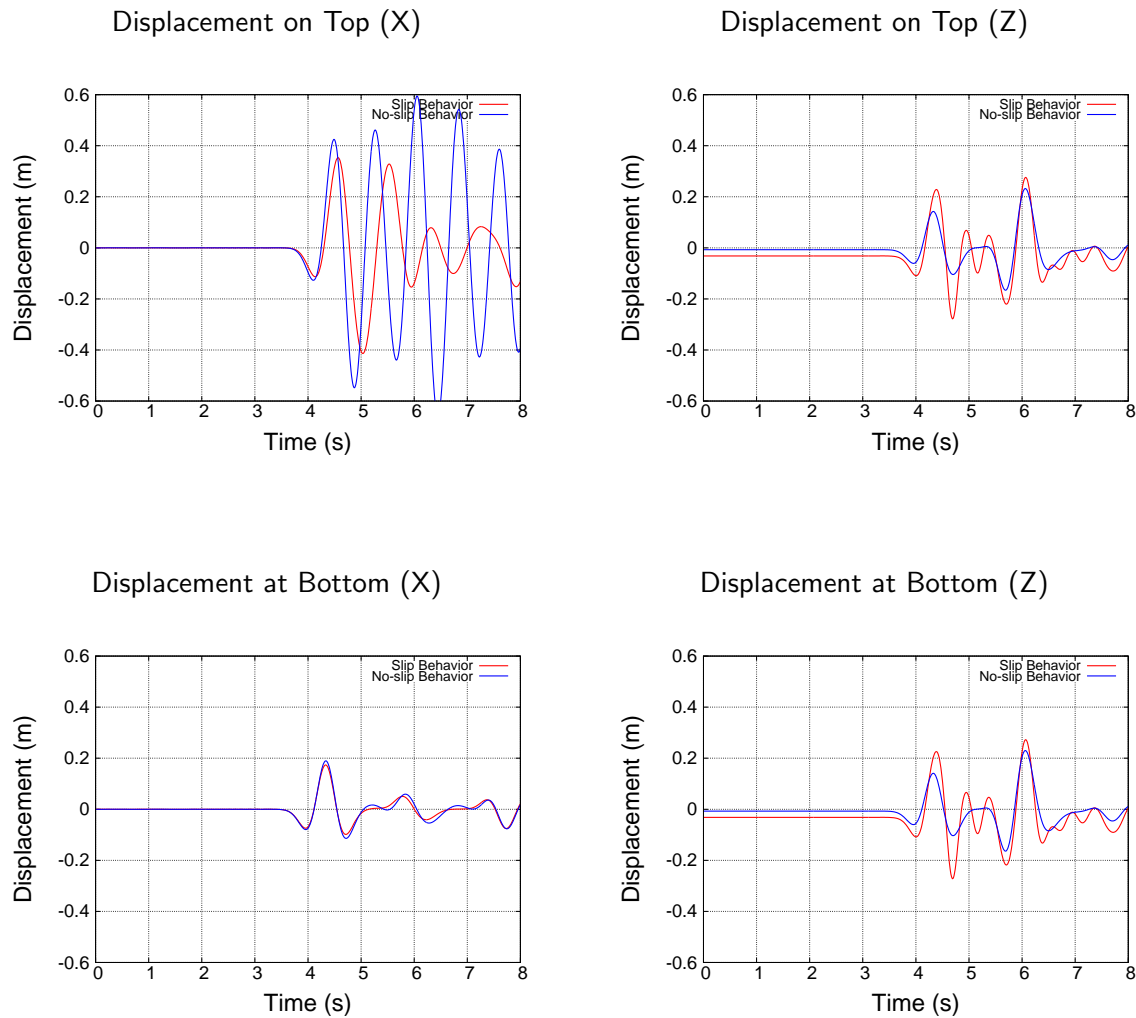


Figure 504.23: Comparison of acceleration time histories of the structure between slipping and no-slipping models for Ricker wave

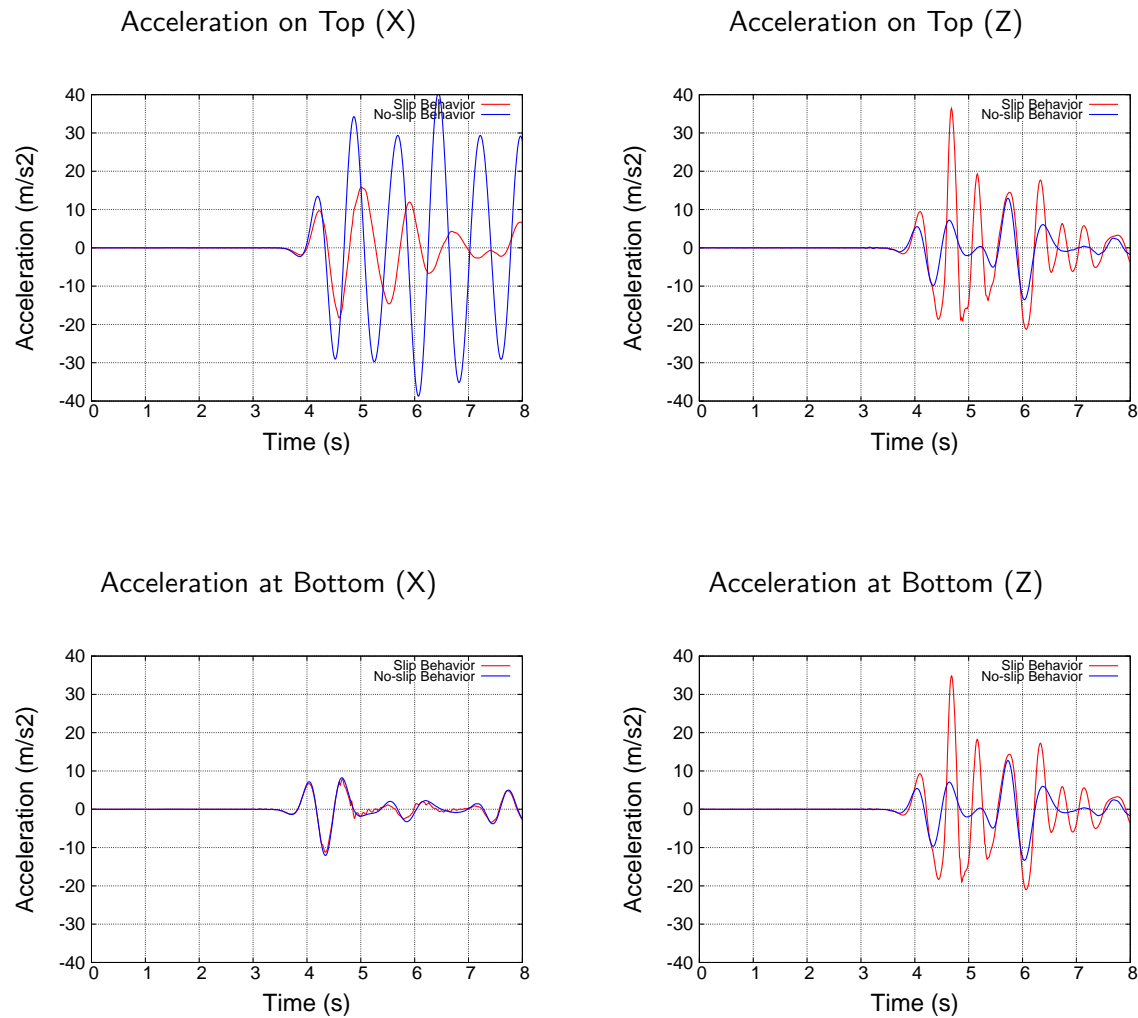


Figure 504.24: Comparison of acceleration time histories of the structure between slipping and no-slipping models for Ricker wave

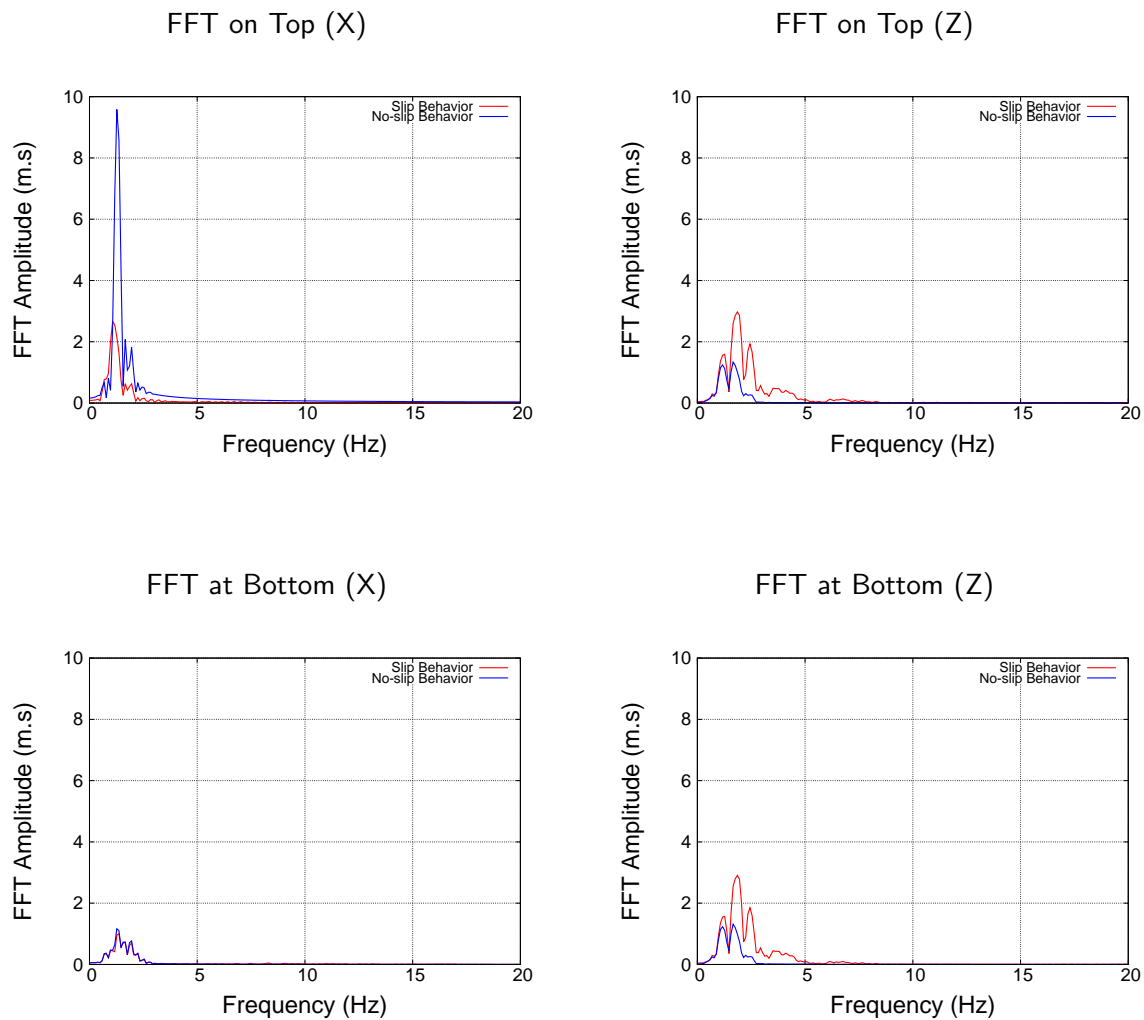


Figure 504.25: Comparison of FFT of the acceleration of the structure between slipping and no-slipping models for Ricker wave

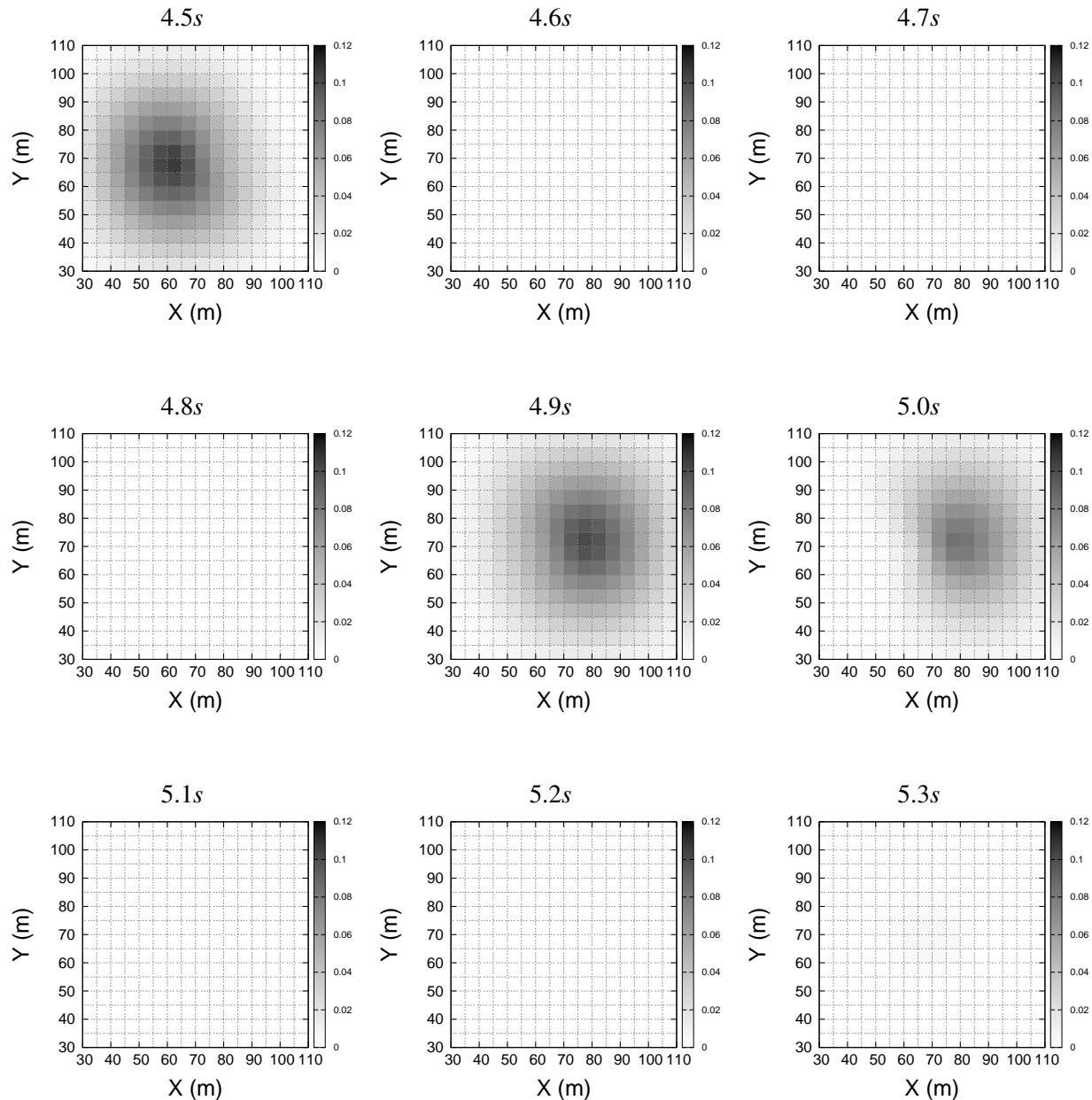


Figure 504.26: Distribution of gap openings along the contact/interface for Ricker wave (gray scale given in meters)

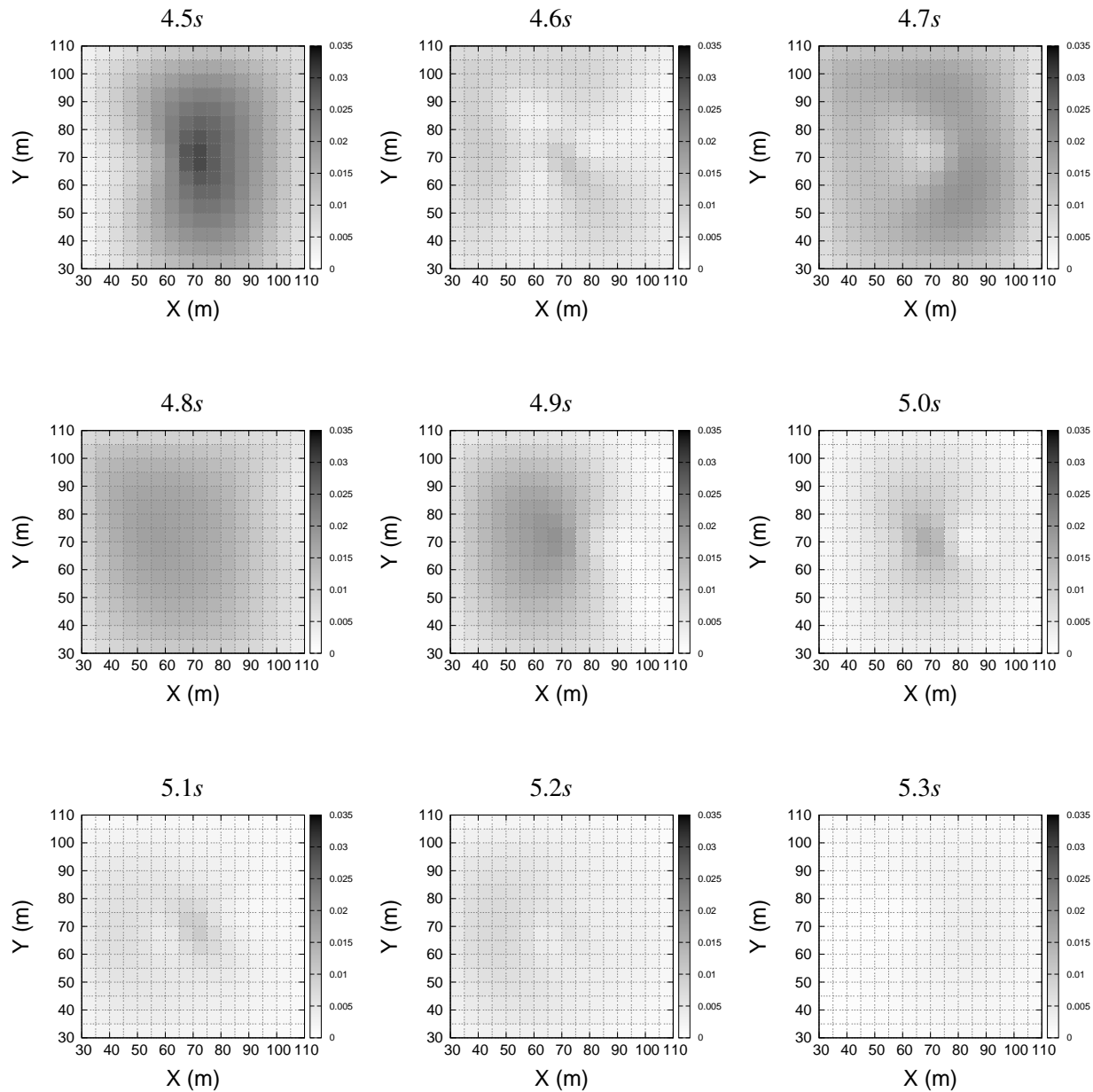


Figure 504.27: Distribution of sliding along the contact/interface for Ricker wave (gray scale given in meters)

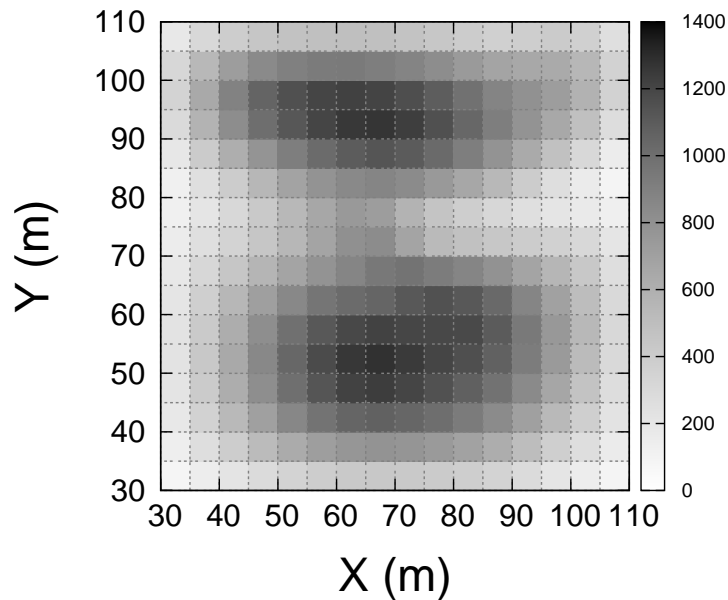


Figure 504.28: Distribution of cumulative dissipated energy due to sliding along the contact/interface for Ricker wave (gray scale given in kJ)

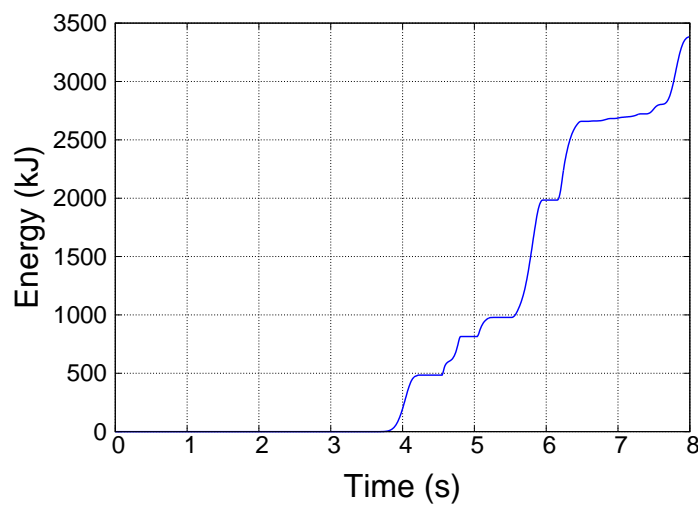


Figure 504.29: Cumulative dissipated energy time history due to sliding at the mid-center of the contact/interface for Ricker wave (gray scale given in kJ)

504.2 Three Dimensional (3C) Seismic Wave Fields and Behavior of Nuclear Power Plants (NPPs)

504.2.1 Development of Seismic Motions: Large Scale Free Field Model

- Large scale seismic free field
- Close up for large scale seismic free field

504.2.2 NPP Response, Model #01

- Free field at NPP location
- NPP response
- NPP response, cut-out of the model, inside response

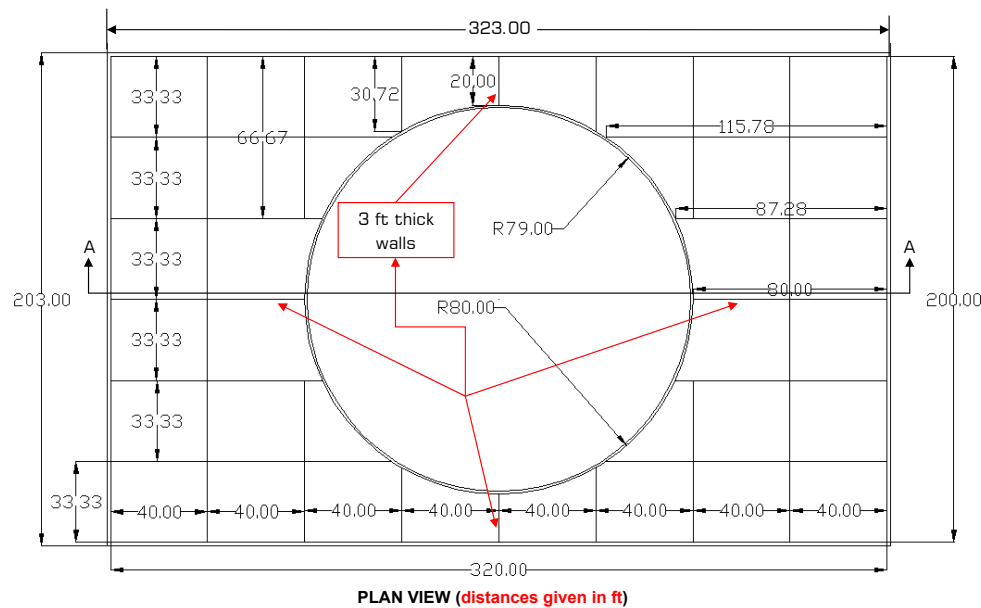
504.3 3D Representative NPP Structure Model(s)

504.3.1 Model #01, Single NPP

Total number degrees of freedom (DOFs, unknowns) for Model 01 is 681,648. Table 504.3.1, gives other basic statistics for this model, while Figures 504.3.1 to 504.3.1 show disposition and views of the finite element mesh.

Table 504.1: Model 01 Statistics

Components	Number of
3 DOF Nodes	205875
6 DOF Nodes	14413
27 node Bricks	23916
ANDES Shells	15627
Contact elements	2124
9 DOF Beams	583



Notes for Auxiliary Building:

- Interior walls except those highlighted above have a thickness = 2 ft.
- Exterior walls have a thickness of 3 ft.

Figure 504.30: Model01: Plan view (dimensions in feet).

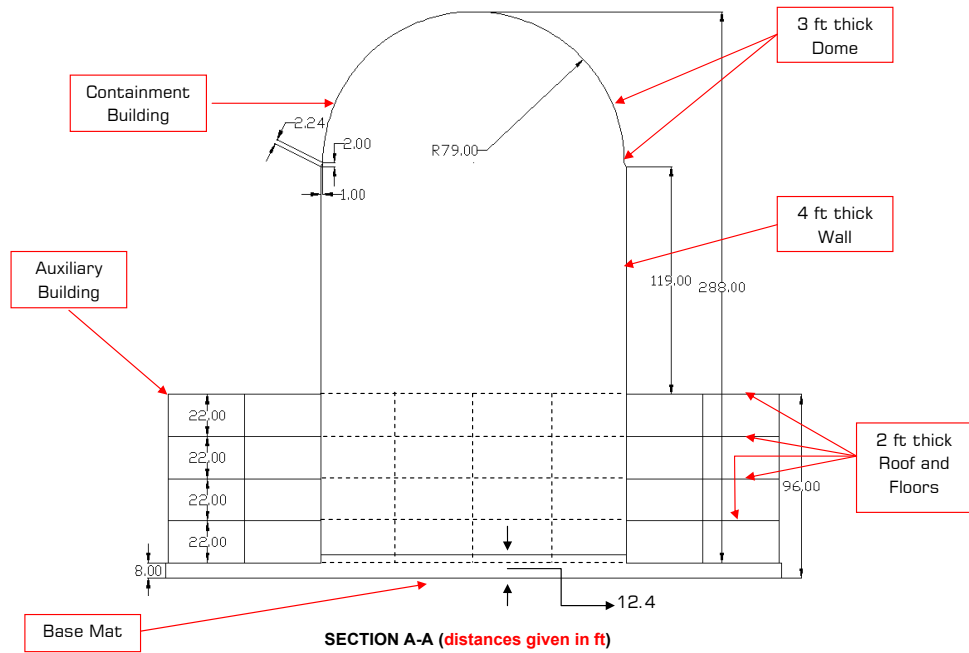


Figure 504.31: Model01: Section view (dimensions in feet).

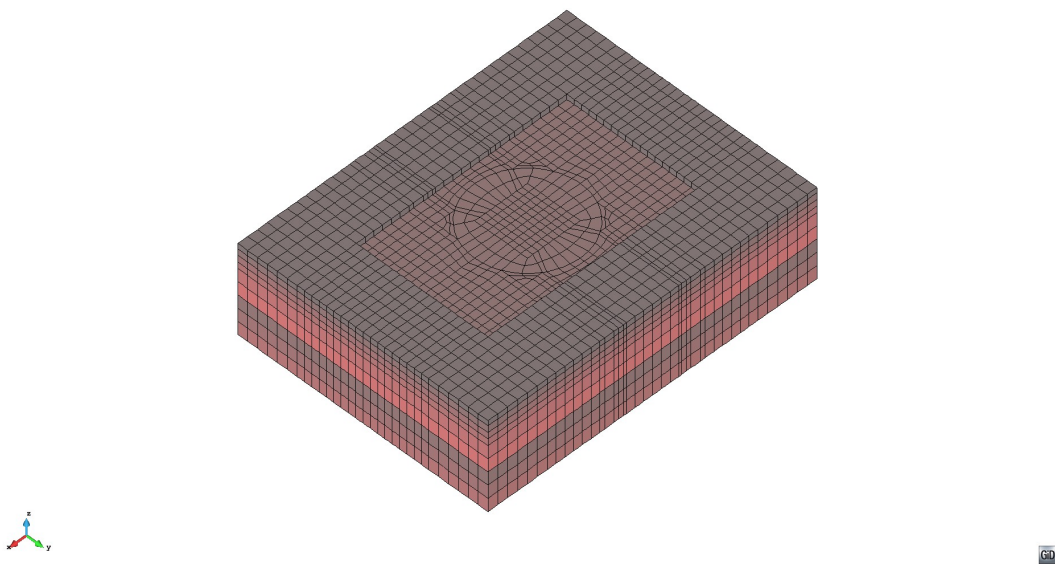


Figure 504.32: Model01: Soil layers.

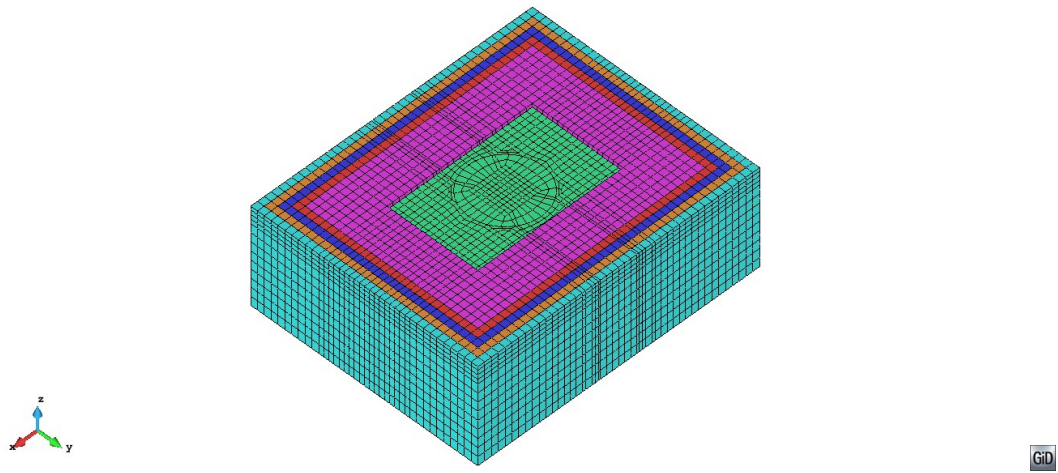


Figure 504.33: Model01: Soil with the DRM (no slab).

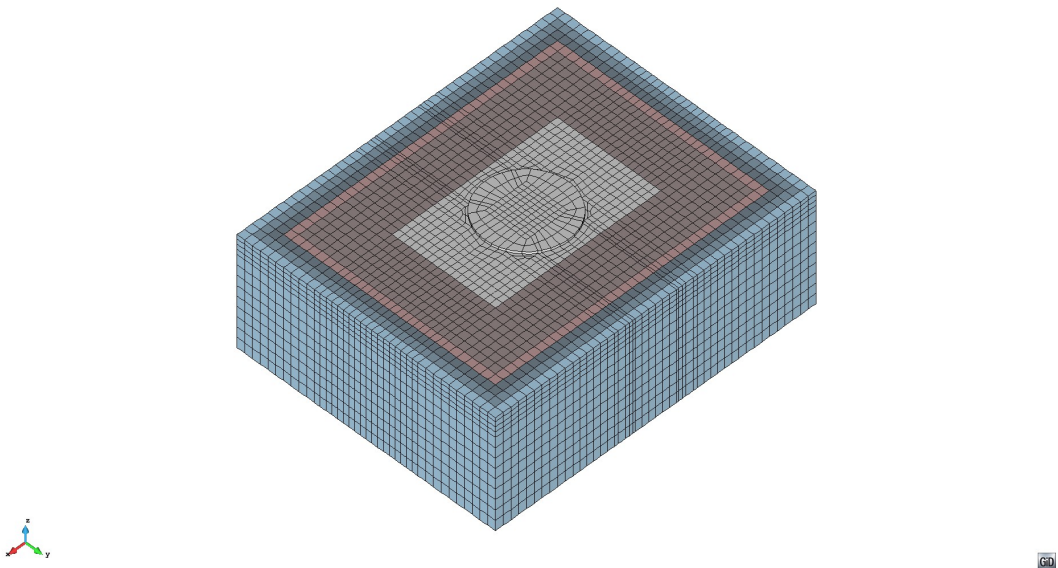


Figure 504.34: Model01: Soil, with the slab and the DRM.

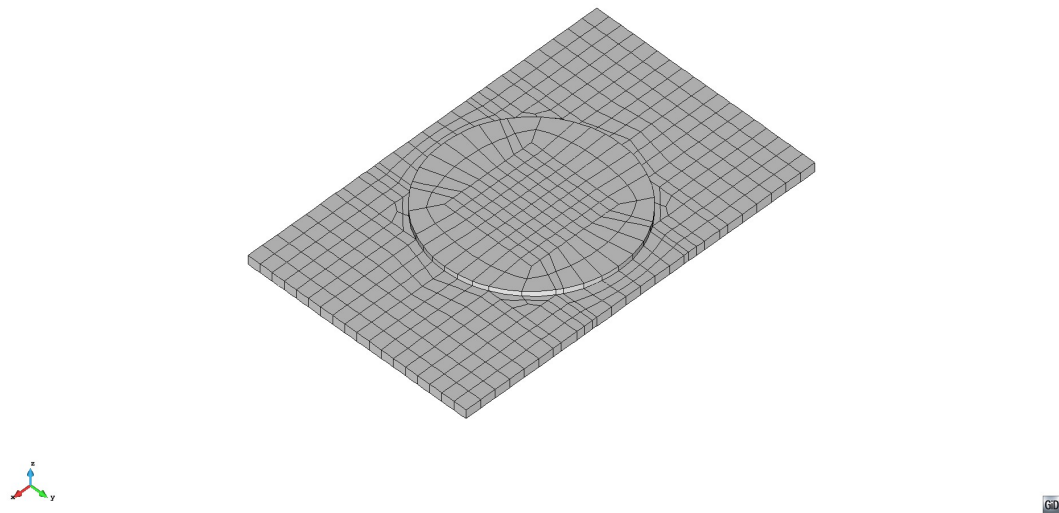


Figure 504.35: Model01: Slab only.

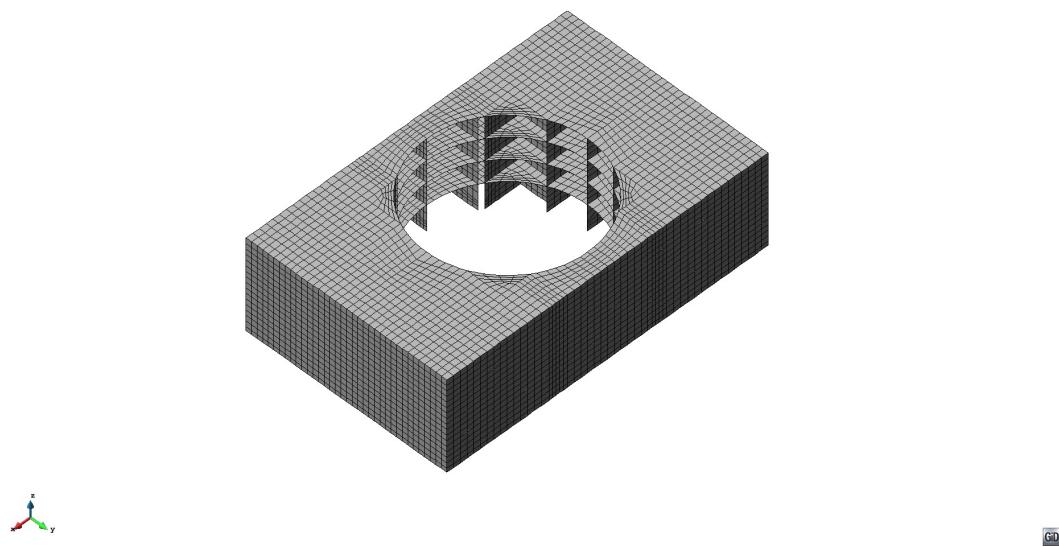


Figure 504.36: Model01: Auxillary building

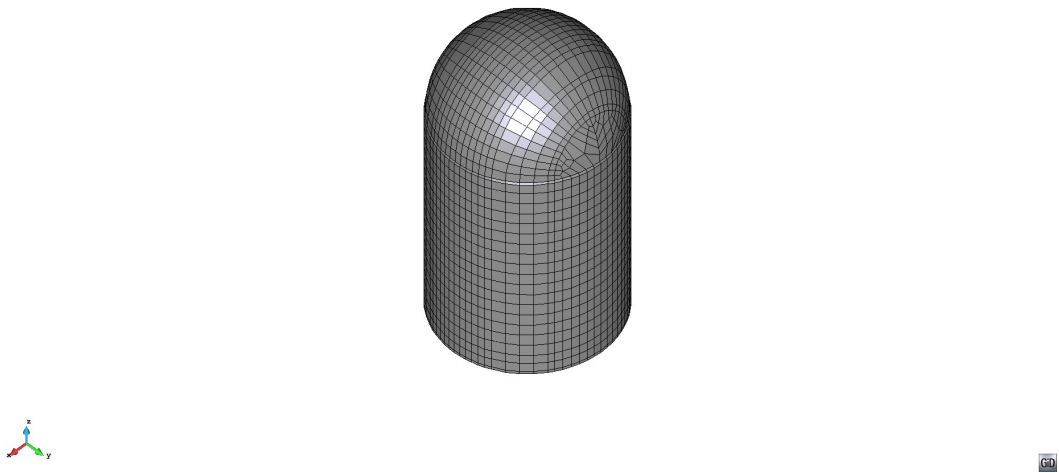


Figure 504.37: Model01: Containment building.

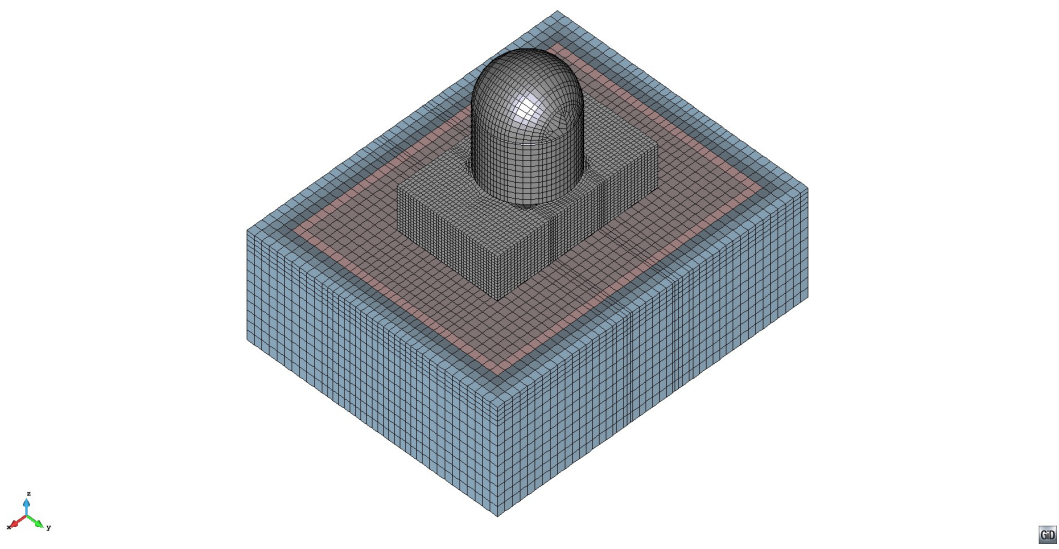


Figure 504.38: Model01: Full view.

504.3.2 Model #02, Single NPP

Simplified Representative 3D Model. Total number degrees of freedom (DOFs, unknowns) for Model 02 is 260,883. Table 504.2, gives other basic statistics for this model, while Figures 504.3.1 to 504.3.2 show disposition and views of the finite element mesh.

Table 504.2: Model 02 Statistics

Components	Number of
3 DOF Nodes	84820
6 DOF Nodes	3263
27 node Bricks	9576
ANDES Shells	8384
Contact elements	1249
9 Node Beams	490

Figure 504.3.2 shows a general disposition of a representative 3D NPP model #02.

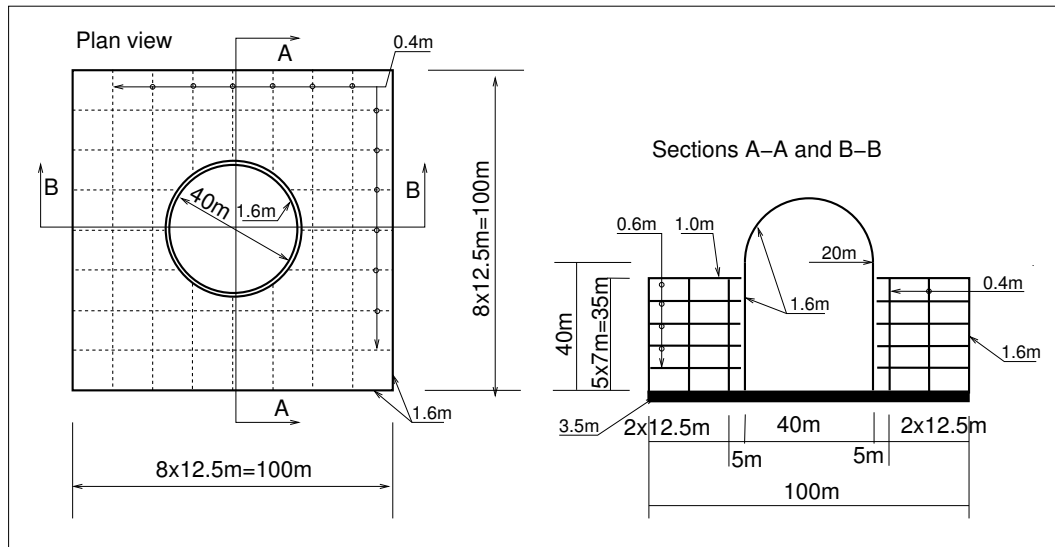


Figure 504.39: General disposition of a representative 3D NPP model (model #02).

The model was developed as a cylindrical containment with dome top, while the auxiliary building surrounds the containment. There is no contact/interface between containment and the auxiliary building and current model has a gap of 0.2m while a new model (currently under development) will reduce this gap space, while still maintaining independence of two structural systems.

Finite element mesh for components and the complete system is shown in Figures 504.3.2 to 504.3.2.

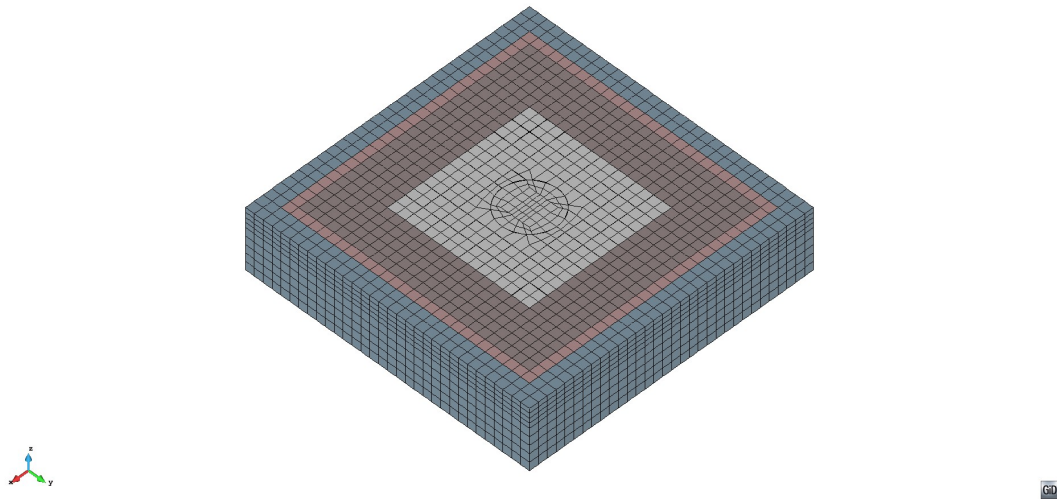


Figure 504.40: Model02: Soil with the fondation slab and the DRM layers.

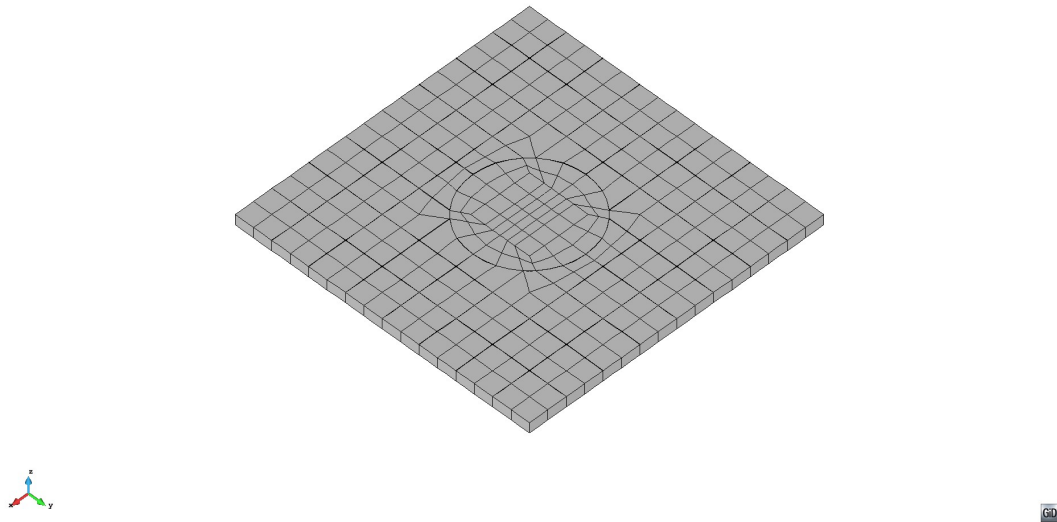


Figure 504.41: Model02: Foundation slab only.

Both structures (containment and auxiliary building) were placed on a slab foundation and then placed on a soil/rock base. Model is flexible enough that soil/rock properties and geology can be

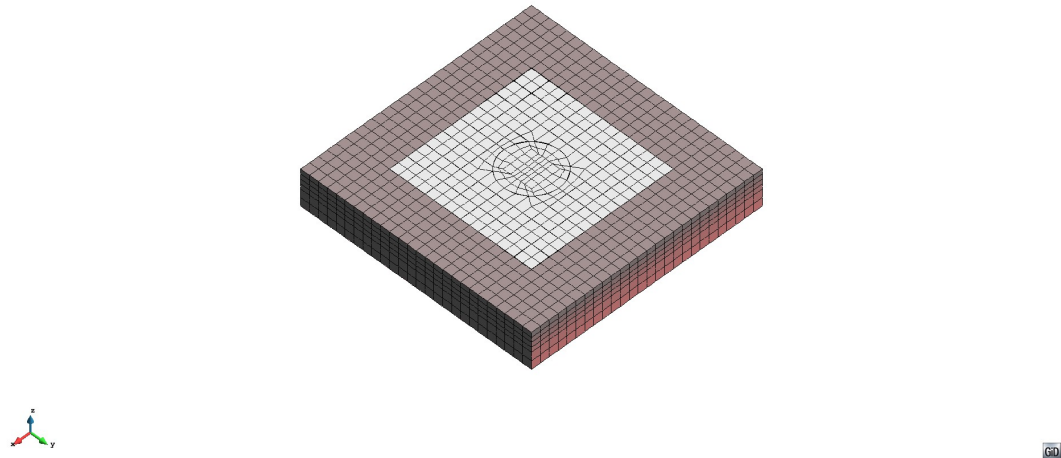


Figure 504.42: Model02: Layered soil.

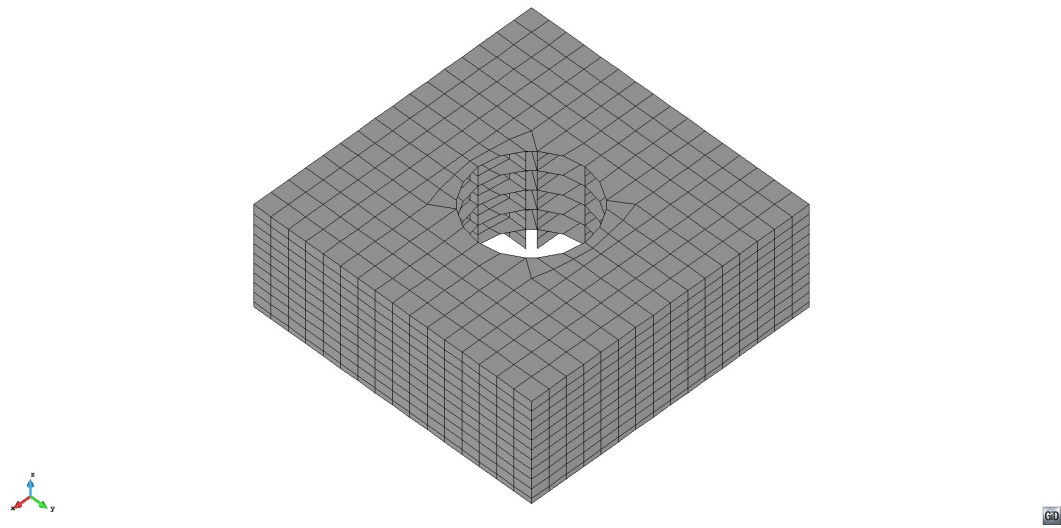


Figure 504.43: Model02: Auxillary building.

varied. The sub-base model also includes a layer of elements for the DRM motion input, as well as two layers of elements outside the DRM layer for damping any outgoing waves. Models with a single NPP (Figure 504.3.2) is developed and used in analysis.

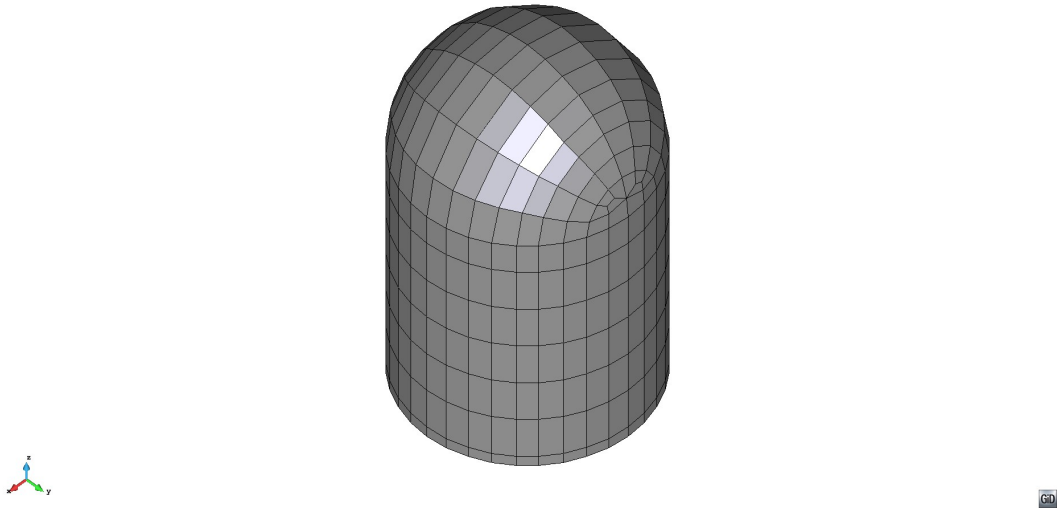


Figure 504.44: Model02: Containment building.

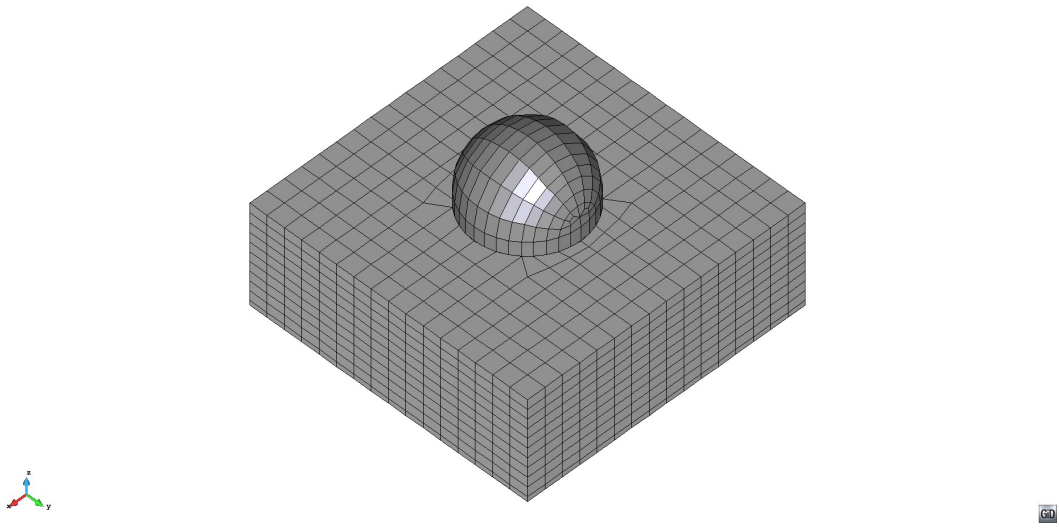


Figure 504.45: Model02: Auxillary and containment buildings.

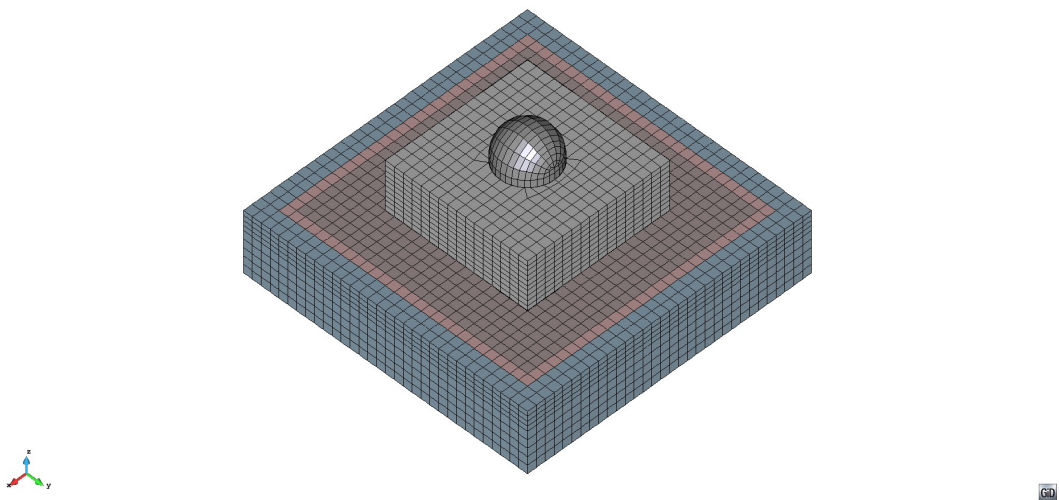


Figure 504.46: Model02: Full view, Finite element model for a single NPP with the containment and auxiliary buildings on a common base mat, as well as the soil/rock sub-base, DRM layer for seismic motions input and the layers outside of DRM for damping out outgoing waves.

504.3.3 Model #03, Double NPP, Soil-Structure-Soil-Structure Interaction

Total number degrees of freedom (DOFs, unknowns) for Model 03 is 518,472. Table 504.3, gives other basic statistics for this model, while Figures 504.3.3 to 504.3.3 show finite element mesh.

Table 504.3: Model III Basic Statistics

Components	Number of
3 DOF Nodes	168405
6 DOF Nodes	6526
27 node Bricks	19152
ANDES Shells	16768
Contact elements	2498
9 Node Beams	950

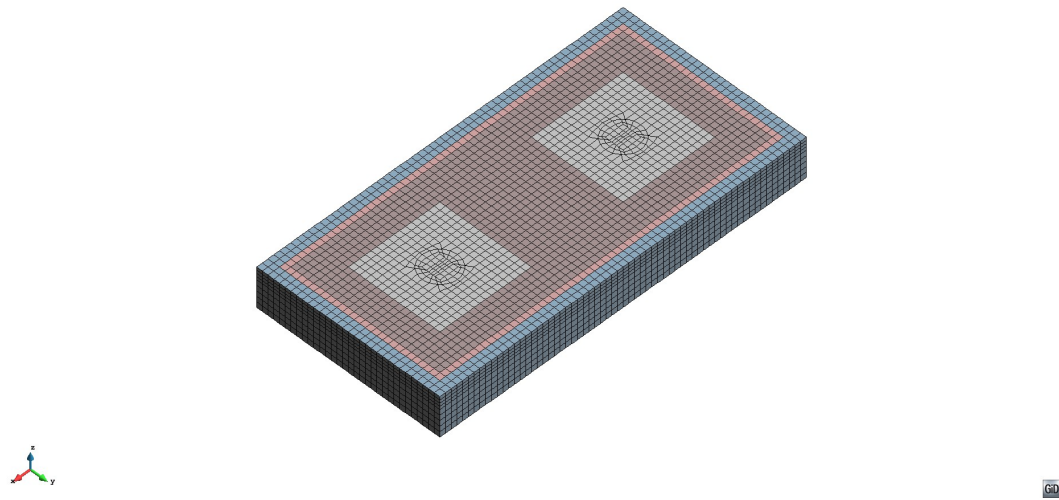


Figure 504.47: Model03: Soil, foundation slabs and the DRM layers.

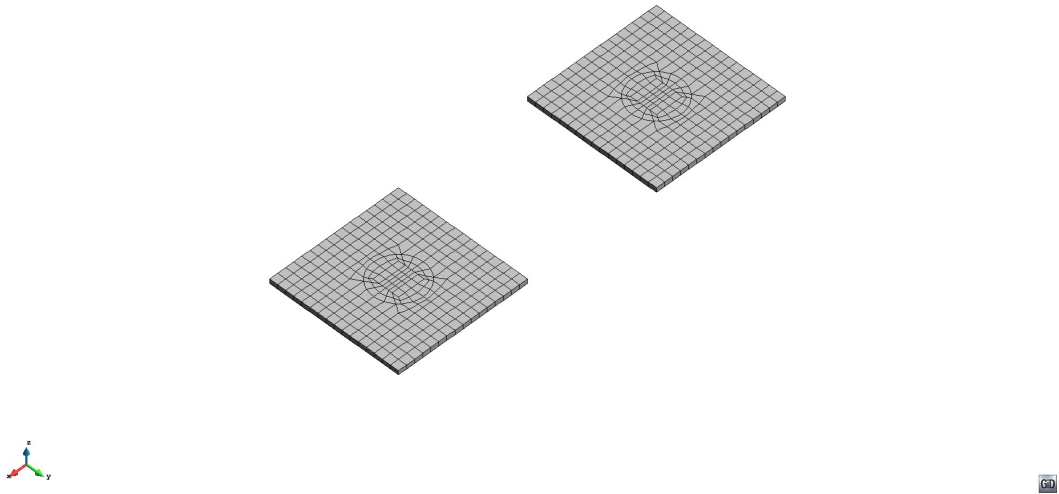


Figure 504.48: Model03: Foundation slabs only.

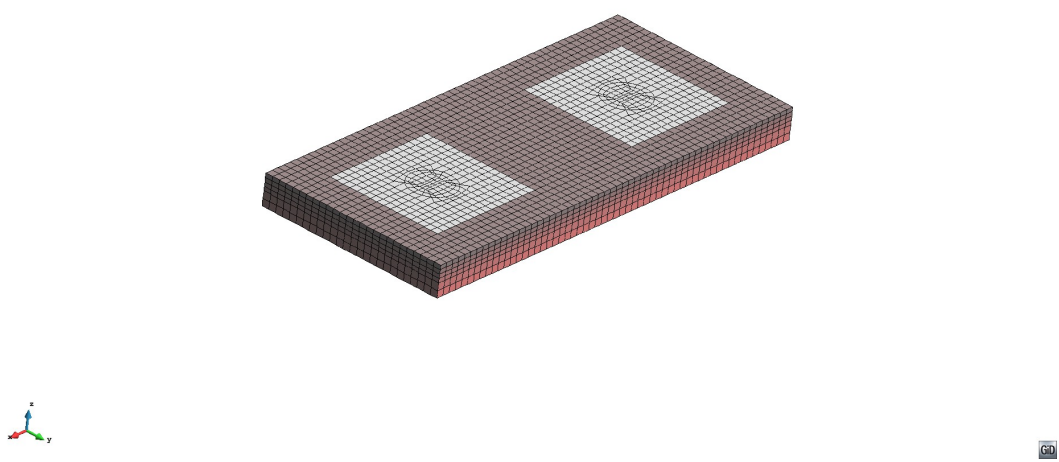


Figure 504.49: Model03: Layered soil.

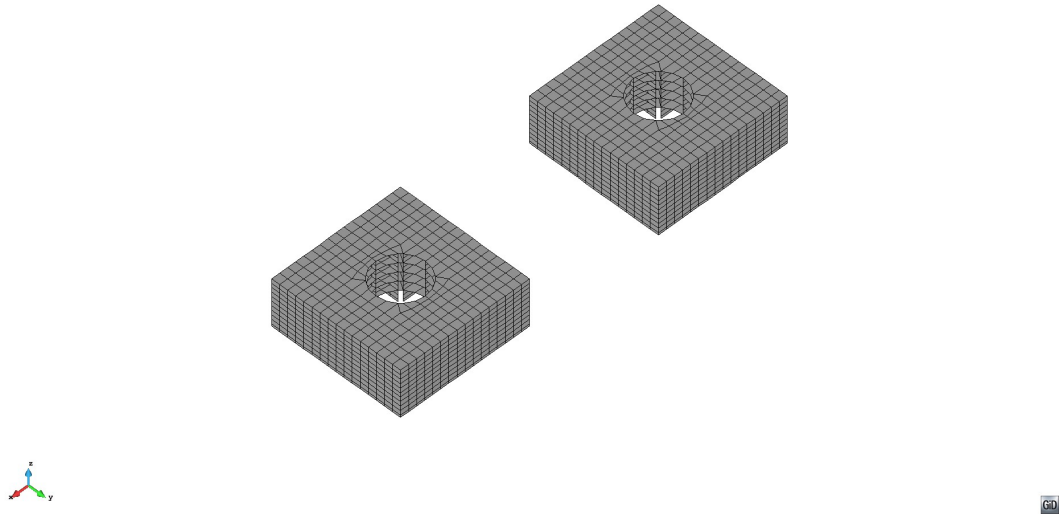


Figure 504.50: Model03: Auxillary buildings.

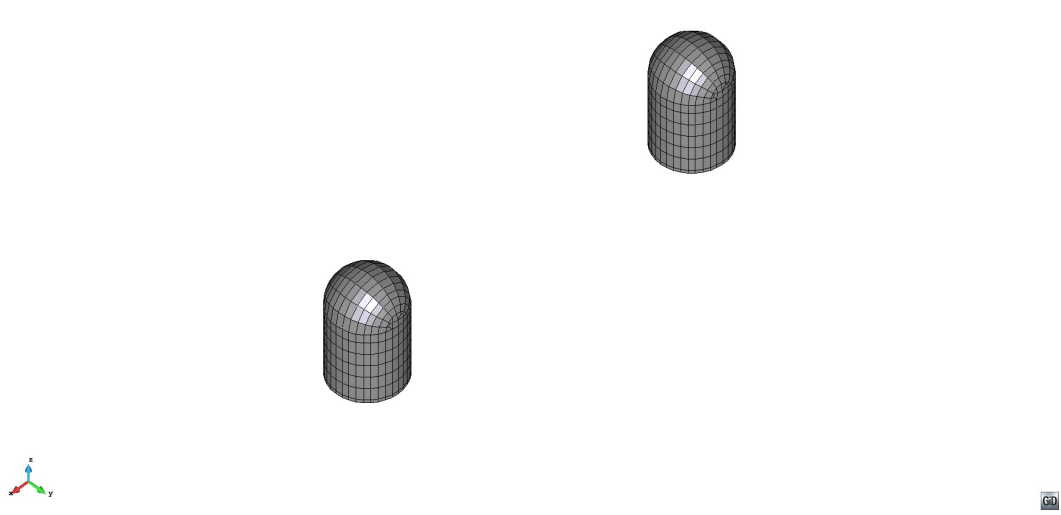


Figure 504.51: Model03: Containment buildings.

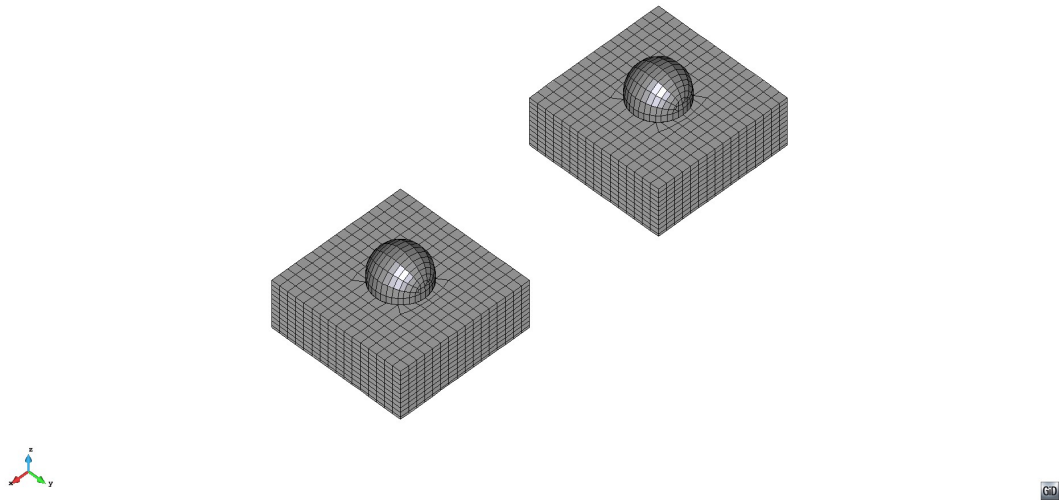


Figure 504.52: Model03: Auxillary and containment buildings.

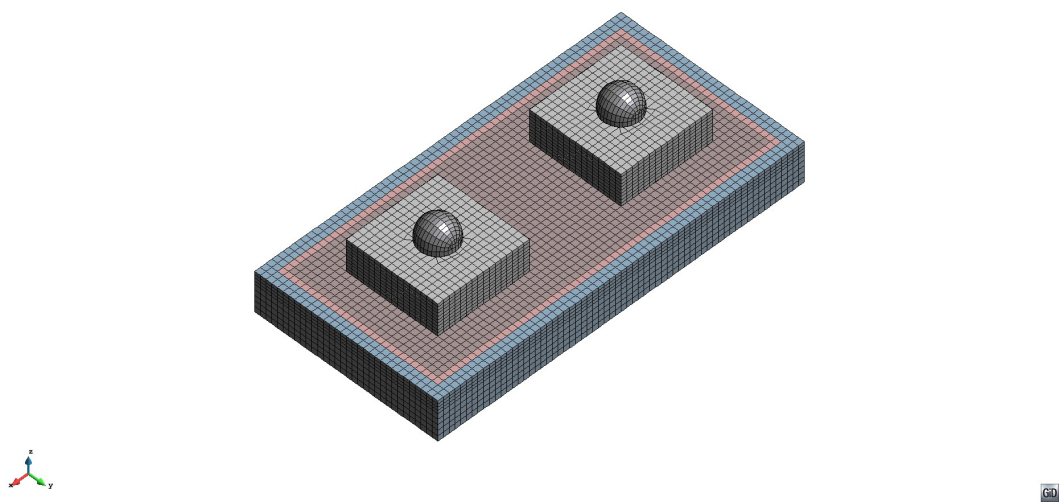


Figure 504.53: Model03: Full view.

Soil-Structure-Soil-Structure Interaction. Soil-Structure-Soil-Structure Interaction (SSSSI) need to be taken into account sometimes, as it might contribute to higher levels of seismic shaking for NPPs. It seems that in the case of making an assumption of elastic soil and rock beneath the NPP foundation, the SSSSI will have a larger effect most of the time, while with the inclusion of elastic-plastic models for soil and rock under the NPP foundation, those SSSSI influences will be reduced most of the time. This is illustrated in one of the models that was developed for analyzing SSSSI. While SSSSI for two NPPs (of similar stiffness and mass) conforms to the above observations, it is noted that SSSSI influences of smaller structures on larger (NPPs) can be mostly neglected, the SSSSI influence of larger structures (NPPs) on smaller structures Probably cannot be neglected.

There are a number of ways to model SSSSI.

- **Direct Models.** The simplest and most accurate is to develop a direct model of both (two or more) structures on subsurface soil and rock, to develop input seismic motions and analyze results. While this approach is the most involved, it is also the most accurate, as it allows for proper modeling of all the structure, foundation and soil/rock geometries and material without making any unnecessary simplifying assumptions.
- **Symmetry and Anti-Symmetry Models.** These models are sometimes used in order to reduce complexity and sophistication of the direct model (see recent paper by Roy et al. (2013) for example). However, there are a number of concerns regarding simplifying assumptions that need to be made in order for these models to work. These models have to make an assumption of a vertically propagating shear waves and as such do not take into account surface waves (Rayleigh, Love, etc) that carry significant amount of seismic energy. These surface waves will additionally excite NPP for rocking and twisting motions, which will then be transferred to adjacent NPP by means of additional surface waves. If only vertically propagating waves are used for input (as is the case for symmetry and anti-symmetry models) energy of input surface waves is neglected. It is noted that depending on the surface wave length and the distance between adjacent structures, a simple analysis can be performed to determine if particular surface waves, emitted/radiated from one structure toward the other one (and in the opposite direction) can influence adjacent structures. It is noted that the wave length can be determined using a classical equation $\lambda = v/f$ where λ is the length of the (surface) wave, v is the wave speed¹ and f is the wave frequency of interest. Table504.4 below gives Rayleigh wave lengths for four different wave frequencies (1, 5, 10, 20 Hz and for three different Rayleigh (very close to shear) wave velocities (300, 1000, 2500 m/s):

¹For Rayleigh surface waves, their speed is just slightly below the shear wave speed (within 10%, depending on elastic properties of material), so a shear wave speed can be used for making these Rayleigh wave length estimates.

Table 504.4: Rayleigh wave length as a function of wave speed [m/s] and wave frequency [Hz].

	1.0Hz	5.0Hz	10.0Hz	20Hz
300m/s	300m	60m	30m	15m
1000m/s	1000m	200m	100m	50m
2500m/s	2500m	500m	250m	125m

It is apparent that for given separation between NPP buildings, different surface wave (frequencies) will be differently transmitted with different effects. For example, for an NPP building that has a basic linear dimension (length along the main rocking direction) of 100m, the surface wave the low frequency waves (1Hz) in soft soil ($v_s \approx 300\text{m/s}$) will be able to encompass a complete building within a single wave length, while for the same soil stiffness, the high frequency (20Hz) will produce waves that are too short to efficiently propagate through such NPP structure. On the other hand, for higher rock stiffness ($v_s \approx 2500\text{m/s}$), waves with frequencies all the way up to approximately 5Hz and maybe even 10Hz, have an extent that can easily be affecting a building with a 100m dimension.

Further comments on symmetric and antisymmetric models:

- Symmetry: motions of two NPPs are out phase and this represents an unrealistic case, unless the wave length of surface wave created by one NPP (toward the other NPP) is so large that half wave length will encompass both NPPs. This type of motions (symmetry) is illustrated in figure 504.3.3 below

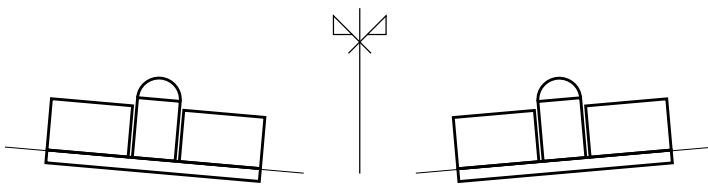


Figure 504.54: Symmetric mode of deformation for two NPPs near each other.

- Antisymmetry: motions of two NPPs are in phase and while that is more realistic than the symmetry case, still requires perfect matching of 1C input motions and the soil/rock conditions beneath, and as such is not realistic. This type of SSSSI is illustrated in figure 504.3.3 below

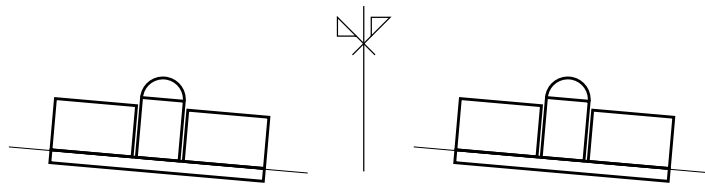


Figure 504.55: Anti-symmetric mode of deformation for two NPPs near each other.

504.3.4 Model #04, Small Modular Reactor (SMR)

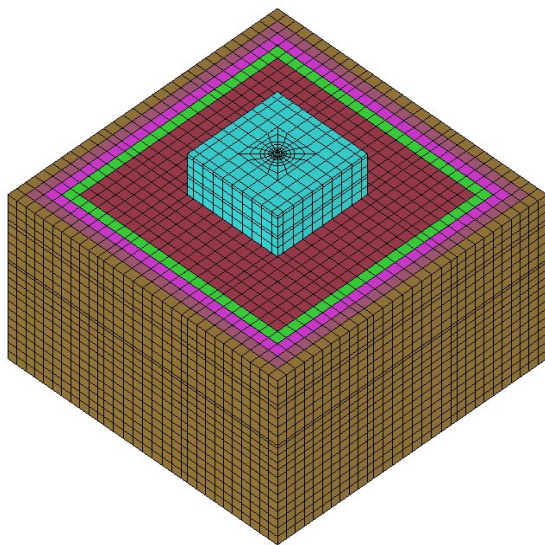


Figure 504.56: Small Modular Reactor model, top (surface) view.

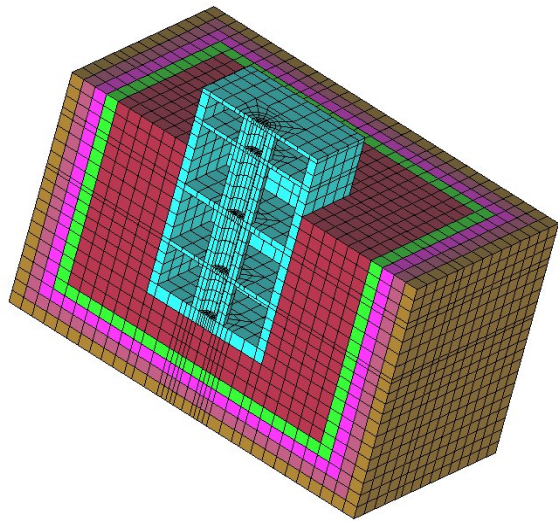


Figure 504.57: Small Modular Reactor model, cross section (half model) view.

504.4 3C (6C) vs 1C Seismic Motions

Realistic seismic wave fields are fully three dimensional, consisting of a body and surface waves, and featuring translational and rotational components of motions at and near the surface. However, current focus of various seismic analysis standards is on 1C motions. These 1C motions are representing one component of a full 3C wave field. More recently, use of 3×1 C wave fields have been advocated, where 1C wave motions are replicated in other horizontal and a vertical direction with certain scaling factors. Use of 3×1 C motions makes an implicit assumption that vertical motions are resulting from 1C compressional waves. This assumption is usually not true, as most of the vertical motions are a result of surface wave motions.

504.4.1 Appropriate Use of 3C and 3×1 C and 1C Seismic Motions

We start by pointing out one of the biggest simplifying assumptions made, is that of a presence and use of 1C seismic waves. As pointed out in section 4.2.1 above, worldwide records do not show evidence of 1C seismic waves. It must be noted, that an assumption of neglecting full 3C seismic wave field and replacing it with a 1C wave field can sometimes be appropriate. However, such assumption should be carefully made, taking into account possible intended and unintended consequences.

A brief discussion on 1C, 3×1 C and 3C seismic wave modelling and effects on SSI is provided below:

- 1C modelling of seismic waves is possible if material modelling for soil is linear or equivalent linear elastic. In this case, 1C motions from different directions (horizontal) can be combined, as superposition principle applies for linear elastic systems (soil in this case). Modeling of vertical motions using 1C approach is abit different as an analysis needs to be performed to decide if the vertical wave is a compressional wave (primary, P wave) or if vertical motions are a consequence of vertical components of surface waves. More on those options is provided below in 3×1 C modelling option.
- 3×1 C modeling of seismic waves is possible, similarly to the above case, if soil material is linear or equivalent linear elastic. As noted above, superposition principle can be applied and motions from each direction can be superimposed to obtained 3C motions at the surface. Since most of the time vertical motions are a results (consequence) of Rayleigh surface waves, it is important to analyze vertical motions and decide if modelling motions as 1C is appropriate. To this end, a wave length of surface wave plays an important role. If the Rayleigh surface wave length (which features both horizontal and vertical components) is longer than 12 times the dimension of the object (NPP), than object rotations, due to differential vertical displacements at object ends, are

indeed fairly small and object does move up and down as if excited with a vertical wave. This is shown in Figure 504.58 as the upper case. On the other hand, if the wave is long less than 12 object dimensions, then vertical motions are gradually replaced by object rotations, while vertical motions are reduced. Case in the lower left corner of Figure 504.58 shows a limiting case where seismic wave is 4 times longer than object dimension, which results in minimal vertical motions of the object, and maximum rotations, due to differential motions of object ends. For shorter surface waves, as shown in Figure 504.58, lower right case, waves might not even be exciting any significant dynamic behavior of the object (except local deformation) as their wave lengths are shorter than twice object length.

- 3C modelling, when done properly will capture all the body and surface wave effects for SSI analysis of NPPs.

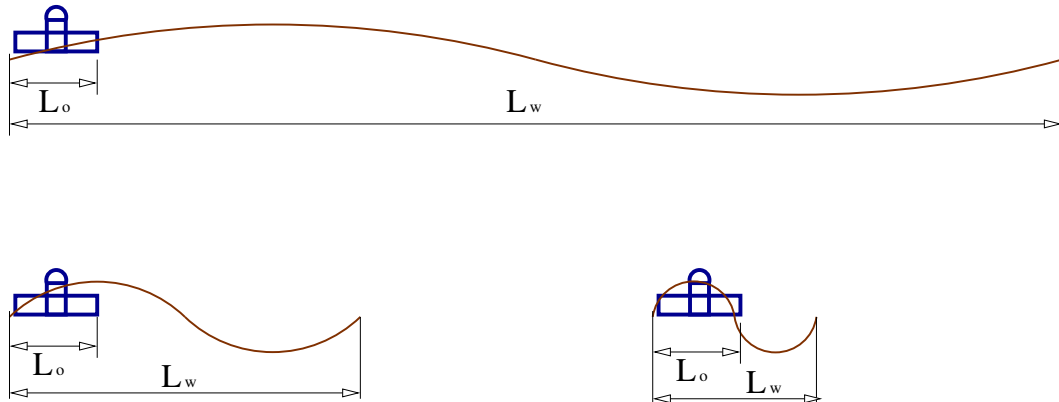


Figure 504.58: 1C vs 3×1 C vs 3C. Three different cases of surface wave wave length. Upper case is where the surface wave length is 12 or more times longer than the object (NPP) dimension. Lower left case is where the surface wave length is only four times longer than the wave length, and lower right case is where the surface wave length is only two times longer than the object length.

504.4.2 Illustration of Use of 3C and 1C Seismic Motions

A simple example can be used to illustrate differences in 1C vs 3C seismic motions. Assume that a full 3C (6C, 3 translational components and 3 rotational components) motions at the surface are only recorded in one horizontal direction. From a 1C recorded component one can develop a vertically propagating shear wave in 1C, that exactly models 1C recorded motion. This is usually done using de-convolution Kramer (1996a). Figure 504.59 illustrates the idea of using a full 3C seismic wave field to develop a reduced, 1C wave field

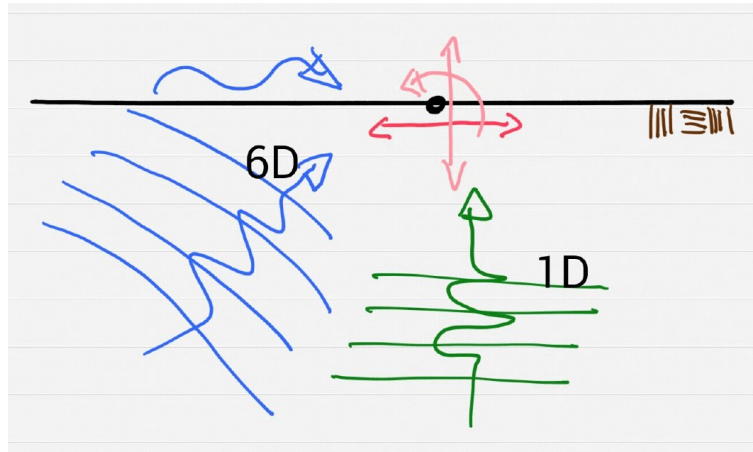


Figure 504.59: Illustration of the idea of using a full 3C (6C) seismic motion field to develop a 1C seismic motion field.

Two seismic wave fields, the original wave field and a subset 1C wave field now exist. The original wave field includes body and surface waves, and features translational and rotational motions. On the other hand, subset 1C wave field only has one component of motions, usually an SV component (vertically polarized component of S (Secondary) body waves).

Figure 504.61 shows a snapshot of a full 3C wave field, resulting from a large scale regional simulation, from a point source (simplified), propagating P and S waves through layers.

Figure 504.62 shows a snapshot of the same wave field as in Figure 504.61, now focused on an immediate vicinity of location of interest, where blue stick is positioned.

It should be noted that regional simulation model shown in Figures 504.62 and 504.61 is rather simple, consisting of a point source at shallow depth in a 3 layer elastic media. Waves propagate, refract at layer boundaries (turn more "vertical") and, upon hitting the surface, create surface waves (in this case, Rayleigh waves). In our case (as shown), out of plane translations and out of plane rotations are not developed, however this simplification will not affect conclusions that will be drawn. A seismic wave field with full 3 translations and 3 rotations (6C) will only emphasize differences that will be shown later.

Figures 504.63 and 504.64 show local free field model with 3C and 1C wave fields respectively.

Please note that seismic motions are input in an exact way, using the Domain Reduction Method Bielak et al. (2003a); Yoshimura et al. (2003a) and how there are no waves leaving the model out of DRM element layer (4th layer from side and lower boundaries). It is also important to note that horizontal motions in one direction at the location of interest (in the middle of the model) are exactly the same for both 3C motions case and for a 1C motions case.

Figure 504.65 shows a snapshot of an animation (available through a link within a figure) of difference

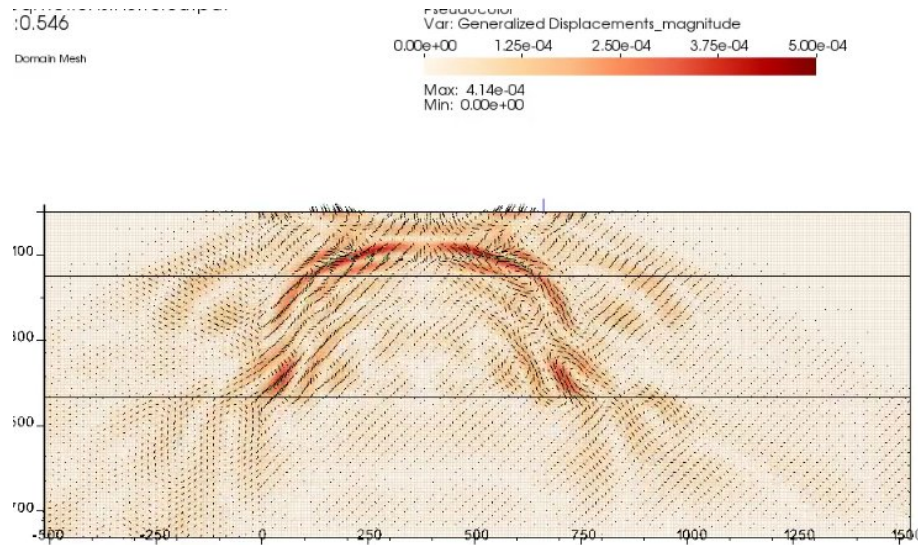


Figure 504.60: Snapshot of a full 3C wave field

Figure 504.61: Snapshot of a full 3C wave field, with body and surface waves, resulting from a point source at 45° at depth, down-left. This is a regional scale model of a (simplified) point source (fault) with soil layers. Figure is a link to an animation of a full wave propagation.

in response of an NPP excited with full 3C (6C) seismic wave field, and a response of the same NPP to 1C seismic wave field.

Figures 504.66 and 504.67 show displacement and acceleration response on top of containment building for both 3C and 1C seismic wave fields.

Figures ?? and ?? show displacement and acceleration response on top of containment building for both 3C and 1C seismic wave fields.

A number of remarks can be made:

- Accelerations and displacements (motions, NPP response) of 6C and 1C cases are quite different. In some cases 1C case gives bigger influences, while in other, 6C case gives bigger influences.
- Differences are particularly obvious in vertical direction, which are much bigger in 6C case.
- Some accelerations of 6C case are larger than those of a 1C case. On the other hand, some displacements of 1C case are larger than those of a 6C case. This just happens to be the case for given source motions (a Ricker wavelet), for given geologic layering and for a given wave speed (and length). There might (will) be cases (combinations of model parameters) where 1C motions model will produce larger influences than 6C motions model, however motions will certainly again

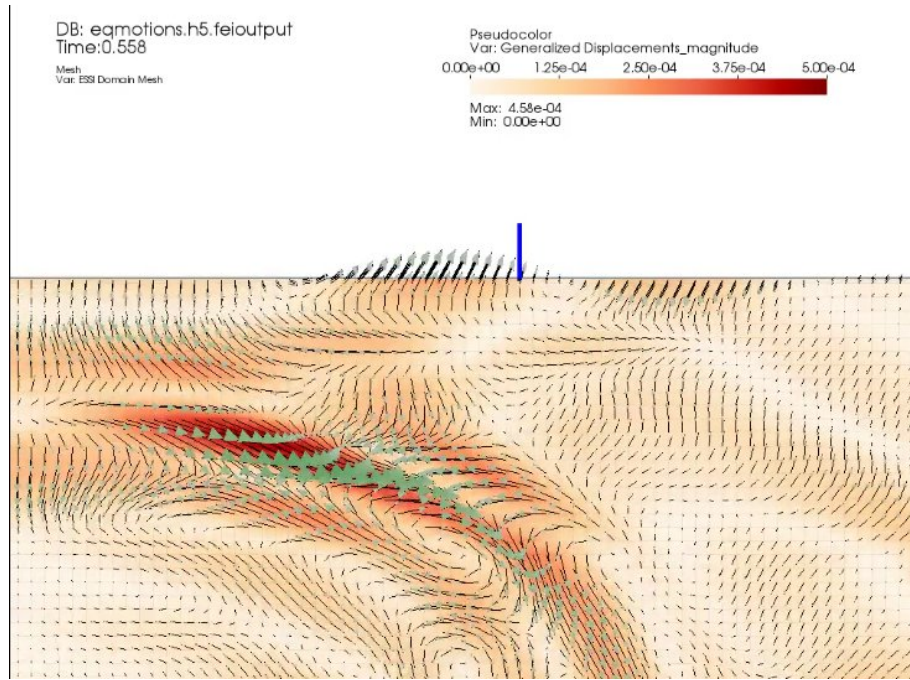


Figure 504.62: Snapshot of a full 3C wave field, with body and surface waves, resulting from a point source at 45° at depth, down-left. This is a large regional scale model of a (simplified) fault with soil layers. Figure is a link to an animation of a full wave propagation.

be quite different. There will also be cases where 6C motions will produce larger influences than 1C motions. These differences will have to be analyzed on a case by case basis.

In conclusion, response of an NPP will be quite different when realistic 3C (6C) seismic motions are used, as opposed to a case when 1C, simplified seismic motions are used.

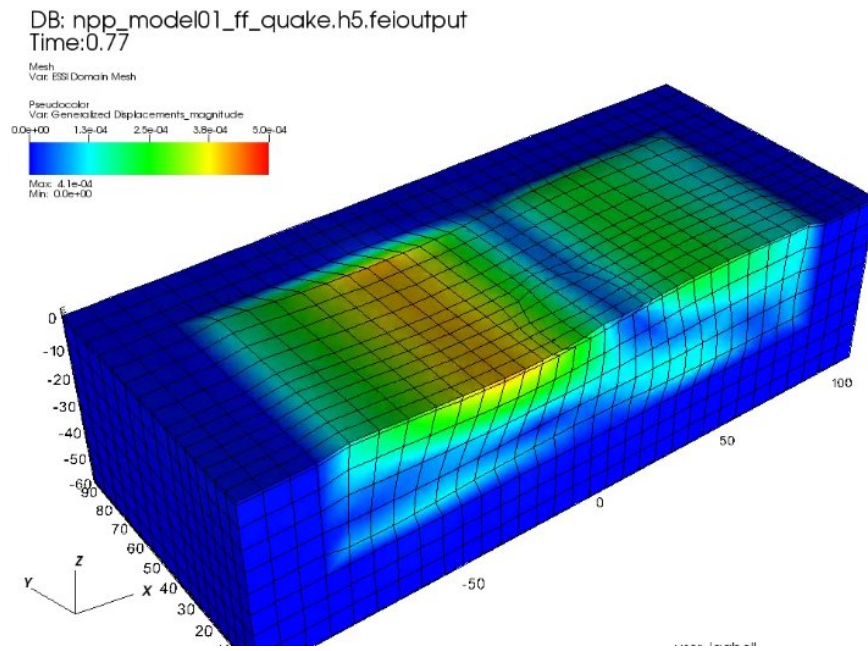


Figure 504.63: Snapshot of a full 3C wave field at the location of interest (where an NPP will be founded), featuring body and surface waves.

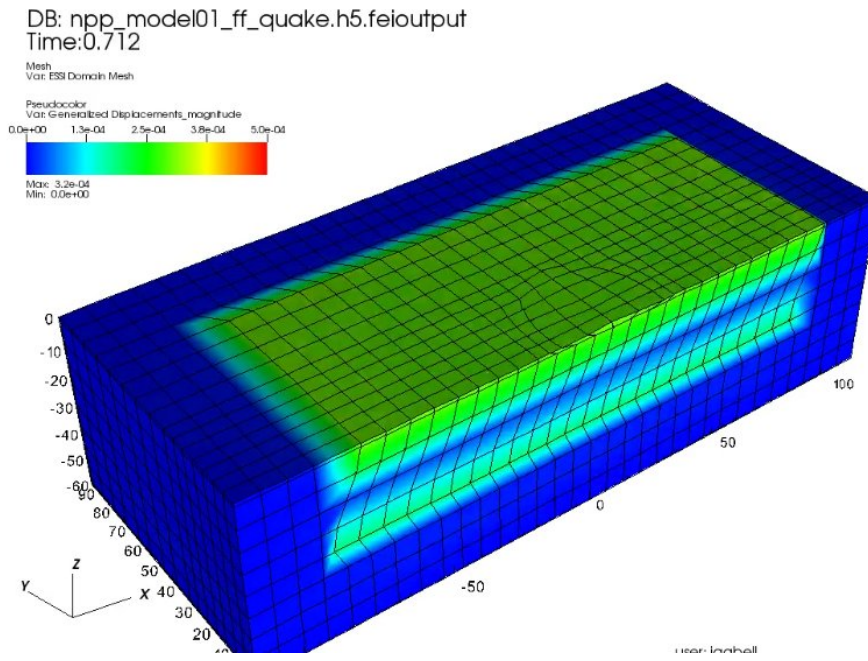


Figure 504.64: Snapshot of a reduced 1C wave field at the location of interest (where an NPP will be founded), featuring just SV body waves.

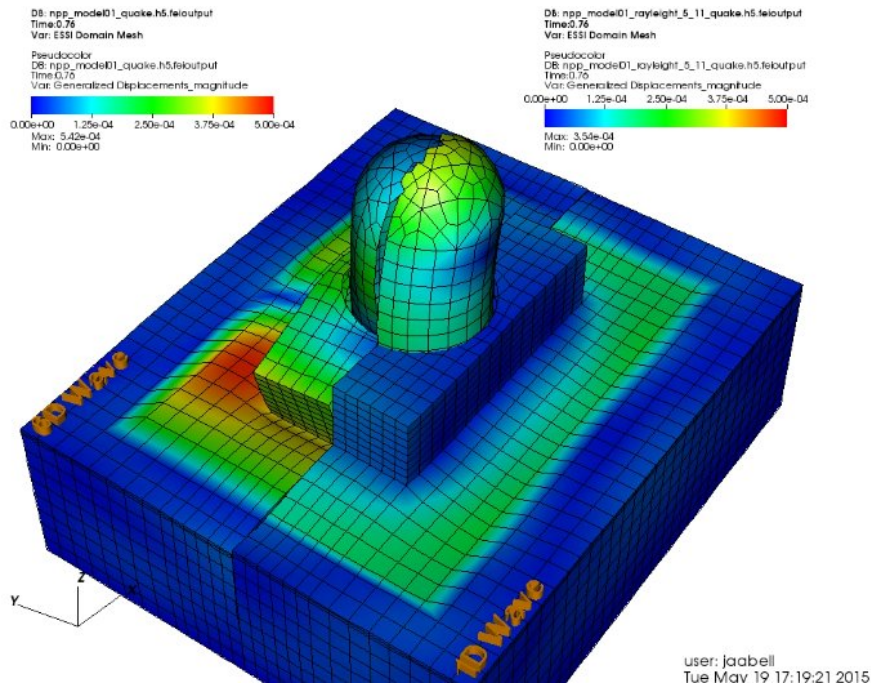


Figure 504.65: Snapshot of a 3C (6C) vs 1C response of an NPP, upper left side is the response of the NPP to full 3C wave field, lower right side is a response of an NPP to 1C wave field.

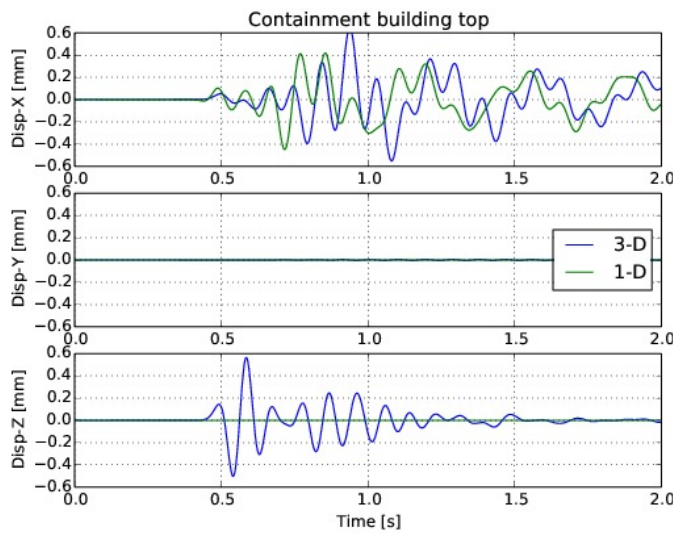


Figure 504.66: Displacements response on top of a containment building for 3C and 1C seismic input.

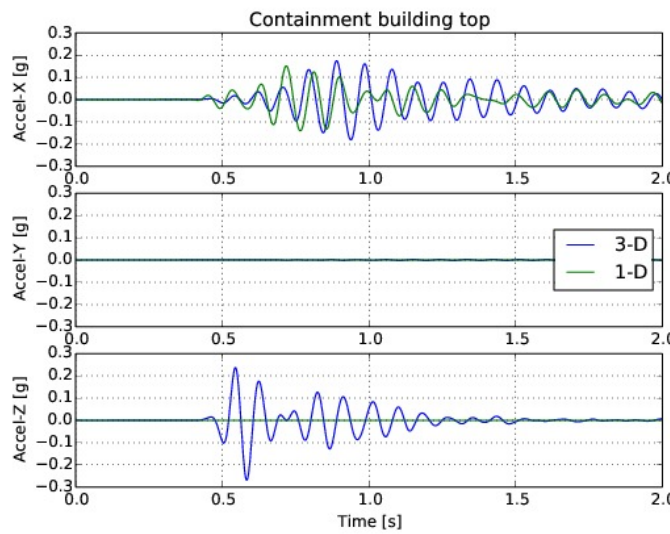


Figure 504.67: Acceleration response on top of a containment building for 3C and 1C seismic input.

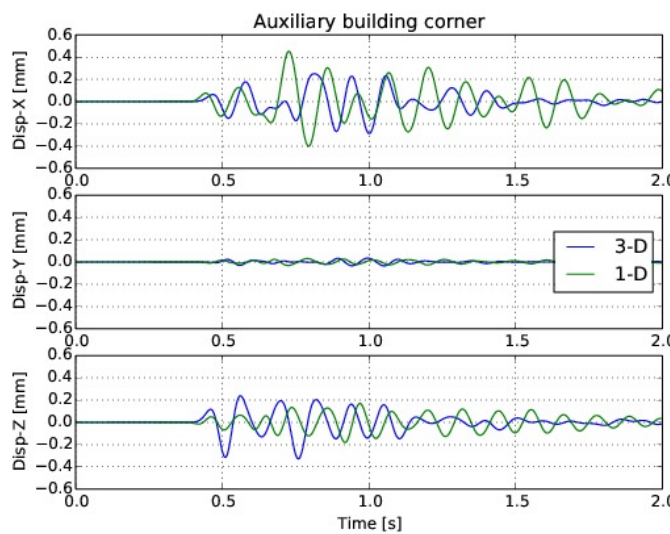


Figure 504.68: Displacements response at the top corner of auxiliary for 3C and 1C seismic input.

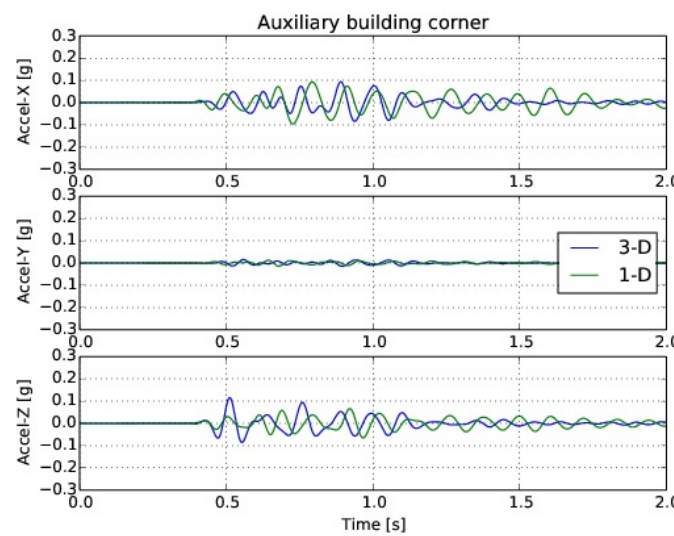


Figure 504.69: Acceleration response at the top corner of auxiliary for 3C and 1C seismic input.

504.5 3C (6C) vs 3 × 1C vs 1C Seismic Motions

This section is from our paper ([Abell et al., 2018](#)).

504.6 3D Nonlinear Modeling for Nuclear Power Plants

This section is based on [Sinha et al. \(2017\)](#).

It noted that input files for these models are available at this [LINK](#), and can be directly simulated using Real-ESSI Simulator, <http://real-essi.us/>, that is available on Amazon Web Services, <https://aws.amazon.com/>.

504.6.1 Introduction

Seismic simulations to structures are often done by 1-D input excitations defined from a family of damped response spectra. These input motions are applied uniformly to the entire base of the structure regardless of its dimension and dynamic characteristics of the soil, foundation and motion itself. This not only ignores the foundation and its contact/interface with soil, soil-structure interaction (SSI) but also the 3C nature and variability of seismic waves.

Interest to study SSI effects has grown significantly in recent years. However [Tyapin \(2007\)](#) and [Lou et al. \(2011\)](#) note that even after four decades of extensive SSI research, there still exists a large gap. [Lou et al. \(2011\)](#) notes that spatial analysis of full model in 3D is hardly done. To reduce the amount of calculations, many existing publications simplify extremely the super-structure to spring mass damper model or consider only limited interaction. Elgamal et al [Elgamal et al. \(2008\)](#) performed a 3D analysis of a full soil–bridge system, focusing on interaction of liquefied soil in foundation and bridge structure. [Jeremić et al. \(2009\)](#) showed a full 3D soil-structure interaction of a prototype bridge, devised as a part of grand challenge, pre-NEESR project.

Investigations of SSI have shown that the dynamic response of a structure supported on elastic-plastic soil may differ significantly from the response of the same structure when supported on a rigid base [Chopra and Gutierrez \(1974\)](#); [Bielak \(1978\)](#). The difference comes because of the dissipation of part of the vibrational energy (seismic energy) by hysteresis action of the soil or structure itself. This results in damping of high frequency components, which could potentially prove quite useful for equipment that are prone to damage from high frequencies. On the other hand [Jeremić et al. \(2004\)](#) found that SSI can have detrimental effects on structural behavior as well and is dependent on the dynamic characteristics of the earthquake motion, the foundation soil and the structure.

Dissipation of energy during seismic events is another important factor to consider in design for its safety and economy. Dissipating energy in structure can lead to material degradation and damage. It is desired to dissipate most of the energy in soil with acceptable level of deformations in structure. A common neglect of plastic free energy has been observed in many publications, which results in clear violation of the second law of thermodynamics. A thermomechanical framework that can correctly

evaluate energy transformation and dissipation in dynamic SSI simulation was presented by Yang et al. (2018, 2019a) based on works of Rosakis et al. (2000); Dafalias et al. (2002). This framework is applied to the prototype NPP model that is being analyzed in this paper. Locations with high possibility of damage are identified and insights on design improvement are discussed.

Only a few full 3D SSI interactions have been studied that too mainly focusing on bridges or small soil-foundation system. However, as per author's knowledge a full 3D non-linear analysis for a structure with soil-foundation-structure and contact/interface effects have not been investigated. Purpose of this paper here is to present a methodology for high fidelity modeling of seismic soil-foundation-structure (SFSI) interaction for a prototype of Nuclear Power Plant (NPP) with surface (shallow) foundation. Presented methodology employs the currently best available models and simulation procedures. In addition to presenting such state-of-the-art modeling, simulation results are used to illustrate non-linear-effects on seismic response of a prototype NPP model.

504.6.2 Model Development and Simulation Details

The Nuclear Power Plant (NPP) modeled here is a symmetric structure with shallow foundation of thickness 3.5m and size 100m. Figure 504.70 shows a slice view of the model in normal y direction (perpendicular to plane of the paper). Solid brick elements were used to model soil and foundation. The NPP structure was modelled by elastic shell elements. This section describes the material and modeling parameters summarized in Table 504.5, foundation, structure, and contact. Given also is a brief description of staged loading and seismic force application using domain reduction method (DRM).

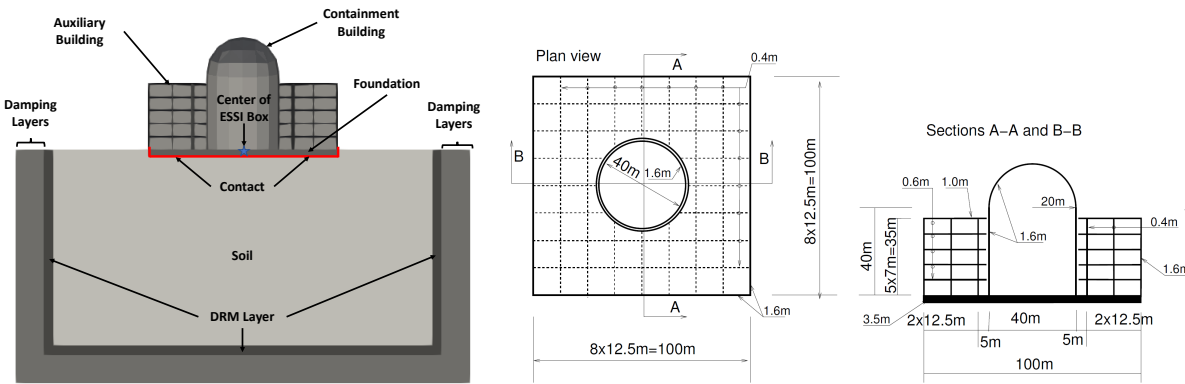


Figure 504.70: Nuclear power plant model with shallow foundation.

Soil	Unit weight , γ [kPa]	21.4	Structure	Unit weight , γ [kPa]	24.0
	Shear velocity , V_s [m/s]	500		Young's modulus , E [GPa]	20
	Young's modulus , E [GPa]	1.3		Poisson's ratio , ν	0.21
	Poisson's ratio , ν	0.25	Contact	Initial normal stiffness , k_n^{init} [N/m]	1e9
	Shear strength , S_u [kPa]	650		Stiffening rate , S_r [/m]	1000
	von Mises radius , k [kPa]	60		Maximum normal stiffness , k_n^{max} [N/m]	1e12
Structure	linear kinematic hardening , h_a [Mpa]	30		Tangential stiffness , k_t [N/m]	1e7
	non-linear kinematic hardening , c_r	25		Normal damping , c_n [Ns/m]	100
	Unit weight , γ [kPa]	24.0		Tangential damping , c_t [Ns/m]	100
Structure	Young's modulus , E [GPa]	20		Friction ratio , μ	0.25
	Poisson's ratio , ν	0.21			

Figure 504.71: Modeling parameters.

504.6.2.1 Structure Model

The NPP structure consists of auxiliary building, containment building and shallow foundation as shown in Figure ???. The auxiliary building consists of 4 floors of 0.6m thickness, ceiling floor of 1m thickness, exterior wall of 1.6m thickness and interior walls of 0.4m thickness. The exterior and interior walls are embedded down to the depth of the foundation. The containment building is a cylinder of diameter 20m and height 40m with wall thickness of 1.6m. There is a gap of 0.2m between the containment and auxiliary building. Top of the containment building is covered by semi-spherical dome of radius 20m. The foundation is square shallow footing of size 100m and thickness 3.5m. The containment building and the auxiliary building were modelled as shell elements and foundation as linear brick elements, both having the properties of concrete of elastic Young's modulus 20GPa, poison's ratio 0.21 and density 2400kg/m³. The containment building which is more flexible than the auxiliary building had its first mode as bending with fundamental frequency at 4Hz.

504.6.2.2 Soil Model

The depth of the soil modelled below the foundation was 120 m, which is also the depth of DRM layer Sec 504.6.2.5. It is assumed that within this range the soil will plastify because of its self-weight, structure and seismic motions. The soil is assumed to be a stiff saturated-clay with undrained behavior having shear velocity of 500 m/s, unit weight of 21.4 kPa and Poisson's ratio of 0.25. To represent the travelling wave accurately for a given frequency, about 10 nodes per wavelength i.e. about 10 linear or 3 quadratic brick elements are required. Here, the seismic waves are analyzed up to $f_{max} = 10\text{Hz}$. The smallest wavelength λ_{min} to be captured thus, can be estimated as

$$\lambda_{min} = v/f_{max} \quad (504.2)$$

where, v is the smallest shear wave velocity of interest. For $v = 500m/s$ and $f_{max} = 10Hz$ the minimum wavelength λ_{min} would be $(500m/s)(10/s) = 50m$. Choosing 10 nodes/elements per wavelength the element size would be 5m. Jeremić et al. (2009); Watanabe et al. (2017) state that even by choosing mesh size $\Delta h = \lambda_{min}/10$, smallest wavelength that can be captured with confidence is $\lambda = 2\Delta h$ i.e. a frequency corresponding to $5f_{max}$. Based on the above analysis, soil was modeled as linear 8-node brick elements with grid spacing of $\Delta h = 5m$.

Because of the complex plastic-behavior of the soil many sophisticated models Yang et al. (2003); Dafalias and Manzari (2004b) have been developed to capture the non-linear response of soil. Wair et al. (2012) provides an empirical correlation to predict the shear strength of soil for given shear velocity V_s . Dickenson (1994) proposed the following relationship Eq 504.3 between V_s and undrained strength S_u for cohesive soils in San Francisco Bay Area.

$$V_s[m/s] = 23(S_u[kPa])^{0.475} \quad (504.3)$$

Thus, for $V_s = 500m/s$, the undrained strength S_u would be $650kPa$. Here, two scenarios of soil properties were considered in analysis. One linear elastic and the other as von-Mises with non-linear kinematic hardening of Armstrong – Frederick type. For S_u of $650kPa$ and $E = 1.3Gpa$, the non-linear inelastic model was calibrated for yield strength achieved at 0.01% shear strain with linear kinematic hardening rate (h_a) as $30MPa$ and non-linear hardening rate (c_r) as 25. The soil properties is summarized in Table 504.5. The stress-strain response for the non-linear material model is shown in Figure ??

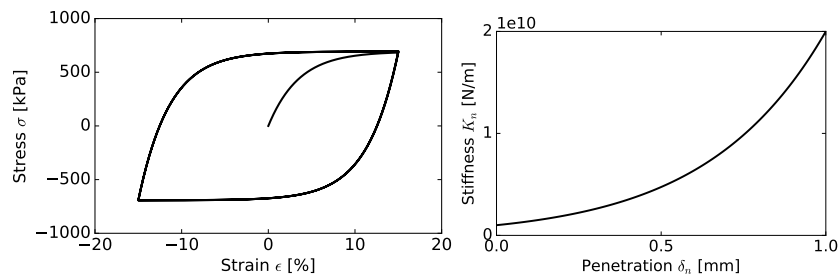


Figure 504.72: Soil and contact/interface modeling.

504.6.2.3 Interface/Contact Modeling

Node-to-node penalty based soft contact/interface element Sinha and Jeremić (2017) was used to model the interaction between foundation and soil as they are not one continuum material. In soft contact, normal contact/interface force F_n from soft-soil is assumed to increases exponential with penetration δ_n

as shown in Eq 504.4. The normal force F_n and stiffness K_n is defined as

$$\begin{aligned} F_n &= k_n^{init} * \exp(S_r * \delta_n) * \delta_n \\ K_n &= \max(k_n^{init} * \exp(S_r * \delta_n) * (1 + k_n^{init} * \delta_n), k_n^{max}) \end{aligned} \quad (504.4)$$

where δ_n refers to the relative displacement between contact/interface node pairs in normal contact direction, k_n^{init} refers to the normal stiffness in normal contact/interface direction, S_r refers to the stiffening rate in normal contact direction. k_n^{Max} refers to maximum normal stiffness and provides a cap on exponentially increasing stiffness to make the solution numerically stable. The soft contact/interface was implemented to capture the phenomenon of increasing stiffness of soil with increasing penetration. Figure ?? shows the stiffness curve with penetration for the chosen contact/interface parameters also shown in Table 504.5.

Contact elements were applied all around the foundation connecting to the soil as shown in Figure ?? in red color zone. To ensure the stability of the numerical solution, the penalty stiffness in normal direction was chosen 2 – 3 order magnitude greater than the stiffness of the soil. The Coulomb's friction coefficient μ between the soil and the foundation was chosen as 0.25. Viscous damping of 100Ns/m in normal and tangential damping was provided to model viscous damping arising from water.

504.6.2.4 Seismic Motions

3C seismic motions were developed by Rodgers (2017) using SW4 (Serpentine Wave Propagation of 4th order) Petersson and Sjögren (2018) for an earthquake of magnitude (M_w) of 5.5 modelled with a point source on a fault of dimension $5.5 \times 5.6\text{km}$ with up-dip rupture slip model. The ESSI (Earthquake Soil Structure Interaction) box to capture the free-field motion was located on the foot-wall of the reverse thrust fault. The generated motion had a directivity effect as the fault slips and propagates in x-direction. Also, since the ESSI box was located perpendicular to the fault, strong motions in y-direction was expected.

Acceleration and displacement time-series of the motion at the center of ESSI box is shown in Figure 504.86. The peak ground acceleration (PGA) in x and y direction is about 0.5g. Significant amount of vertical motions PGA of 0.2g can be observed which is neglected in many conventional seismic simulations. Since, the fault is located at foot-wall side of reverse thrust fault, there is permanent subsidence of about 50mm in z-direction at the end of shaking event. Fourier transform and response spectrum of the motions are shown in Figure 504.87. The frequency range of the motion is within 20Hz. Response spectrum plot shows amplification for natural frequency greater than 2Hz. Since, many equipments in nuclear industry operate at high frequencies, determination of high frequency excitation of NPP building is critical for design.

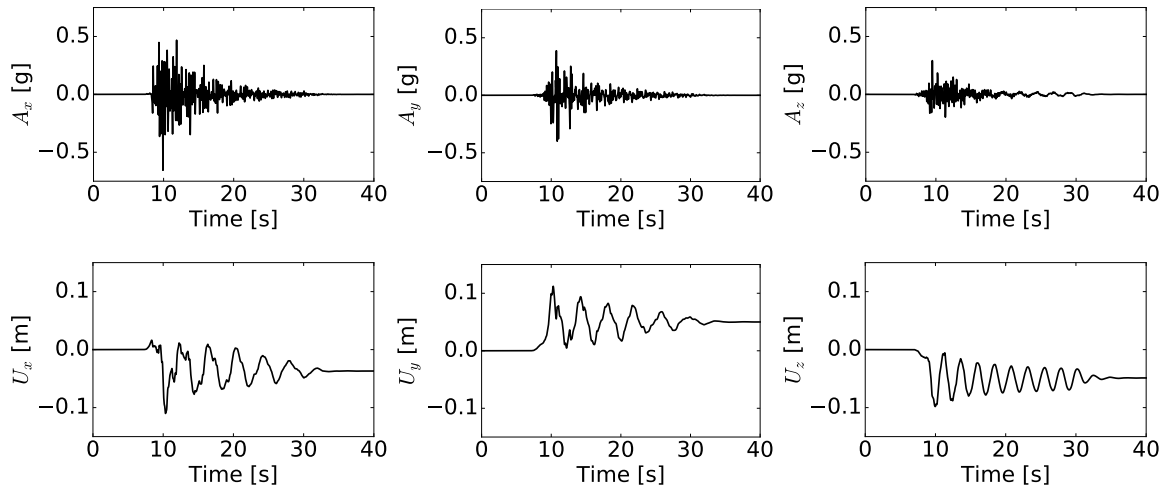


Figure 504.73: Acceleration and displacement time series.

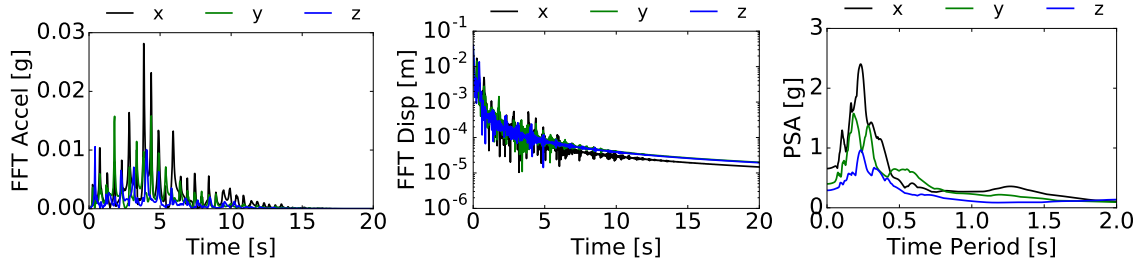


Figure 504.74: Strong motion Fourier transform and response spectrum.

504.6.2.5 Domain Reduction Method

Domain Reduction Method (DRM) [Bielak et al. \(2003a\)](#) was used to apply 3C seismic motions generated from SW4 all around the model as shown in Figure ???. DRM is one of the best methods that can apply free field 3C ground motions to a finite-element model. It features a two-stage strategy for a complex, realistic 3D earthquake engineering simulation. First, is the generation of free field model with correct geology and second is the application of the generated free-field to the structure of interest. The DRM layer here is modeled as a single layer of elastic soil. Three damping (absorbing) layers adjacent to DRM layer were modeled to prevent incoming of reflected waves. For this analysis, 60% Rayleigh damping was applied in each of the damping and DRM layers. The Rayleigh damping was applied in the frequency range of 1-5Hz.

504.6.2.6 Staged Simulation

The whole analysis was simulated with two loading stages. First stage was static self-weight to get the initial stress state of the soil and contact/interface elements. In second stage, seismic motion was applied using DRM method. For each stage, equilibrium was achieved using full Newton-Raphson method with a small tolerance of $1e^{-4}N$ on second-norm of unbalanced force. For dynamic analysis, Newmark integration method with numerical damping $\gamma = 0.7$ was used. Rayleigh damping of 2% in structure and 30% in soil was applied. The time step considered here was 0.02 seconds with simulation running in total for 40 seconds.

The analysis was run in parallel in Real-ESSI Simulator [Jeremić et al. \(1988-2025\)](http://real-essi.info), <http://real-essi.info>. on eight CPUs. The model consisted of about 300k degrees of freedoms (dofs). Four scenarios (a) elastic no contact/interface (b) elastic with contact (c) elastic-plastic no contact and (d) elastic-plastic with contact/interface were performed. In this paper, unless specified *elastic* means elastic without contact/interface and *inelastic* means elastic-plastic with contact.

504.6.3 Simulation Results

Due to the space restriction, only few locations are selected to study the non-linear effects on NPP structure. The selected locations are shown in Figure 504.75. Since the containment building is more flexible than auxiliary building, location (D) in Figure 504.75 located on the top of the containment building is naturally the point of interest as it describes maximum drift during shaking. Three locations (A), (B) and (C) located at center of foundation is also selected to study the slip at interface during shaking.

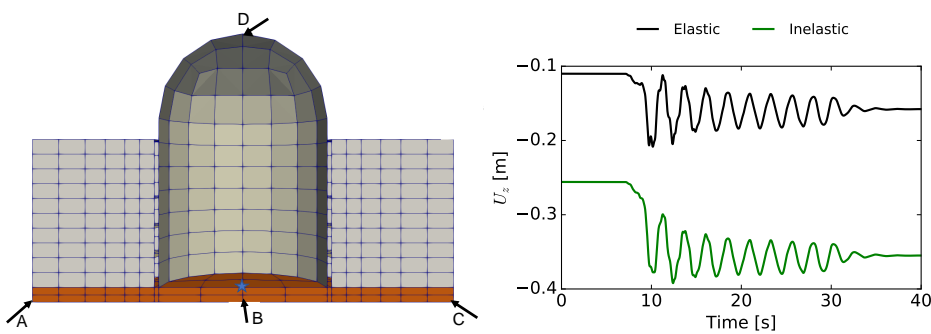


Figure 504.75: Locations selected to study non-linear effects and plot of total displacement at center of model *Elastic* (elastic with contact) and *Inelastic* (Elastic-Plastic with contact).

Since the site is located on the foot wall, during seismic shaking the whole structure along with soil subsides down by about 50mm in elastic and 100mm in inelastic case. Overall, if self-weight stage is also

included, the soil settles by 150mm in elastic and 350mm in inelastic case as shown in Figure ??.

It is important to predict the development of high frequency excitation during shaking because it can prove to be alarming (when close to fundamental frequency) for nuclear-equipment. These high frequencies are thus, important to be monitored, predicted during earthquakes, for design of nuclear building to ensure the safety of equipment. Figure 504.76 plots the acceleration and its Fourier amplitude for the location (D). It is interesting to observe, the elastic-plastic analysis kills high frequency excitations in the structure which are persistent in elastic analysis. Elastic-plastic soil shows natural damping to some high frequencies because of dissipation of energy in form of heat by hysteresis loop. This can prove to be bigly useful for safe operation of nuclear equipments even at strong seismic events. The effects of contacts coupled with elastic-plastic material leads to huge dissipation of energy reducing the high frequency modes. In Z-direction, very little significant excitation was observed.

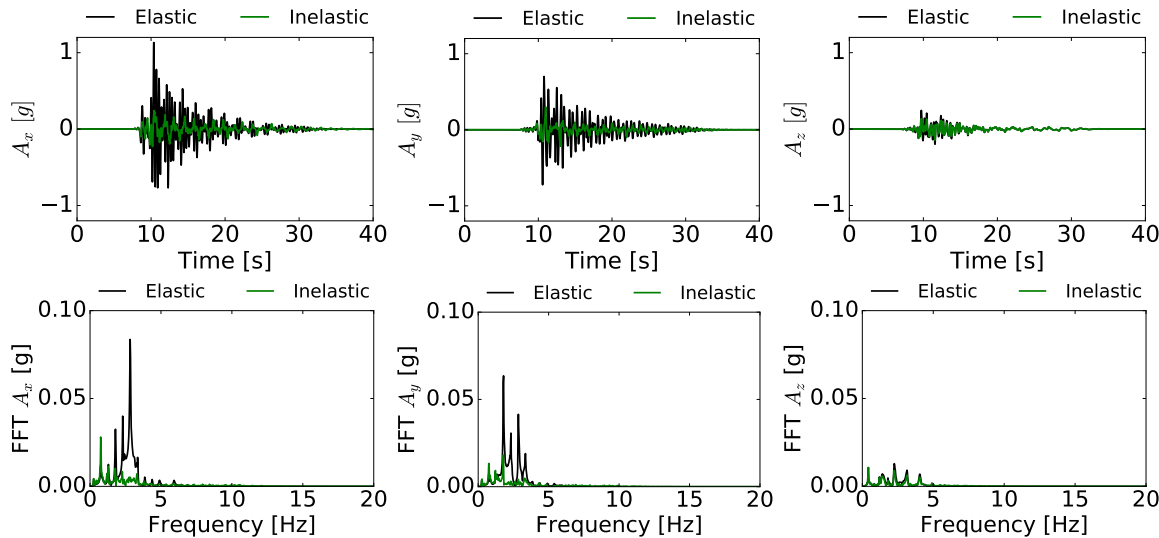


Figure 504.76: Seismic response at top of containment building *Elastic* (elastic without contact) and *Inelastic* (elastic-plastic with contact).

The introduction of contact/interface can result in opening and closing of gaps at the soil-foundation interface for stronger earthquakes. However, here for the considered seismic motion for both elastic and inelastic case with contact, no uplift was observed. Figure 504.77 shows the relative displacement of NPP structure for elastic and inelastic analysis at 11 seconds. In elastic case, the structure drifts a lot while the deformation in soil remains small. Whereas, in the inelastic case, the soil deforms and plastify in z-direction keeping the structure deformation small. Thus the elasto-plastic soil acts as a natural base isolators material. This demonstrates that for the considered earthquake motions, the elastic-plastic soil can prove to quite beneficial because of small deformation and excitation in structure.

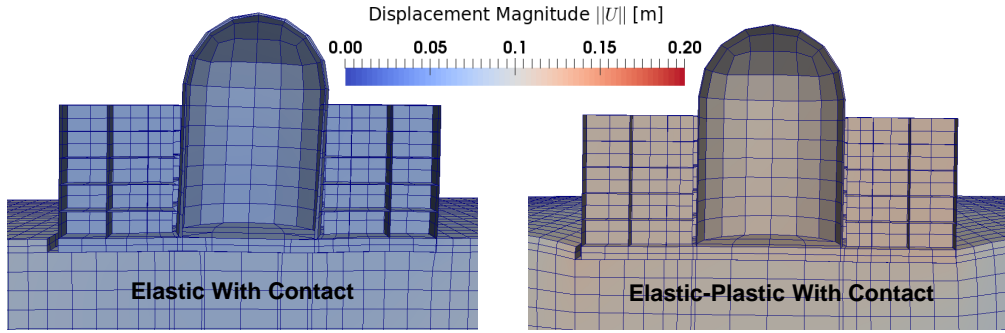


Figure 504.77: Deformation of the NPP structure at 11 seconds (scaled 100 times).

Figure 504.78 plots the inter-slip of foundation with respect to soil at location (A), (B) and (C) for elastic and elastic-plastic case with contact. It can be observed that point (A) and (B) slips both relatively towards each other describing the presence of surface waves. The center of the foundation (B) bends and slides comparatively less than the exterior ends. This also strongly shows the directivity effects of the motion coming from the $-x$ to $+x$ direction. The directivity effect is more pronounced in inelastic analysis resulting in comparatively more slip and permanent deformation. Careful observation of sliding in x-direction, shows a permanent slip of 18mm for elastic-plastic soil. Although not shown in figure, the whole NPP structure show tendency of rotation about its center of mass during the DRM stage.

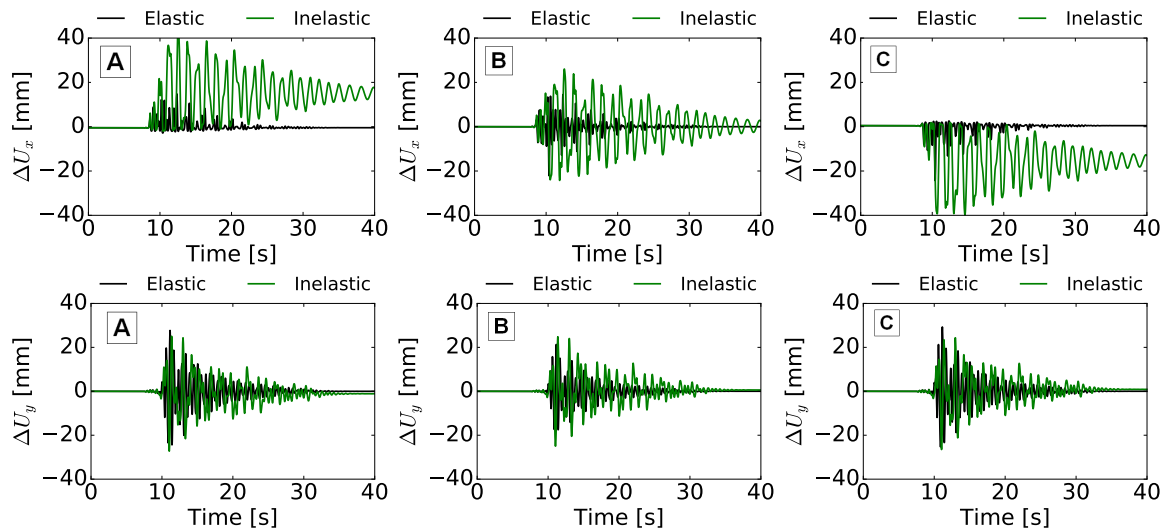


Figure 504.78: Slip of foundation with respect to soil beneath it in x-y slice plane for *Elastic* (elastic with contact) and *Inelastic* (Elastic-Plastic with contact).

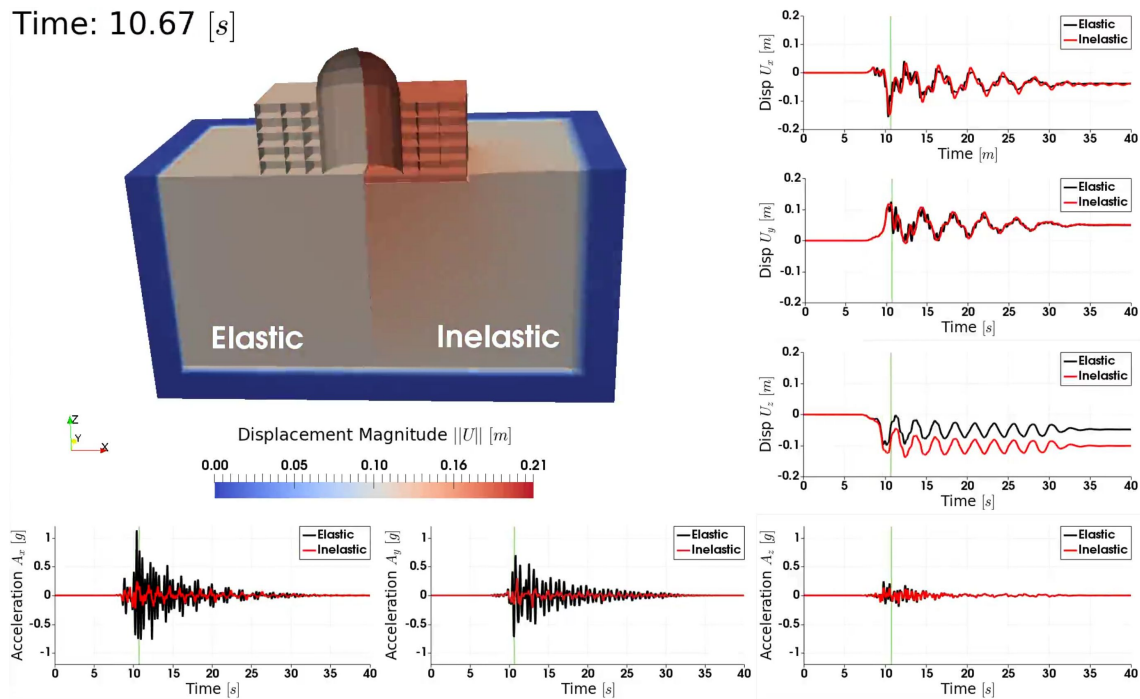


Figure 504.79: Animation of a linear elastic vs inelastic response of an NPP.

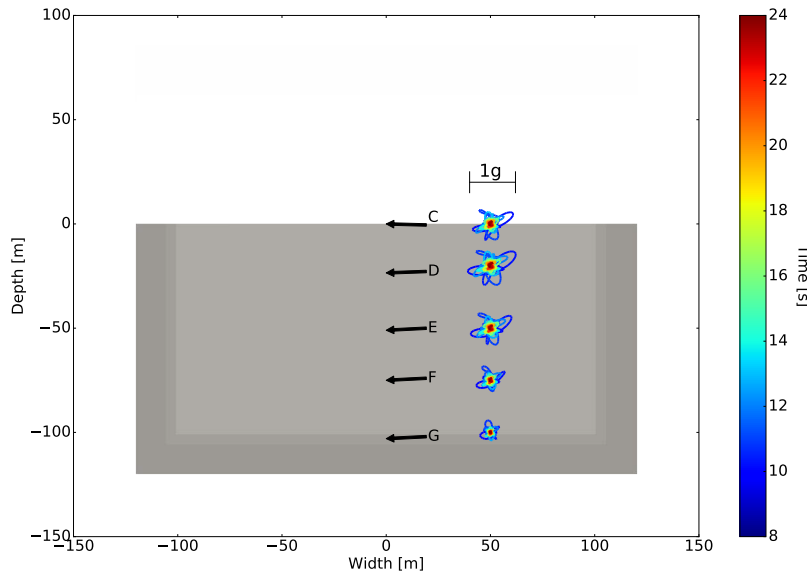


Figure 504.80: Free Field.

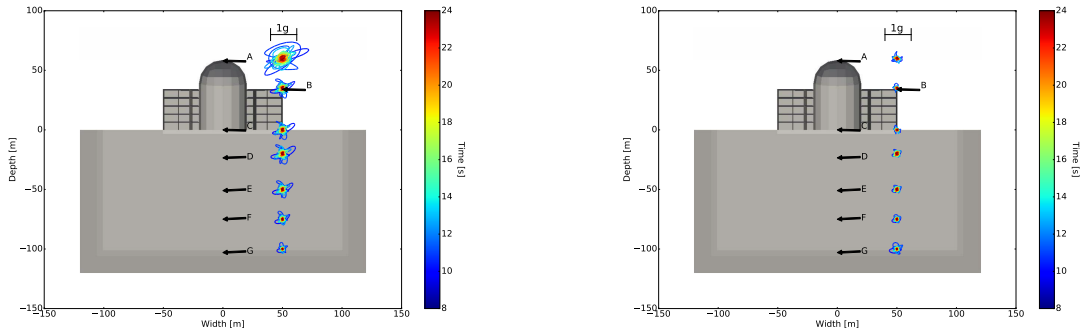


Figure 504.81: Acceleration traces, elastic vs inelastic.

504.6.4 Energy Dissipation

The energy dissipation in decoupled elastic plastic material under isothermal condition is given by [Yang et al. \(2019a\)](#):

$$\Phi = \sigma_{ij}\dot{\epsilon}_{ij} - \sigma_{ij}\dot{\epsilon}_{ij}^{el} - \rho\dot{\psi}_{pl} \geq 0 \quad (504.5)$$

where Φ is the rate of change of energy dissipation per unit volume (or dissipation density), σ_{ij} and ϵ_{ij} are the stress and strain tensors respectively, $\dot{\epsilon}_{ij}^{el}$ is the elastic part of the strain tensor, ρ is the mass density of the material, and $\dot{\psi}_{pl}$ is the plastic free energy per unit volume (or plastic free energy density). Note that Equation 504.8 is derived from the first and second laws of thermodynamics, which indicate the conditions of energy balance and nonnegative rate of energy dissipation, respectively. Considering all possible forms of energy inside SSI system, the energy balance between input mechanical work W_{Input} and the combination of internal energy storage E_{Stored} and energy dissipation $E_{Dissipated}$ can be expressed as:

$$W_{Input} = E_{Stored} + E_{Dissipated} = KE + SE + PF + PD \quad (504.6)$$

where KE is the kinetic energy, SE is the elastic strain energy, PF is the plastic free energy, and PD is the energy dissipation due to material plasticity. Equations for each energy component can be found in [Yang et al. \(2018\)](#). Note that the plastic dissipation term PD includes energy dissipated in both elastic plastic solids (soil) and contact/interface elements.

Figure ?? shows the accumulated plastic dissipation density field of the NPP model at the end of seismic event. The super-structure does not dissipate energy since it is modeled as a linear elastic material. Significant amount of seismic energy is dissipated in the contact/interface zone between the structure and underlying soil, especially at regions around the corners and edges of the foundation.

An arch-shaped elastic region is formed under the structure, where the soil moves together with the foundation and dissipates little energy. Such observation is consistent with classic bearing capacity analysis, which also indicates the formation of a relatively undeformed "active zone" beneath foundation.

As can be observed in Figure ??, the plastic dissipation density at location (A) is the highest. From Figure ??, it can be observed that more than 80% of the total input work is dissipated due to material plasticity or contact slipping. About 70% of the energy dissipation happens due to contact/interface slipping, which indicates that the property and behavior of the interface between foundation and soil is crucial in SSI system. It is worth pointing out that there is about 10% of the input work transformed into plastic free energy, which falls in the typical range reported by [Taylor and Quinney \(1934\)](#).

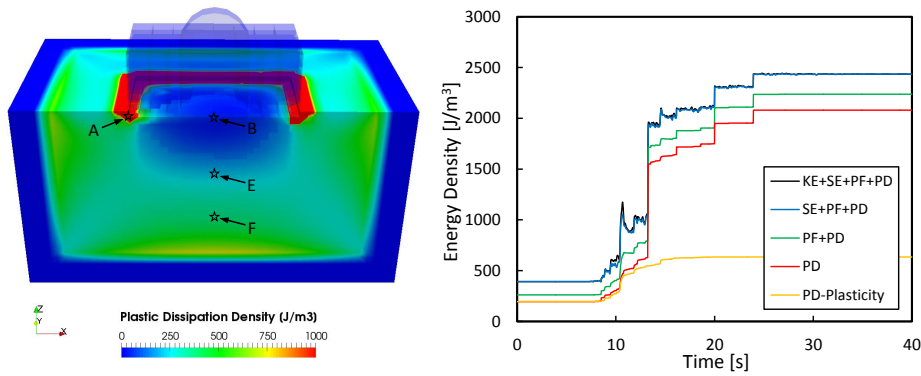


Figure 504.82: Energy dissipation in SMR model for inelastic (elastic-plastic soil with contact).

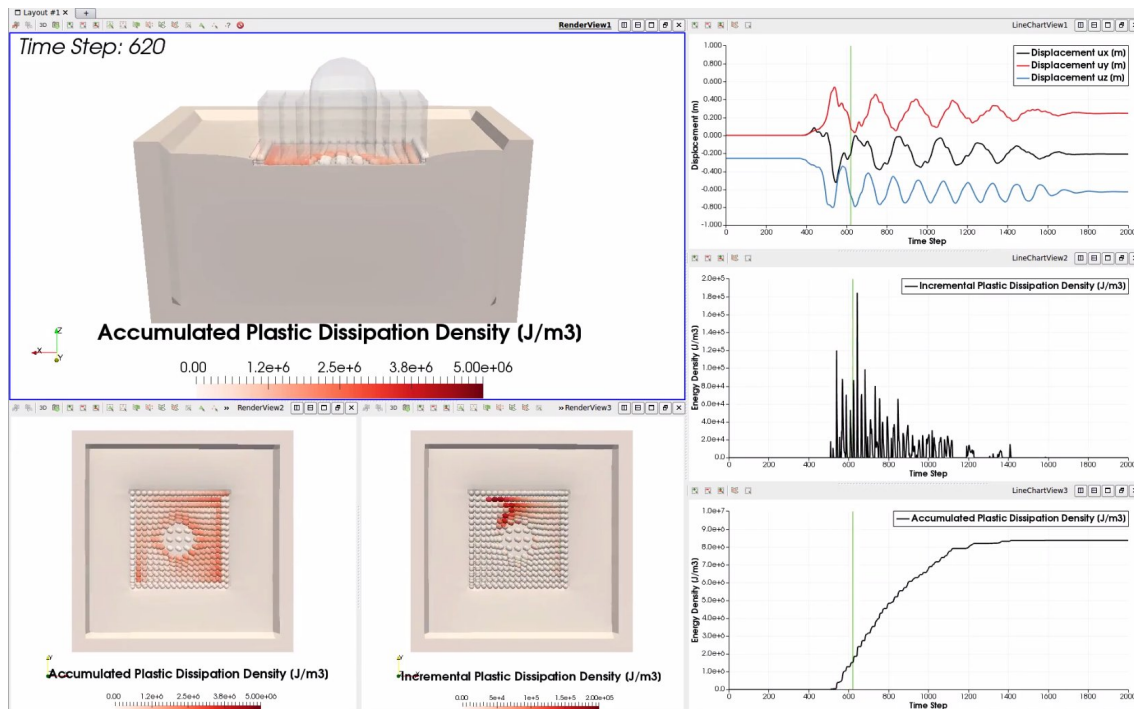


Figure 504.83: Animation of energy dissipation for an NPP.

504.6.5 Conclusion

Presented was a high fidelity seismic simulation methodology for investigating non-linear SSI effects on NPP structures. The site being in foot-wall of the reverse thrust fault, results in permanent subsidence in vertical direction. Due to plastification, elastic-plastic soil produces comparatively more vertical settlement than linear elastic soil. It also leads to damping of some higher frequency waves. This effect of non-linear material could be beneficial to the machines which are fatal to high frequency waves. It was found that with elastic-plastic soil, there was comparatively less seismic excitation and deformation in the NPP structure for the considered seismic motion. This illustrates that the stiff soil does not necessarily help in seismic behavior of structure. This also emphasizes the fact that linear elastic modeling of soil can lead to wrong conclusions resulting in huge capital loss. With the advancement of super-computers, uncertainty in modeling can be significantly reduced by following the high-fidelity modelling techniques discussed in this paper.

The non-linear effect studied here is with respect to the specific motion (Mw 5.5 up-dip slip fault). The non-linear effect cannot be fully described using this motion itself. More similar kind of research studies using different motions and geology needs to be carried out to find out the overall non-linear and geology effects on soil-structure interaction. The author also feels that new quantities needs to be formulated to study and compare different models to categories and unify the nonlinear effects on Soil Structure Interaction (SSI) effects. Energy dissipation analysis showed that the soil close to the corners and edges of the NPP structure dissipates large amount of seismic energy. An arch-shaped elastic region was identified where design can be improved so that soil strength at these locations can contribute to the overall safety of the SSI system.

504.7 3D Nonlinear Modeling for Small Modular Reactors (SMRs)

Figure 504.84 shows a generic model (half is only shown, full model is simulated) of an SMR. It is

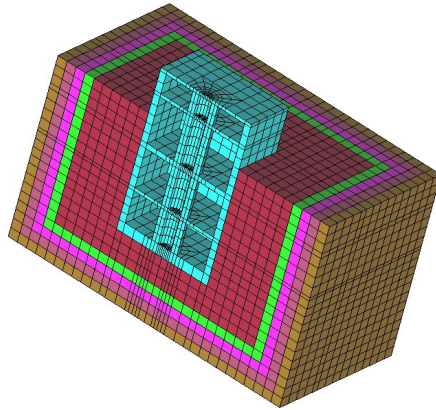


Figure 504.84: Generic model of a Small Modular Reactor (SMR).

important to note extensive contact/interface zone of SMR walls with surrounding soil. This brings forward a number of modeling and simulation issues for SMRs:

- Seismic Motions: There will be a difference in seismic wave fields at the surface and at depth. Surface waves do extend somewhat into depth (about two wave lengths at most [Aki and Richards \(2002\)](#)), so different motion frequencies, wave lengths, and depending on soil stiffness, SMR will experience very different motions at the surface and at the base. This seismic motion incoherence will affect seismic response of an SMR.
- Nonlinear/Inelastic Contact: Large contact/interface zone, with its nonlinear/inelastic behavior will have significant effect on dynamic response of a deeply embedded SMR.
- Nonlinear/Inelastic Soil Behavior: With deep embedment, dynamic behavior of an SMR is significantly influenced by the nonlinear/inelastic behavior of adjacent soil.
- Buoyant Forces: With deep embedment, and (a possible) presence of underground water (water table that is within depth of embedment), water pressure on walls of SMR will create buoyant forces. During earthquake shaking, those forces will change dynamically, with possibility of cyclic mobility and liquefaction (even for dense soil, due to water pumping during shaking).
- Uncertainty in Motions and Material: Due to large contact/interface area and significant embedment, significant uncertainty and variability (incoherence) in seismic motions will be present.

Moreover, uncertainties in properties of soil material surrounding SMR will add to uncertainty of the response.

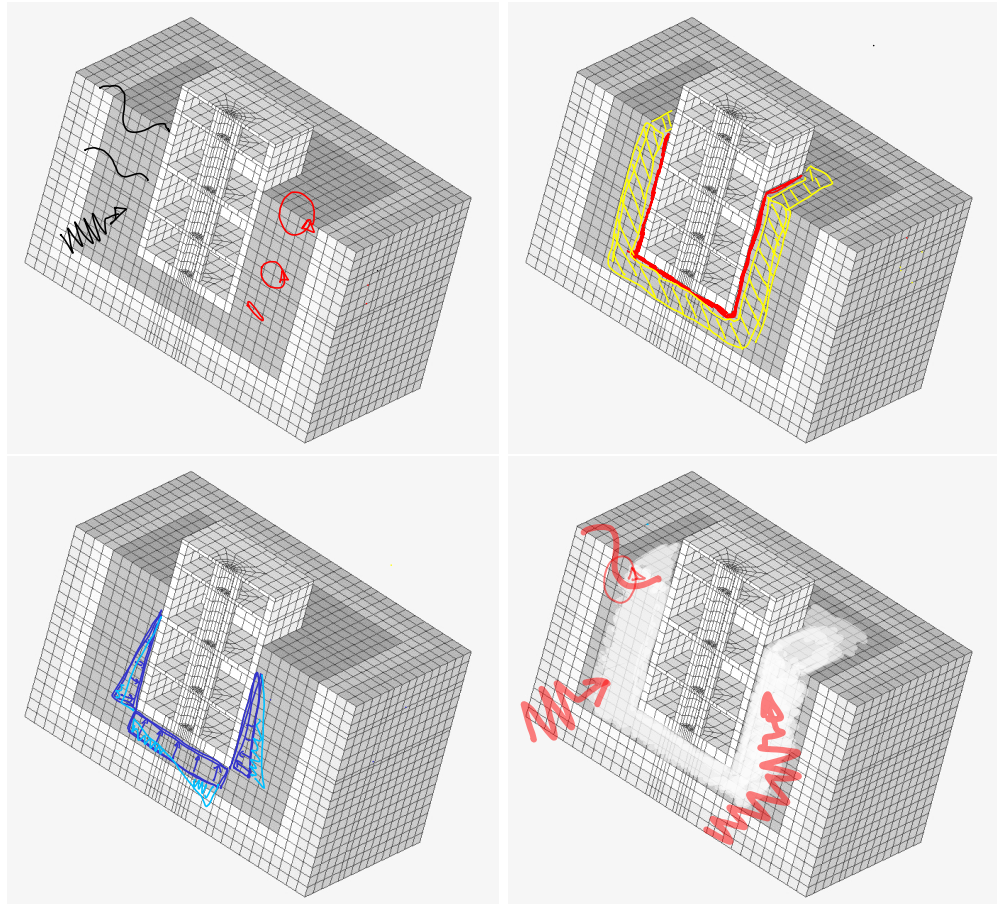


Figure 504.85: Four main issues for realistic modeling of Earthquake Soil Structure Interaction of SMRs: variable weave field at depth and surface, inelastic behavior of contact/interface and adjacent soil, dynamic buoyant forces, and uncertain seismic motions and material.

Writeup that follows is based on [Wang et al. \(2017\)](#).

It noted that input files for this model are available at this [LINK](#), and can be directly simulated using Real-ESSI Simulator, <http://real-essi.info/>, that is available on Amazon Web Services, <https://aws.amazon.com/>.

504.7.1 Introduction

Seismic performance of nuclear facilities is carefully analyzed considering the significant problems that damage of such structures can bring. The structure investigated here is a deeply embedded Small

Modular Reactor (SMR). Model SMR structure analyzed here is deeply embedded (36 meters) with only 14 meters of structure above ground.

In recent years, many researchers ([Spyrakos et al. \(1989\)](#); [El Ganainy and El Naggar \(2009\)](#); [Iida \(2012\)](#)) made efforts to perform realistic modeling of dynamic SSI system and seismic response of underground structure. [Romero et al. \(2013\)](#) coupled FEM and BEM method to model wave propagation in elastic foundation and corresponding dynamic response of the structure. [Fatahi and Tabatabaiefar \(2013\)](#) investigated the seismic performance of mid-rise buildings on soft soils using existing earthquake records. An elastoplastic SSI analysis was conducted by [Shahrour et al. \(2010\)](#) to explore the seismic response of tunnels in soft soils. However, some inherent modeling uncertainties still existed in these previous studies and were not well addressed:

- A very important modeling uncertainty comes from the ground motion. For surface structures, it is common to use historical earthquake records and simplified 1C seismic wave propagation models ([Paolucci et al. \(2008\)](#)). Vertical ground motion are usually neglected. However, [Oprsal and Fäh \(2007\)](#) has emphasized the necessity to use 3C ground motion by showing the big difference between 1C and 3C computation result. The modeling uncertainty of input motion for seismic modeling of underground structure is even higher. Due to the lack of ground motion observations along the depth, deconvolution method is usually adopted in many studies ([Elgamal et al. \(2008\)](#)) to get the excitation motion at certain depth. The deconvolution procedure represents a 1C linear inverse analysis. This inverse analysis is seemingly simple but it can introduce considerable confusion and uncertainties to the modeling system ([Mejia and Dawson \(2006\)](#)).
- Another uncertainty comes from the method that is used to input seismic motion into SSI system. Usually free field motion are directly imposed to the structure without considering ESSI effects. This is especially common for underground structures where simplified static loads are directly imposed and these structures are simply designed to accommodate the estimated free field deformation([Hashash et al. \(2001\)](#)).
- Nonlinear ESSI effects are also important factor that is neglected or simplified in many existing studies. There are three sources of significant nonlinearity in an ESSI system: (a) Inelastic (elastic-plastic) behavior of soil, (b) inelastic (elastic-plastic) behavior of the contact/interface zone, and (c) inelastic (elastic-damage-plastic) behavior of the structure. Early works found that structural response can be quite different when elastoplasticity of surrounding soil is considered ([Bielak \(1978\)](#); [Iguchi and Luco \(1981\)](#)). In addition to that [Jeremić et al. \(2004\)](#) reported that ESSI behavior can have both beneficial and detrimental effects on structural behavior. The nonlinear

contact (interface) was analyzed by [Hu and Pu \(2004\)](#) and it was shown that its accurate modeling is a key part to realistic modeling of ESSI systems.

Due to computational limitations and complicated nature of ESSI problems mentioned above, there exist only few high-fidelity ESSI simulations, for bridges ([Jeremić et al. \(2009\)](#)) and tunnels ([Corigliano et al. \(2011\)](#)). To the Author's knowledge, there is no high fidelity (realistic 3C motions, realistic elastic plastic soil modeling, and realistic contact/interface modeling) for a deeply embedded SMR structure. In this paper, we present high fidelity modeling of SMR using state-of-the-art ESSI methodology. Realistic 3C free field seismic motions are modeled using regional scale wave propagation models. Developed free field motions are then input into ESSI system using Domain Reduction Method ([Bielak et al. \(2003a\)](#)). Modeling description section presents inelastic/nonlinear modeling details for elastic-plastic models of surrounding soils and nonlinear interface/contact behavior. The inelastic/nonlinear modeling result are compared with linear elastic in Simulation Results section.

In addition to accurate modeling of 3C motions and nonlinear effects, energy propagation through the model is also accurately modeled. Energy dissipation is a widely used indicator of material damage in elastic plastic materials. A common misconception does exist, however, on the meaning of plastic work and plastic energy dissipation, as observed in a number of publications. Correct evaluation of energy dissipation should follow the principles of thermodynamics that incorporated plastic free energy ([Rosakis et al., 2000; Dafalias et al., 2002](#)). The thermodynamics framework presented by [Yang et al. \(2018, 2019a\)](#) is implemented in the Real-ESSI Simulator [Jeremić et al. \(1988-2025\)](#), and is used to perform energy analysis on the SMR model in this paper. Energy dissipation in the SMR model is discussed in some detail.

504.7.2 Domain Reduction method

Input seismic motions into finite element model is an indispensable step for the simulation of soil structure interaction. The method we used here is called Domain Reduction Method, developed by [Bielak et al. \(2003a\)](#). It is a modular, two-step dynamic procedure aimed at reducing the large computation domain to a more manageable size. Firstly, large scale regional free field model is developed encompassing causative fault and location of SMR structure (however SMR structure is not present, it is a free field model). Time series of free field motions (displacements and accelerations) are recorded at locations of DRM elements, a single layer of finite elements encompassing soil structure SMR model. Those motions are then used in the second step, to develop effective forces that are used to input free field motions into ESSI SMR model.

504.7.3 3C Free Field Motions

Development of free field motions was done using a fourth order finite difference program SW4 ([Petersson and Sjögren \(2018\)](#)) developed at LLNL. Modeled was propagation of fault rupture in a model with dimensions $9\text{km} \times 6\text{km} \times 20\text{km}$. The magnitude of simulated earthquake is 5.5. The shear wave velocity of soils in surface layer (500 meters thick) is $V_s = 500\text{m/s}$. Motions were recorded in a box with dimensions $300\text{m} \times 300\text{m} \times 200\text{m}$

The characteristic ground motions recorded by ESSI nodes are plotted in Figure 504.86. The peak ground acceleration (PGA) in x and y direction is about 1g. Apart from that, significant amount of vertical motions with PGA 0.5g is also observed. The peak ground displacement (PGD) is about 0.1m in horizontal direction. Since ESSI box is located in the foot wall of the reverse fault, the permanent ground subsidence of about 6cm is recorded. Fourier transformation and response spectrum of the motions are shown in figure 504.87. The frequency range of the motion is within 15Hz. The dominant frequency of the motion is around 5 Hz. In response spectrum, we also see significant resonance effects for structure whose fundamental period is around 0.2s corresponding to 5 Hz fundamental frequency.

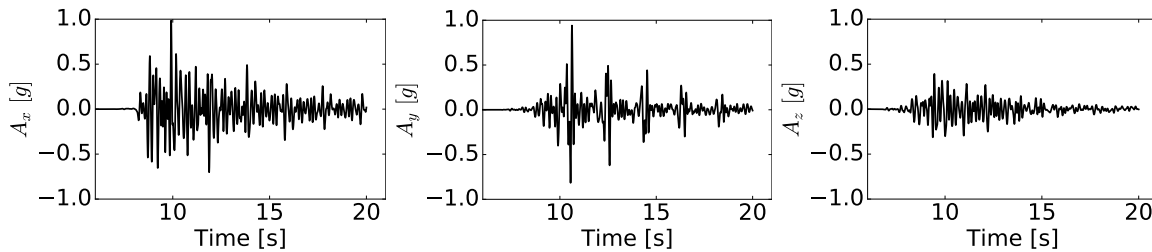


Figure 504.86: Acceleration and Displacement Time Series of Motion

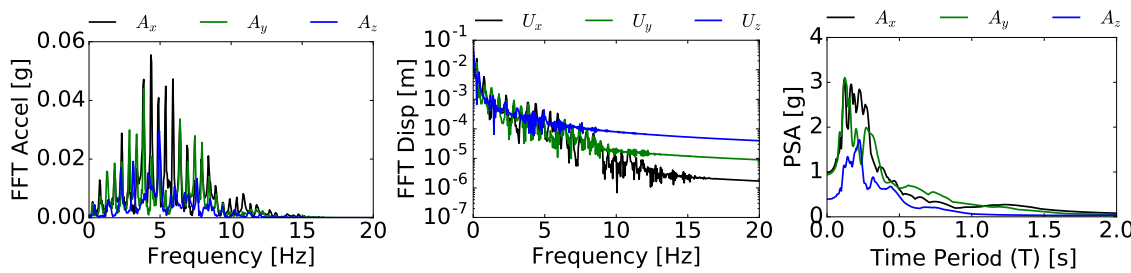


Figure 504.87: Strong Motion Fourier Transform and Response Spectrum

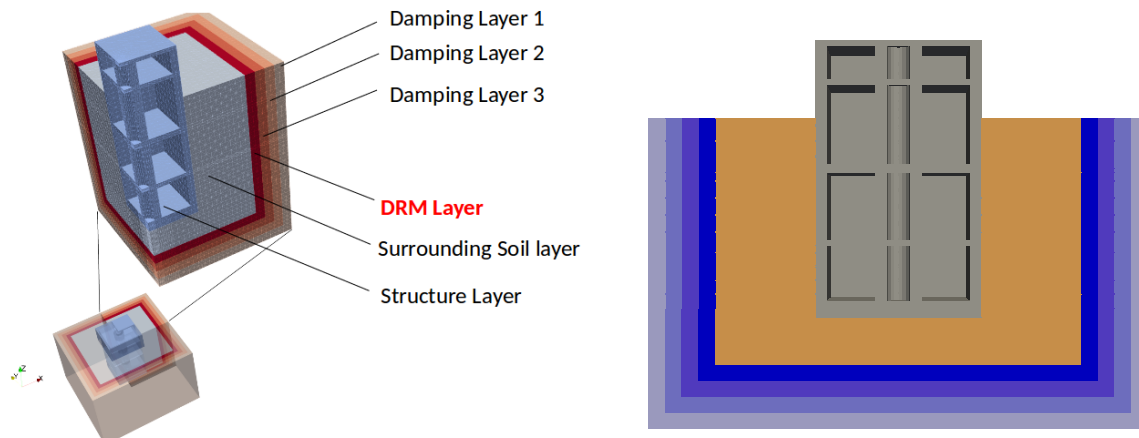


Figure 504.88: FEM model for an SMR.

504.7.4 Model Description

In order to reduce model size using DRM method, we develop our target model with 6 layers. As shown in figure 504.88, the innermost part is a structure layer, which is surrounded by a soil layer. Following that, there is a DRM layer used to apply equivalent earthquake force. Outside DRM layer, there are three damping layers. These damping layers are designed to add high Rayleigh damping so that the outgoing wave (vibrations of structure, radiation damping) can be adsorbed. Table 504.5 shows the material used. The size of whole FEM model is $72m \times 72m \times 56m$. There are 177,806 nodes, 20172 27-node brick elements, 3,177 contact/interface elements (modeling the interface between soil and embedded structure), with a total of over 533 thousand degrees of freedom (DoFs). The average mesh size is 3 meters. Newmark time integration method is used in this study with parameters $\gamma = 0.7$ and $\beta = 0.36$ adding numerical damping that reduces high frequency motions that were introduced by SW4. In order to capture the wave propagation in FEM model, mesh size should be controlled so that there is no artificial filtering to motions above certain frequency (Watanabe et al., 2017). As pointed out by Hughes (1987), 10 linear interpolation finite elements and 2 quadratic interpolation elements are needed per wave wavelength. Since second order 27 node brick element are used here, the minimum wave length captured is 6 meters. Considering shear wave velocity $v_s = 500m/s$, the maximum frequency calculated by equation 504.7 is 83 Hz. Even when material plasticifies (becomes softer), model is still propagating high frequencies of up to required $f_{max} \leq 15Hz$.

$$f_{max} = v_s / \lambda_{min} \quad (504.7)$$

504.7.4.1 Embedded Nuclear Structure

Small Modular Reactor (SMR) analyzed here is a 4 storied reinforced concrete structure with total height 50 meters and 36 meters embedded in the ground. The length and width of the structure is 30 meters. The whole structure is modeled using 27-node solid brick element with linear elastic material. The Young's modulus is selected as $E = 30\text{GPa}$ and Poisson's ratio $\nu = 0.2$. Single layer of 27 node bricks can accurately model (beam and plate) bending, and is hence chosen for structural model.

504.7.4.2 Soil Model

The depth of the model surrounding the structure is 45m. The soil is assumed to be saturated soil with undrained behavior during the earthquake. In order to considering nonlinear site effects, the soil is modeled with elastoplastic material. In the past 20 years, many 3D constitutive models [Yang et al. \(2003\)](#); [Dafalias and Manzari \(2004b\)](#); [Park and Byrne \(2004\)](#); [Pisanò and Jeremić \(2014\)](#) have been developed. Undrained behavior can be approximately modeled using von Mises material model ([Yang and Jeremić, 2003](#)). Elastic plastic von Mises material model with linear kinematic hardening rule is used here. The material parameters are presented in table 504.5. Backward Euler implicit algorithm ([Jeremić and Sture \(1997\)](#)) is used for the equilibrium iterations at constitutive level.

504.7.4.3 Soft Contact Element

Model for contact/interface (axial contact, gap opening and closing and slip behavior) of the interface between structure and surrounding soil, relies on a node-to-node soft contact/interface element ([Sinha and Jeremić \(2017\)](#)). In soft contact, the normal stiffness exponentially grows as the relative displacement between two contact/interface nodes increases and finally reaches maximum normal stiffness. 3,177 contact elements are placed at the soil-structure interface. Contact/Interface parameters are shown in Table 504.5.

504.7.4.4 Simulation Procedure

The nonlinear ESSI analysis was conducted using Real-ESSI Simulator ([Jeremić et al. \(1988-2025\)](#)) developed at UC Davis and LBNL. Two SMR simulation models were simulated. First model uses linear elastic soil without contact element and second model uses inelastic/nonlinear soil with inelastic/nonlinear contact. In both cases, two loading stages were modeled: First loading stage is a self weight, developed by adding a uniform gravity field. This is a necessary stage for inelastic analysis in order to develop initial stress state of structure and surrounding soil before earthquake comes. Self weight was also applied to the elastic model, just so that we have comparable displacement results. Then second loading stage

Table 504.5: Modeling parameters

Material parameters	shear wave velocity [m/s]	500
	Young's modulus [GPa]	1.25
	Poisson ratio	0.25
	von Mises radius [kPa]	60
	kinematic hardening rate [MPa]	0
Contact parameters	initial normal stiffness [N/m]	1e9
	hardening rate [/m]	1000
	maximum normal stiffness [N/m]	1e12
	tangential stiffness [N/m]	1e7
	normal damping [N/(m/s)]	100
Damping parameters	tangential damping [N/(m/s)]	100
	friction ratio	0.25
	structure layer	5%
Damping parameters	surrounding soil	15%
	DRM layer	20%
	outside layer 1	20%
	outside layer 2	40%
	outside layer 3	60%

is an earthquake load. Simulations were performed on a local parallel computer with parallel version of the Real-ESSI Simulator using 10 CPUs. It is noted that Real-ESSI Simulator is also available on Amazon and Google cloud parallel computers as well as on large national parallel computers at the LBNL (EDISON and CORI). Local parallel computer (a workstation) was used in order to illustrate versatility of Real-ESSI Simulator and to show that high fidelity parallel computations do not need to require high price parallel computers.

504.7.5 Simulation Results

Figure 504.89 shows time series acceleration response of top center of SMR.

The elastic results represent simulation case where the surrounding soil is modeled using linear elastic material and no contact elements in soil-structure interface. The inelastic results represent simulation case where the surrounding soil is modeled using inelastic soil material and an inelastic contact. Signifi-

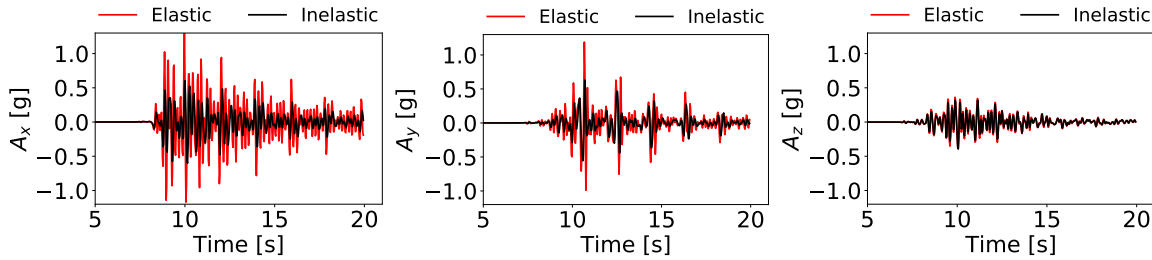


Figure 504.89: Time Series Acceleration Response.

cant acceleration decreases can be seen in the inelastic case. The horizontal peak acceleration values is reduced by almost 40%. This is due to plastification of soil and inelastic response of the contact/interface zone. Moreover significant seismic energy is dissipated, so that inelastic soil and inelastic contact/interface act as seismic dissipators and isolators during seismic event. The acceleration difference in vertical, z direction is less significant than horizontal direction.

Figure 504.90 shows Fourier magnitude that high frequency component of horizontal acceleration was significant decreased in inelastic case.

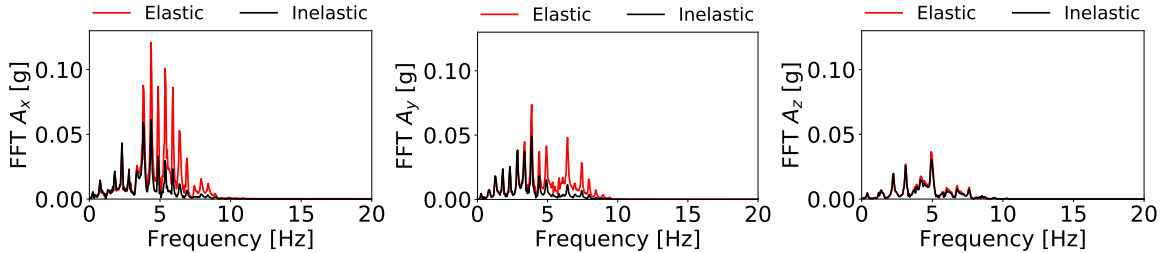


Figure 504.90: Acceleration Response in frequency domain

Material Modeling Influence on Results is Shown in Figure 504.91.

SMR: Variation of Acceleration with Depth is Shown in Figures 504.92 and 504.93.

SMR: PGA and PGD Depth Variation is Shown in Figure 504.94.

- The PGA & PGD of SSI systems are (very) different from free field motions,
- Material nonlinearity has significant effect on acceleration response.

SMR: Elastic vs Inelastic response is shown in Figure 504.95.

Figure 504.96 shows the distribution of plastic strain in surrounding soil. There are two main plastic zones near two bottom corners of the structure. Also the plastic strain at the soil-structure interface is higher than adjacent area. It is interesting to note that there is an elastic zone beneath structure. The

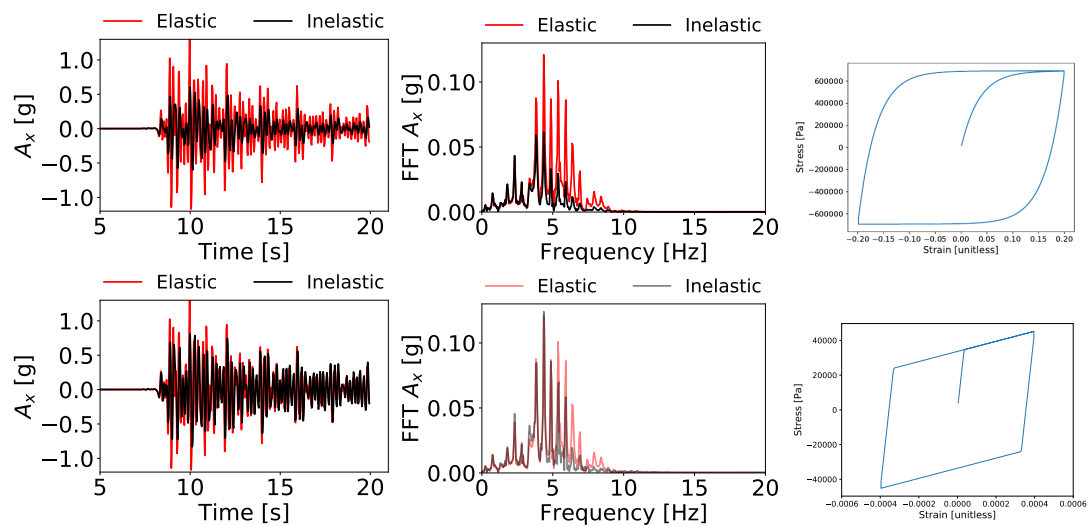


Figure 504.91: Upper: Material A: nonlinear, vM - AF; Lower: Material B: Bilinear.

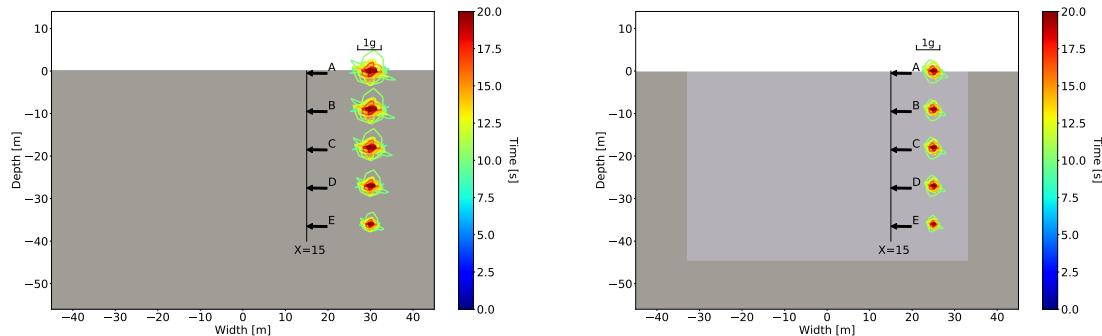


Figure 504.92: Free field response, left: elastic, right, inelastic.

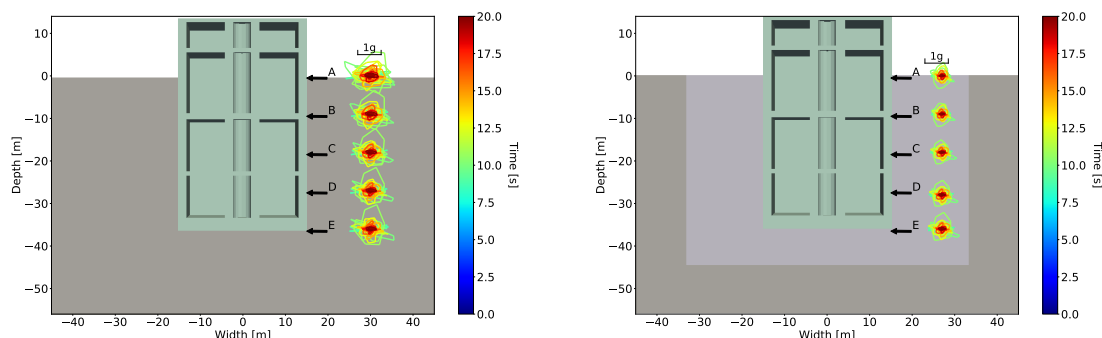


Figure 504.93: ESSI for an SMR response, left: elastic, right, inelastic.

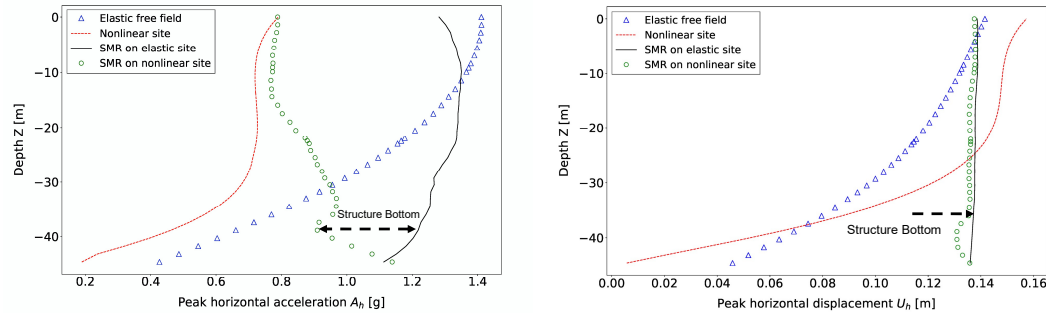


Figure 504.94: SMR: PGA and PGD variation with depth.

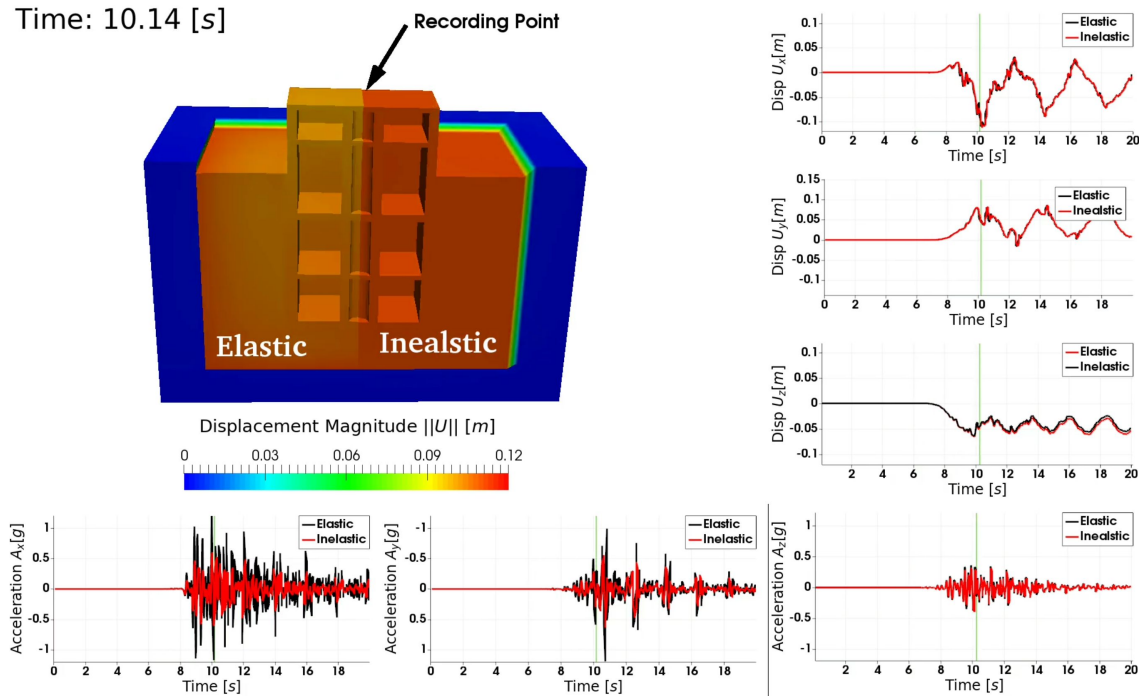


Figure 504.95: Animation of a linear elastic vs inelastic response of an SMR.

shape of the elastic zone resembles a bulb and is due to self weight and stiffness of the structure that compresses soil beneath

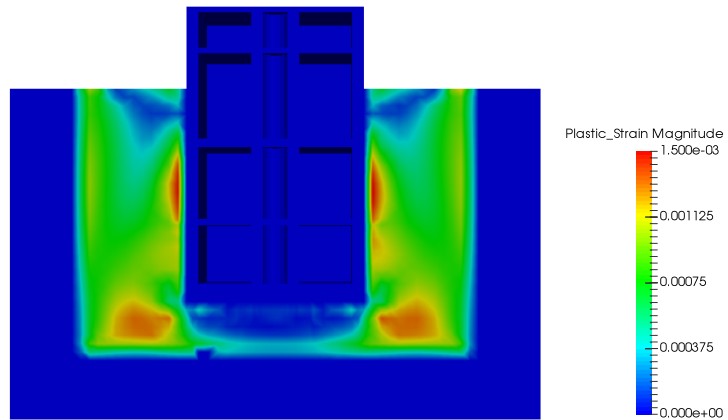


Figure 504.96: Distribution of the magnitude of plastic strain

504.7.6 Energy Dissipation

According to the thermodynamics framework presented by Yang et al. (2019a), the energy dissipation in any decoupled material undergoing isothermal process can be expressed as:

$$\Phi = \sigma_{ij}\dot{\epsilon}_{ij} - \sigma_{ij}\dot{\epsilon}_{ij}^{el} - \rho\dot{\psi}_{pl} \geq 0 \quad (504.8)$$

where Φ is the rate of change of energy dissipation per unit volume (or dissipation density), σ_{ij} and ϵ_{ij} are the stress and strain tensors respectively, ϵ_{ij}^{el} is the elastic part of the strain tensor, ρ is the mass density of the material, and ψ_{pl} is the plastic free energy per unit volume (or plastic free energy density). Equation 504.8 ensures the energy balance and nonnegative energy dissipation conditions that correspond to the first and second law of thermodynamics.

With Equation 504.8, the energy balance of a SSI system is simply given by:

$$W_{Input} = E_{Stored} + E_{Dissipated} = KE + SE + PF + PD \quad (504.9)$$

where W_{Input} is the input work due to external loading, KE is the kinetic energy, SE is the elastic strain energy, PF is the plastic free energy, and PD is the energy dissipation due to material plasticity. Formulation for each energy component can be found in Yang et al. (2018). Note that in Equation 504.9, it is assumed that no other forms of energy dissipation exists in the system.

Figure 504.97 (a) shows the distribution of plastic dissipation density in the SMR model at the end of simulation. The case presented in this section is elastic plastic soil without contact/interface element. Note that the structure is modeled with elastic material, so they do not dissipate any energy. As expected, more seismic energy is dissipated around the corners and edges of the structure due to stress concentration. It can be observed that there are several elastic regions around the boundaries of the structure, which means that the soil there does not plastify much and moves together with the structure. Economy of the design can be improved by better utilizing the strength of soil around these locations.

Figure 504.97 (b) show the evolution of energy components at location A. It can be observed that the amount of plastic energy dissipation is much larger than the other forms of energy, indicating that the nonlinear effect is quite significant in deeply embedded structure. Another interesting observation is the small amount of plastic free energy whose quantity largely depends on material hardening parameters and loading conditions. It should be pointed out that even if it is small, plastic free energy should never be neglected so that the condition of nonnegative incremental energy dissipation can be upheld Rosakis et al. (2000); Taylor and Quinney (1934).

SMR: Energy Dissipation for an SMR, Figure 504.98.

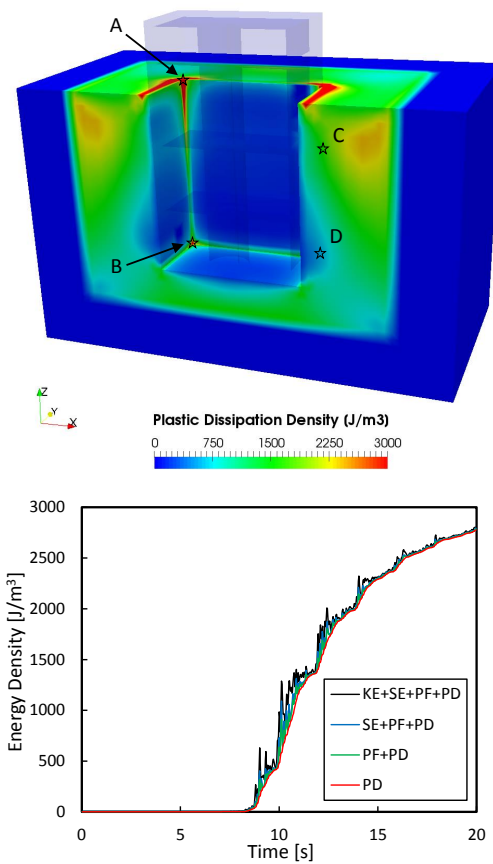


Figure 504.97: Energy dissipation in SMR model: (a) Plastic dissipation density field at the end of simulation; (b) Evolution of energy components at location A.

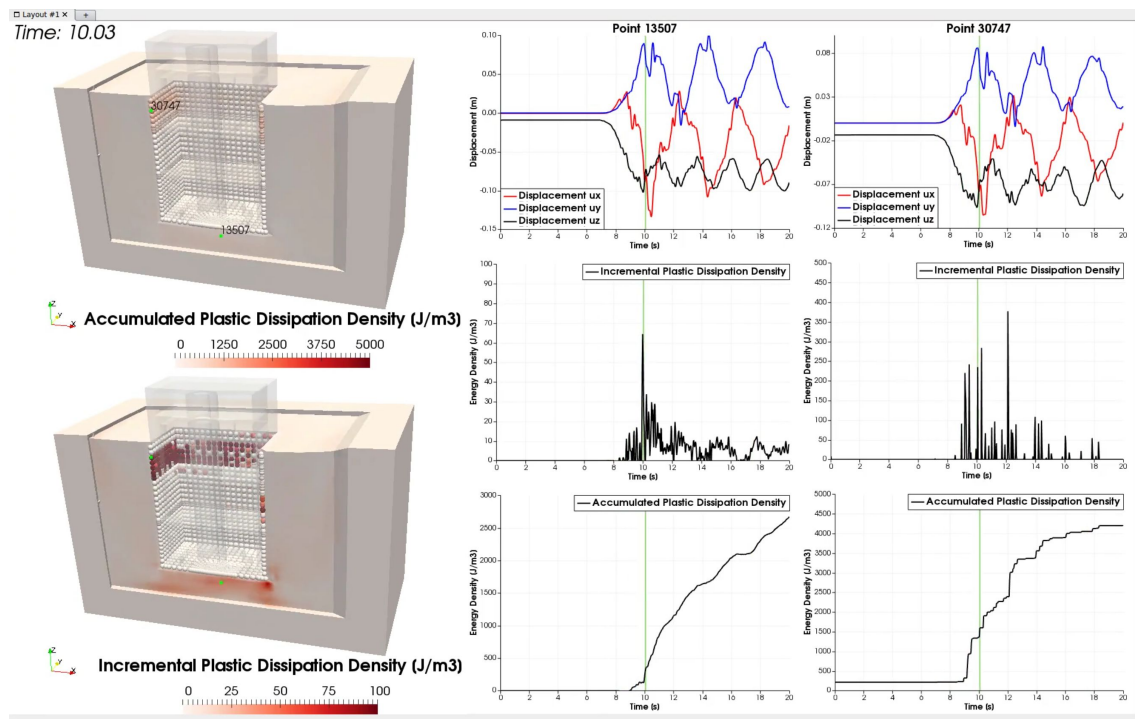


Figure 504.98: Animation of energy dissipation for an SMR.

504.7.7 SMR Inelastic Modeling Conclusions

The seismic response of an embedded SMR has been modeled with high fidelity. Using state-of-the-art nonlinear ESSI simulation techniques, many modeling uncertainties have been eliminated. The methodology shown here is also applicable to many other ESSI problems (buildings, bridges, dams, etc.). The simulation result of SMR shows that the acceleration response of the structure decreases with nonlinear effects properly modeled. In addition, the high frequency component of acceleration is significantly damped out in inelastic case due to soil plastification.

Energy dissipation analysis shows that the soil close to the edge of the SMR structure dissipates large amount of seismic energy during shaking. Such observation also indicates significant nonlinear effect when elastoplastic material is used for soil modeling. Several elastic regions are identified where design can be improved so that soil strength at these locations can contribute to the safety of the SSI system.

504.8 Inclined Waves, Free Field and SMR Modeling

Methodology developed by [Wang et al. \(2020a\)](#) and presented in section [109.2.5](#) on page [557](#) is illustrated here. This is really a repeat of results from [Wang et al. \(2020a\)](#).

Input files for these models are available [HERE](#).

Presented WPF-DRM method is implemented in the Real-ESSI Simulator ([Jeremić et al., 1988-2025](#)). Described examples and publicly available executables for the Real ESSI sequential and parallel programs are available through Real ESSI Simulator web site <http://real-essi.info/>. All numerical examples presented here are analyzed using Real-ESSI Simulator version 20.01, in parallel computing mode, on UC Davis and Amazon Web Services parallel computers.

504.8.1 Free Field Modeling and Verification

Free field response of layered ground excited by an inclined incident seismic wave is used to illustrate and verify developed methodology. Analytic solutions based on Thomson-Haskell propagation matrix technique ([Thomson, 1950](#); [Haskell, 1953](#); [Silva, 1976](#)) are used for verification.

A finite element model for the free field, that is 300m wide and 200m deep, consisting of three layers, as described in Table [504.6](#), is used.

It is noted that dimension of analyzed model is 300m × 200m, however there exist additional finite elements outside this domain: DRM layer is a single layer of finite elements that surround the interior domain. Beside the DRM layer, there are absorbing layers consisting of multiple layers of finite elements with high viscous damping. These damping layers should be thick enough to absorb the outgoing waves.

Table 504.6: Properties of layers: thickness d , density ρ , shear wave velocity V_s , compressional wave velocity V_p and Poisson's ratio ν .

Layer	d [m]	ρ [kg/m^3]	V_s [m/s]	V_p [m/s]	ν
1	50	2100	500	816.5	0.2
2	100	2300	750	1403.1	0.3
3	∞	2500	1000	2081.7	0.35

The thickness and damping parameters of these absorbing layers are determined such that the response of exterior damping layer given by earthquake soil structure interaction analysis is negligible compared to the inner part. A fixed boundary condition is applied to the outer boundary. It is also noted that theoretically there should be no waves propagating outside of the DRM layer for a free field response. Additional damping layers are added in order to accommodate further, non-free field model expansions and additions. Finite element size is set to 5m, and with 10 finite elements per wave length, this mesh can accurately propagate waves of up to $f = 10\text{Hz}$, for surface soil with shear wave velocity of $V_s = 500\text{m/s}^2$, as per [Lysmer and Kuhlemeyer \(1969\)](#); [Watanabe et al. \(2017\)](#).

A number of monochromatic, single frequency plane SV wave, represented by a cosine function, with variable inclinations $\theta = 10^\circ, 45^\circ, 60^\circ, 80^\circ$ and variable frequencies, $f = 1.0, 2.5, 5.0, 10.0\text{Hz}$, are applied to the layered ground model using developed methodology. The incident SV wave magnitude from the depth is 0.06m and is kept the same for all the analyzed cases. It is noted that inclination angle θ is measured between a wave propagation direction vector and vertical axes. The wave inclination θ depends on many factors, e.g., source focal mechanism and radiation pattern, wave propagation path and local site geology and topography. The typical range of inclination is $0^\circ \sim 40^\circ$ ([Tabatabaie et al., 1986](#); [Sigaki et al., 2000](#)). For example, [Tabatabaie et al. \(1986\)](#) estimated that the incidence angle of shear waves at the SMART-1 array site is around 20 degrees using the recorded motions from 1981 Taiwan earthquake. For far-field, flat engineering site with large impedance contrast (e.g., soft soil overlying stiff bedrock), the assumption of vertical wave propagation can be adopted due to very small inclination of incident seismic waves. However, for near-field, hard rock site with low impedance contrast or engineering site with significant topography, incidence angle of seismic waves tends to be large and inclined wave propagation should be carefully modeled.

Free field motions are developed and introduced into the model through WPF-DRM. Figure 504.99 shows snapshots of wave displacements in the model, for a wave frequency of $f = 5\text{Hz}$, for different input plane wave inclinations, $\theta = 10^\circ, 45^\circ, 60^\circ, 80^\circ$. Figure 504.100 shows snapshots of wave displacements in the model, for a wave that is inclined at $\theta = 60^\circ$, for variable input plane wave frequencies $f = 1.0, 2.5, 5.0, 10.0\text{Hz}$.

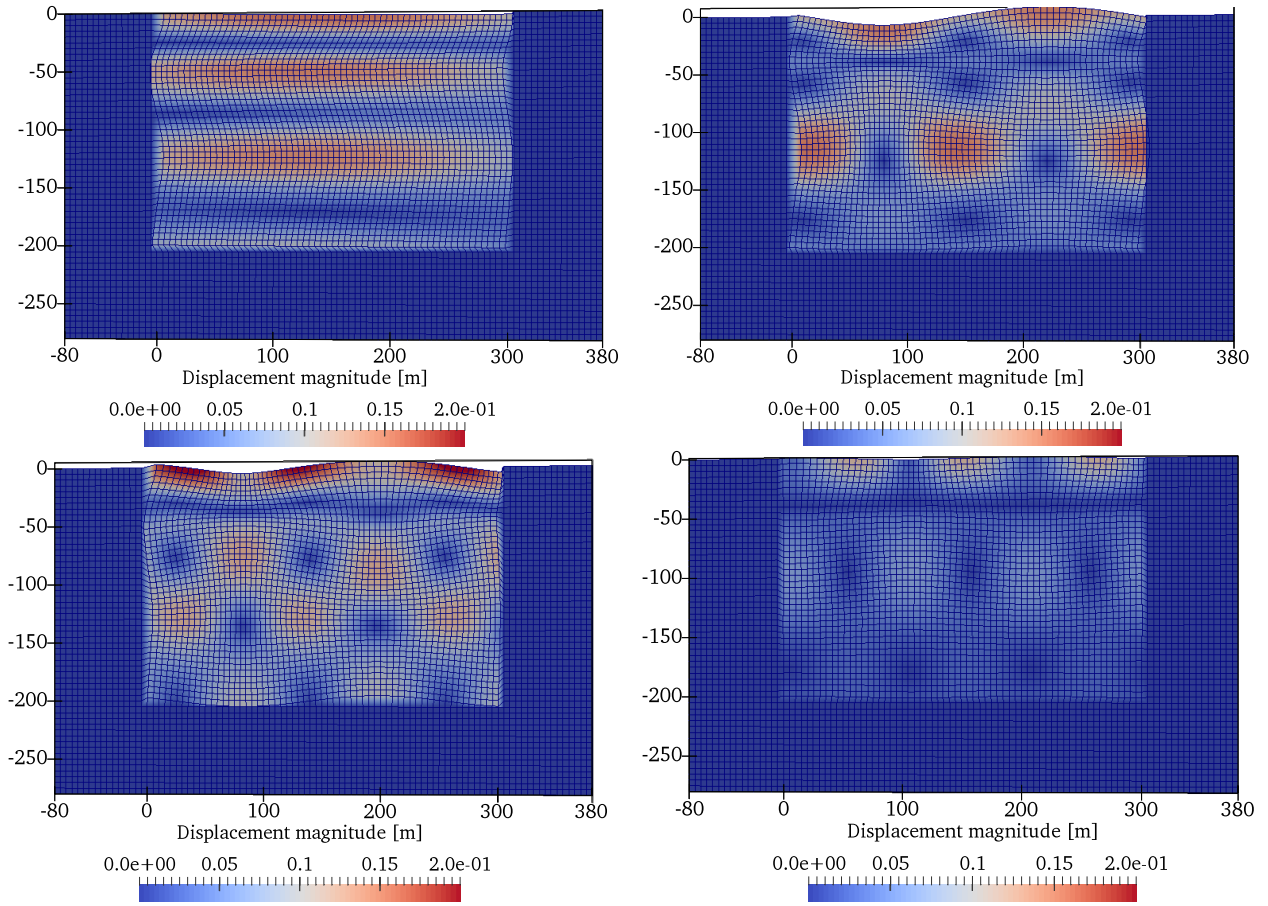


Figure 504.99: Displacement magnitudes for a free field response under incident SV wave, frequency $f = 5\text{Hz}$, with different incident wave inclinations: (a) $\theta = 10^\circ$ (b) $\theta = 45^\circ$ (c) $\theta = 60^\circ$ (d) incident angle $\theta = 80^\circ$.

Few notes are in order upon visual inspection of results in Figures 504.99 and 504.100. The outgoing waves in exterior region, outside DRM layer, are negligibly small, almost zero for all the cases. This is indeed expected, as it follows from the theory of the domain reduction method (Bielak et al., 2003a; Yoshimura et al., 2003a), whereby the so called residual field (w_e) should be non-existent for free field motions, that were used to develop effective DRM forces.

Comparing free field responses for SV wave with different incident angles, Figure 504.99, the $\theta = 10^\circ$ case behaves very similar to 1D vertically propagating motion field that is commonly used in engineering practice. It is noted, however that there are still vertical motions at the surface due to such almost vertical SV wave interacting with the free surface. For cases where wave inclination is more significant, for $\theta = 45^\circ$ and $\theta = 60^\circ$, significant surface motions are observed, with pronounced vertical and horizontal motions. When the incident wave inclination is $\theta = 80^\circ$, seismic wave propagates almost horizontally

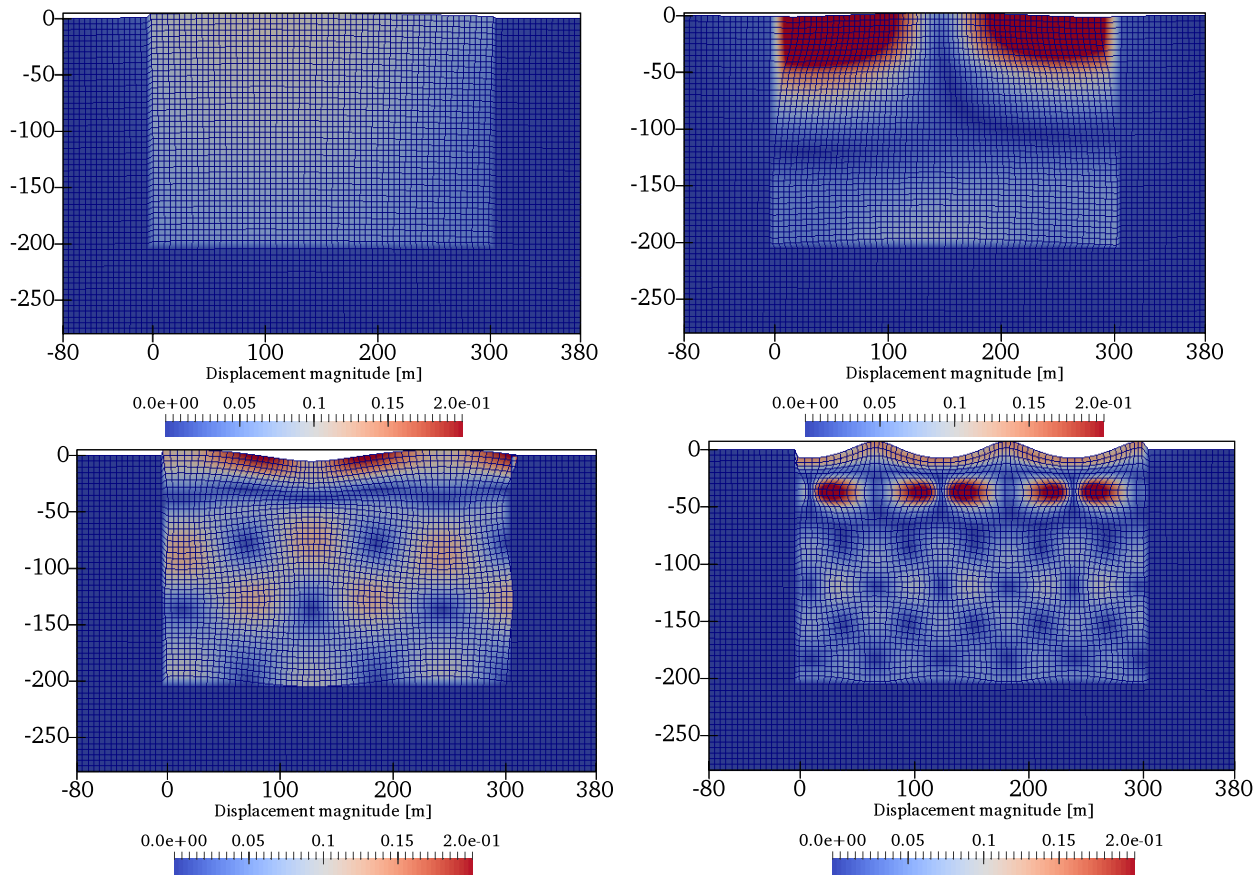


Figure 504.100: Displacement magnitudes for a free field response under incident SV wave at an angle of $\theta = 60^\circ$, with different frequencies: (a) $f = 1.0\text{Hz}$ (b) $f = 2.5\text{Hz}$ (c) $f = 5.0\text{Hz}$ (d) $f = 10.0\text{Hz}$.

without generating significant surface motions. It is also noted that the displacement magnitude of the seismic wave field for wave inclination case $\theta = 80^\circ$ is much smaller than for the other cases. This is reasonable considering the site amplification for other free field cases comes, in part, from the impedance contrast of vertical wave propagation.

Results, snapshots of displacement field magnitudes for wave fields of different frequencies are shown in Figure 504.100 for seismic motion inclined SV wave field at $\theta = 60^\circ$. It is noted that layer boundaries, impedance contrasts, are at -50m , and at -150m . Those layer boundaries can be visually identified from distribution of waves through model depth with positive and negative interference reflected and refracted waves within different layers of the domain.

Figures 504.101 and 504.102 compare simulated free field horizontal and vertical displacement magnitudes against corresponding analytical solutions along the depth. It is noted that acceleration magnitudes can be obtained by multiplying displacement magnitudes with w^2 . Very good agreement is observed

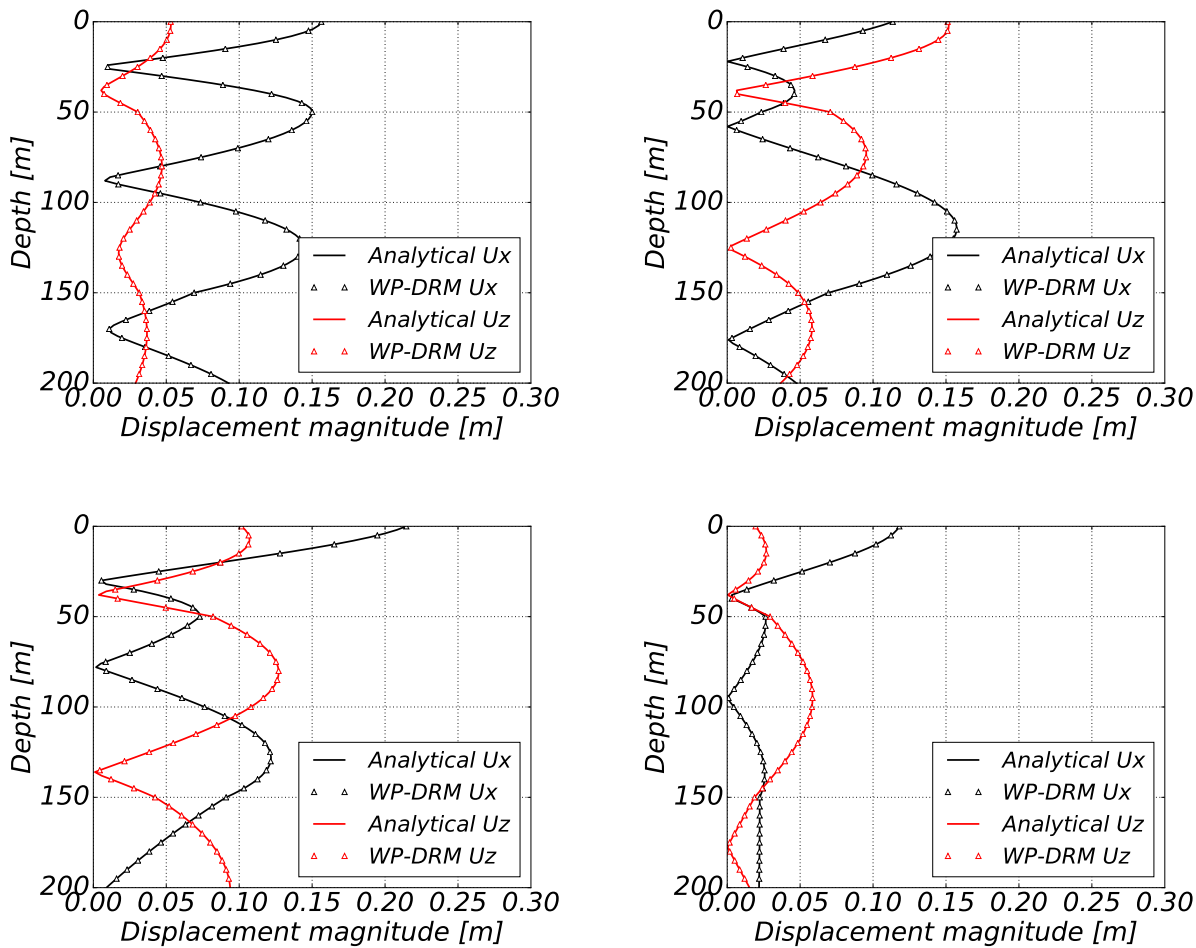


Figure 504.101: Verification of free field modeling under incident SV wave $f = 5\text{Hz}$ with different incident angles θ : (a) $\theta = 10^\circ$, (b) $\theta = 45^\circ$, (c) $\theta = 60^\circ$ (d) $\theta = 80^\circ$.

between results given by WPF-DRM simulation and analytical solutions. Several interesting observations can also be made:

1. Along with the increase in frequencies, the vertical wave length becomes shorter, and that results in more wave interferences along the depth.
2. The existence of layers and interfaces at $z = -50\text{m}$ and $z = -150\text{m}$ complicates the spatial variation of wave field along the depth, especially for higher frequencies, $f = 5\text{Hz}$ and 10Hz . The response curves at depths $0 \sim 50\text{m}$ and $50 \sim 150\text{m}$ are quite different in both amplitude and variation pattern.

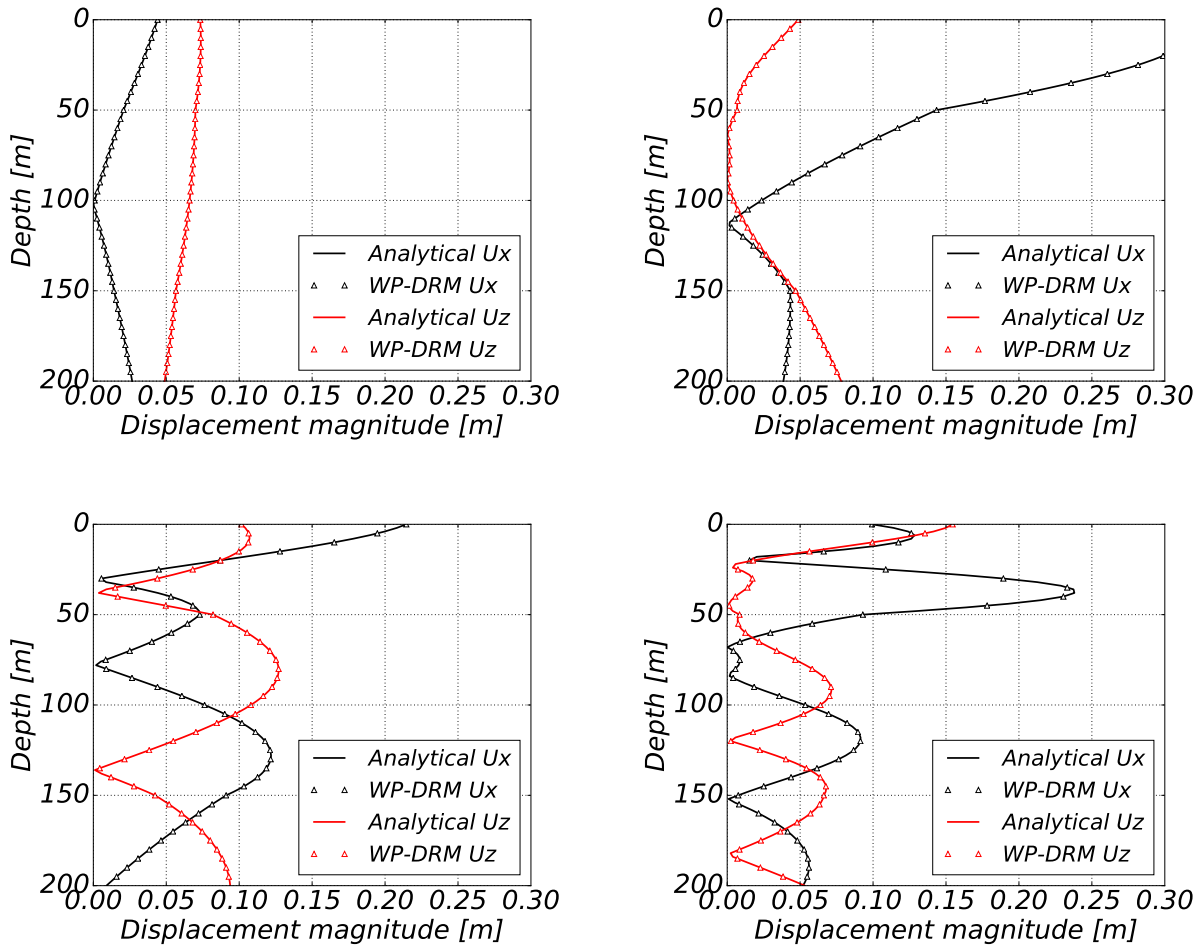


Figure 504.102: Verification of free field modeling under incident $\theta = 60^\circ$ SV wave with different frequencies f : (a) $f = 1.0\text{Hz}$, (b) $f = 2.5\text{Hz}$, (c) $f = 5.0\text{Hz}$, (d) $f = 10.0\text{Hz}$.

3. From Fig. 504.101, it can be seen that inclination angle of input SV wave also plays a crucial role in the interference characteristic of inclined wave field. Periodic peaks and troughs shown in the case of 10° inclination are typical interference characteristics of 1D homogeneous, vertically propagating wave field. However, the interference characteristics given by other wave inclinations show significant differences. These different variation patterns along the depth, that might not make much difference for shallow founded surface structures, can result in very different seismic response for deeply embedded structures.

504.8.2 Deeply Embedded Soil-Structure Model

Deeply embedded structural model, a model of a Small Modular Reactor (SMR) is analyzed and used to illustrate developed methodology. The FEM model of an SMR structure embedded in layered ground is shown in Figure 504.103(a). The embedment depth is 36m, while the height of SMR structure above ground is 14m. The structure width is 30m and the whole model width of SSI system is 150m. It is noted that the lateral extent of soil domain should be large enough such that the outgoing waves passing through DRM layer are insignificant. These waves can then be damped out through the absorbing layer and would have negligible influence on the dynamic response of SMR. Key factors to determine the model width of SSI system include structural width, intensity of seismic excitations, etc. Detailed discussions regarding the required lateral extent of soil domain for dynamic SSI analysis can be found in [Sharma et al. \(2020\)](#). Eleven representative points, point A to point K in Figure 504.103(b), are selected to monitor the dynamic response of SMR. The layered ground parameters are the same as those used in free field study given in Table 504.6.

To proper model wave propagation, the finite element size and time step should be carefully controlled to reduce discretization errors. For linear displacement approximation within finite element, in this case eight-node brick elements, at least 10 nodes per wavelength should be used ([Watanabe et al., 2017](#)). The time step length Δt is limited by Courant-Friedrichs-Lowy condition ([Courant and Hilbert, 1989](#)) for stability. In addition, following requirement needs to be met to accurately capture the propagation of wave front ([Jeremić et al., 2009](#)), where Δh is the mesh size and v is the highest wave velocity.

$$\Delta t < \frac{\Delta h}{v} \quad (504.10)$$

In this study, eight-node brick element with 4m mesh size is used for spatial discretization. The maximum frequency the model can propagate is about 12.5Hz considering the minimum elastic shear wave velocity 500m/s. Time step is chosen as $\Delta t = 0.005$ s. Newmark time integration method ([Newmark, 1959](#)) is used with Newmark parameters $\gamma = 0.505$ and $\beta = 0.25(0.5 + \gamma)^2$. Since parameter $\gamma > 0.5$, a small amount of numerical, algorithmic damping is introduced to damp out unrealistic high frequency responses from spatial discretization ([Argyris and Mlejnek, 1991](#)). See [Yang et al. \(2019b,c\)](#) for more information about the proper selection of Newmark parameters for dynamic analysis. Gradually increasing Rayleigh damping (7%, 15% and 30%) is assigned to the inner, middle and exterior part of the absorbing layers, outside of the DRM layer, to prevent reflection of radiated outgoing waves ([Jeremić et al., 2009](#); [Abell et al., 2018](#)). These damping values are determined such that after dynamic SSI analysis the response of the exterior absorbing layer is negligible compared to the inner part.

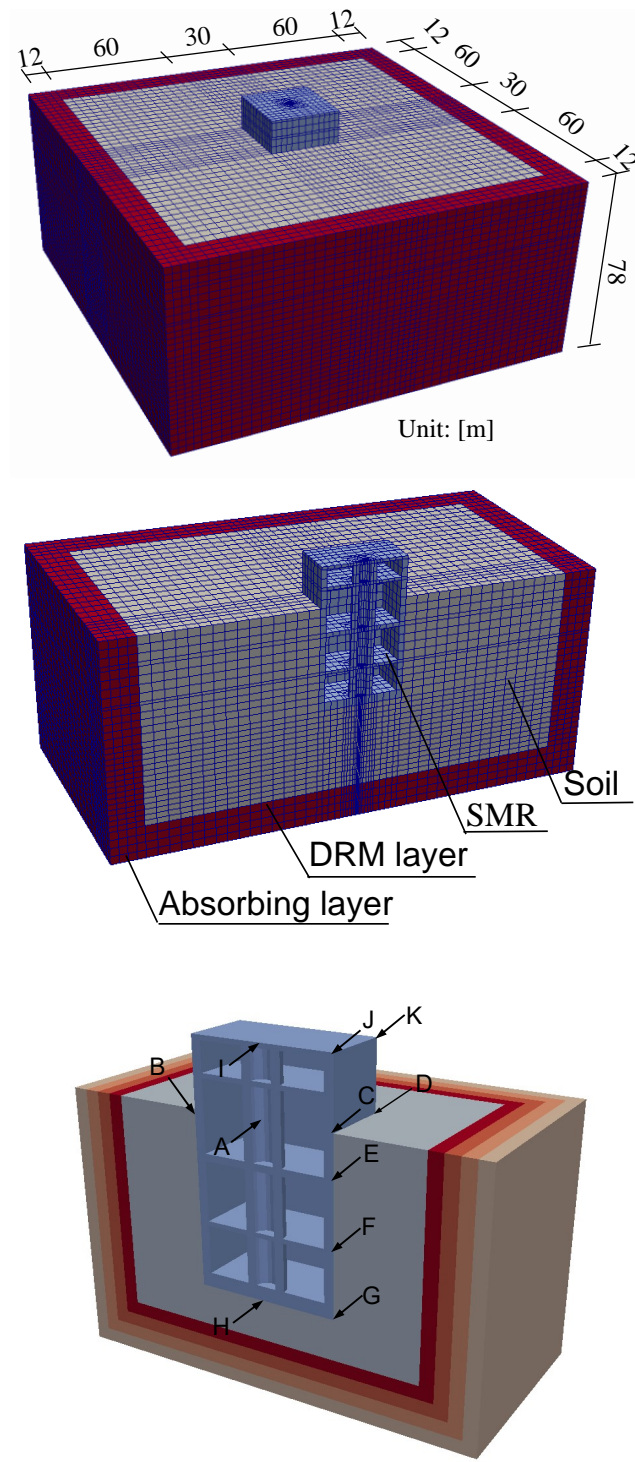


Figure 504.103: FEM model of embedded SMR and representative points.

504.8.3 SMR Excited with Inclined SV Waves

Deeply embedded SMR structure is excited with inclined plane waves, at inclination angles of $\theta = 10^\circ, 45^\circ, 60^\circ$ and 80° . Seismic wave frequency used for this set of numerical test was set at $f = 5\text{Hz}$. As described in table 504.6 on page 2544, shear wave velocities of top 50m layer is $V_s = 500\text{m/s}$ while the lower layer is 100m think and has a shear wave velocity of $V_s = 750\text{m/s}$. Due to presence of layers, seismic wave field close to the surface is made up Rayleigh and Stoneley waves (Aki and Richards, 2002; Semblat and Pecker, 2009). It might thus be difficult to separate influence of these different surface waves the response of the SMR. For example, in Figure 504.99 on page 2545, that shows displacement magnitudes at certain time, for different inclination of incident plane wave, Stoneley wave is apparent close to depth of 50m. In addition, Rayleigh wave is also apparent close to free field surface. Those wave fields, when applied to the SMR SSI system, produce response, at location of point A² on SMR structure, as shown in Figures 504.104 and 504.105.

It is noted that corresponding free field motions at the same location are also plotted for comparison. Variations of displacement magnitudes caused by different inclinations of incident SV wave are quite noticeable for vertical displacements and accelerations, while influence on horizontal displacements and accelerations is much less significant. The reduction of vertical displacement and accelerations that is observed in all the four cases, is consistent with the concept of “base averaging”, “ironing out” of seismic motions by Housner (1957). The most significant reduction occurs for the case of incident wave at an angle $\theta = 45^\circ$ while little reduction is seen in the case of $\theta = 80^\circ$.

The deformed shapes of SMR at $t = 0.4\text{s}$ for four scenarios are shown in Figure 504.106. In the cases of seismic waves at inclinations $\theta = 45^\circ$ and $\theta = 60^\circ$, rocking responses of SMR are quite evident when compared with the cases of almost vertical wave propagation ($\theta = 10^\circ$) and almost horizontal wave propagation ($\theta = 80^\circ$).

²Location of point A is in the middle of SMR structure, where center of the free field model would be, please see Figure 504.103 on page 2550.

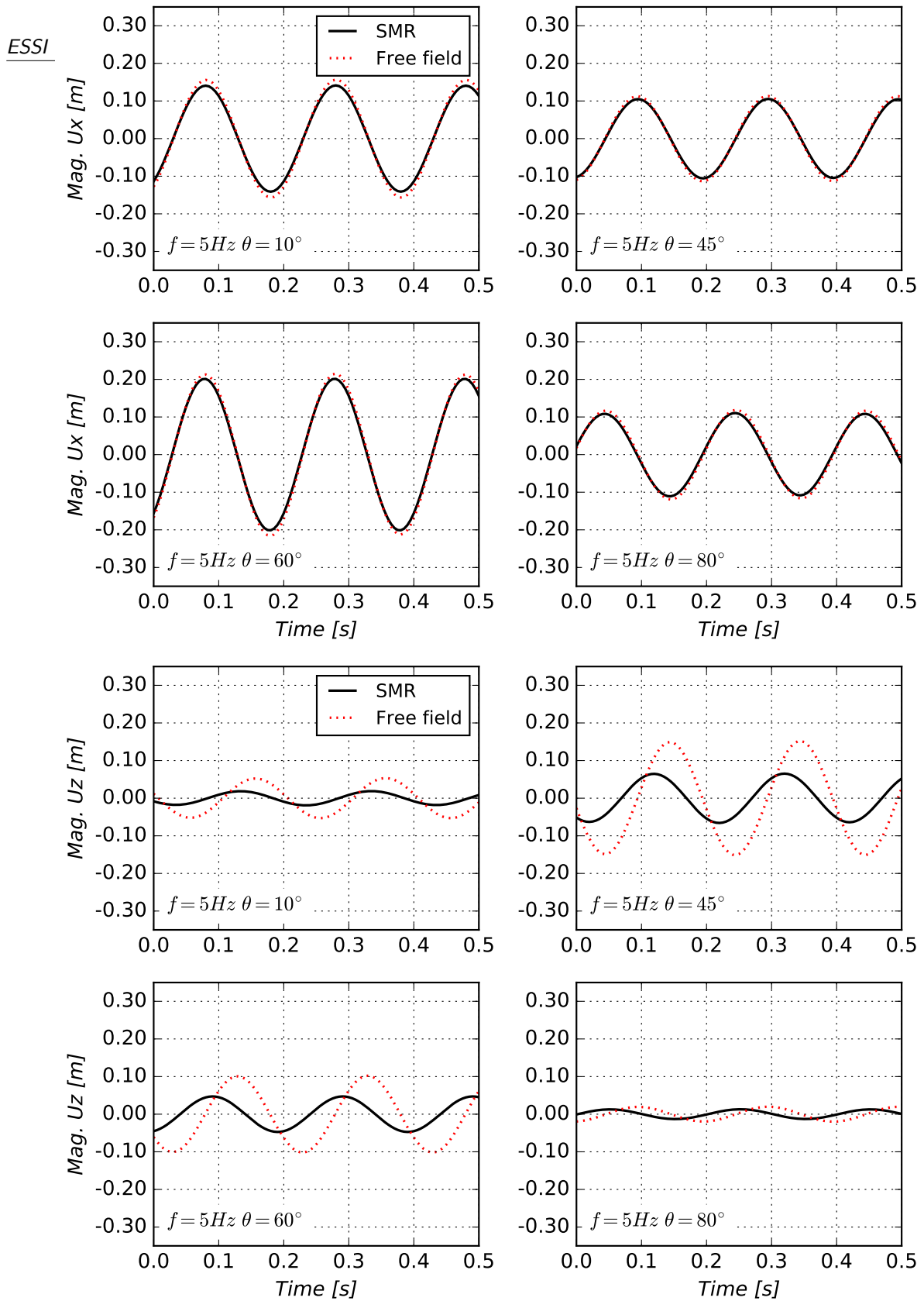


Figure 504.104: Displacement response of point A within embedded SMR, excited by an inclined SV wave with $f = 5\text{Hz}$ and different inclination angles, $\theta = 10^\circ, 45^\circ, 60^\circ$ and 80° : (a) horizontal displacement (b) vertical displacement.

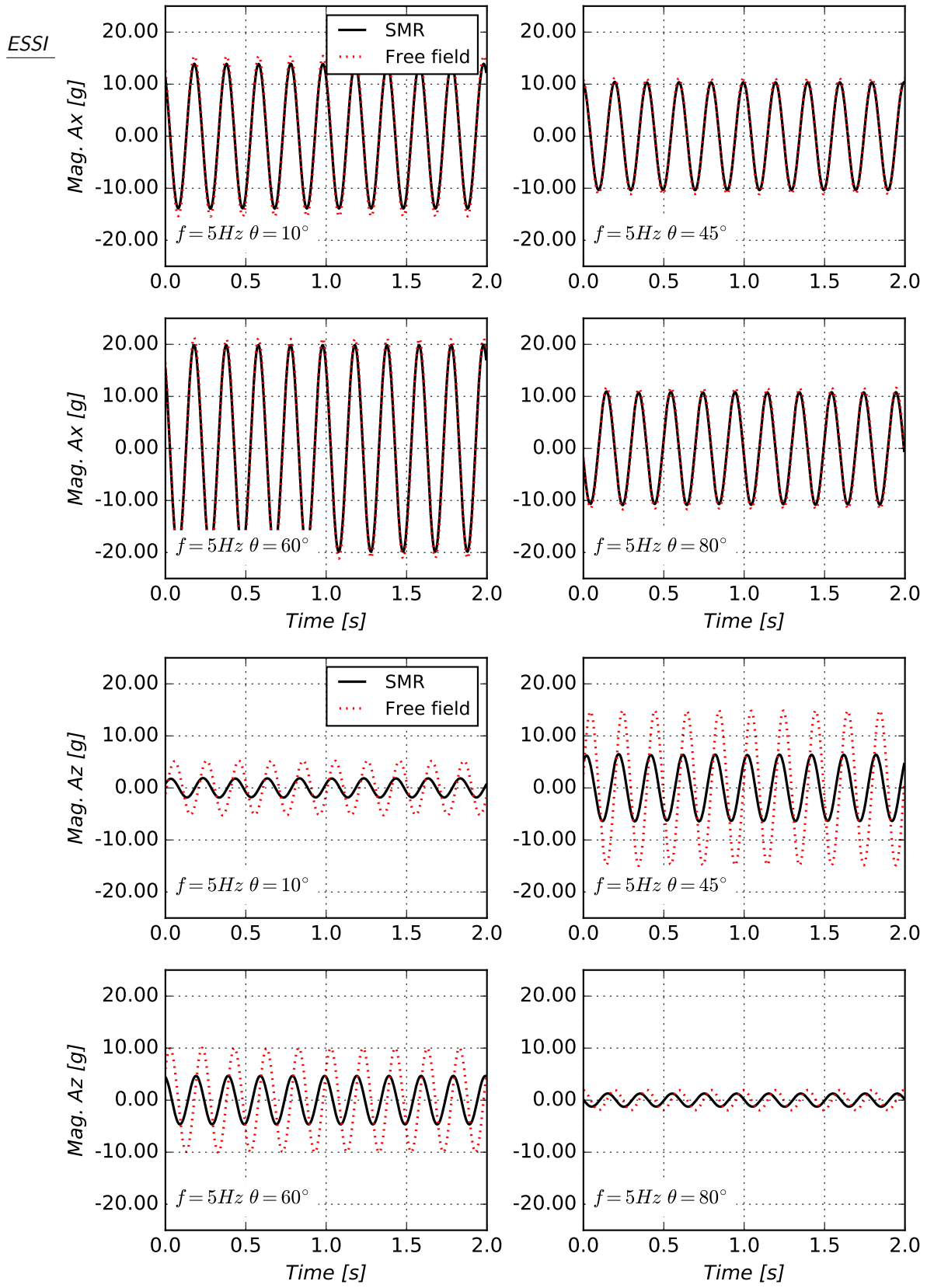


Figure 504.105: Acceleration response of point A within embedded SMR, excited by an inclined SV wave with $f = 5\text{Hz}$ and different inclination angles, $\theta = 10^\circ, 45^\circ, 60^\circ$ and 80° : (a) horizontal acceleration (b) vertical acceleration.

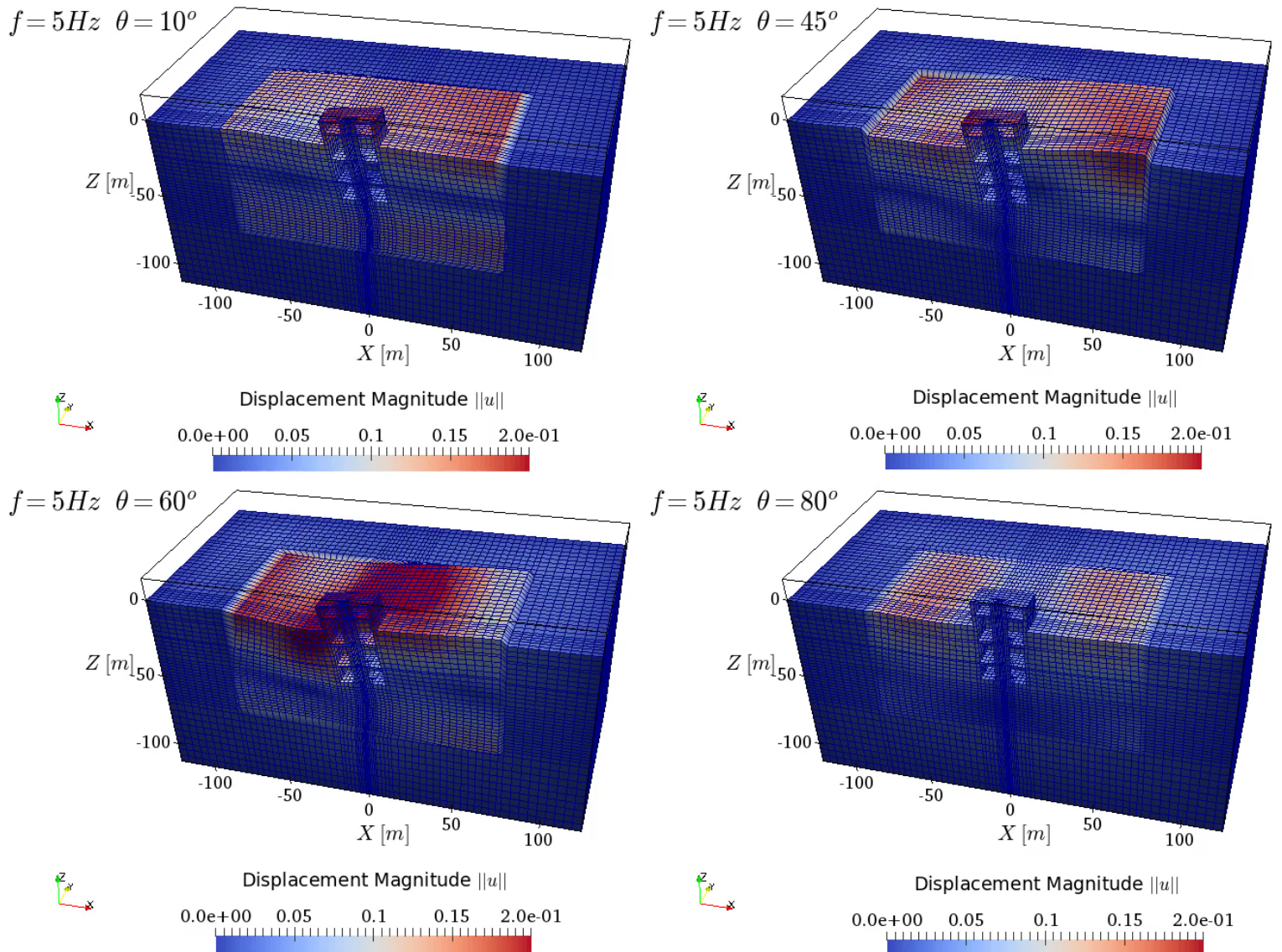


Figure 504.106: The deformed shapes of SMR at $t = 0.4 \text{ s}$ for incident SV wave at different inclinations $\theta = 10^\circ, 45^\circ, 60^\circ$ and 80° .

504.8.4 SMR Excited with Variable Frequency Inclined SV Waves

Keeping incidence angle constant, at $\theta = 60^\circ$, dynamic responses of an SMR under different frequencies of SV wave ($f = 1\text{Hz}, 2.5\text{Hz}, 5\text{Hz}$ and 10Hz) is investigated next. Figures 504.107 and 504.108, show displacement and acceleration responses at point A of SMR model.

It is noted that, again, free field response at the location of point A is also shown for comparison purposes. Significantly variation in displacement and acceleration responses are produced by incident SV wave at different frequencies. The largest horizontal displacement magnitude 0.30m is observed for the case of frequency of $f = 2.5\text{Hz}$ while the smallest horizontal magnitude of 0.047m for $f = 1\text{Hz}$. The vertical displacement responses varies from 0.02m for $f = 2.5\text{Hz}$ to 0.085m for $f = 10\text{Hz}$. SSI effects are almost negligible in the case of $f = 1\text{Hz}$ due to long horizontal wave length of 1154m. This observation follows similar observation made many years ago by [Housner \(1957\)](#) for large stiff buildings. Both horizontal and vertical displacements of SMR overlap with corresponding free field response for $f = 1\text{Hz}$. Along with the increase of incident frequency, SSI effects become more significant, especially for the vertical components of displacement and acceleration. In the cases of $f = 2.5\text{Hz}$ and $f = 5\text{Hz}$, horizontal response of SMR is still very close to its free field counterpart, for both displacements and accelerations, however the reduction of vertical response of SMR becomes more significant for frequency of $f = 5\text{Hz}$. For relatively high frequency of $f = 10\text{Hz}$, both horizontal and vertical response of SMR are significantly different from free field modeling in both displacements and accelerations.

The spatial variation of displacements at the surface of free field model and at the same location within SMR model, along the horizontal line through SMR (i.e. $x \in [-75\text{m}, 75\text{m}], y = 0\text{m}, z = 0\text{m}$), at $t = 3.5\text{s}$ are shown in Figure 504.109. It is noted that SMR structure occupies space for $x \in [-15\text{m}, 15\text{m}]$, where flat trace of displacements within a stiff structure is observed. The base slab averaging is observed for higher frequency, shorter wave length cases of $f = 5\text{Hz}$ and $f = 10\text{Hz}$, while it is almost negligible for incident waves at frequencies of $f = 1\text{Hz}$ or $f = 2.5\text{Hz}$ due to the wavelength being longer than object size for those low frequencies.

Similar spatial variation of displacement along the transverse axis (i.e. $x = 0\text{m}, y \in [-75\text{m}, 75\text{m}], z = 0\text{m}$) is shown in Figure 504.110. Since the incident SV wave propagates within the XZ plane, uniform distribution of both horizontal and vertical free field response along the transverse axis (Y axis) is expected and presented in Figure 504.110. However, the existence of SMR alters the original uniform distribution, and a wave field in this, out plane of polarization direction. Significant wave field disturbance effects can be observed within the structure part ($y \in [-15\text{m}, 15\text{m}]$) in the cases of medium ($f = 5\text{Hz}$) to high frequency ($f = 10\text{Hz}$). In other words, 3C dynamic response of soils surrounding the structure has been induced from 2C excitation by an SV wave due to SSI and transverse wave field disturbance effects.

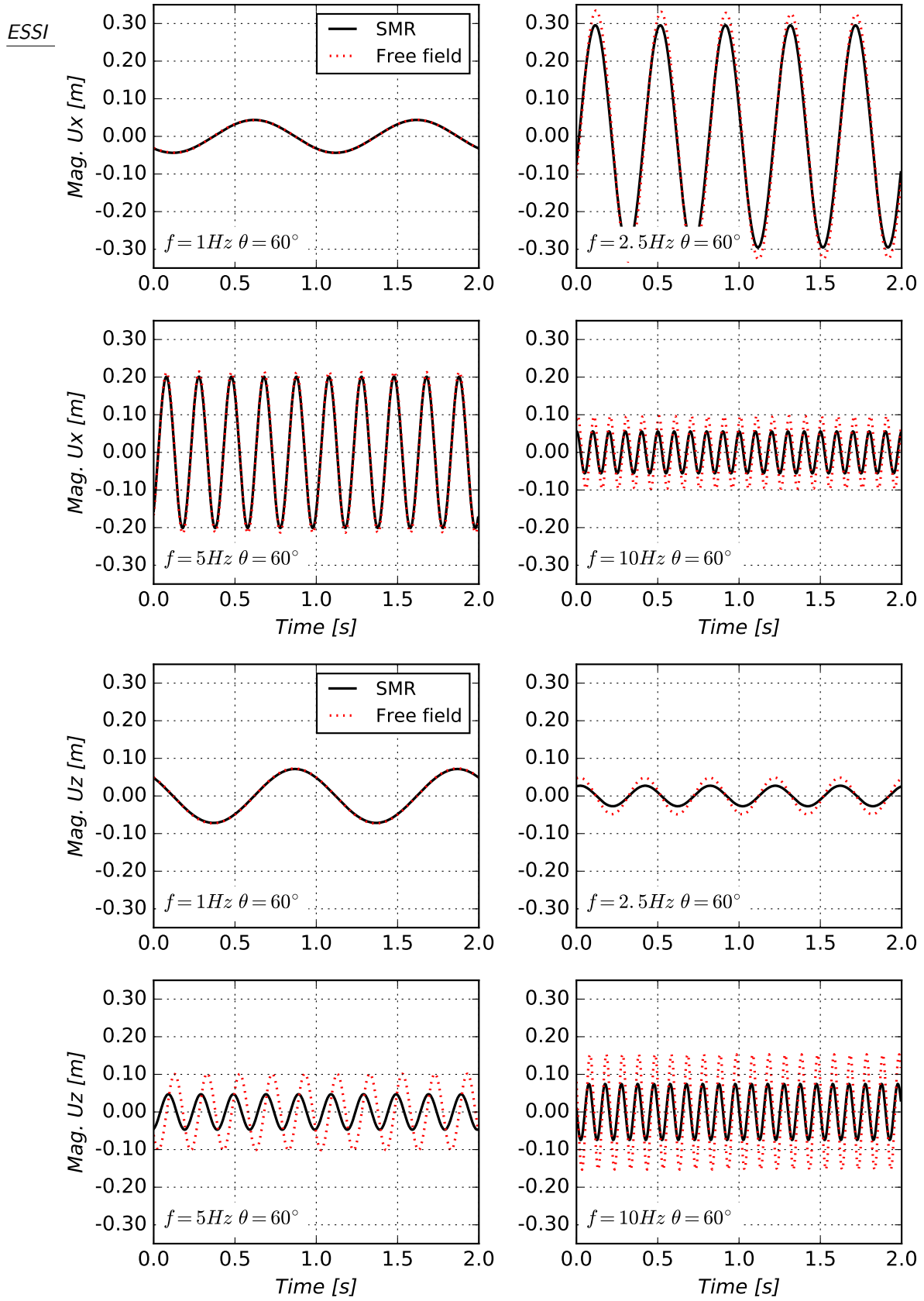


Figure 504.107: Displacement response of point A for scenarios with different frequencies of incident SV wave: (a) Horizontal displacement (b) Vertical displacement.

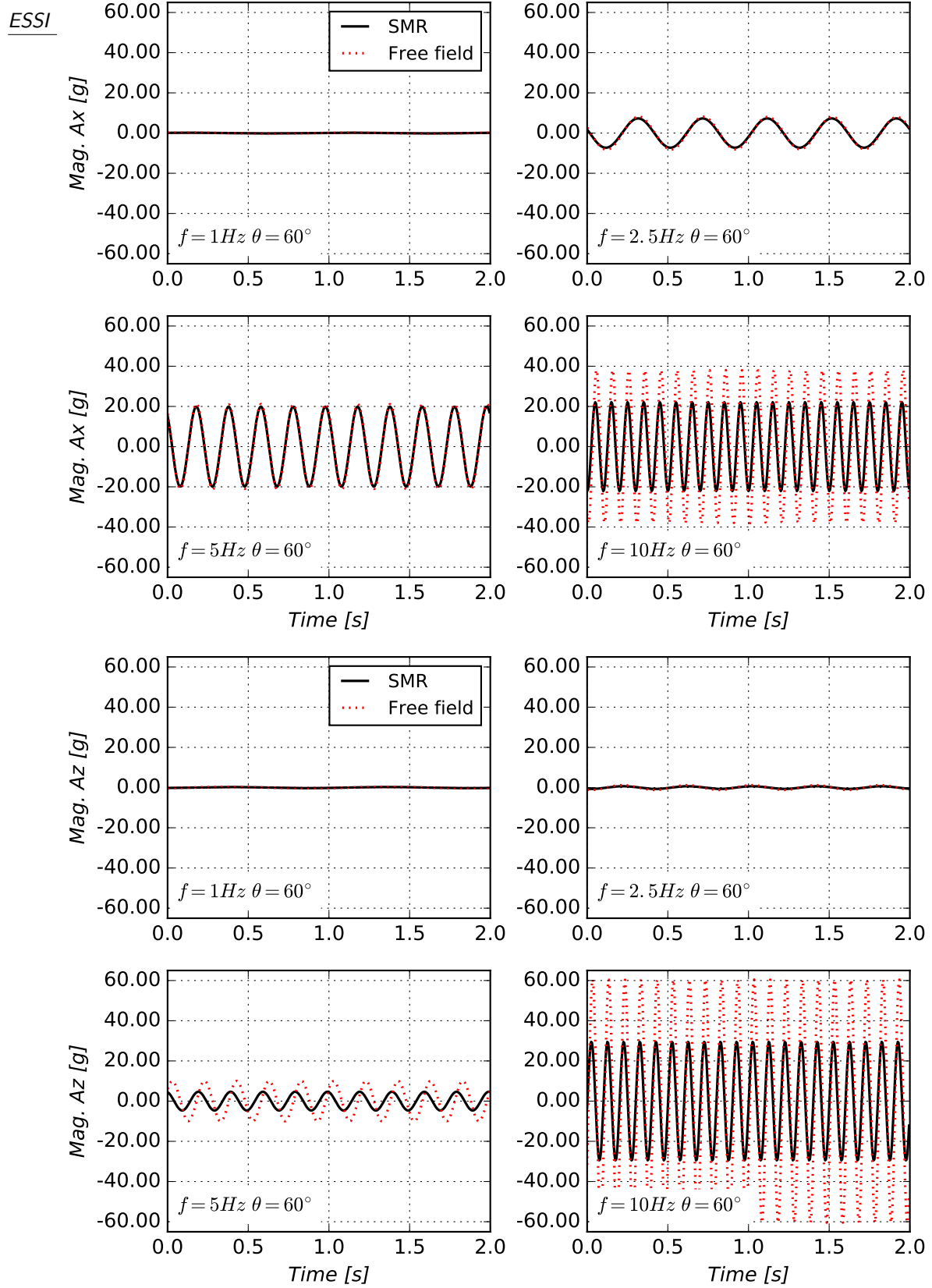


Figure 504.108: Acceleration response of point A for scenarios with different frequencies of incident SV wave: (a) Horizontal acceleration (b) Vertical acceleration.

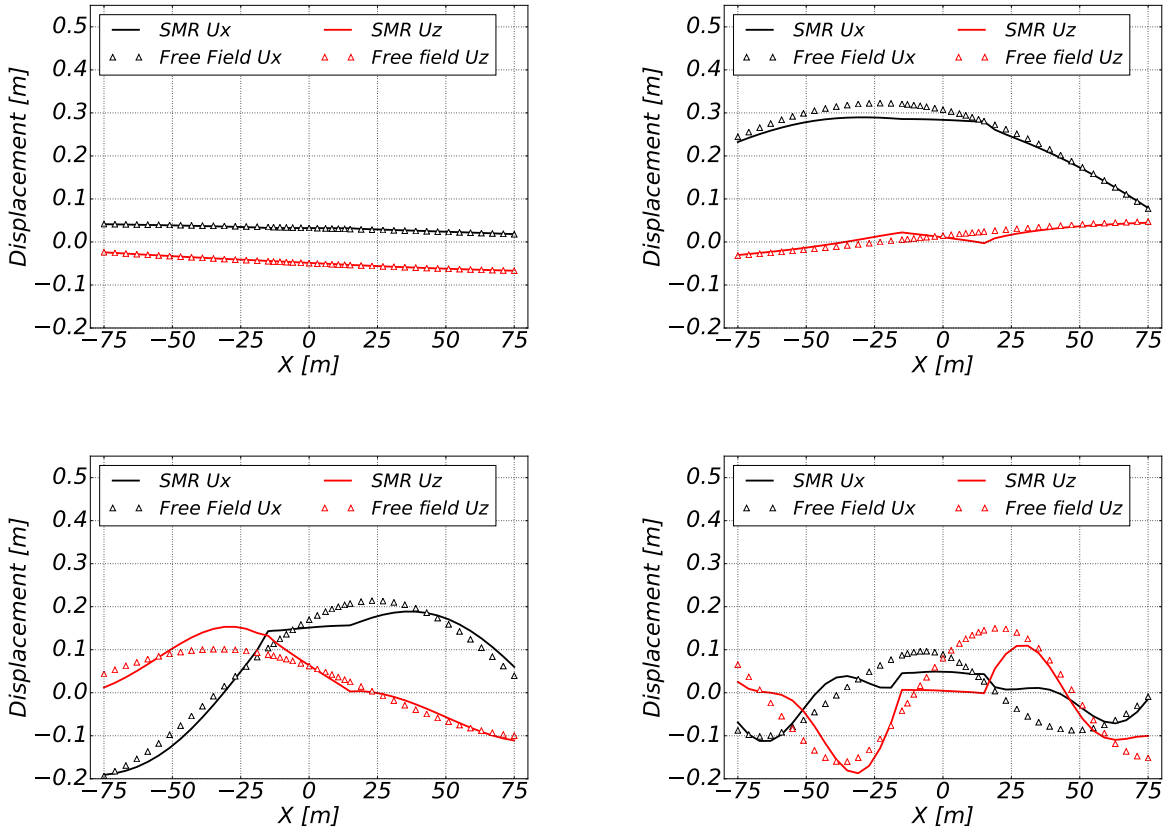


Figure 504.109: Spatial variation of displacement along the horizontal axis at $t = 3.5s$ for a wave at $\theta = 60^\circ$ different incident wave frequencies (a) $f = 1\text{Hz}$ (b) $f = 2.5\text{Hz}$ (c) $f = 5\text{Hz}$ (d) $f = 10\text{Hz}$.

Another important observation from Fig. 504.110(d) is that, although the reduction of displacement amplitude is observed within the structure, in locations where $y \in [-15\text{m}, 15\text{m}]$, near field motions close to the structure can be amplified, for example, motion within region $y \in \pm[25\text{m}, 50\text{m}]$ in this case. This implies that there are potentially significant structure-soil-structure dynamic effects for closely spaced structures.

The deformed shapes of SMR for four frequency scenarios at $t = 0.3s$ with different frequencies are shown in Fig. 504.111. The aforementioned wave field disturbance effects are clearly visible for the low wave length, high frequency case of $f = 10\text{Hz}$. The existence of local structure has significantly altered the near field seismic wave due to strong SSI effect, since wave lengths are shorter than the dominant dimension of the structure.

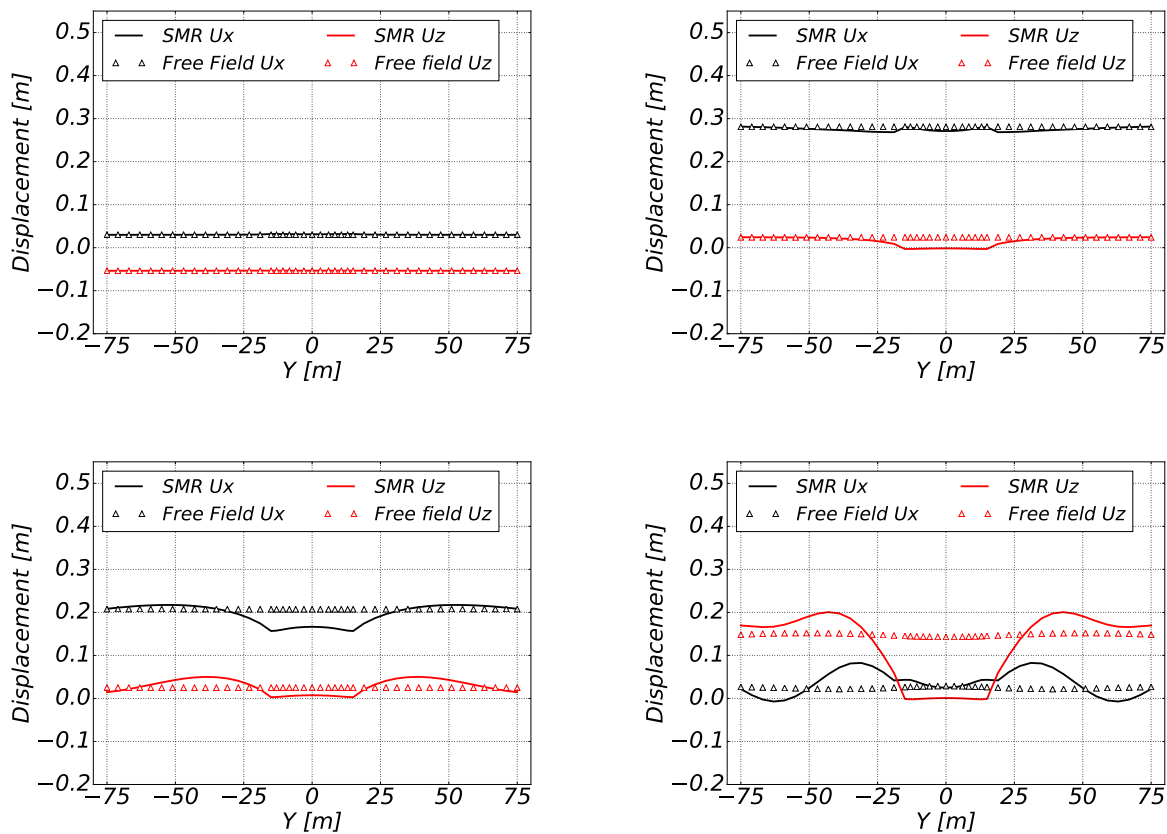


Figure 504.110: Spatial variation of displacement along the transverse axis at $t = 3.5s$ for a wave at $\theta = 60^\circ$ at different incident wave frequency (a) $f = 1\text{Hz}$ (b) $f = 2.5\text{Hz}$ (c) $f = 5\text{Hz}$ (d) $f = 10\text{Hz}$.

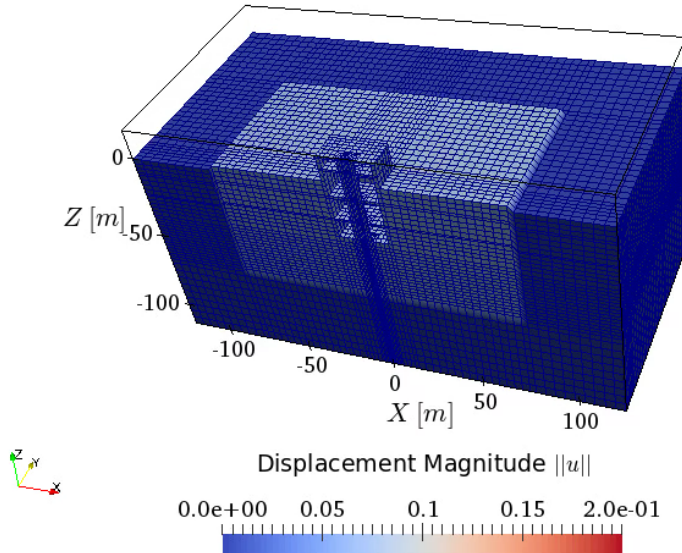
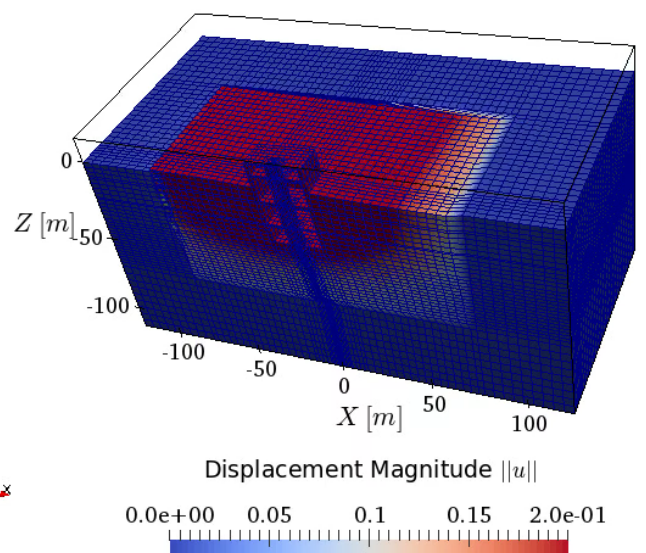
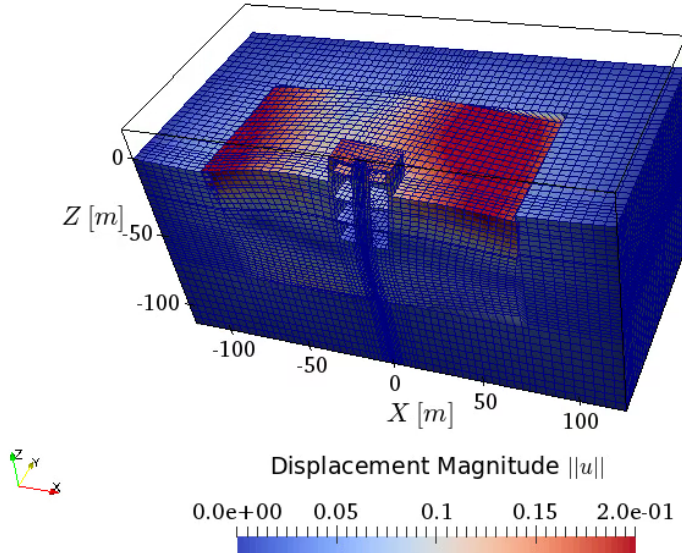
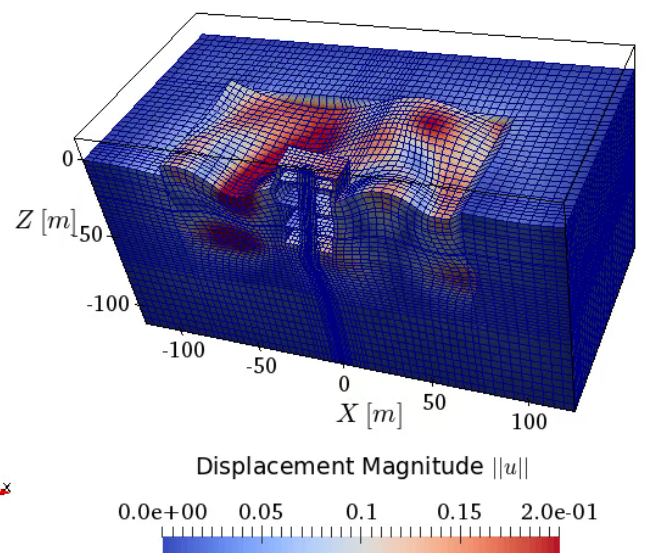
$f = 1\text{Hz}$  $f = 2.5\text{Hz}$  $f = 5\text{Hz}$  $f = 10\text{Hz}$ 

Figure 504.111: The deformed shapes of SMR at $t = 0.3\text{s}$ for four scenarios.

504.9 Three Dimensional (3D) Inelastic Modeling for Structure Soil Structure Interaction

504.10 Case Study of Cruas Nuclear Power Plant under Seismic Load from Le Teil Earthquake

504.10.1 Introduction

Seismic hazard in different regions of Central Europe has been recently revised, see, e.g., (Renault et al., 2013). The studies have been based on the historical evidence, like the earthquake in Basel, Switzerland, in 1356 (Mayer-Rosa and Cadiot, 1979). It turns out that quite a few nuclear facilities are located in areas where a weak to moderate seismic activity has been recorded.

Much effort has lately been put into the assessment of existing nuclear stations and into the design of new ones in these earthquake-prone areas. Hence the knowledge on the mechanical behavior of the so-called *earthquake-soil-structure interaction* (ESSI) systems is currently of significant importance in structural and geotechnical engineering.

The nuclear power plant (NPP) in Cruas is located in the south of France, on the right bank of the Rhône River. This NPP was built in the 1970s and it is seismically isolated at the base. On November 11, 2019, the NPP was excited by an earthquake near Le Teil (Viallet et al., 2022). The resulting ground motions were recorded at different locations, both, near Le Teil and at Cruas NPP. The structural vibrations of the NPP were also measured.

Here, simulation of the ground motions and of the mechanical behavior of the NPP under the earthquake load is conducted. For this purpose, the Real-ESSI Simulator (Jeremić et al., 1988-2025) is used. It is a finite element (FE) system developed to reproduce the behavior of soils and structures, and their interaction, under static and dynamic loads. The results obtained in this research are evaluated by comparison with the available field data. In this way, the current design and assessment of ESSI systems can be validated and possibly improved.

This study is conducted within the *SMATCH benchmark*³ organized by the Institut de Radioprotection et de Sûreté Nucléaire (IRSN), Électricité de France (EDF) and Organisation for Economic Co-operation and Development-Nuclear Energy Agency (OECD-NEA).

³<https://www.smatch-benchmark.org/>

504.10.2 Notation

Bold-face letters, like σ , are vectors or second rank tensors. Sans-serif letters, like E , are fourth rank tensors. Gibbs notation, like $\dot{\sigma} = E : \dot{\epsilon}$, or index notation, $\dot{\sigma}_{ij} = E_{ijkl}\dot{\epsilon}_{kl}$, in the Cartesian coordinate system with usual summation over repeated (dummy) indices is used. The mechanical sign convention is applied to stress, σ , and strain, ϵ , with compression negative.

The basic Latin variables are explained below.

E	Young modulus
f	frequency
\mathbf{u}	displacement
\mathbf{x}	location
V_p	primary, compressional, wave velocity
V_s	secondary, shear, wave velocity

The basic Greek variables are given below.

ϵ	strain
λ, μ	Lamé constants
ν	Poisson ratio
ρ	mass density
σ	stress, tension positive

The following notation is used.

- $\dot{\square}$ material rate of \square , $\dot{\square} = \partial \square / \partial t = \square_t$
- $\ddot{\square}$ material acceleration of \square , $\partial^2 \square / \partial t^2 = \square_{tt}$

The essential abbreviations are listed below.

DRM	Domain Reduction Method
ESSI	Earthquake-Soil-Structure Interaction
FE	Finite Element
NPP	Nuclear Power Plant
THMM	Thomson-Haskell Matrix Method

504.10.3 Le Teil Earthquake

Some basic knowledge about Le Teil earthquake is indispensable to determine the seismic load in the simulation of the mechanical behavior of Cruas NPP. After a brief introduction of the necessary seismological definitions, a short description of the earthquake in Le Teil is given. It will allow to establish the *seismic input* in Section 504.10.7.

504.10.3.1 A Short Résumé on the Seismological Description of Earthquakes

Origins of Earthquakes Tectonic plates, pieces of the Earth's litosphere, move, due to, i.a., the convection in the Earth's mantel (Andel, 2008; Bragg, 2022), and interact with each other at *interfaces*. An interface, also known as a *fault*, between two tectonic plates is rough, jigsaw-like, and the movement of the plates is hindered. This is similar to shearing along a fault in a rock (Wittke, 2014).

During shearing along an interface, the jigsaw-like boundaries of the plates undergo the plastic deformation. Stress at the interface is being increased, which is known as *hardening*, and the *plastic work* is being done at the interface. A part of the plastic work, the so-called *frozen elastic energy*, also known as the *plastic free Helmholtz energy*, is being accumulated at the fault.

When the stress limit is reached, the peak friction is mobilized, at the fault, a sudden, *dynamic*, brittle *slip* occurs and causes an *earthquake*. A slip is a movement of the plates along the interface. A ductile slip is also possible but it is *aseismic* (Kramer, 1996a) and hence it is not considered here. A brittle slip is also called a *rupture*.

The strain is localized along the fault and the stress decreases, which is known as *softening*. The frozen elastic energy accumulated at the interface is transformed into other forms of energy, like *acoustic energy* or heat. In seismology, the origins of earthquakes are explained with the so-called *elastic-rebound theory* (Kramer, 1996a; Bragg, 2022). It is based on the assumption of repeatable accumulation and release of the frozen elastic energy at a fault.

However, an earthquake may also result from various, natural or anthropogenic, events within a single tectonic plate (Kramer, 1996a; Semblat and Pecker, 2009), for example, from a large underground explosion, a volcanic eruption or a slip triggered by *fracking*. A slip may generally occur along, e.g., an interface between two rock masses and not necessarily along an interface between two tectonic plates.

Here, a shallow earthquake, triggered at a depth of less than 5 km, is examined. It was caused by a slip

along a fault in a rock.

Types of Faults A slip is described by jump in displacement $\llbracket \mathbf{u} \rrbracket$ between two rock masses, or two tectonic plates. This $\llbracket \mathbf{u} \rrbracket$ is measured along the slip plane, π . At a fault, discontinuity, in a rock, $\| \llbracket \mathbf{u} \|$ can achieve several kilometers (Wittke, 2014). Two rock masses, or two tectonic plates, can (Wittke, 2014; Bragg, 2022; Andel, 2008):

- slide past each other at a *transform fault*, particularly:
 - in horizontal direction at a *strike-slip fault*, inclined or vertical, Figure 504.112(a)
 - in vertical direction at a *dip-slip fault*, vertical, Figure 504.112(b)
 - in both, horizontal and vertical, directions at an *oblique-slip fault*, vertical, Figure 504.112(c)
- move towards each other, collide, at a *reverse fault*, also called *thrust fault*, inclined or horizontal, Figure 504.112(d)
- move apart from each other at a *normal fault*, inclined or horizontal, Figure 504.112(e).

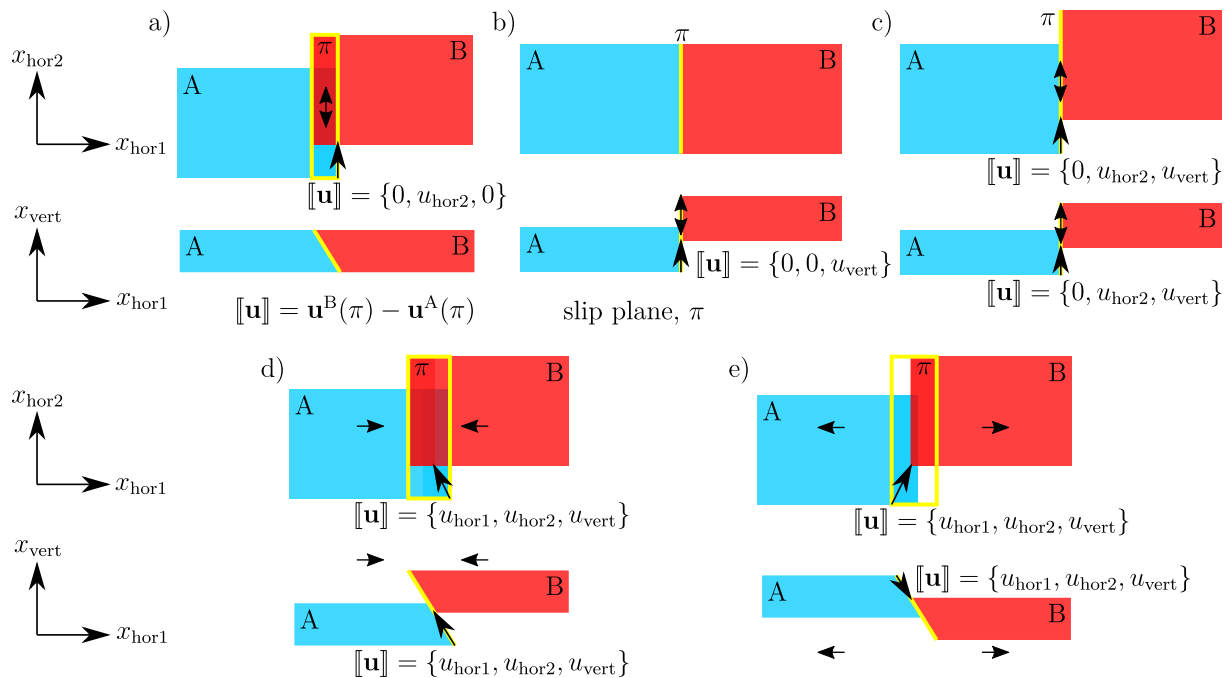


Figure 504.112: Types of faults: a) strike-slip fault, here, inclined; b) dip-slip fault; c) oblique-slip fault; d) reverse fault, here, inclined; e) normal fault, here, inclined.

Mechanism and Orientation of a Slip in a Cartesian Coordinate System Mechanism and orientation of a slip are commonly described in a Cartesian coordinate system using the so-called *focal mechanism*. It is a graphic representation of the slip and it is known in the seismological community as the “beach ball”⁴. A focal mechanism is defined by *strike angle*, *dip angle* and *rake angle* (Aki and Richards, 2002; Wittke, 2014), see Figure 504.113.

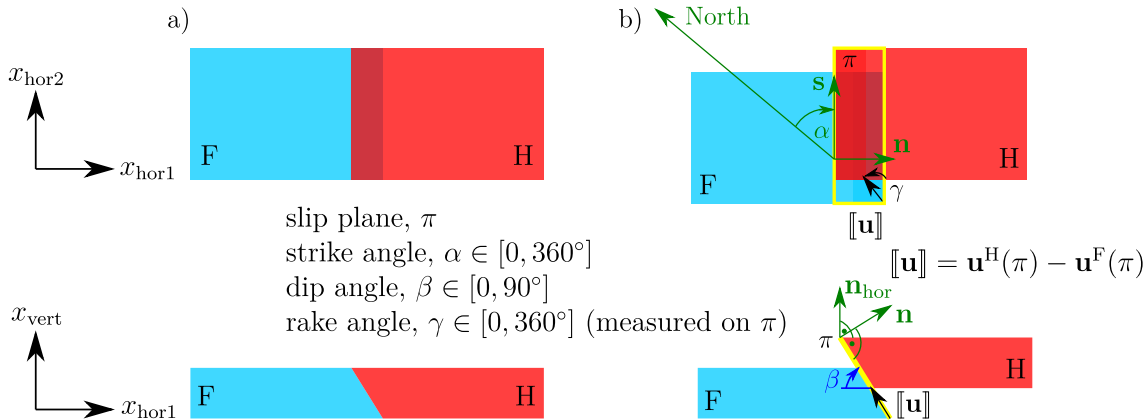


Figure 504.113: a) Inclined fault before a slip; b) Inclined fault after a reverse slip: the slip plane, π , is defined by the unit normal vector, \mathbf{n} , that points upwards; \mathbf{n}_{hor} is a unit vector that is normal to the horizontal plane and points upwards; $\mathbf{s} = (\mathbf{n}_{\text{hor}} \times \mathbf{n})^\rightarrow$; strike angle, $\alpha \in [0, 360^\circ]$, is the azimuth of \mathbf{s} ; dip angle, $\beta \in [0, 90^\circ]$, describes the inclination of π ; rake angle, $\gamma \in [0, 360^\circ]$, is measured anticlock-wise from \mathbf{s} to the jump in displacement, $[\![\mathbf{u}]\!]$, on π . F is the so-called *foot wall* and H is the *hanging wall*.

Strike angle, dip angle and rake angle can be found in MATHEMATICA for a slip plane, π , defined by the unit normal vector, \mathbf{n} , with given displacement of the foot wall, $\mathbf{u}^F(\pi)$, and of the hanging wall, $\mathbf{u}^H(\pi)$, along π .

```
n = Normalize[{1, 1, 1}]; nhor = {0, 0, 1}; s = Normalize[Cross[nhor, n]]; north = {0, 1, 0};
rotclockwise = {{Cos[a], Sin[a], 0}, {-Sin[a], Cos[a], 0}, {0, 0, 1}};
solua = Solve[rotclockwise.north == s, a][[1]] /. C[1] -> 0; (* solve for strike angle *)
rotanticlockwise = {{Cos[a], -Sin[a], 0}, {Cos[a], Sin[a], 0}, {0, 0, 1}}; nprime = (rotanticlockwise.n) /. solua;
solub = Solve[Tan[b] == nprime[[3]]/nprime[[1]], b][[1]] /. C[1] -> 0; (* solve for dip angle *)
uF = {0, 0, 0}; uH = {1, 1, -2}; jump = uH - uF;
solug = Solve[((rotclockwise /. a -> g).jump/Norm[jump])[[1]] == 1, g][[1]] /. C[1] -> 0; (* solve for rake angle *)
```

⁴Focal mechanism is briefly explained under https://www.iris.edu/hq/inclass/animation/focal_mechanisms_explained. Knowing the strike, dip and slip angle, one can easily plot the focal mechanism in MATHEMATICA using the code by Prof. Scherbaum from the University of Potsdam, available on the Internet, <https://demonstrations.wolfram.com/EarthquakeFocalMechanism/>.

```
{a // .solua, b /.solub, Re[g /.solug]} // N (* strike angle, dip angle, rake angle *)
```

504.10.3.2 Slip along Rouvière Fault near Le Teil

Le Teil earthquake was recorded on November 11, 2019 ([Marconato et al., 2022](#); [Ritz et al., 2020](#); [Viallet et al., 2022](#)). This earthquake resulted from a slip along Rouvière fault within the existing les Cévennes faults system in Southern France, near Le Teil, Figure [504.114](#). The slip might have been caused by a reduction of the effective stress at Rouvière fault either due to the increase in the ground water level, caused by a heavy rain, ([Burnol et al., 2023](#)) or due to the progressive unloading of the ground in the nearby quarry ([Novellis et al., 2020](#)).

Basic characteristics of the slip that caused shallow Le Teil earthquake are given in Table [504.7](#) and explained in Figure [504.113](#). The location of the source of the earthquake is shown in Figure [504.114](#).

Table 504.7: Basic characteristics of the slip along Rouvière fault

Latitude °	Longitude °	Depth km	Mw -	Dip angle °	Strike angle °	Rake angle °	Velocity m/s
44.5188 ± 0.01	4.6694 ± 0.01	1 ± 0.5	4.9 ± 0.1	55 ± 5	45 ± 5	90 ± 10	1800

504.10.3.3 Site Description

A number of free-field and in-structure instruments were used to record the seismic motions at Cruas NPP, the local site, and near Le Teil. The data are accessed via the SMATCH project. Unfortunately, the elastic soil and rock parameters are available at the epicenter of the earthquake and at two locations at the local site only.

Locations of the Free-field Recordings Locations of the free-field instruments are given in Table [504.8](#) and shown in Figure [504.114](#). In-structure recordings are discussed in Section [504.10.6](#).

Elastic Soil and Rock Parameters The elastic soil and rock parameters at station 1 and station 2, at Cruas NPP, and at the epicenter of the earthquake are given in Table [504.9](#). The elevations at station 1 and 2 are given in Table [504.8](#). The elevation of the epicenter, ≈ 260 m, can be estimated using, e.g., an online map with elevation contours.

Table 504.8: Locations of the free-field instruments at Cruas NPP and near Le Teil

Station	Latitude °	Longitude °	Elevation m
1	44.636253	4.758796	77
2	44.630001	4.753816	80.5
3	44.37408	4.76974	90
4	44.307	4.689	46
5	44.3561	4.8572	141.2
6	44.324346	4.73236	68

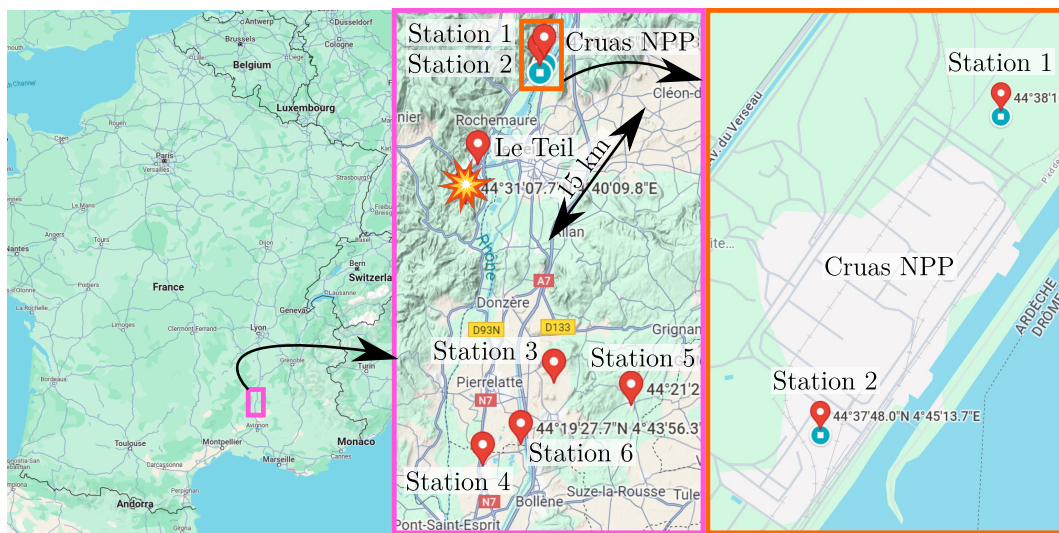


Figure 504.114: Locations of the free-field instruments near Le Teil and at Cruas NPP and location of the source of the earthquake

Table 504.9: Elastic soil and rock parameters at station 1 and station 2, at Cruas NPP, and at the epicenter of the earthquake

Station 1				Station 2				Epicenter of the earthquake			
z	ρ	V_s	ν	z	ρ	V_s	ν	z	ρ	V_s	ν
m	kg/m ³	m/s	-	m	kg/m ³	m/s	-	m	kg/m ³	m/s	-
0	1988	300	0.48	0	2039	300	0.48	0	2500	2047	0.21
1	1978	160	0.45								
3	2141	450	0.45								
7	2350	800	0.45	6.5	1937	180	0.45				
				7.5	2141	450	0.45				
				12.5	2500	1600	0.4				
17	2500	1600	0.4								
62	2500	60 + 23.7 z	0.4	65.5	2500	60 + 23.7 z	0.4				
100	2500	2500	0.4	103.5	2500	2500	0.4				
				628	2600	3645	0.21				
				1197	2300	1200	0.20				
				1416	2500	2291	0.22				
				2026	2500	2314	0.23				
				2194	2600	3457	0.23				
				5956	2600	3616	0.21				

504.10.4 FE Simulation of Ground Motions from Le Teil Earthquake

Ground motions from Le Teil earthquake had been intensively studied within the SIGMA2 project⁵ (Viallet et al., 2022). Two kinds of methods for the simulation of seismic motions had been used, that is, the empirical ones and the physically based ones. The latter include both 1D (Fasan, 2016; Fasan et al., 2016; Hassan et al., 2020; Magrin et al., 2016; Magrin, 2012; Panza et al., 2012) and 3D (Mazzieri et al., 2013; Paolucci et al., 2020, 2021) simulations. Some recent 3D numerical calculations of seismic motions from Le Teil earthquake are reported in (Lehmann et al., 2023; Smerzini et al., 2023).

Elastic soil and rock parameters are available at three locations only, see Table 504.9. This scarcity of data alone precludes a realistic FE reproduction of Le Teil earthquake. Different assumptions about the regional geology could be made, of course. Then, a parametric back-analysis of the earthquake could be conducted to match the measured ground motions. However, such analysis would require a very large FE domain to avoid the corruption of the obtained results by an unreal behavior at the model boundaries, which generally cannot be avoided, see, e.g., (Baffet et al., 2012). It is well-known that in dynamics a parametric FE calculation with a large spatial domain involves a considerable computation time.

Here, we aim to save the computation time. For this purpose, we make a few physically justified simplifying assumptions about the ground motions from Le Teil earthquake. Based on these assumptions, the seismic input will be determined and used in a computationally efficient simulation of the mechanical behavior of Cruas NPP, Section 504.10.7. To establish the necessary assumptions, we first conduct a preliminary FE calculation of the seismic wave field from Le Teil earthquake using the Real-ESSI Simulator (Jeremić et al., 1988-2025).

504.10.4.1 Preliminary 2D Simulation of Le Teil Earthquake

In the case of a shallow earthquake, the incident angle larger than the critical angle, $\alpha_i > \alpha_{ic}$, see (504.13) and (504.14), should be expected at the ground surface. Such $\alpha_i > \alpha_{ic}$ results in a *Rayleigh* wave, see, e.g., (Nowacki, 1974).

A preliminary simulation of the earthquake in Le Teil is performed and used to examine the possible presence of a Rayleigh wave. The calculated ground motions will be validated by a qualitative comparison with the field measurements.

⁵<https://www.sigma-2.net/>

The geometry, geology, material description and mechanism of the slip are simplified. The FE model represents $2000 \times 1 \times 300 \text{ m}^3$ ground with a 280 m thick rock that is overlayed by a 20 m thick soil, see Figure 504.115, cf. Table 504.9.

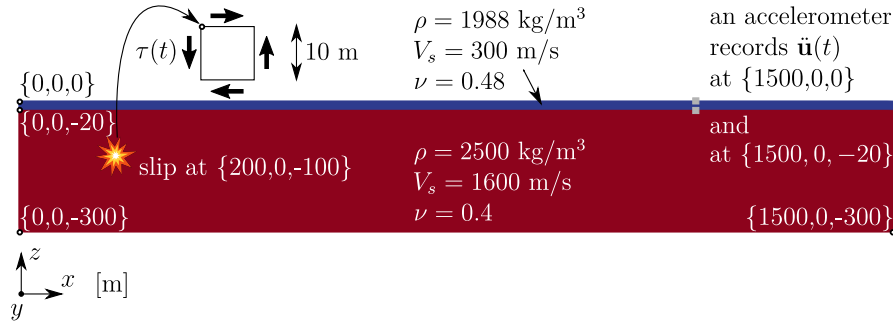


Figure 504.115: FE model used in the preliminary 2D simulation of Le Teil earthquake

Both materials are isotropic linear elastic with parameters given in Table 504.10 (with Young modulus $E = 2\rho V_s^2(1 + \nu)$).

Table 504.10: Material properties in preliminary 2D simulation of Le Teil earthquake

Material	z m	ρ kg/m^3	V_s m/s	ν
Soil	[0, -20]	1988	300	0.48
Rock	[-20, -300]	2500	1600	0.4

The ground is discretized into a single layer (in y direction, Figure 504.115) of 6000 27NodeBrick elements. The size of the element is 10 m.

The slip is simulated as the *pure shear* of an element at $x = \{200, 0, -100\}$. The dynamic disturbance is introduced onto faces of the element in the form of a shear load, $\tau(t) = \tau^{\text{ampl}} \sin(2\pi ft)$ with $\tau^{\text{ampl}} = -60 \text{ GPa}$ and the frequency $f = 1 \text{ Hz}$.

Newmark integration procedure is used in search of the dynamic equilibrium. Numerical damping is introduced using parameters $\gamma = 0.6$ and $\beta = 0.3025$ in the Newmark algorithm.

Time functions of the horizontal displacement, $u_x(t)$, and the vertical displacement, $u_z(t)$, at the ground

surface, $\mathbf{x} = \{1500, 0, 0\}$ m, and at the top of the rock layer, $\mathbf{x} = \{1500, 0, -20\}$ m, are plotted in Figure 504.116(a) and in Figure 504.117(a), respectively. Additionally, the corresponding hodographs, $u_z(u_x)$, are shown in Figure 504.116(b) and in Figure 504.117(b). The horizontal ground acceleration, $\ddot{u}_x(t)$, and the vertical ground acceleration, $\ddot{u}_z(t)$, at $\mathbf{x} = \{1500, 0, 0\}$ m and at $\mathbf{x} = \{1500, 0, -20\}$ m are plotted in Figure 504.118(a) and in Figure 504.119(a). The corresponding diagrams $\ddot{u}_z(\ddot{u}_x)$ are shown in Figure 504.118(b) and in Figure 504.119(b).

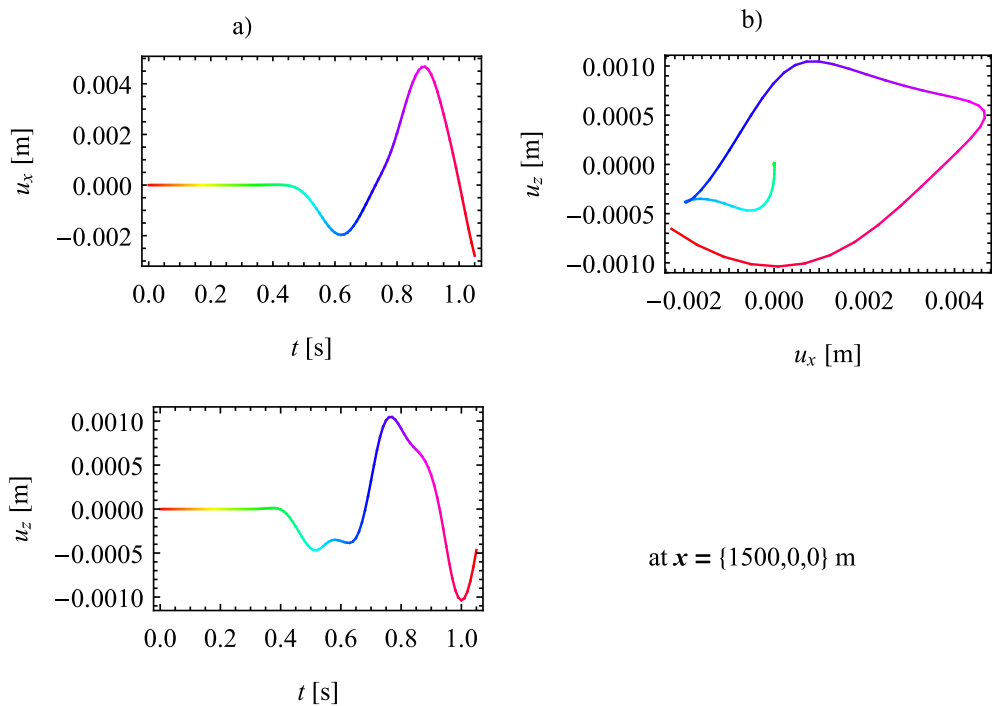


Figure 504.116: Preliminary 2D simulation of Le Teil earthquake: a) $u_x(t)$ and $u_z(t)$, and b) $u_z(u_x)$ at the ground surface, $\mathbf{x} = \{1500, 0, 0\}$ m

Judging by the hodograph from Figure 504.116(b), the motions at the ground surface can be interpreted as a Rayleigh wave, a surface wave. It is probably overlapped by the Stoneley wave from Figure 504.117(b) which propagates along the interface between the soil and the rock.

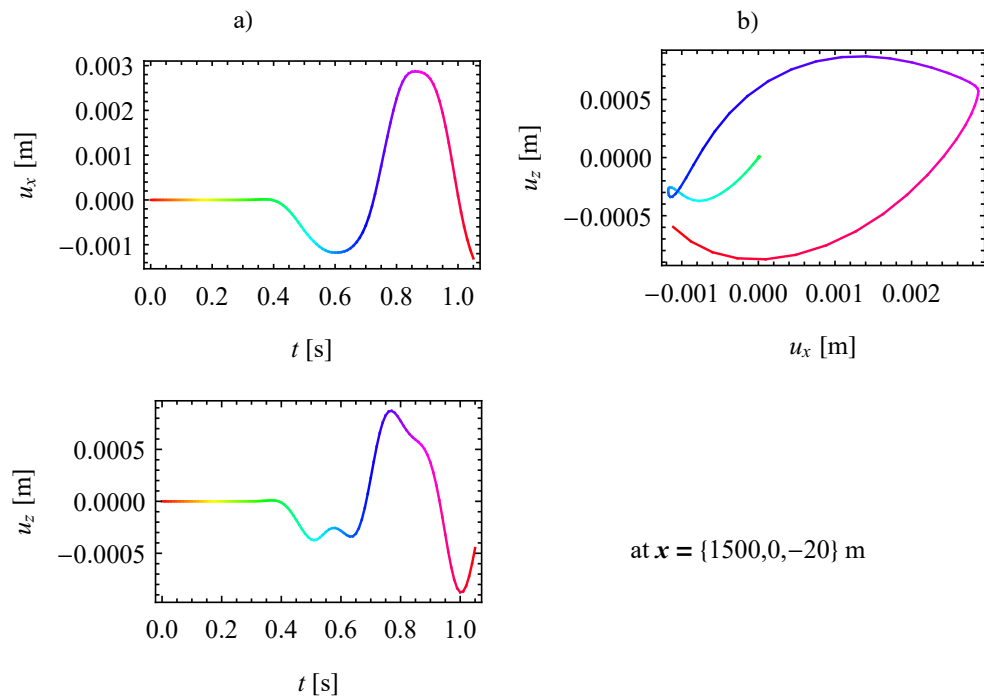


Figure 504.117: Preliminary 2D simulation of Le Teil earthquake: a) $u_x(t)$ and $u_z(t)$, and b) $u_z(u_x)$ at the top of the rock layer, $x = \{1500, 0, -20\}$ m

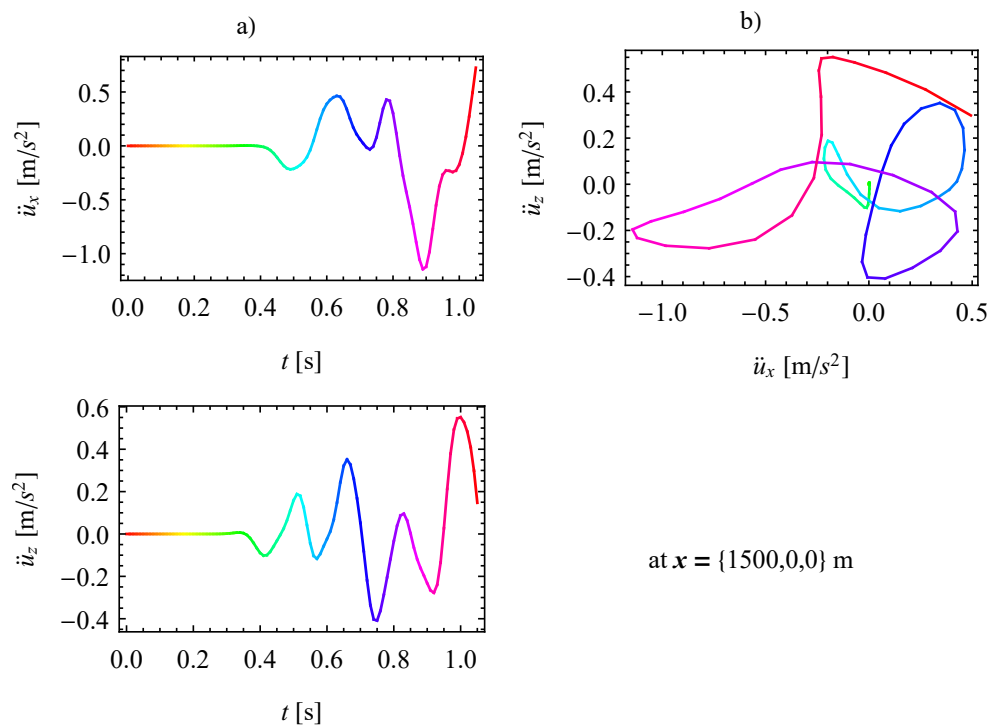


Figure 504.118: Preliminary 2D simulation of Le Teil earthquake: a) $\ddot{u}_x(t)$ and $\ddot{u}_z(t)$, and b) $\ddot{u}_z(\ddot{u}_x)$ at the ground surface, $x = \{1500, 0, 0\}$ m

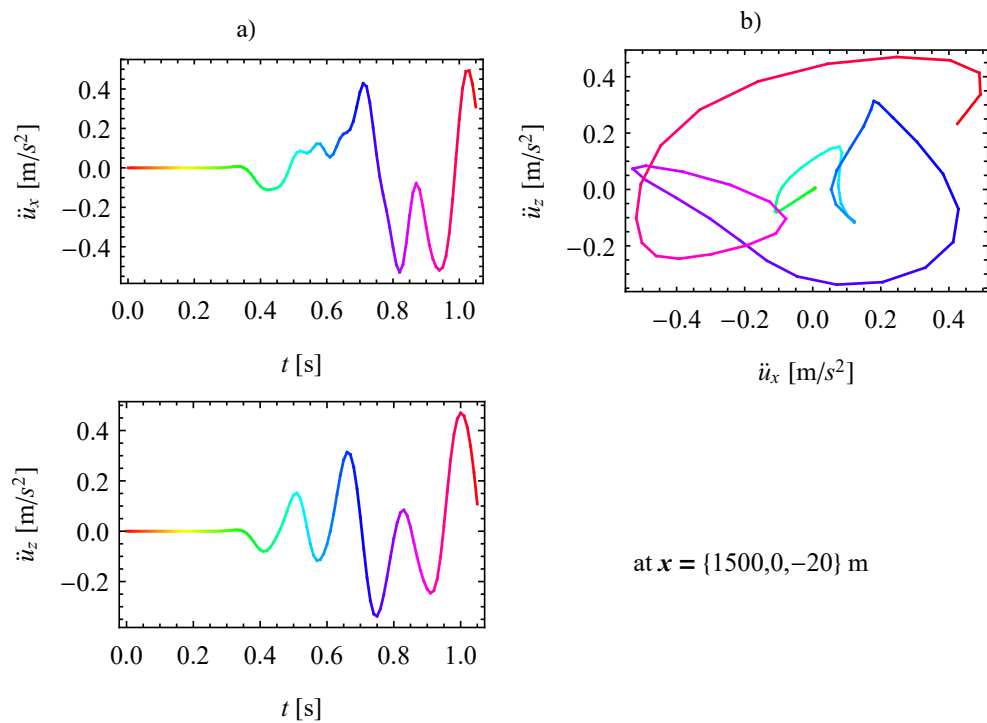
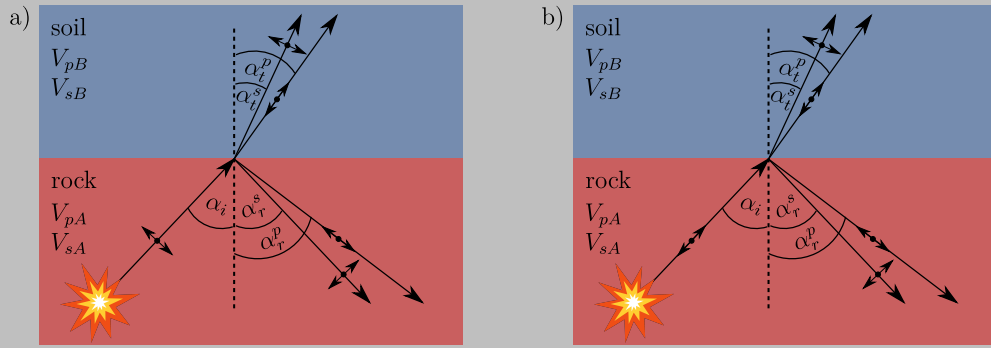


Figure 504.119: Preliminary 2D simulation of Le Teil earthquake: a) $\ddot{u}_x(t)$ and $\ddot{u}_z(t)$, and b) $\ddot{u}_z(\ddot{u}_x)$ at the top of the rock layer, $x = \{1500, 0, -20\}$ m

Some “unreal” *reflections* and *refractions* of the waves, at the bottom and side boundaries of the model, are present in the simulation due to the very small size of the model. Reflection and refraction of a wave is governed by the *Snell law*. It is assumed that the “unreal” waves do not corrupt the preliminary results significantly.

Let us consider a 2D S-wave, see Figure (a) below, or a 2D P-wave, Figure (b) below, that travels from the source, through the rock.



The incident wave arrives at the interface between the rock and the soil at an incident angle, $\alpha_i \in [0, 90^\circ]$, and it is *reflected* and *refracted*. Component of the wave that is normal to the interface is reflected back into the rock at α_r^P and transmitted, refracted, into the soil at α_t^P as a P-wave. Component tangent to the interface is reflected back into the rock at α_r^S and transmitted into the soil at α_t^S as a S-wave.

According to the Snell law, the following holds

$$\begin{aligned} \frac{\sin \alpha_i}{V_{sA}} &= \frac{\sin \alpha_r^P}{V_{pA}} = \frac{\sin \alpha_r^S}{V_{sA}} = \frac{\sin \alpha_t^P}{V_{pB}} = \frac{\sin \alpha_t^S}{V_{sB}} && \text{for the incident wave being a S-wave and} \\ \frac{\sin \alpha_i}{V_{pA}} &= \frac{\sin \alpha_r^P}{V_{pA}} = \frac{\sin \alpha_r^S}{V_{sA}} = \frac{\sin \alpha_t^P}{V_{pB}} = \frac{\sin \alpha_t^S}{V_{sB}} && \text{for the incident wave being a P-wave,} \end{aligned} \quad (504.11)$$

wherein

$$V_p = \sqrt{\frac{\lambda}{\rho} + 2V_s^2} \quad \text{with} \quad \lambda = \frac{E\nu}{(1+\nu)(1-2\nu)} \quad (504.12)$$

and V_{pA}, V_{sA} denote the wave velocities in material from which a wave arrives at the interface and V_{pB}, V_{sB} denote the wave velocities in material into which the wave is transmitted.

Additionally, one defines the so-called *critical angle*, α_{ic} . It is the incident angle for which the incident

wave is transmitted or reflected parallel to the interface between two layers, here, rock and soil,

$$\begin{aligned}\sin \alpha_{ic}^{spp} &= \frac{V_{sA}}{V_{pA}} \quad \text{with} \quad \alpha_r^p = 90^\circ \quad \text{and} \quad V_{sA} < V_{pA} \quad \text{for an incident S-wave reflected as the P-wave} \\ \sin \alpha_{ic}^{stp} &= \frac{V_{sA}}{V_{pB}} \quad \text{with} \quad \alpha_t^p = 90^\circ \quad \text{and} \quad V_{sA} \leq V_{pB} \quad \text{for an incident S-wave transmitted as the P-wave} \\ \sin \alpha_{ic}^{sts} &= \frac{V_{sA}}{V_{sB}} \quad \text{with} \quad \alpha_t^s = 90^\circ \quad \text{and} \quad V_{sA} \leq V_{sB} \quad \text{for an incident S-wave transmitted as the S-wave}\end{aligned}\tag{504.13}$$

and

$$\begin{aligned}\sin \alpha_{ic}^{ptp} &= \frac{V_{pA}}{V_{pB}} \quad \text{with} \quad \alpha_t^p = 90^\circ \quad \text{and} \quad V_{pA} \leq V_{pB} \quad \text{for an incident P-wave transmitted as the P-wave} \\ \sin \alpha_{ic}^{pts} &= \frac{V_{pA}}{V_{sB}} \quad \text{with} \quad \alpha_t^s = 90^\circ \quad \text{and} \quad V_{pA} \leq V_{sB} \quad \text{for an incident P-wave transmitted as the S-wave.}\end{aligned}\tag{504.14}$$

If the incident angle, α_i , exceeds the critical angle, α_{ic} , it follows that

$$\sin \alpha_i > \sin \alpha_{ic} \quad \text{with} \quad V_A \leq V_B \quad \frac{V_A}{V_B} \sin \alpha_t > \frac{V_A}{V_B} \quad \sin \alpha_t > 1\tag{504.15}$$

for transmission of the incident wave from layer A to layer B or, analogously,

$$\sin \alpha_i > \sin \alpha_{ic} \quad \text{with} \quad V_{sA} < V_{pA} \quad \frac{V_{sA}}{V_{pA}} \sin \alpha_r^p > \frac{V_{sA}}{V_{pA}} \quad \sin \alpha_r^p > 1\tag{504.16}$$

for reflection of the incident S-wave as the P-wave in layer A. If (504.15) or (504.16) holds, then an interface wave is present, e.g., the *Rayleigh wave*.

504.10.5 Validation of the Preliminary 2D Simulation of Le Teil Earthquake

Ground accelerations at station 1, at Cruas NPP, see Table 504.8 and Figure 504.114, are plotted as time functions, $\ddot{u}_{NS}(t)$, $\ddot{u}_{EW}(t)$, $\ddot{u}_{UD}(t)$, in Figure 504.120(a). Indices NS, EW and UD denote the North-South, East-West and up-down components of $\ddot{\mathbf{u}}$, respectively. Accelerations $\ddot{u}_{NS}(t)$, $\ddot{u}_{EW}(t)$, $\ddot{u}_{UD}(t)$ were integrated over time t into displacements u_{NS} , u_{EW} , u_{UD} . Functions $u_{NS}(t)$, $u_{EW}(t)$, $u_{UD}(t)$ are given in Figure 504.120(b).

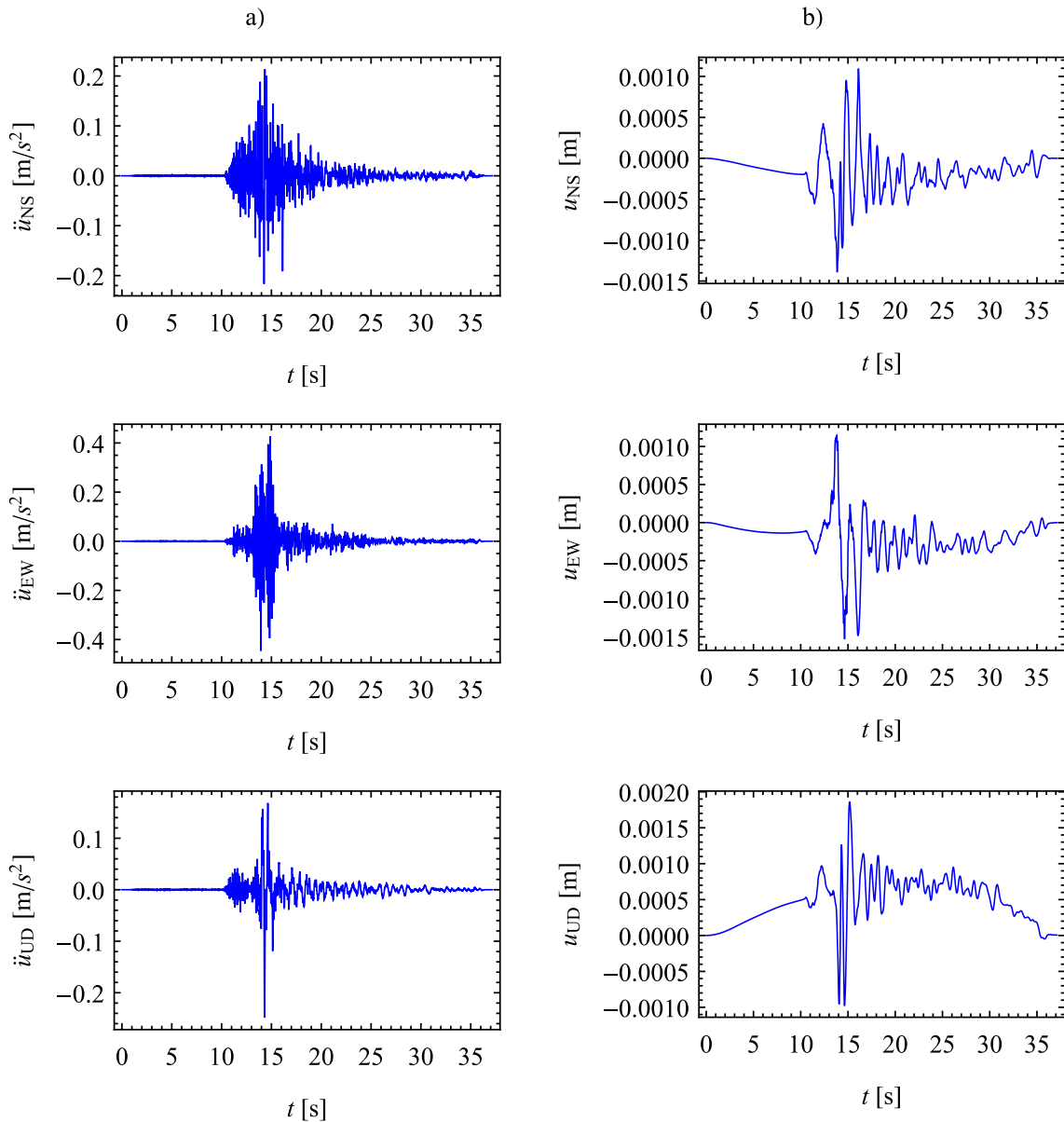


Figure 504.120: Ground motions from Le Teil earthquake recorded at station 1, at Cruas NPP: a) accelerations $\ddot{u}_{\text{NS}}(t)$, $\ddot{u}_{\text{EW}}(t)$, $\ddot{u}_{\text{UD}}(t)$ and b) displacements $u_{\text{NS}}(t)$, $u_{\text{EW}}(t)$, $u_{\text{UD}}(t)$.

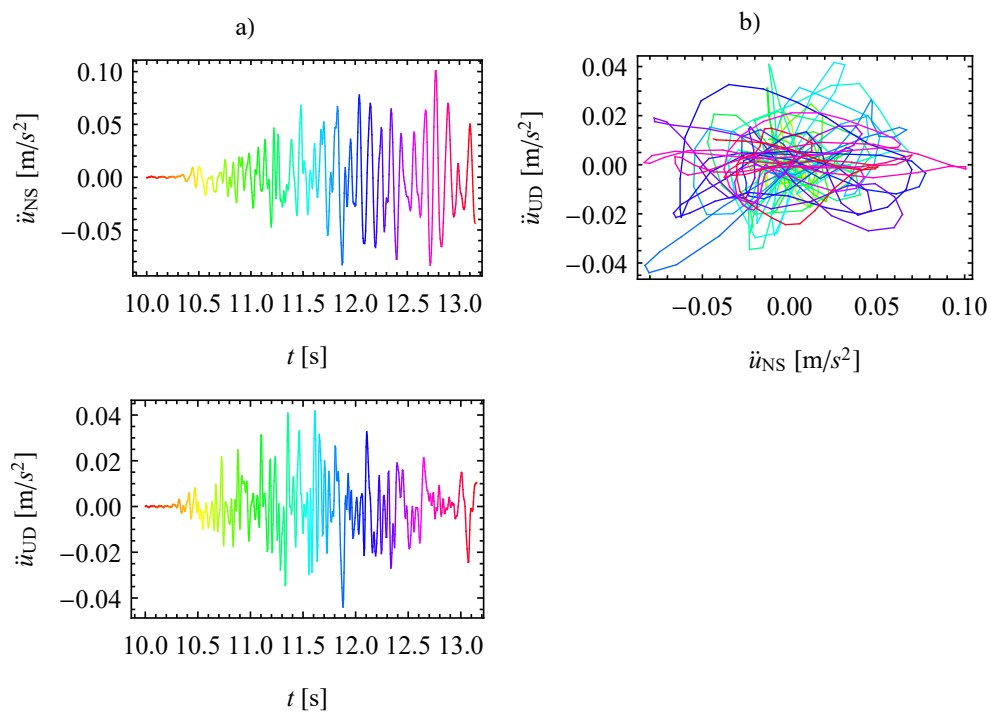


Figure 504.121: Ground accelerations from Le Teil earthquake recorded at station 1, at Cruas NPP, for $t \in [10, 13.15]$ s: a) $\ddot{u}_{NS}(t)$, $\ddot{u}_{UD}(t)$ and b) $\ddot{u}_{UD}(\ddot{u}_{NS})$.

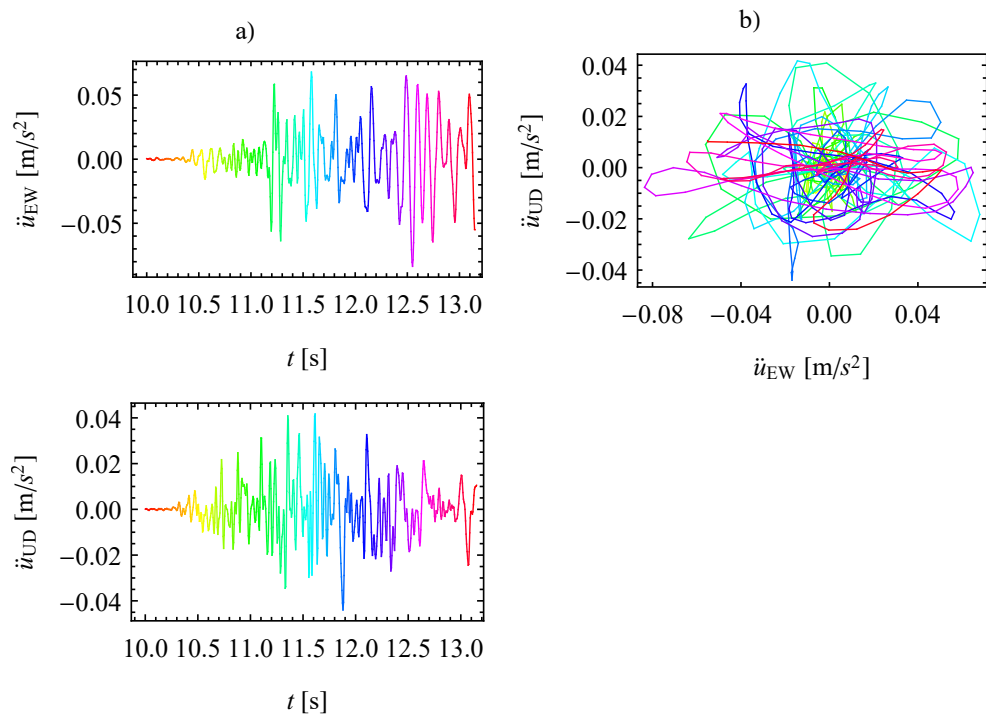


Figure 504.122: Ground accelerations from Le Teil earthquake recorded at station 1, at Cruas NPP, for $t \in [10, 13.15]$ s: a) $\ddot{u}_{EW}(t), \ddot{u}_{UD}(t)$ and b) $\ddot{u}_{UD}(\ddot{u}_{EW})$.

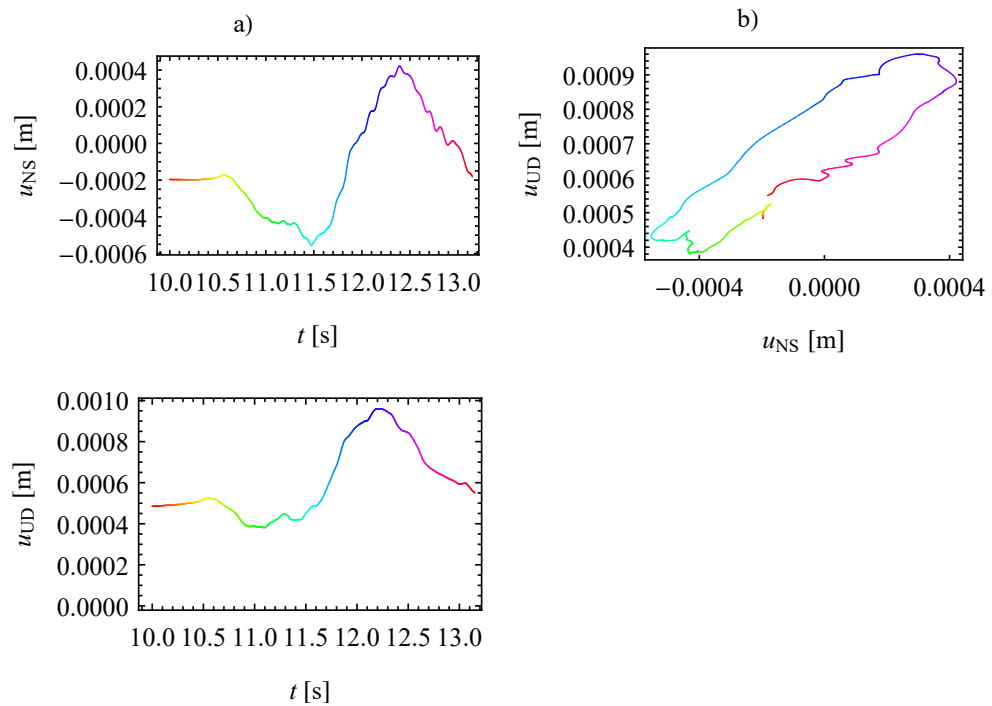


Figure 504.123: Ground displacements from Le Teil earthquake recorded at station 1, at Cruas NPP, for $t \in [10, 13.15]$ s: a) $u_{NS}(t)$, $u_{UD}(t)$ and b) $u_{UD}(u_{NS})$.

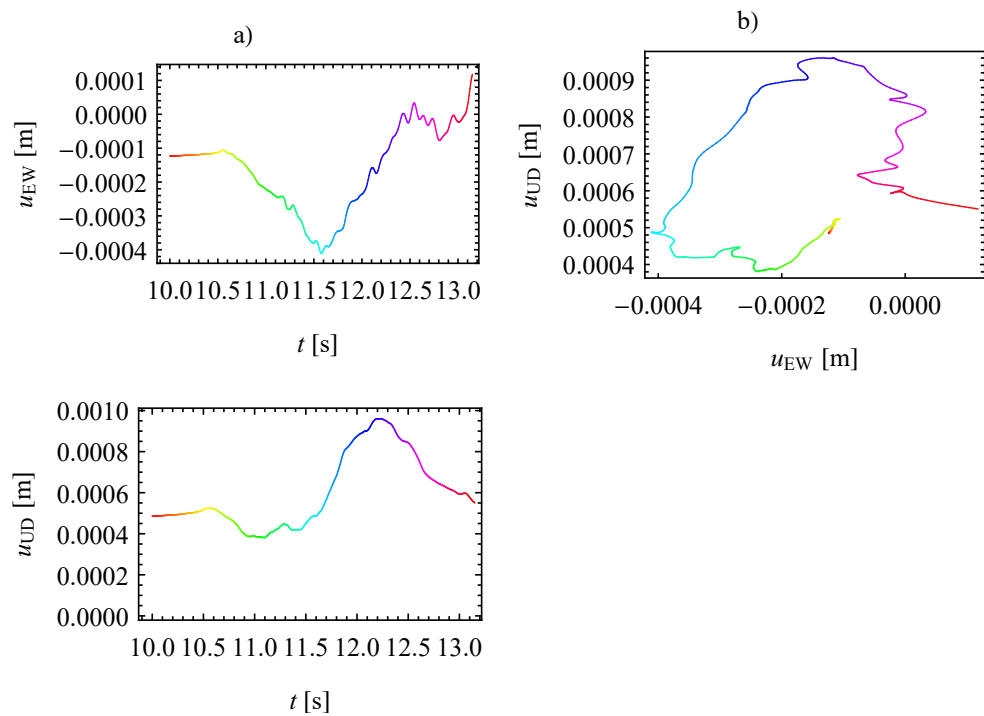


Figure 504.124: Ground displacements from Le Teil earthquake recorded at station 1, at Cruas NPP, for $t \in [10, 13.15]$ s: a) $u_{\text{EW}}(t)$, $u_{\text{UD}}(t)$ and b) $u_{\text{UD}}(u_{\text{EW}})$.

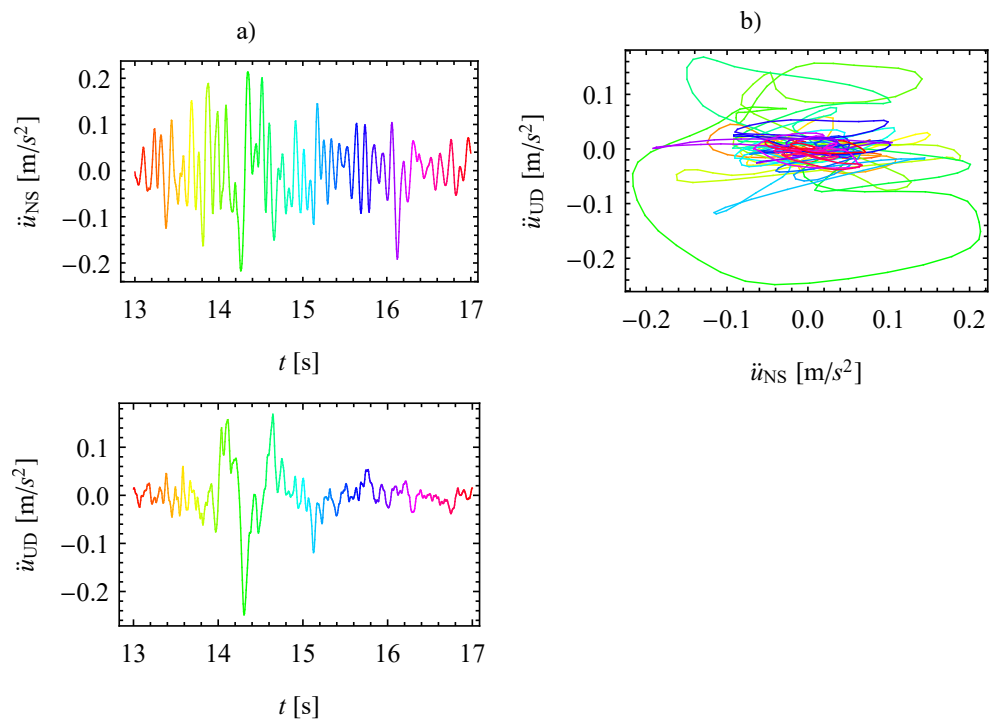


Figure 504.125: Ground accelerations from Le Teil earthquake recorded at station 1, at Cruas NPP, for $t \in [13, 17]$ s: a) $\ddot{u}_{NS}(t)$, $\ddot{u}_{UD}(t)$ and b) $\ddot{u}_{UD}(\ddot{u}_{NS})$.

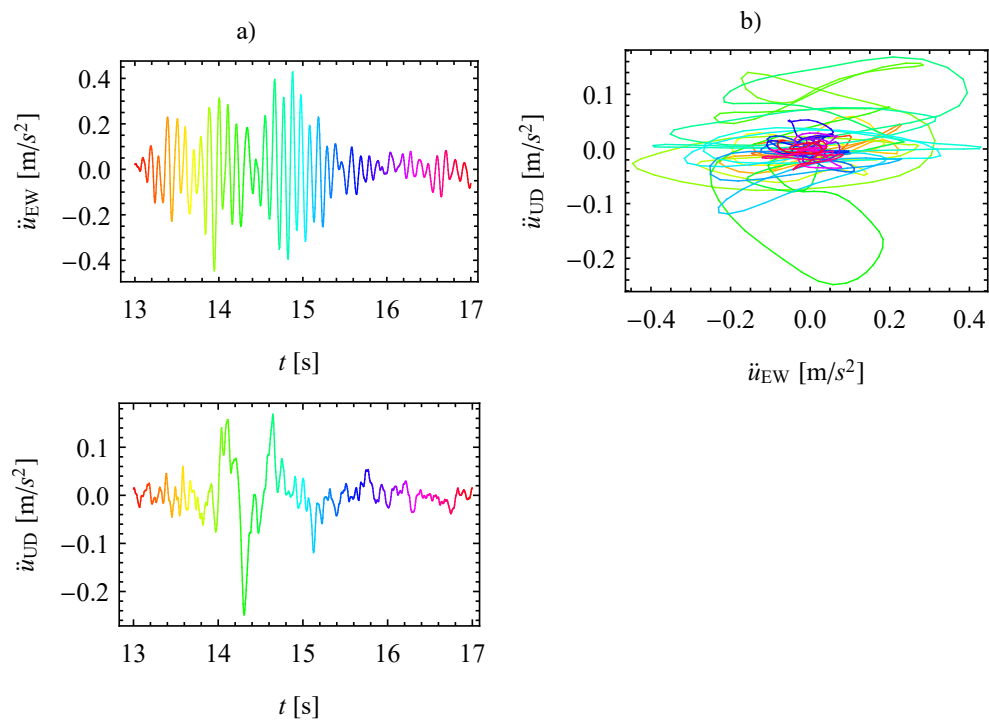


Figure 504.126: Ground accelerations from Le Teil earthquake recorded at station 1, at Cruas NPP, for $t \in [13, 17]$ s: a) $\ddot{u}_{\text{EW}}(t), \ddot{u}_{\text{UD}}(t)$ and b) $\ddot{u}_{\text{UD}}(\ddot{u}_{\text{EW}})$.

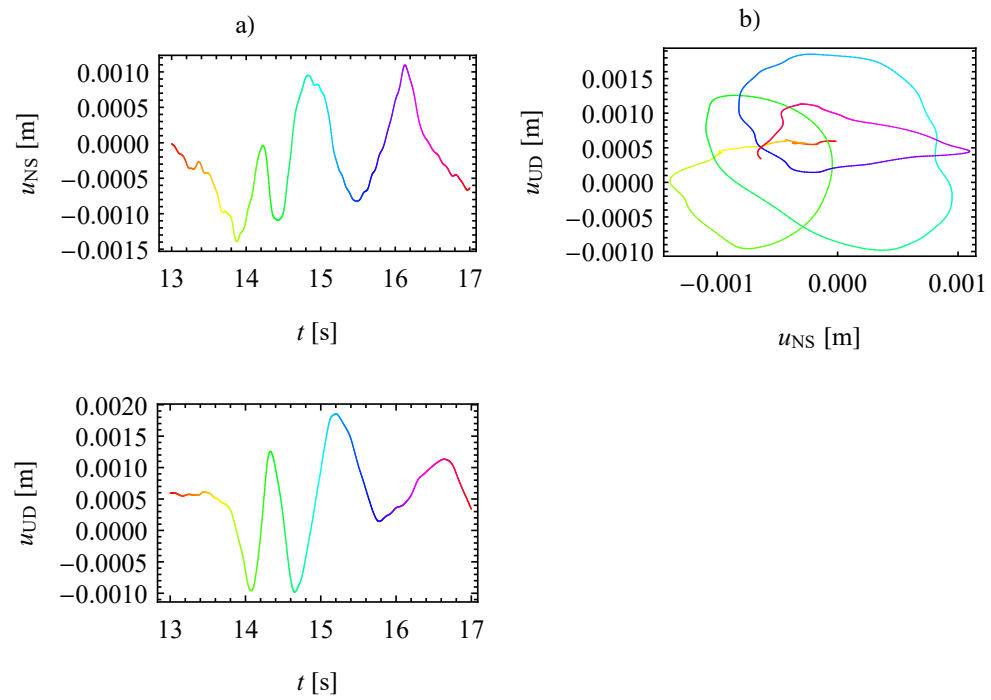


Figure 504.127: Ground displacements from Le Teil earthquake recorded at station 1, at Cruas NPP, for $t \in [13, 17]$ s: a) $u_{NS}(t)$, $u_{UD}(t)$ and b) $u_{UD}(u_{NS})$.

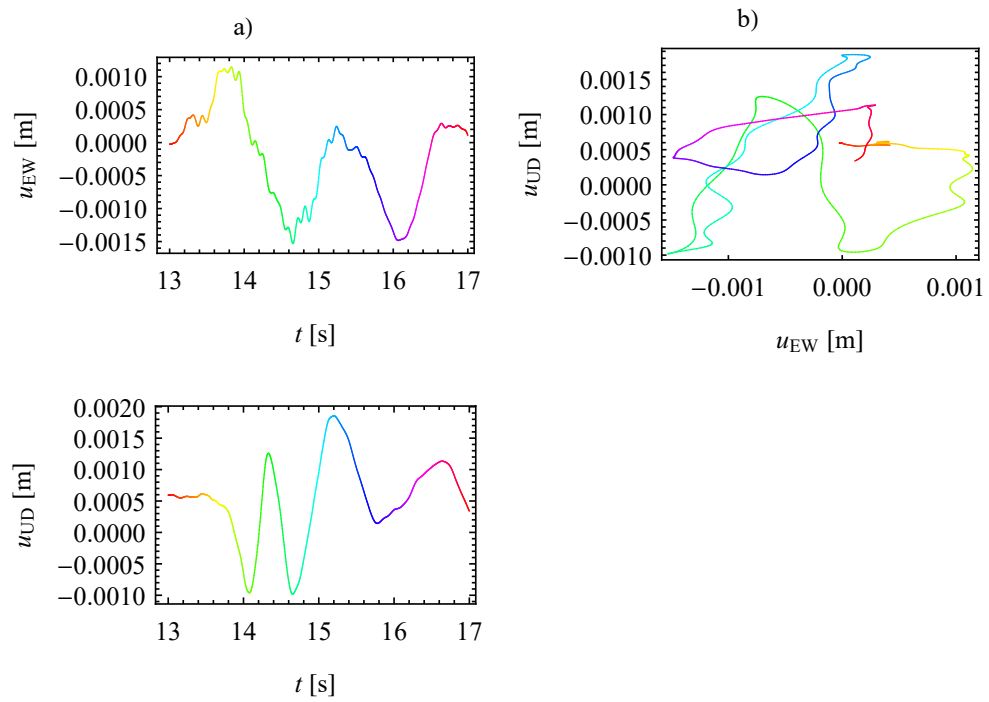


Figure 504.128: Ground displacements from Le Teil earthquake recorded at station 1, at Cruas NPP, for $t \in [13, 17]$ s: a) $u_{EW}(t), u_{UD}(t)$ and b) $u_{UD}(u_{EW})$.

504.10.5.1 Estimation of the Seismic Input

Seismic loads on ESSI systems are generally uncertain. Different earthquake scenarios and regional geology are probable. A parametric FE simulation of the mechanical behavior of an ESSI system using models at the regional scale would be required. It is usually quite problematic due to large computation time, however. Apart from that, unrealistic reflections of the waves at the model boundaries cannot be avoided (Baffet et al., 2012). Even larger FE models, and computation time, would be needed to ensure that the obtained results are not corrupted by the resulting so-called spurious waves. Hence it is advantageous to test ESSI systems parametrically using models at the local scale.

Different simplified approaches have been used in the literature (Semblat and Pecker, 2009; Zienkiewicz et al., 1999b) in order to shorten the computation time in FE solutions of the seismic wave propagation in ESSI systems. These methods rely on reduction of the size of the model and replacement of the distant earthquake load with a *proxy seismic load* applied at the local scale using some simplifying assumptions. Here, the *domain reduction method* (DRM) (Bielak et al., 2003a) is adapted. The proxy seismic input, also called the *DRM load*, will be used to “stress” -test Cruas NPP efficiently and fairly realistically.

An earthquake load usually arrives at the local site in the form of a plane seismic wave. This is due to the large distance between the source and the local site. The inclination of this incident plane wave has been shown, e.g., in (Hori, 2006; Teisseyre et al., 2006; Trifunac, 1982), to have significant influence on the mechanical behavior of ESSI systems. For this reason, Cruas NPP will be tested under an inclined plane wave, an incoherent wave. The DRM load will be obtained using the *Thomson-Haskell matrix method* (THMM) (Haskell, 1953). It is a closed-form solution of the propagation of an inclined monochromatic plane wave in a 3D linear elastic medium with horizontal isotropic layers.

Domain Reduction Method (DRM) The DRM (Bielak et al., 2003a; Yoshimura et al., 2003a) allows to significantly shorten the computation time in a FE solution of the seismic wave propagation in an ESSI system. However, some simplifying assumptions are needed. It is assumed that the real seismic ground motions do not differ significantly from the approximate ground motions. These approximate seismic ground motions correspond to:

- the *far field* simplified into the linear elastic medium and
- the *local site* simplified into the linear elastic *free field*, i.e., without the structure.

The earthquake load at the source is replaced by a proxy load at the local site. This proxy load is also called the DRM load. It can be calculated analytically, possibly with additional simplifying assumptions. Here, a plane wave is assumed to arrive at Cruas NPP, the local site, and the THMM is used.

It will be shown sufficient to apply the proxy load to solely a single layer of elements around the FE domain at the local scale. In this way, the regional domain can be remarkably reduced. The single layer of elements is called the *DRM layer*. The formulation of the DRM is given in what follows.

Global System of Equations We recall the global system of equations for dynamics, here, without an artificial damping,

$$K_{\alpha i \beta j} U_{\beta j} + M_{\alpha i \beta j} \ddot{U}_{\beta j} = F_{\alpha i}^{\text{ext}} \quad \text{at given } t. \quad (504.17)$$

Eq. (504.17) describes the discretized, in space only, weak form of the dynamic equilibrium equation (EE) and it is solved numerically in a FE calculation for a given time, t . The global tangent stiffness matrix is $K_{\alpha i \beta j}$. It stores the contributions from all elements and, generally, it can be either elastic, $K_{\alpha i \beta j}^{\text{el}}$, or elasto-plastic, $K_{\alpha i \beta j}^{\text{el-pl}}$. The Greek indices, $\alpha, \beta = 1, 2, \dots, N$, correspond to the global node numbers and the Latin indices, $i, j = 1, 2, 3$, denote the degrees of freedom (DOFs). The displacement at node β in direction j is $U_{\beta j}$. Analogously, $M_{\alpha i \beta j}$ is the constant global mass matrix that stores the contributions from all elements. The acceleration at node β in direction j is $\ddot{U}_{\beta j}$. The external force at node α in direction i is $F_{\alpha i}^{\text{ext}}$.

Global System of Equations in the Regional Model The regional domain includes the source of the earthquake and it is denoted as R. The local-site domain, with the structure, is denoted as L, Fig. 504.129(a). Let us write (504.17) for R, L and the boundary, Γ , between R and L,

$$\begin{bmatrix} K_{\alpha i \beta j}^{\text{el}} & K_{\alpha i b j}^{\text{el}} & 0_{\alpha i B j} \\ K_{a i \beta j}^{\text{el}} & K_{a i b j}^{\text{R el}} + K_{a i b j}^{\text{L el-pl}} & K_{a i B j}^{\text{el-pl}} \\ 0_{A i \beta j} & K_{A i b j}^{\text{el-pl}} & K_{A i B j}^{\text{el-pl}} \end{bmatrix} \cdot \begin{Bmatrix} U_{\beta j} \\ U_{b j} \\ U_{B j} \end{Bmatrix} + \begin{bmatrix} M_{\alpha i \beta j} & M_{\alpha i b j} & 0_{\alpha i B j} \\ M_{a i \beta j} & M_{a i b j}^{\text{R}} + M_{a i b j}^{\text{L}} & M_{a i B j} \\ 0_{A i \beta j} & M_{A i b j} & M_{A i B j} \end{bmatrix} \cdot \begin{Bmatrix} \ddot{U}_{\beta j} \\ \ddot{U}_{b j} \\ \ddot{U}_{B j} \end{Bmatrix} = \begin{Bmatrix} F_{\alpha i}^{\text{ext}} \\ 0_{a i} \\ 0_{A i} \end{Bmatrix}, \quad (504.18)$$

wherein $K_{a i b j}^{\text{R el}}, M_{a i b j}^{\text{R}}$ correspond to the elements in R and $K_{a i b j}^{\text{L el-pl}}, M_{a i b j}^{\text{L}}$ correspond to the elements in L. The Greek indices, $\alpha, \beta = 1, 2, \dots, N$, denote the nodes in R. The lower-case sans-serif letters, $a, b = 1, 2, \dots, N$, denote the nodes at Γ and the upper-case ones, $A, B = 1, 2, \dots, N$, denote the nodes in L. Domain R is much, say, $10^3 \times$, larger than domain L. The Neumann BC, $F_{\alpha i}^{\text{ext}}$, is prescribed to the nodes in R only. The materials in R are assumed to be linear elastic. The material behavior in L

may be strongly non-linear. Hence L may require some sophisticated constitutive description and a fine discretization, both, in space and time. Computational cost of this regional model is mainly related to the size of domain R and to the material non-linearity inside domain L.

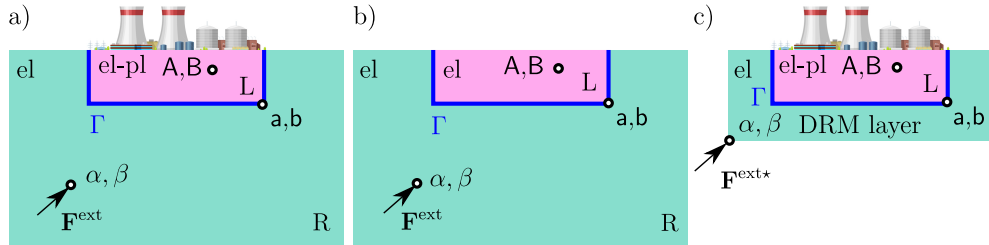


Figure 504.129: DRM: a) regional model, b) regional model with the simplified local site and c) reduced model. L is the local-site domain, R is the regional domain and Γ is the boundary between L and R. The BC, \mathbf{F}^{ext} , is replaced by the proxy load, $\mathbf{F}^{\text{ext}*}$, applied to the DRM layer only.

Global System of Equations in the Regional Model with the Simplified Local Site Let us temporarily remove the structure from domain L, Fig. 504.129(b), and assume the linear elastic behavior within L. We rewrite (504.18) using index \square^* for a quantity, \square , that corresponds to the regional model with the simplified local site. The following holds.

$$\begin{bmatrix} K_{\alpha i \beta j}^{\text{el}} & K_{\alpha i b j}^{\text{el}} & 0_{\alpha i B j} \\ K_{a i \beta j}^{\text{el}} & K_{a i b j}^{\text{el}} + K_{a i b j}^{\text{Lel}} & K_{a i B j}^{\text{el}} \\ 0_{A i \beta j} & K_{A i b j}^{\text{el}} & K_{A i B j}^{\text{el}} \end{bmatrix} \cdot \begin{Bmatrix} U_{\beta j}^* \\ U_{b j}^* \\ U_{B j}^* \end{Bmatrix} + \begin{bmatrix} M_{\alpha i \beta j} & M_{\alpha i b j} & 0_{\alpha i B j} \\ M_{a i \beta j} & M_{a i b j}^R + M_{a i b j}^{L*} & M_{a i B j}^* \\ 0_{A i \beta j} & M_{A i b j}^* & M_{A i B j}^* \end{bmatrix} \cdot \begin{Bmatrix} \ddot{U}_{\beta j}^* \\ \ddot{U}_{b j}^* \\ \ddot{U}_{B j}^* \end{Bmatrix} = \begin{Bmatrix} F_{\alpha i}^{\text{ext}} \\ 0_{a i} \\ 0_{A i} \end{Bmatrix} \quad (504.19)$$

The simplification of L does not influence either the stiffness matrices or the mass matrices corresponding to the elements in R. Neither the BC, $F_{\alpha i}^{\text{ext}}$, is affected.

Material in the far field is assumed linear elastic independently of the temporary simplification of L, so the displacement and its time derivates are additive, that is,

$$\Delta U_{\beta j} = U_{\beta j} - U_{\beta j}^* \quad \text{and} \quad \Delta \ddot{U}_{\beta j} = \ddot{U}_{\beta j} - \ddot{U}_{\beta j}^* \quad (504.20)$$

hold in R.

Global System of Equations in the Reduced Model The force

$$F_{\alpha i}^{\text{ext}} = K_{\alpha i \beta j}^{\text{el}} U_{\beta j}^* + K_{\alpha i b j}^{\text{el}} U_{b j}^* + M_{\alpha i \beta j} \ddot{U}_{\beta j}^* + M_{\alpha i b j} \ddot{U}_{b j}^* \quad (504.21)$$

from (504.19) can be substituted together with (504.20) into (504.18) and one obtains the following system of equations.

$$\begin{bmatrix} K_{\alpha i \beta j}^{\text{el}} & K_{\alpha i b j}^{\text{el}} & 0_{\alpha i B j} \\ K_{a i \beta j}^{\text{el}} & K_{a i b j}^{\text{R el}} + K_{a i b j}^{\text{L el-pl}} & K_{a i B j}^{\text{el-pl}} \\ 0_{A i \beta j} & K_{A i b j}^{\text{el-pl}} & K_{A i B j}^{\text{el-pl}} \end{bmatrix} \cdot \begin{Bmatrix} \Delta U_{\beta j} \\ U_{b j} \\ U_{B j} \end{Bmatrix} + \begin{bmatrix} M_{\alpha i \beta j} & M_{\alpha i b j} & 0_{\alpha i B j} \\ M_{a i \beta j} & M_{a i b j}^{\text{R}} + M_{a i b j}^{\text{L}} & M_{a i B j} \\ 0_{A i \beta j} & M_{A i b j} & M_{A i B j} \end{bmatrix} \cdot \begin{Bmatrix} \Delta \ddot{U}_{\beta j} \\ \ddot{U}_{b j} \\ \ddot{U}_{B j} \end{Bmatrix} = \begin{Bmatrix} K_{\alpha i b j}^{\text{el}} U_{b j}^* + M_{\alpha i b j} \ddot{U}_{b j}^* \\ -K_{a i \beta j}^{\text{el}} U_{\beta j}^* - M_{a i \beta j} \ddot{U}_{\beta j}^* \\ 0_{A i} \end{Bmatrix} \quad (504.22)$$

The RHS of (504.22),

$$\begin{Bmatrix} F_{\alpha i}^{\text{ext*}} \\ F_{a i}^{\text{ext*}} \\ 0_{A i} \end{Bmatrix} = \begin{Bmatrix} K_{\alpha i b j}^{\text{el}} U_{b j}^* + M_{\alpha i b j} \ddot{U}_{b j}^* \\ -K_{a i \beta j}^{\text{el}} U_{\beta j}^* - M_{a i \beta j} \ddot{U}_{\beta j}^* \\ 0_{A i} \end{Bmatrix}, \quad (504.23)$$

can be used as the BC instead of \mathbf{F}^{ext} from (504.18).

It is evident in (504.23) that the proxy forces, $\mathbf{F}^{\text{ext*}}$, take on non-zero values for elements with nodes a, b, in domain R, or both, a, b, in domain R, and α, β , at boundary Γ , only. This means that $\mathbf{F}^{\text{ext*}}$ can be applied to solely the single layer of elements adjacent to Γ , namely, the DRM layer, and hence the model can be reduced, Fig. 504.129(c).

The discrete proxy load, $\mathbf{F}^{\text{ext*}}$, is only a rough estimation of the real seismic load because it corresponds to the simplified local site. Hence using the DRM, one saves the computation time at the cost of the reliability of the obtained results.

This $\mathbf{F}^{\text{ext*}}$ is obtained in Real-ESSI Simulator from an inclined plane wave in horizontally layered soil using the THMM.

Thomson-Haskell Matrix Method (THMM) The propagation of an inclined plane wave in a linear elastic ground with horizontal isotropic layers is solved analytically using the Thomson-Haskell matrix method (THMM) (Haskell, 1953; Thomson, 1950). In this way, reflections and refractions of the wave at interfaces between the layers are captured. Also, the Rayleigh wave is taken into account. The use of a closed-form solution eliminates the problem of unrealistic reflections of the wave at the boundaries of the FE model.

The THMM holds for monochromatic waves only. If the wave is non-monochromatic, it can be decomposed into harmonic components with the Fourier analysis. The THMM is then used for each

monochromatic component and the solutions are synthesized using, again, the Fourier analysis.

The analytical solution of the wave propagation is generally established from the boundary conditions at the interfaces between the layers and at the surface. The Helmholtz decomposition theorem is incorporated and the wave field is separated into two parts, i.e., the part pertaining to the purely volumetric deformation and the part related to the pure rotation of material particles ([Nowacki, 1974](#)). The Snell law describes reflections and refractions of the waves at the interfaces between the layers and at the surface. In the THMM, the governing equations are conveniently rewritten into a matrix form to ease the computation of the wave propagation.

A comprehensive description of the implementation of the THMM into Real-ESSI Simulator is given in ([Wang et al., 2021](#)).

504.10.5.2 Preliminary 2D Simulation of Le Teil Earthquake using DRM with THMM

Rock is isotropic, linear elastic, E, ν with $E = 2\rho V_s^2(1 + \nu)$, Table 504.11.

Table 504.11: Material properties in preliminary 2D simulation of the earthquake in Le Teil using DRM with THMM

Material	z m	ρ kg/m ³	V_s m/s	ν
Rock	[0, $-\infty$]	2500	1600	0.4

Time functions of the horizontal ground acceleration, $\ddot{u}_x(t)$, and the vertical ground acceleration, $\ddot{u}_z(t)$, at $x = \{140, 0, 0\}$ m is plotted in Figure 504.130(a). The corresponding hodograph, $u_z(u_x)$, is shown in Figure 504.130(b).

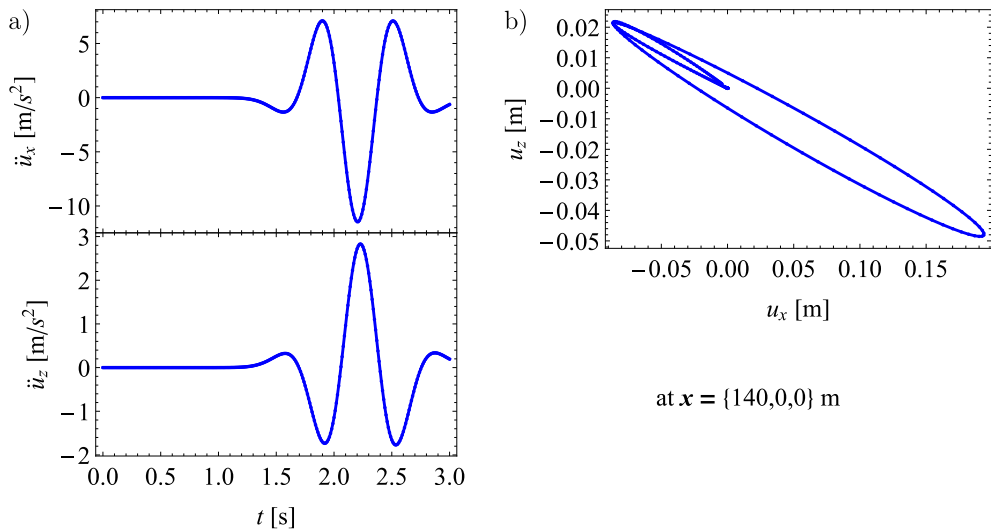


Figure 504.130: Preliminary 2D simulation of the earthquake in Le Teil using DRM with THMM:
a) $\ddot{u}_x(t)$ and $\ddot{u}_z(t)$, and b) $u_z(u_x)$ at $x = \{140, 0, 0\}$ m.

504.10.6 Cruas Nuclear Power Plant (NPP)

Base isolators are located at approximately -9.0 to -12.0 m. This means that the NPP is founded on rock, see the soil profile from Table 504.9 on page 2570.

Cruas NPP presentation Plant overview

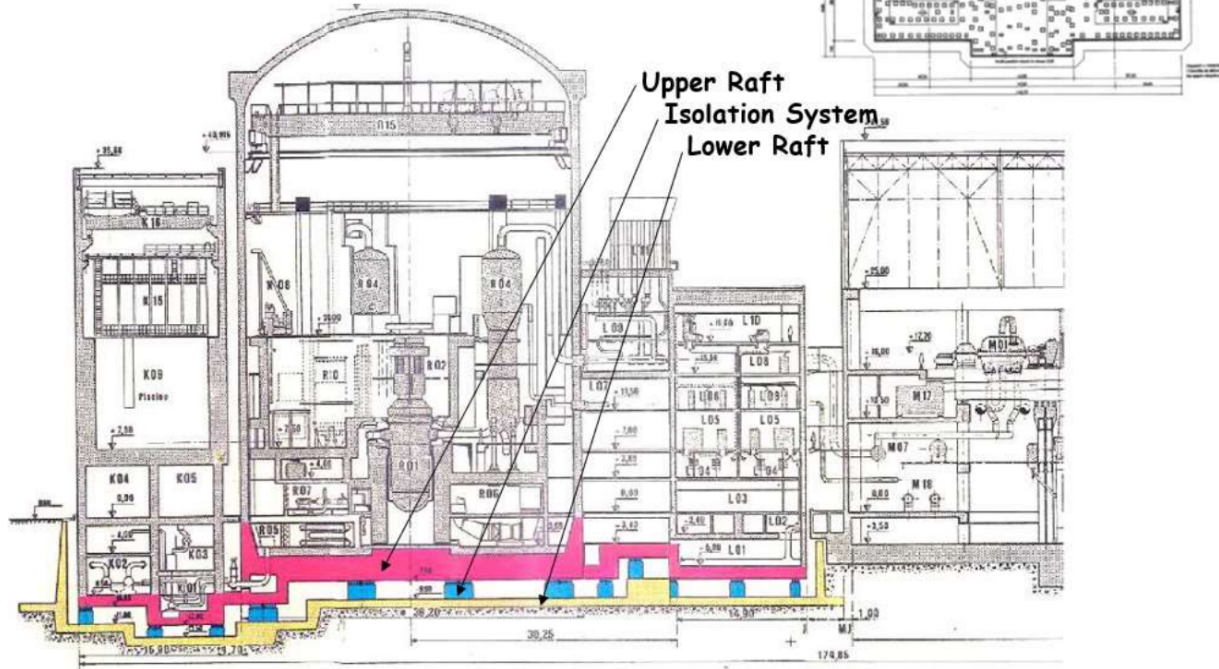


Figure 504.131: Cruas NPP, section 01, according to Viallet et al. (2022).

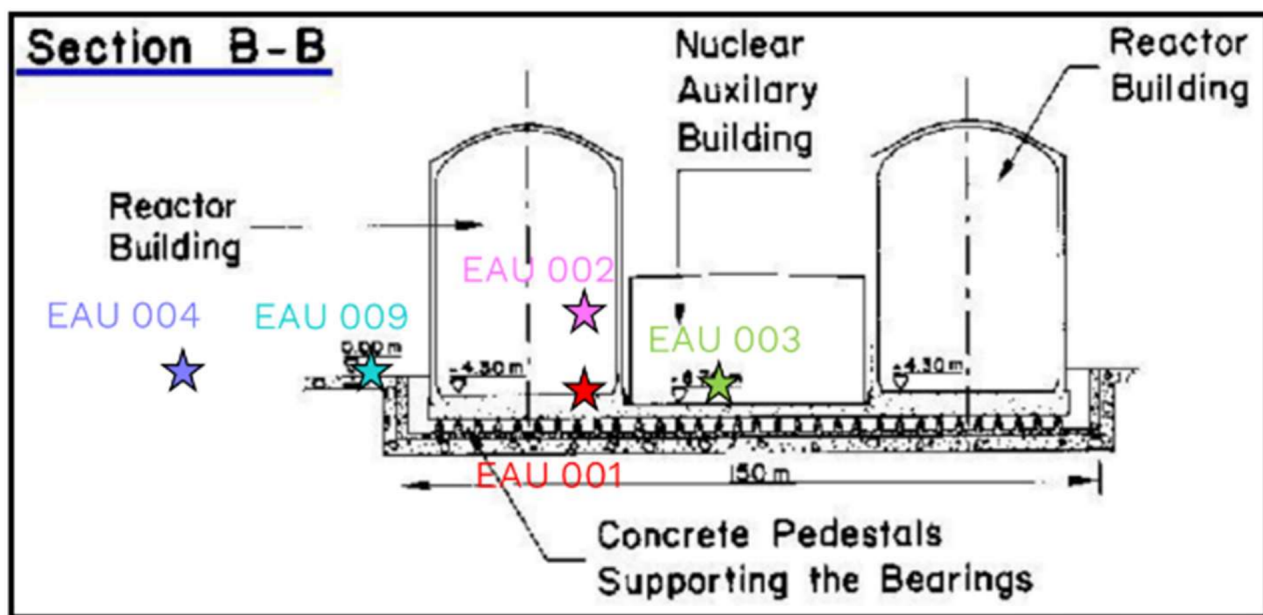


Figure 504.132: Cruas NPP, section 02, according to Viallet et al. (2022).

504.10.7 FE Simulation of Cruas NPP under Seismic Load from Le Teil Earthquake

...

504.10.7.1 Verification of the Simulation

FE simulation of an ESSI system requires one to specify:

- the domain of simulation (both, in space and in time)
- the boundary conditions (BCs)
- the initial conditions (ICs)
- the material laws
- the material parameters
- the discretization (in space and in time) and
- the numerical procedures used in the calculation,

wisely. A parametric study using a simple FE model may be helpful in understanding the influence of the above aspects on the results of the simulation. This influence can be additionally quantified in a sensitivity study ([Sobol, 2001](#)). Also, in the case of a simple model, the numerical solution can be compared with the corresponding analytical one. In this way, a complex FE model can be verified.

Element Tests The mechanical behavior of chosen critical parts of Cruas NPP (being an ESSI system) is investigated in suitable element tests. They are conducted on different structural materials and on different soils with various:

- BCs (displacement, seismic load)
- ICs (initial stress and strain)
- material laws
- material parameters.

The resulting evolution of the stress, $\sigma(\mathbf{x}, t)$, and strain, $\varepsilon(\mathbf{x}, t)$, fields is examined.

Beam Element Tests on Reinforced Concrete A cantilever beam is tested on reinforced concrete with different material laws for concrete and for steel in:

- uniaxial compression or extension, Figure ...
- uniaxial bending, Figure ...
- biaxial bending, Figure ...
- torsion, Figure

A (displacement-based) *fiber beam-column element* similar to the one from (Taucer et al., 1991) is used. It is called BeamColumnDispFiber3d_Corotational. The co-rotational formulation by (Crisfield, 1990) is implemented. The local coordinate system co-rotates with the element during a rigid body rotation and hence BeamColumnDispFiber3d_Corotational is applicable also in the case of the *geometric non-linearity*, i.e., when *large deformations* are involved. Otherwise, during a large deformation with a significant rigid body rotation, an excessive stiffness might be obtained in such beam element.

The element has two nodes and the user defines the number of Gauß points along the element.

BeamColumnDispFiber3d_Corotational may represent multiple 1D so-called *fibers*. They are simply connected in parallel, Figure 504.133. A fiber is defined by its cross-section, A , and location in the element cross-section, $\{y, z\}$. The cross-section is constant along the beam.

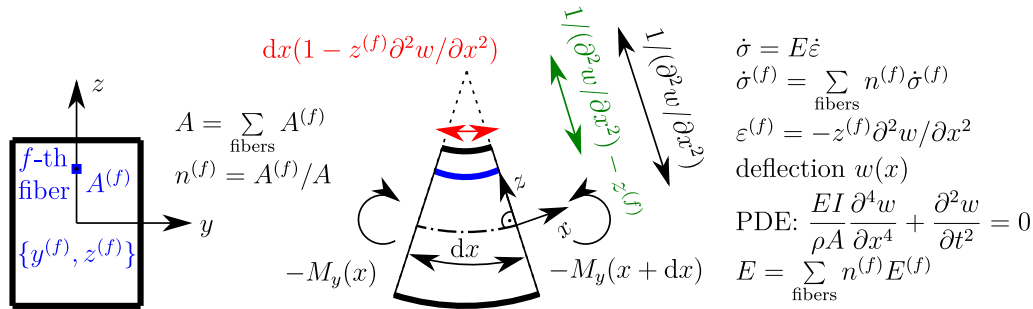


Figure 504.133: Fiber beam-column element in uniaxial bending: The second moment of area, I , pertains to the whole cross-section and the density, ρ , describes the average density of the material.

Each fiber has a prescribed material law. Different material laws can be prescribed to different fibers. The strain in a single fiber is obtained assuming that the cross-section remains plane and normal to the beam axis during the deformation. This means that BeamColumnDispFiber3d_Corotational is an *Euler-Bernoulli beam*. The shear stress is neglected which is allowed in beams for which the cross-sectional

dimensions are much smaller than the length, see, e.g., ([Nowacki, 1974](#)).

However, the cross-section is additionally (independently of the fibers) described by the product, GJ , of the shear modulus, G , and the torsional constant, J . Hence the element has four nodal degrees of freedom (DOFs) altogether, i.e., three translations and the angle of twist due to the torsional moment, M_x .

Shell Element Tests on Concrete ...

Solid Element Tests on Concrete Different constitutive laws for concrete are tested in:

- triaxial compression, Figure [504.134\(a\)](#),
- simple shear, Figure [504.134\(b\)](#),
- pure shear (here, understood as isochoric shear with no rotation of the principal stress and strain directions), Figure [504.134\(c\)](#).

The 3D solid brick element, 8NodeBrick, is used.

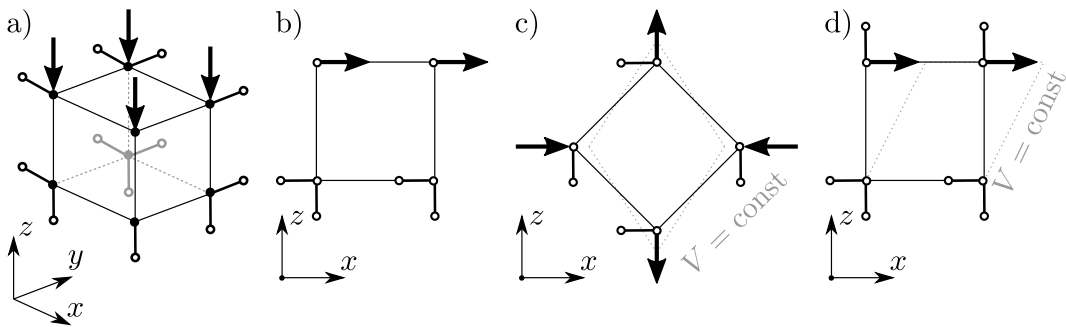


Figure 504.134: Solid element tests: a) triaxial compression, b) simple shear, c) pure shear (isochoric with no rotation of the principle stress and strain directions), d) pure shear (in soil mechanics, commonly understood as isochoric shear).

Solid Element Tests on Soil Similarly as in the case of the solid element tests on concrete, different constitutive laws for soils are tested in:

- triaxial compression, Figure [504.134\(a\)](#),
- simple shear, Figure [504.134\(b\)](#),

- pure shear (here, understood as isochoric shear with no rotation of the principal stress and strain directions), Figure 504.134(c).

The 3D solid brick element, 8NodeBrick, is used.

Interface Element Tests . . .

Seismic Isolator and Dissipator Element Tests . . .

Report for Phase 2 of Stage 1, Simulation of the Ground Motions

Ground motions from the Le Teil earthquake had been intensively studied within the SIGMA2 project⁶ ([Viallet et al., 2022](#)). Two types of methods for the simulation of seismic motions had been used, the empirical methods and the physically based methods. The latter include both, 1D ([Fasan, 2016](#); [Fasan et al., 2016](#); [Hassan et al., 2020](#); [Magrin et al., 2016](#); [Magrin, 2012](#); [Panza et al., 2012](#)) and 3D ([Mazzieri et al., 2013](#); [Paolucci et al., 2020, 2021](#)) simulations. Some recent 3D numerical calculations of seismic motions from the Le Teil earthquake are reported in ([Lehmann et al., 2023](#); [Smerzini et al., 2023](#)).

Seismic input due to the Le Teil earthquake is needed to simulate the inelastic behavior of the Cruas NPP. A FE simulation of the wave field from the earthquake is conducted using the Real-ESSI Simulator ([Jeremić et al., 1988-2025](#)). Unfortunately, the knowledge about the local and regional geology is very limited. Soil and rock profiles are available at three locations only. This scarcity of data precludes the preparation of a realistic model at the regional scale. Hence an accurate reproduction of the seismic wave field from the earthquake in Le Teil is impossible.

Based on a preliminary simplified FE simulation and the recent work by [Viallet et al. \(2022\)](#), some important observations are made about the studied seismic wave field.

- The preliminary simulation using a simple 2D model with a shallow point source reveals a possible occurrence of the Stoneley wave and the Rayleigh wave. This should, indeed, be expected from a shallow earthquake, particularly with the rupture that achieves the surface.
- Based on [Viallet et al. \(2022\)](#), the horizontal and vertical components of ground motions at the Cruas NPP occur almost simultaneously. We interpret these motions as the overlapping Rayleigh and Stoneley waves.
- Earthquake loads are usually simulated as one dimensional (1D), one component (1C) waves, possibly superposed, wherein 1D pertains to the direction of propagation, either vertical or horizontal, while 1C corresponds to the direction of polarization, analogously, either vertical or horizontal. The probable presence of the Rayleigh wave and the Stoneley wave excludes this common approach to modelling of seismic loads. In the case of the surface and interface waves, the simulated seismic wave field is shown to be significantly different than the one obtained using the common approach. The seismic response of a structure will also be different depending on the seismic input. The difference is most evident in the case of shorter wave lengths, that is, for higher wave frequencies.

⁶<https://www.sigmac-2.net/>

These and other observations will be presented during the next SMATCH benchmark meeting in November 2023.

504.10.8 Finite Element Models

Cruas NPP presentation Plant overview

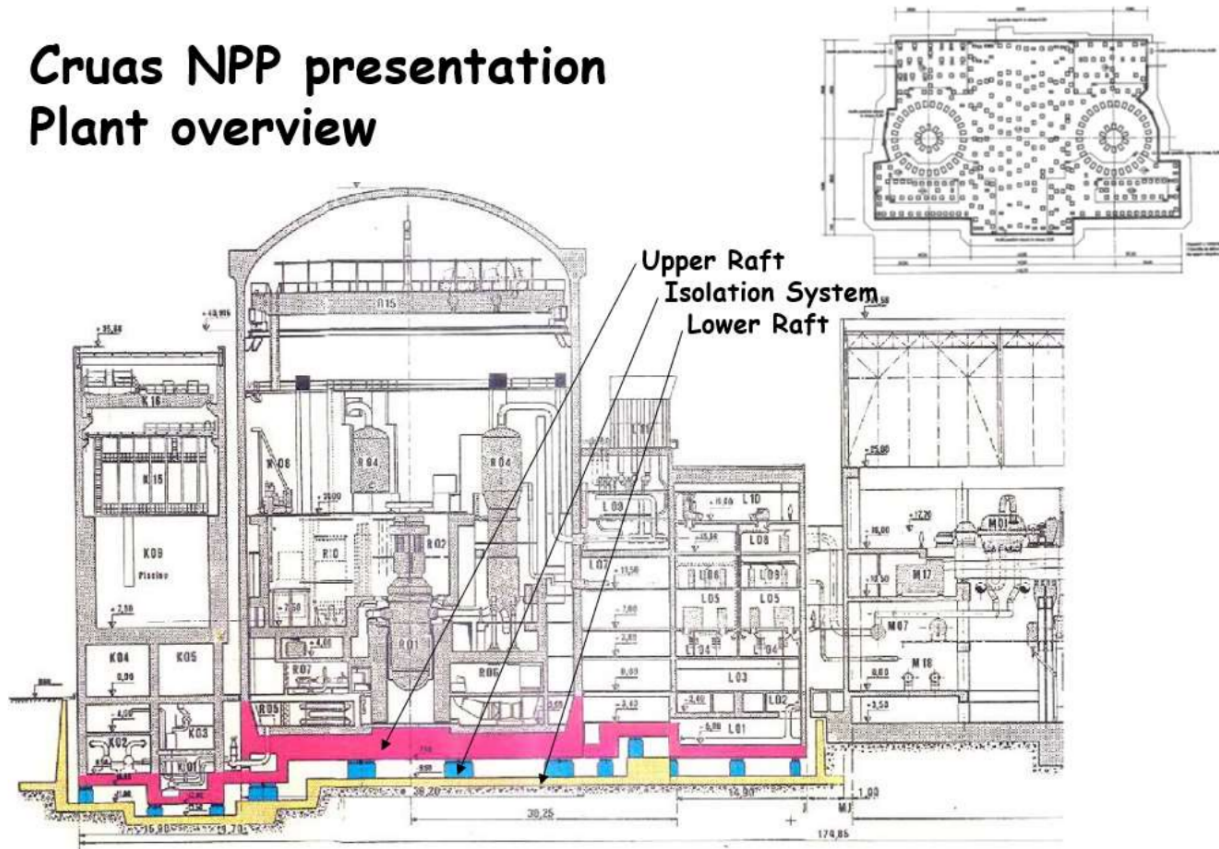


Figure 504.135: Cruas NPP, section 01, according to Viallet et al. (2022).

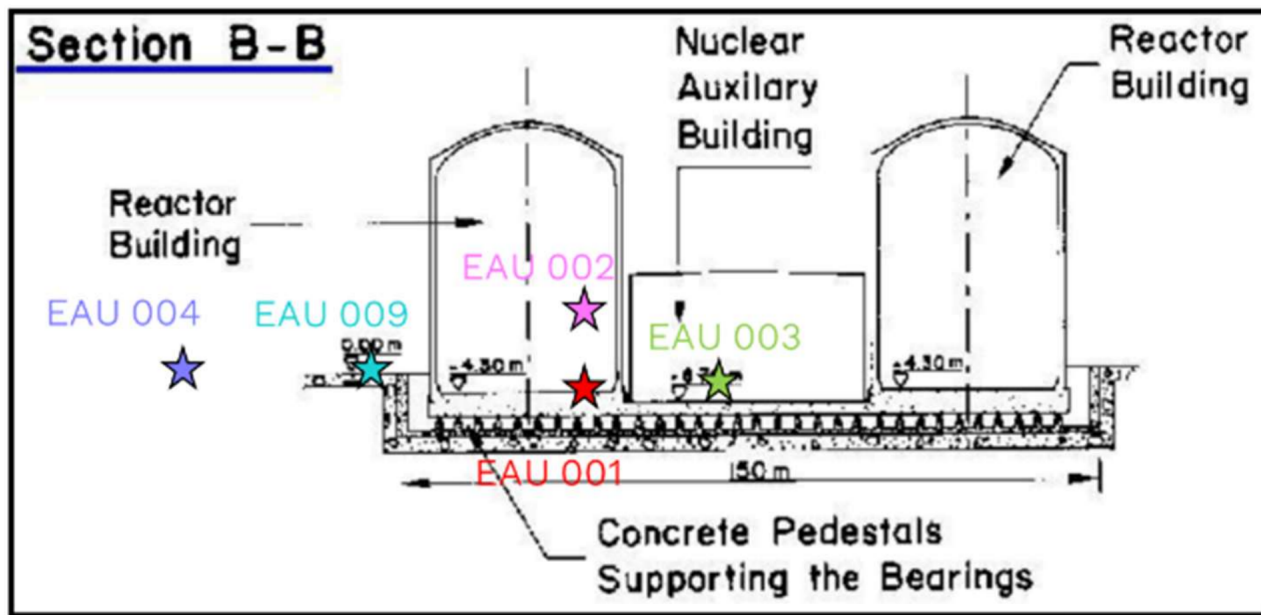
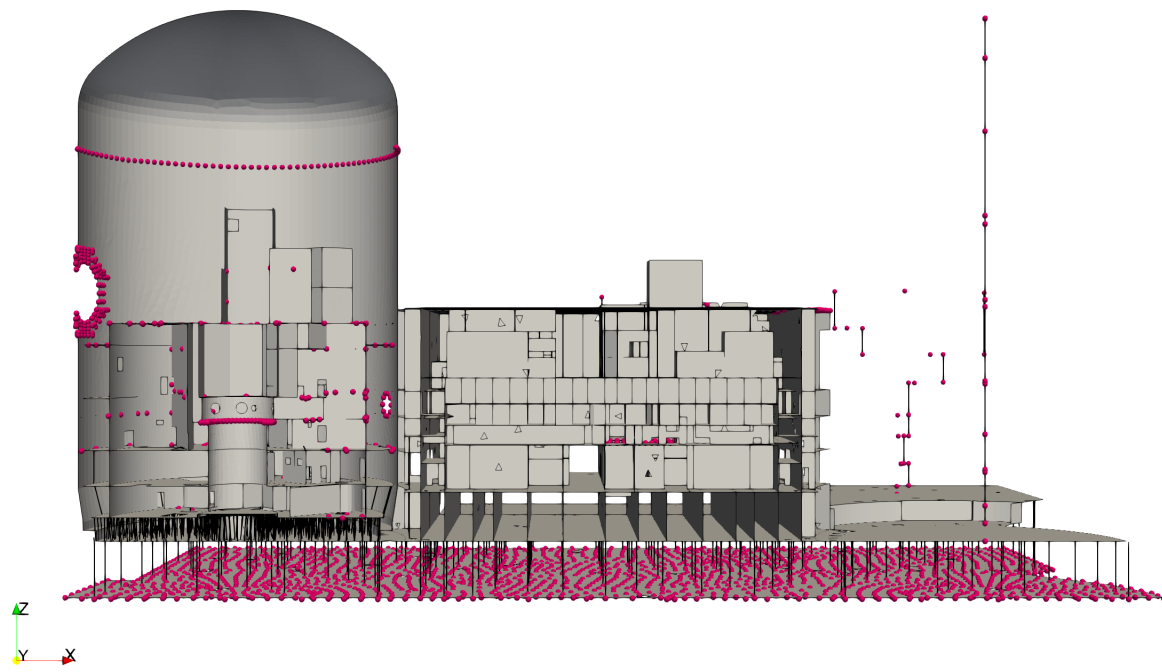
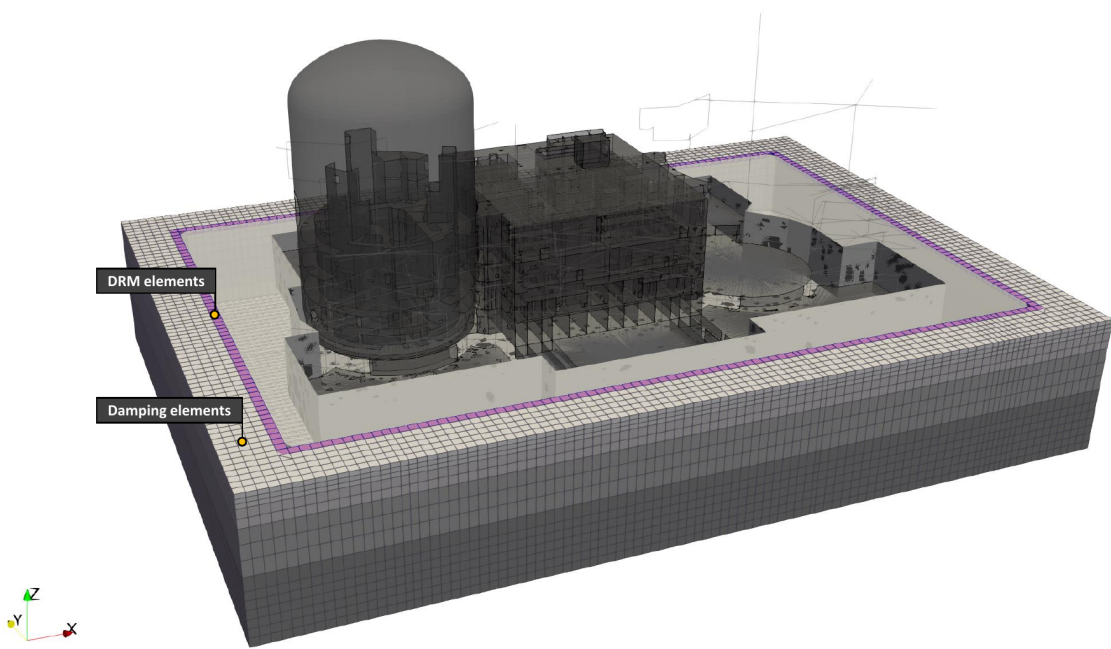


Figure 504.136: Cruas NPP, section 02, according to Viallet et al. (2022).





Chapter 505

Liquefaction and Cyclic Mobility

(2002-2006-2009-2021-)

(In collaboration with Dr. Zhao Cheng, and Dr. Panagiota Tasiopoulou)

505.1 Chapter Summary and Highlights

505.2 Introduction

Liquefaction is one of the most complex phenomena in earthquake engineering. Liquefaction also represents one of the biggest contributors to damage of constructed facilities during earthquakes ([Kramer, 1996a](#)). Prediction of behaviors of liquefiable soils is difficult but achievable. There are number of methods that can be utilized to predict such behaviors. Methods currently used can have varying prediction accuracy and certainty. Of particular interest in this paper is the description of verified and validated numerical simulation methodology based on rational mechanics that is used to model, simulate and predict behavior of a single pile in liquefiable soil subjected to seismic loading. Both level and sloping ground pile systems are modeled and simulated. Detailed description of background theory, formulation and implementation were recently given by [Cheng et al. \(2007\)](#) and [Jeremić et al. \(2008\)](#).

It should be noted that presented development does show great promise in analyzing a myriad of liquefaction related problems in geotechnical and structural engineering. The effectiveness and power of numerical simulation tools for analyzing liquefaction problems becomes even more important and prominent in the light of potential disadvantages of models used in experimental simulations. These disadvantages, related to proper scaling ([Wood, 2004](#)) and problems in maintaining appropriate similarities ([Harris and Sabinis, 1999](#)) for first order important phenomena, can render scaled models ineffective, when used for physical simulations (under one-step or multiple-step gravity loading).

In what follows, a brief literature review is provided. The literature review comprises sections on observations of liquefaction behavior in case studies, non-continuum modeling efforts, review of redistribution of voids and pore fluid volume/pressures phenomena and continuum modeling efforts.

Observation of Behavior. Liquefaction behavior was observed during a number of earthquakes in the past. During Alaskan Earthquake (1964), liquefaction was the main cause of severe damage to 92 highway bridges, moderate to light damage to another 49 highway bridges, and moderate to sever damage to 75 railroad bridges ([Youd and Bartlett, 1989](#)). During Niigata Earthquake (1964) liquefaction induced damage to foundation piles under Yachiya bridge ([Hamada, 1992](#)). During that same earthquake, girders of Showa Bridge toppled as the support structure and piles moved excessively due to liquefaction ([Japanese Society of Civil Engineers, 1966](#)). During Kobe Earthquake (1995), liquefaction was the primary cause of damage to many pile supported or caisson supported bridges and structures. For example, Shin-Shukugawa bridge was subjected to excessive pile foundation movement due to liquefaction ([Yokoyama et al., 1997](#)).

Opposed to these failures and collapses, there were a number of bridges with pile foundations that

did not suffer much or even minor damage even though there was liquefaction around foundations. For example, pile foundations of the Landing Road Bridge in New Zealand performed quite well during Edgecumbe earthquake (1987) even with a significant liquefaction recorded (Berril et al., 1997; Dobry and Abdoun, 2001). In addition to that, Second Maya Bridge piles (large steel pipes) were not damaged during Kobe earthquake despite significant liquefaction in surrounding soils (Yokoyama et al., 1997).

Non–Continuum Modeling Efforts. Modeling and simulation of piles in liquefied grounds has been focus of a number of recent studies. The simple approach, based on scaling of p-y springs has been suggested early by Japanese Road Association (1980), Architectural Institute of Japan (1988), Liu and Dobry (1995), Miura et al. (1989) and O'Rourke (1991). However, large inconsistencies with material parameter selection are present when p-y spring approach is used for piles in liquefied soils. Since p-y methodology for liquefied soils is not based on rational mechanics, appropriate choice of material parameters is primarily based on empirical observations of behaviors of piles in liquefied soils in experimental studies. A number of experimental studies have carefully examined pile behaviors in liquefiable soils. We mention Tokida et al. (1992), Liu and Dobry (1995), Abdoun et al. (1997), Horikoshi et al. (1998) and Boulanger and Tokimatsu (2006). Studies using physical model can be used to obtain very high quality data on behavior of piles in liquefied soils, provided that similarity of important physical phenomena is maintained (Wood, 2004; Harris and Sabnis, 1999). Some of the recent papers that discussed use of these models and gave recommendations about parameter choices are listed for reference: Tokimatsu and Asaka (1998), Martin et al. (2002), Dobry et al. (2003), Liyanapathirana and Poulos (2005), Rollins et al. (2005), Čubrinovski and Ishihara (2006), Brandenberg et al. (2007).

Redistribution of Voids and Pore Fluid Volume/Pressures. Mechanics of pile behavior in liquefiable grounds is based on the concept of redistribution of voids and pore fluid volume/pressures (RVPFVP). It should be emphasized that geomechanics phenomena of redistribution of voids – pore fluid volume/pressure is used here in purely mechanistic way. That is, RVPFVP is a phenomena that occurs in saturated soils and that phenomena is responsible for (is manifested in) liquefaction related soil behaviors with or without piles. This is noted as in some recent publications, RVPFVP terminology is explicitly used for problems of liquefaction induced failures of sloping grounds without piles. Our understanding of the RVPFVP phenomena is that RVFVP is responsible for many more facets of behavior of liquefied soils, rather than only failure of liquefied slopes.

The early investigation of the RVPFVP phenomena was related to the behavior of infinite slopes. For example, loss of shear strength in infinite slopes is one of the early understood manifestations of RVPFVP (Whitman, 1985; National Research Council, 1985; Malvick et al., 2006). Laboratory investigation of

sand was also used to observe the RVPFVP phenomena ([Casagrande and Rendon, 1978](#); [Gilbert, 1984](#))

Continuum Modeling Efforts. Continuum based formulations for modeling liquefaction problems have been present for over two decades. In a landmark paper, [Zienkiewicz and Shiomi \(1984\)](#) presented three possible coupled formulations for modeling of soil skeleton – pore fluid problems. The most general and complete one is the so called u-p-U formulations while the other two, the u-p and the u-U have a number of restrictions on the domain of application. Here, the unknowns are the soil skeleton displacements u ; the pore fluid (water) pressure p ; and the pore fluid (water) displacements U . The u-p formulation captures the movements of the soil skeleton and the change of the pore pressure, and is the most simplistic one of the three mentioned above. This formulation neglects the differential accelerations of the pore fluid (it does account for acceleration of pore fluid together with soil skeleton, but not the differential one if it exists), and in one version neglects the compressibility of the fluid (assuming complete incompressibility of the pore fluid). In the case of incompressible pore fluid, the formulation requires special treatment of the approximation function (shape function) for pore fluid to prevent the volumetric locking ([Zienkiewicz and Taylor, 2000](#)). The majority of the currently available implementations are based on this formulation. For example [Elgamal et al. \(2002\)](#) and [Elgamal et al. \(2003\)](#) developed an implementation of the u-p formulation with the multi-surface plasticity model by [Prevost \(1985b\)](#), while [Chan \(1988\)](#) and [Zienkiewicz et al. \(1999a\)](#) used generalized theory of plasticity [Pastor et al. \(1990\)](#).

The u-U formulation tracks the movements of both the soil skeleton and the pore fluid. This formulation is complete in the sense of basic variables, but might still experience numerical problems (volumetric locking) if the difference in volumetric compressibility of the pore fluid and the solid skeleton is large.

The u-p-U formulation resolves the issues of volumetric locking by including the displacements of both the solid skeleton and the pore fluid, and the pore fluid pressure as well. This formulation uses additional dependent unknown field of pore fluid pressures to stabilize the solution of the coupled system. The pore fluid pressures are connected to (dependent on) displacements of pore fluid. With known (given) volumetric compressibility of the pore fluid, pore fluid pressure can be calculated. Despite its power, the u-p-U formulation has rarely been implemented into finite element code, and has never (at least to our knowledge) been used to analyze pile – liquefied soil interaction. This can be attributed in part to a sophistication of implementation that is required, and to a sizable increase in computational cost for u-p-U elements.

505.3 Liquefaction of Level and Sloping Grounds

Material presented here is from Cheng et al. (2007); Jeremić et al. (2008).

Liquefaction of level and sloping grounds represents a very common behavior during earthquakes. Of interest is to estimate settlement for level ground, and horizontal movements for sloping grounds. In next few sections, presented are results for a 1D, vertical (level ground) and sloping ground cases for dense and loose sand behavior during seismic shaking.

505.3.1 Model Description

Vertical soil column consists of a multiple-elements subjected to an earthquake shaking. The soil is assumed to be Toyoura sand and the calibrated parameters are from Dafalias and Manzari (2004a), and are given in the Table (505.1).

Table 505.1: Material parameters of Dafalias-Manzari model.

material parameter		value	material parameter		value
Elasticity	G_0	125 kPa	Plastic modulus	h_0	7.05
	v	0.05		c_h	0.968
Critical state	M	1.25		n_b	1.1
	c	0.712		A_0	0.704
	λ_c	0.019		n_d	3.5
	ξ	0.7		z_{max}	4.0
Yield surface	e_r	0.934	Fabric-dilatancy	c_z	600.0
	m	0.01			

The other parameters, related to the boundary value problem are given in table (505.2).

For tracking convenience, the mesh elements are labeled from E01 (bottom) to E10 (surface) and nodes at each layers are labeled from A (bottom) to K (surface).

A static application of gravity analysis is performed before seismic excitation. The resulting fluid hydrostatic pressures and soil stress states along the soil column serve as initial conditions for the subsequent dynamic analysis.

It should be noted that the self weight loading is performed on an initially zero stress (unloaded) soil column and that the material model and numerical integration algorithms are powerful enough to follow through this early loading with proper evolution. The boundary conditions are such that the soil and water displacement degree of freedom (DOF) at the bottom surface are fixed, while the pore pressure

Table 505.2: Additional parameters used in boundary value problem simulations (other than material parameters from the Table (505.1)).

Parameter	Symbol	Value
Solid density	ρ_s	2700 kg/m^3
Fluid density	ρ_f	1000 kg/m^3
Solid particle bulk modulus	K_s	$3.6 \times 10^7 \text{ kN/m}^2$
Fluid bulk modulus	K_f	$2.2 \times 10^6 \text{ kN/m}^2$
permeability	k	$5.0 \times 10^{-4} \text{ m/s}$
HHT parameter	α	-0.2

DOFs are free; the soil and water displacement DOFs at the upper surface are free upwards to simulate the upward drainage. The pore pressure DOFs are fixed at surface thus setting pore pressure to zero. On the sides, soil skeleton and water are prevented from moving in horizontal directions while vertical movement of both is free. It is emphasized that those displacements (of soil skeleton and pore fluid) are different. In order to simulate the 1D behavior, all DOFs at the same depth level are connected in a master-slave fashion. Modeling of sloping ground is done by creating a constant horizontal load, sine of inclination angle, multiplied by the self weight of soil column, to mimic sloping ground. In addition to that, for a sloping ground, there should be a constant flow (slow) downhill, however this is neglected in our modeling. The permeability is assumed to be isotropic $k = 5.0 \times 10^{-4} \text{ m/s}$. The input acceleration time history (Figure (505.1)) is taken from the recorded horizontal acceleration of Model No.1 of VELACS project Arulanandan and Scott (1993) by Rensselaer Polytechnic Institute, <http://geoinfo.usc.edu/gees/velacs/>. The magnitude of the motion is close to 0.2 g, while main shaking lasts for about 12 seconds (from 1 s to 13 s). For the sloping ground model a slope of % 3 was considered.

It should be emphasized that the soil parameters are related to Toyoura sand, not Nevada sand which is used in VELACS project. The purpose of presented simulation is to show the predictive performance using verified and validated formulation, algorithms, implementation and models.

505.3.2 Behavior of Saturated Level Ground

Figure (505.2) describes the response of the sample with loose sand $e_0 = 0.85$. This figure shows the typical mechanism of cyclic decrease in effective vertical stress due to pore pressure build up as expected for the looser than critical granular material. The lower layers show only the reduction of effective vertical stress from the beginning. Once the effective vertical (and therefore confining) stress

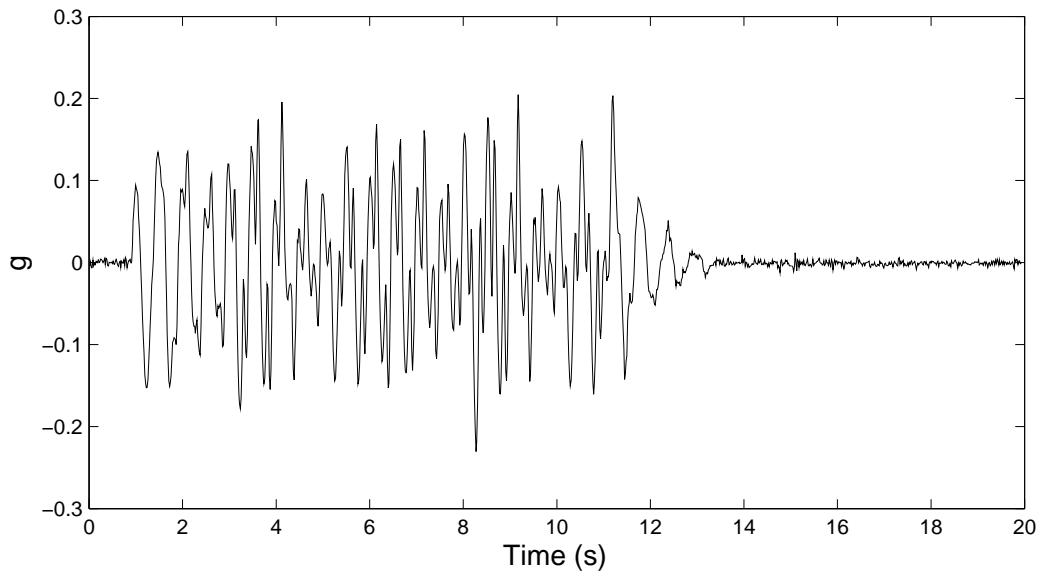


Figure 505.1: Input earthquake ground motion for the soil column.

approaches the smaller values, signs of the so-called butterfly shape can be observed in the stress path. Similar observation can be made in the upper layers which have the smaller confining pressure comparing to the lower layers from the very beginning due to lower surcharge. The upper layers have lower confining pressure (lower surcharge) at the beginning of the shaking, hence less contractive response is expected in these layers; however, soon after the initiation of the shaking these top layers start showing the liquefaction state and that type of response continues even after the end of the shaking. The top section of the model has remained liquefied well past the end of shaking. This is explained by the large supply of pore fluid from lower layers, for which the dissipation starts earlier. For example, for the lowest layer, the observable drop in excess pore pressure starts as soon as the shaking ends, while, the upper layers then receive this dissipated pore fluid from lower layers and do liquefy (or continue being liquefied) well past end of shaking (which happens at approximately 13 seconds). It is very important to note the significance of this incoming pore water flux on the pore water pressure of the top layers. Despite the less contractive response of soil skeleton at the top elements, the transient pore water flux, that enters these elements from the bottom, forces those to a liquefaction state. In other words, the top elements have not liquefied only due to their loose state but also because of the water flow coming from the bottom layers. The maximum horizontal strains can be observed in the middle layers due to liquefaction and prevents upper layers from experiencing larger strains. The displacements of water and soil are presented in the last column. It shows that in all layers the upward displacement of water is larger than the downward displacement of soil. This behavior reflects soil densification during shaking.

Figure (505.3) describes the response of the sample with dense sand ($e_0 = 0.75$). This figure also shows the typical mechanism of cyclic decrease in effective vertical stress. However, in case of this dense sample the decreasing rate of the effective confining pressure is much smaller than what was observed in the loose sample. Signs of the partial butterfly shape in the effective stress path can be observed from early stages of shaking. The butterfly is more evident in the upper layers with the lower confining pressure, i.e. more dilative response. In later stages of the shaking, i.e. when the confining pressure reduces to smaller value the butterfly shape of the stress path gets more pronounced due to having more dilative response in the lower confining pressure based on CSSM concept. In comparing this dense case to the case of shaking the loose sand column, the current case does not show any major sign of liquefaction (when stress ratio $r_u = 1$). This is due to the less contractive (more dilative) response of the sand in this case, which is coming from the denser state of the sample. Because of having partial segments of dilative response, the whole column of the sand has not lost its strength to the extent that happened for the case of loose sand and therefore smaller values of horizontal strains have been observed in the results. The absolute values of soil and water vertical displacements are also smaller than the case of loose sand which can be again referred to the less overall contractive response in this case.

Overall, it can be noted that the response in the case of loose sand ($e_0 = 0.85$) is mainly below the dilatancy surface (phase transformation surface) while the denser sand sample with $e_0 = 0.75$ shows partially dilative response referring to the denser than critical state.

505.3.3 Behavior of Saturated Sloping Ground

Figures (505.4) and (505.5) present the result of the numerical simulations for shaking the inclined soil columns (toward right) with loose and dense sand samples, respectively. The inclination of the soil column results in presence of the offset shear stress to the right side. This essentially poses asymmetric horizontal shear stresses (toward the direction of inclination) during cycles of shaking. On one hand, this offset shear stress makes the sample more dilative in the parts of shaking toward the right side (think about the state distance from the phase transformation line or dilatancy line in the $p - q$ space). As a result asymmetric butterfly loops will be induced causing the soil to regain its stiffness and strength (p) in the dilative parts of the corresponding cycles, therefore only instantaneous spikes of $r_u = 1$ can be observed in case of the sloped columns of soil. There is also a permanent liquefaction in terms of having stationary portions of $r_u = 1$ in this case. On the other hand, the offset shear stress results generation of more horizontal strains in the portions of loading which are directed toward the right side than those which are directed back toward the left side. As a result the horizontal shear strains will accumulative toward the right side and create larger permanent horizontal displacement comparing

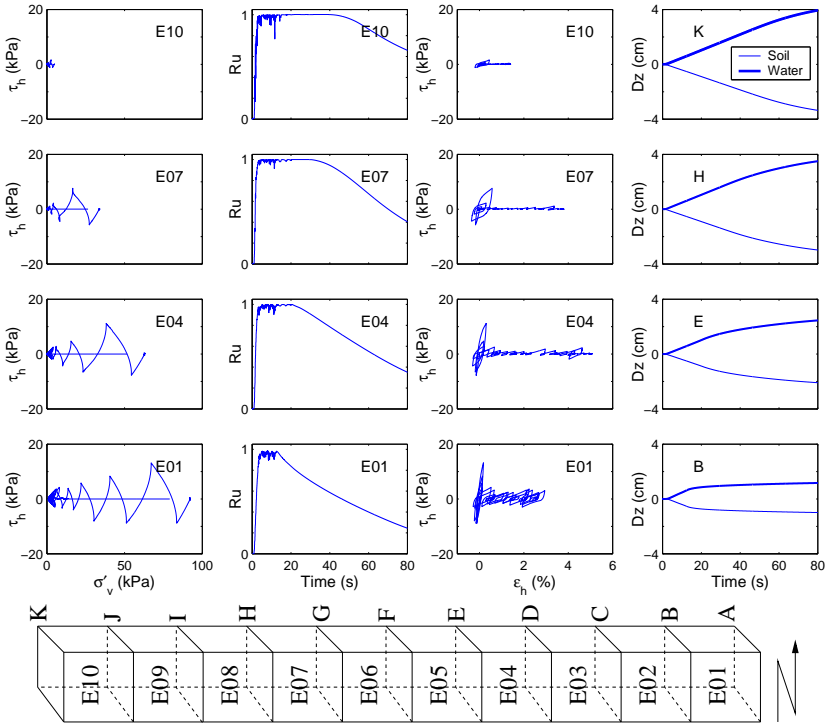


Figure 505.2: Seismic results for (loose sand) soil column in level ground ($e_0 = 0.85$).

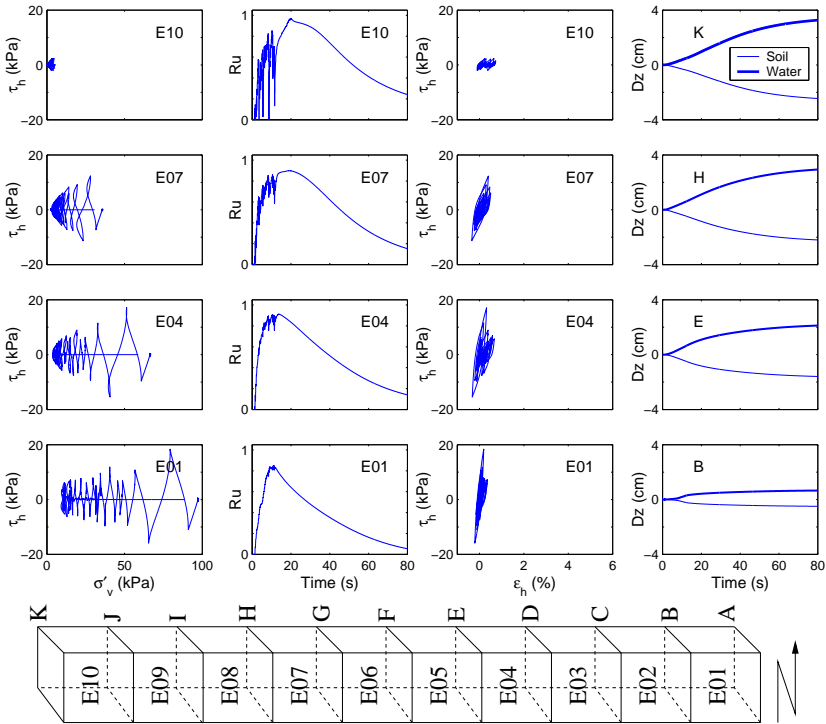


Figure 505.3: Seismic results for (dense sand) soil column in level ground ($e_0 = 0.75$).

to the case of level ground soil column. Since the overall dilative response of the dense sample, i.e. Figure (505.5), is larger than that of the loose sample, i.e. Figure (505.4), the dense sample shows stiffer response and therefore less accumulative horizontal shear strains than the loose sample. The difference in predicted horizontal displacements is almost three times, that is, for the dense sample the final, maximum horizontal displacement is approx. 0.5 m, while for the loose sand sample, it almost 1.5 m,

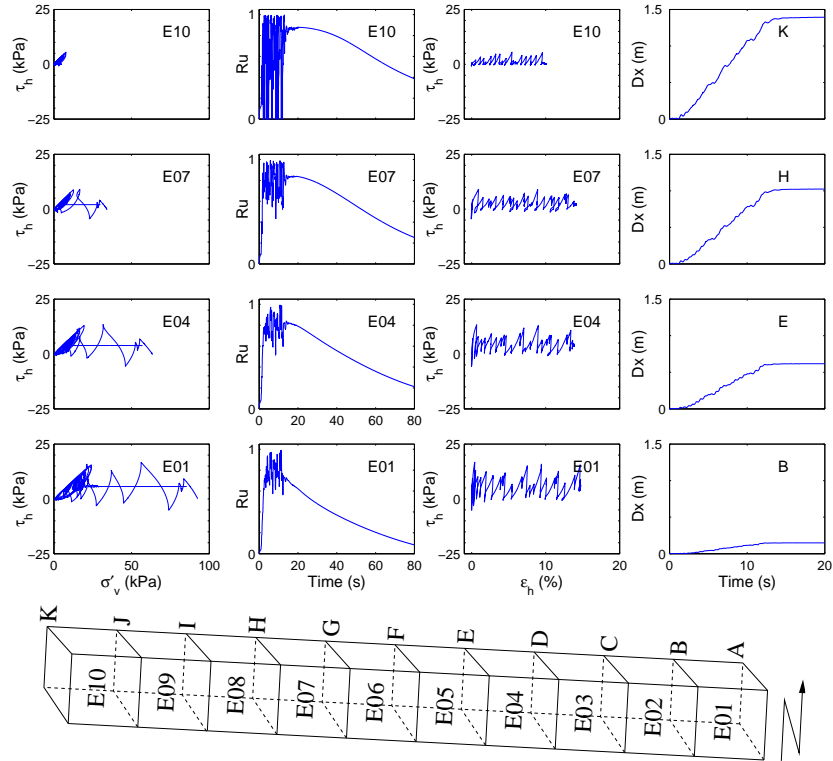


Figure 505.4: Seismic results for (loose sand) soil column in sloping ground ($e_0 = 0.85$).

505.4 Pile in Liquefied Ground, Staged Simulation Model Development

Material presented here is from [Cheng and Jeremić \(2009a,b\)](#) Model development for a pile in the liquefiable soil follows physics (mechanics) of the problem as close as possible. Numerical simulation of such problems in geomechanics is usually based on stages of loading and increments within those stages.

All load stages are applied to a series of finite element models, all of which share features of an initial soil model. This initial soil model consists of a soil block with dimension of $12 \times 12 \times 15$ m (length \times width \times depth). Due to the symmetry of the model, only half of the block is modeled. Symmetry assumptions is based on assumption that all the loads, dynamic shaking and other influences are symmetric with

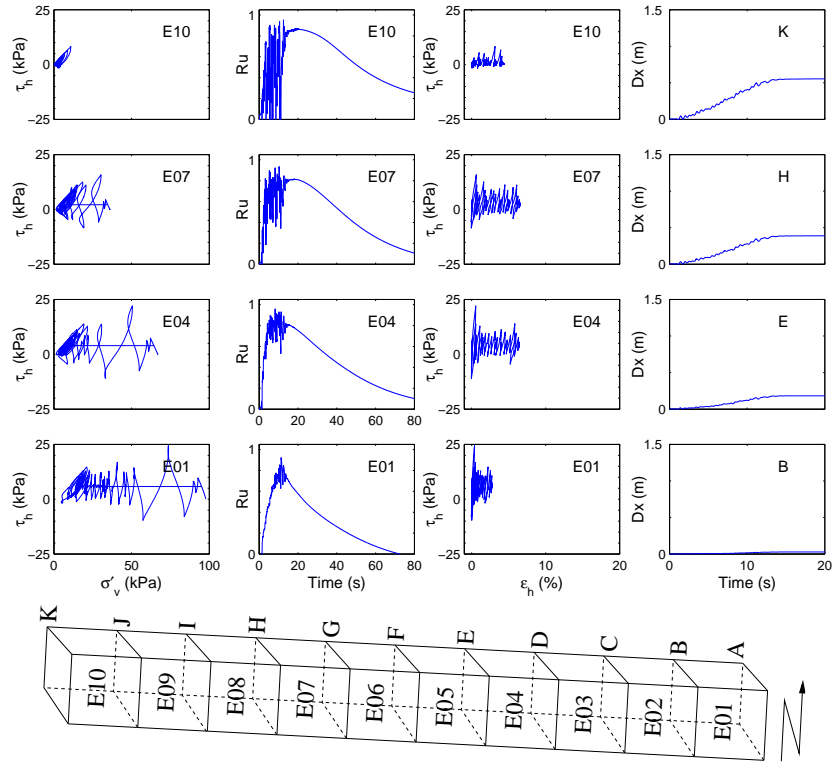


Figure 505.5: Seismic results for (dense sand) soil column in sloping ground ($e_0 = 0.75$).

respect to the plane of symmetry. This specialization to symmetric model reduces model generality (for example this use of symmetry will preclude analysis of dynamic shaking perpendicular to sloping ground dip). However, as our goal is to present a methodology of analyzing behavior of piles in liquefying ground, this potential drawback is not deemed significant in this study. Finite element mesh for the model is presented in Figure (505.6). The initial mesh consists of 160 eight node u-p-U elements.

Each node of the mesh has 7 degrees of freedom, three for soil skeleton displacements (u_i), one for pore water pressure (p), and three for pore water displacement (U_i). While it can be argued that the mesh is somewhat coarse, it is well refined around the pile, yet to be installed, in place of gray region in the middle.

A single set of parameters is used with the Dafalias-Manzari material model. Soil is modeled as Toyoura sand and material parameters (summarized in Table 505.4) are calibrated using tests by [Verdugo and Ishihara \(1996\)](#), while initial void ration was set to $e_0 = 0.80$. It is very important to emphasize that the state of stress and internal variables from initial state (zero for stress and given value for void ratio and fabric) will evolve through all stages of loading by proper modeling and algorithms, by using single set of material parameters. Table 505.4 presents additional parameters, other than material parameters

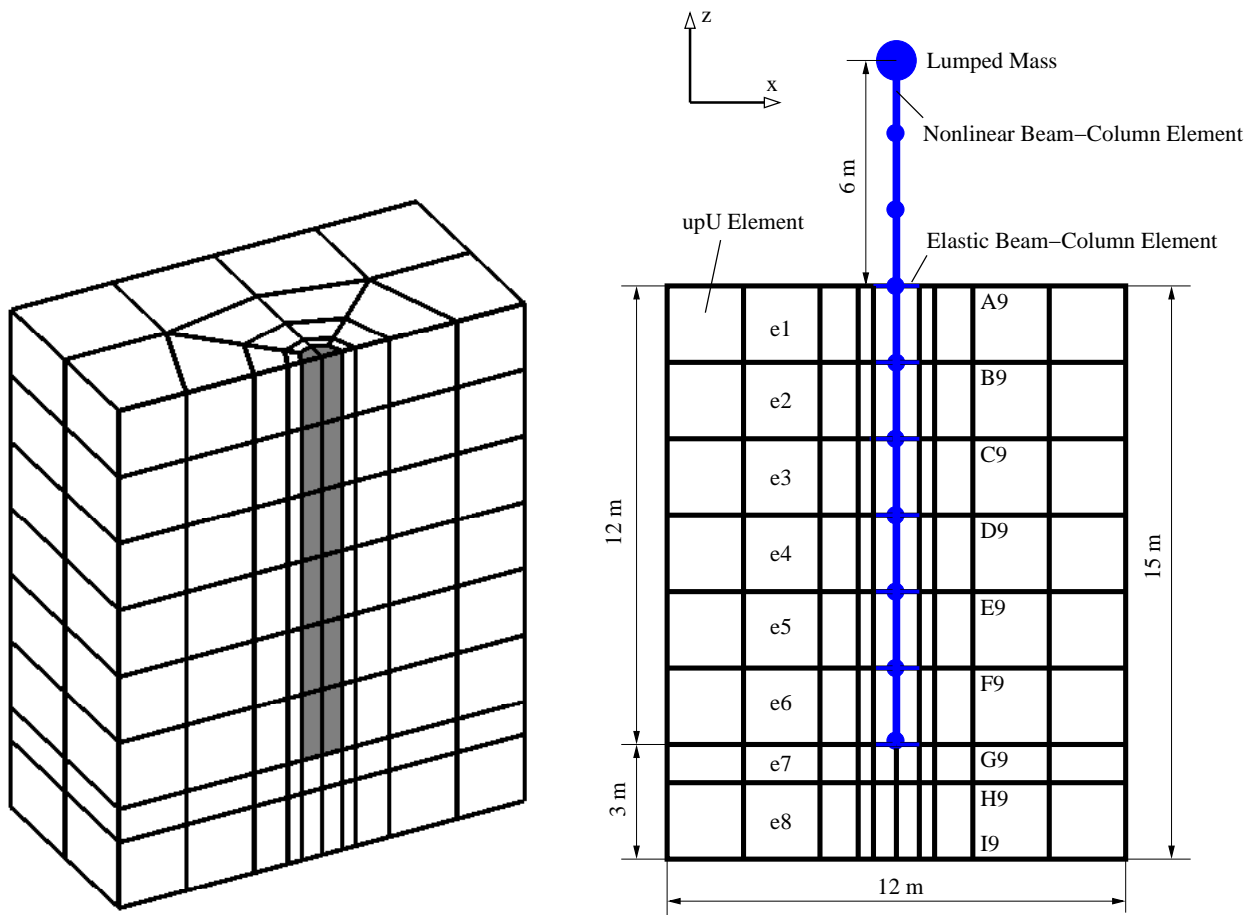


Figure 505.6: Left: Three dimensional finite element mesh featuring initial soil setup, where all the soil elements are present. The gray region of elements is excavated (numerically) and replaced by a pile during later stages of loading; Right: Side view of the pile-soil model with some element and node annotation, used to visualize results.

presented in Table 505.4, used for numerical simulations.

505.4.1 First Loading Stage: Self Weight

The initial stage of loading is represented by the application of self weight on soil, including both the soil skeleton and the pore water. Initial state in soil before application of self weight is of a zero stress and strain while void ratio and fabric are given initial values. The state of stress/strain, void ratio and fabric will evolve upon application of self weight. At the end of self weight loading stage, soil is under appropriate state of stress (K_0 stress), the void ratio corresponds to the void ratio after self weight (redistributed such that soil is denser at lower layers), while soil fabric has evolved with respect to stress

Table 505.3: Material parameters used for Dafalias–Manzari elastic–plastic model.

Material Parameter		Value	Material Parameter		Value
Elasticity	G_0	125 kPa	Plastic modulus	h_0	7.05
	v	0.05		c_h	0.968
	Critical state	M		n_b	1.1
		c		A_0	0.704
		λ_c		n_d	3.5
		ξ		z_{max}	4.0
		e_r		c_z	600.0
Yield surface		m			

Table 505.4: Additional parameters used in FEM simulations.

Parameter	Value	
Solid density	ρ_s	2800 kg/m^3
Fluid density	ρ_f	1000 kg/m^3
Solid particle bulk modulus	K_s	$1.0 \times 10^{12} \text{ kN/m}^2$
Pore fluid bulk modulus	K_f	$2.2 \times 10^6 \text{ kN/m}^2$
permeability	k	$1.0 \times 10^{-4} \text{ m/s}$
Gravity	g	10 m/s^2

induced anisotropy. All of these changes are modeled using Dafalias–Manzari material model and using constitutive and finite element level integration algorithms developed within UC Davis Computational Geomechanics group in recent years.

Boundary conditions (BC) for self weight stage of loading are set in the following way:

- Soil skeleton displacements (u_i), are fixed in all three directions at the bottom of the model. At the side planes, nodes move only vertically to mimic self-weight effect. All other nodes are free to move in any direction.
- Pore water pressures (p), are free to develop at the bottom plane and at all levels of the models except at the top level at soil surface where they are fixed (set to zero, replicating drained condition),
- Pore water displacements (U_i), are fixed in all three directions at the bottom, are free to move only vertically at four sides of the model and are free to move in any direction at all other nodes.

These boundary condition are consistent with initial self-weighting deformation condition for soil and pore water at the site.

For the case of sloping ground, an additional load sub-stage is applied after self weight loading, in order to mimic self weight of inclined (sloping) ground. This is effectively achieved by applying a resultant of total self weight of the soil skeleton times the sine of the inclination angle at uphill side of the model. This load is applied only to the solid skeleton DOFs, and not on the water DOFs. Physically it would be correct to consider the sloping ground effects on the pore water as well. This will create a constant flow field of the water downstream, which, while physically accurate, is small enough that it does not have any real effect on modeling and simulations performed here.

505.4.2 Second Loading Stage: Pile–Column Installation

After the first loading stage, comprising self weight applications (for level or sloping ground, as discussed above), second loading stage includes installation (construction) of the pile–column. Modeling changes performed during loading stage included:

- Excavation of soil occupying space where the pile will be installed. This was done by removing elements, nodes and loads on elements shown in gray in Figure (505.6).
- These elements were replaced by very soft set of elements with small stiffness, low permeability. This was done in order to prevent water from rushing into the newly opened hole in the ground after original soil elements (used in the first loading stage) are removed.
- Installation of a pile in the ground and a superstructure (column) above the ground. Nonlinear beam–column elements were used for both pile and column together with addition of appropriate nodal masses at each beam-column node, and with the addition of a larger mass at the top representing lumped mass of a bridge superstructure. Pile beam-column elements were connected with soil skeleton part of soil elements using a specially devised technique.

As mentioned earlier, the volume that would be physically occupied by the pile in the pile hole, is “excavated” during this loading stage. Beam–column elements, representing piles, are then placed in the middle of this opening. Pile (beam–column) elements are then connected to the surrounding soil elements by means of stiff elastic beam–column elements. These “connection” beam–column elements extend from each pile node to surrounding nodes of soil elements. The connectivity of nodes to soil skeleton nodes is done only for three beam–column translational DOFs, while the three rotational DOFs from the beam–column element are left unconnected. These three DOFs from the beam–column side are connected to first three DOFs of the u-p-U soil elements, representing displacements of the soil skeleton

(u_i) . Water displacements (U_i) and pore water pressures (p) are not connected in any way. Rather, these two sets of DOFs representing pore water behave in a physical manner (cannot enter newly created hole around pile beam–column elements) because of the addition of a soft, but very impermeable set of u-p-U elements, replacing excavated soil elements. By using this method, both solid phase (pile with soil skeleton) and the water phase (pore water within the soil) are appropriately modeled. Figure (505.7) shows in some detail schematics of coupling between the pile and soil skeleton part finite elements.

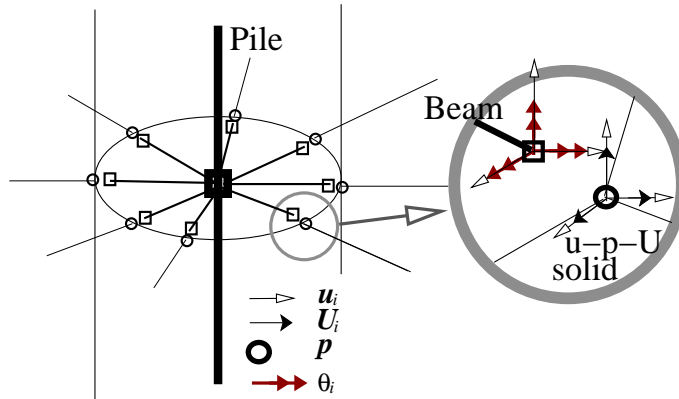


Figure 505.7: Schematic description of coupling of displacement DOFs (u_i) of beam–column element (pile) with displacement DOFs (u_i) of u-p-U elements (soil).

Nonlinear force based beam–column elements (Spacone et al., 1996a,b) were used for modeling the pile–column. Pile was assumed to be made of aluminum. This was done in order to be able to validate simulations with centrifuge experiments (when they become available). Presented models were all done in prototype scale, while for (possible future) validation, select results will be carefully scaled and compared with appropriate centrifuge modeling. Pile and the column were assumed to have a diameter of $d = 1.0$ m, with Young's modulus of $E = 68.5$ GPa, yield strength $f_y = 255$ kPa, and the density $\rho = 2.7$ kg/m³. Wall thickness of prototype pile–column is $t = 0.05$ m. Lumped mass of pile and column was distributed along the beam–column nodes, while an additional mass was added on top ($m = 1200$ kg) that represents (small) part of the superstructure mass. This particular mass ($m = 1200$ kg) comes from a standard (scaled up in our case) centrifuge model for pile–column–mass used at UCD.

Figure (505.6) (right side) shows side view of the column-pile-soil model after second stage of loading.

505.4.3 Third Loading Stage: Seismic Shaking

After the application of self weight on the uniform soil profile, excavation and construction of the single pile with column and super structure mass on top and application of their self weight, the model is at the

appropriate initial state for further application of loading. In this case, this additional loading comprises seismic shaking. For this stage, fixed horizontal DOFs used on the side planes during the first stage are removed (set free).

The input acceleration time history, shown in Figure (505.8) was taken from the recorded horizontal acceleration of Model No.1 of VELACS project [Arulanandan and Scott \(1993\)](#) by Rensselaer Polytechnic Institute, <http://geoinfo.usc.edu/gees/velacs/>. The magnitude of the motion is close to 0.2 g,

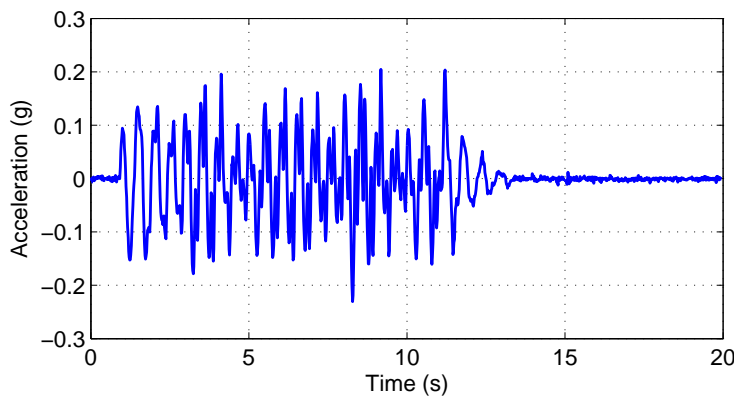


Figure 505.8: Input earthquake ground motions.

while main shaking lasts for about 12 seconds (from 1 s to 13 s). Although the input earthquake motions last until approx. 13 seconds, simulations are continued until 120 seconds so that both liquefaction (dynamic) and pore water dissipation (slow transient) can be appropriately simulated during and after earthquake shaking ([Jeremić et al., 2008](#)).

505.4.4 Free Field, Lateral and Longitudinal Models

Six models were developed during the course of this study. First three models (model numbers I, II and III) were for level ground, while last three models (model numbers IV, V, and VI) were for sloping ground. First in each series of models (model I for level ground and model IV for sloping ground) were left without the second loading stage, without a pile–column system. Other four models (numbers II, III, V and VI) were analyzed for all three loading stages. Second in each series of models (models number II and V) had all displacements and rotations of pile–column top (where additional mass representing superstructure was placed) left free, without restraints. Thus, these two models represent lateral behavior of a bridge. Third in each series of models (model numbers III and VI) had rotations in y directions fixed at the pile–column top, thus representing longitudinal behavior of a bridge. Modeling longitudinal behavior of a bridge by restraining rotations perpendicular to the bridge superstructure is appropriate if

the stiffness of a bridge superstructure is large enough, which in this case it was, as it was assumed to be a post-tensioned concrete box girder, so that realistically, the top of a column does not rotate (much) during application of loads. Table 505.5 summarizes models described above.

Table 505.5: Cases descriptions.

Case	Model sketch	Descriptions
I		horizontal ground, no pile
II		horizontal ground, single pile, free column head
III		horizontal ground, single pile, no rotation at column head
IV		sloping ground, no pile
V		sloping ground, single pile, free column head
VI		sloping ground, single pile, no rotation at column head

505.5 Simulation Results

505.5.1 Pore Fluid Migration

Figures (505.9) through (505.11) show the R_u time history for up to 30 seconds, for elements (at one of Gauss point) e1, e3, e5 and e7 (refer to right side of Figure (505.6)). It is important to note that R_u is defined as the ratio of the difference of initial mean and current mean effective stresses over the initial mean effective stress:

$$R_u = \frac{p'_{initial} - p'_{current}}{p'_{initial}}$$

where mean effective stress is defined as $p' = \sigma'_{kk}/3$. This is different from traditional definition for R_u , that uses ratio of excess pore pressure over the initial mean effective stress ($p'_{initial}$). However, these two definitions are essentially equivalent, as soil is in the state of liquefaction for $R_u = 1$ (so that $p'_{current} = 0$), while there is no excess pore pressure for $R_u = 0$ (so that $p'_{initial} = p'_{current}$). However,

the former definition is advocated here as it avoids the interpolation of pore pressure or extrapolation of the stresses (as the latter definition requires), since for the u-p-U element, stresses are available at Gauss points while pore pressures are available element nodes. In particular, Figure 505.9 shows R_u time

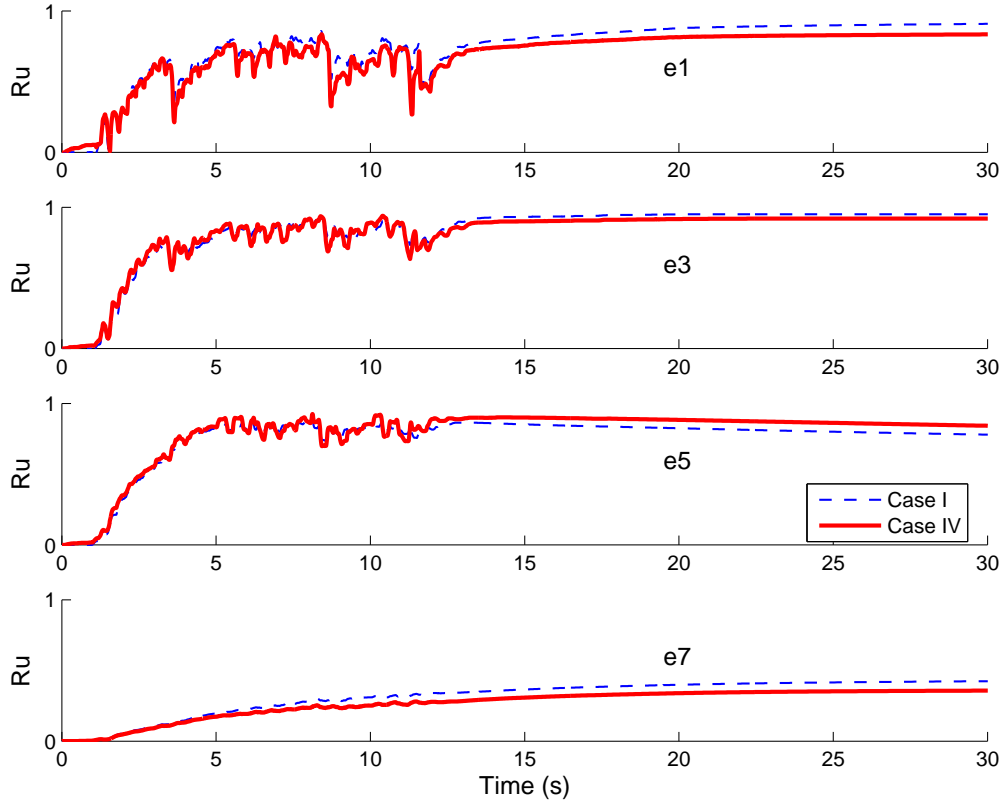


Figure 505.9: R_u times histories for elements e1 (top element), e3, e5, and e7 (bottom element) Gauss point for Cases I (level ground, no pile) and IV (sloping ground, no pile).

histories for four points for models I (level ground without pile) and model IV (sloping ground without pile). It is noted that differences are fairly small. It is interesting to observe that lower layers do not liquefy as supply of pore fluid for initial void ratio of $e_0 = 0.8$ is too small, and the pore fluid dissipation upward seems to be too rapid. On the other hand, the upper soil layers do reach close to or liquefaction state ($R_u = 1$). This is primarily due to the propagation of pore fluid pressure/volume from lower layers upward (pumping effect) and, in addition to that, to a local excess pore fluid production. These results can also be contrasted with those of Jeremić et al. (2008), where similar pumping scenario has been observed. The main difference between soil used by Jeremić et al. (2008) and here is in the coefficient of permeability. Namely, here $k = 1.0 \times 10^{-4} \text{ m/s}$ was used (Čubrinovski et al., 2008; Uzuoka et al., 2008) while Jeremić et al. (2008) used $k = 5.0 \times 10^{-4} \text{ m/s}$. It is important to note that other values of permeability for Toyoura sand have also been reported (Sakemi et al., 1995), but current value was

chosen based on Čubrinovski (2007 –).

In addition to that, similar to Jeremić et al. (2008), sloping ground case shows larger R_u spikes, since there is static shear force (stress) that is always present from gravity load on a slope. This static gravity on a slope will result in an asymmetric horizontal shear stresses in the down-slope direction during cycles of shaking. This asymmetric shear stress induces a more dilative response for down-slope shaking which will help soil regain its stiffness in the dilative parts of the loading cycles. This observation can be used to explain smaller R_u spikes for the sloping ground case. Of course, this asymmetry in loading will result in larger accumulation of down-slope deformation.

While R_u ratios for level and sloping ground cases are fairly similar along the depth of the model, the response changes when the pile is present. Figure (505.10) shows R_u responses at four different points (along the depth) approximately midway between the pile and the model boundary, in the plane of shaking (see location of those elements in Figure (505.6) on page 2616). In comparison to behavior without the pile (Figure (505.9)), it is immediately obvious that addition of a pile with a mass on top reduces R_u during shaking for the top element (e1). This is to be expected as presence of a pile–column–mass (PCM) system changes the dynamics of the top layers of soil significantly enough to reduce total amount of shear. This is particularly true for the top layers of soil as effects of column–mass tend to create compressive and extensive movements (compression when the PCM system moves toward soil and extension, and possibly even tension, when PCM system moves away from soil). However, this extension, or possible tension, is not directly observable in presented plots since array of elements where we follow R_u (e1, e3, e5, e7) is some distance away from the pile–soil interface. Middle layers (e3 and e5), on the other hand, display similar response to that of Cases I and IV, as shown in Figure (505.9). It is noted that in a case with of sloping ground with pile, the R_u measurements are always larger than those for level ground (this is also observed for Cases III and VI, as shown in Figure (505.11)). This is expected as presence of a pile in loose sand, and particularly the dynamic movement of a pile during seismic shaking, create an additional shearing deformation field (in the soil adjacent to the pile) that provides for additional (faster) compression of soil skeleton and thus creates additional volume of pore fluid, that is then distributed to adjacent soil (adjacent to the pile).

Particularly interesting are R_u results for soil element e7, which is located below pile tip level (see Figure (505.6)). Observed R_u for Case V in element e7 is significantly larger than for the same element for Case II. Similarly, simulated R_u is larger than what was observed in cases without a pile (see bottom of Figure (505.9)). This increase in R_u for Case V (sloping ground with pile) is explained by noting that the pile “reinforces” upper soil layers and thus prevents excess shear deformation in the upper 12.0 m of soil (above pile tip). The reduction of deformation in upper layers of soil (top 12.0 meters) results in transfer of excessive soil deformation to soil layers below pile tip (where element e7 is located). This,

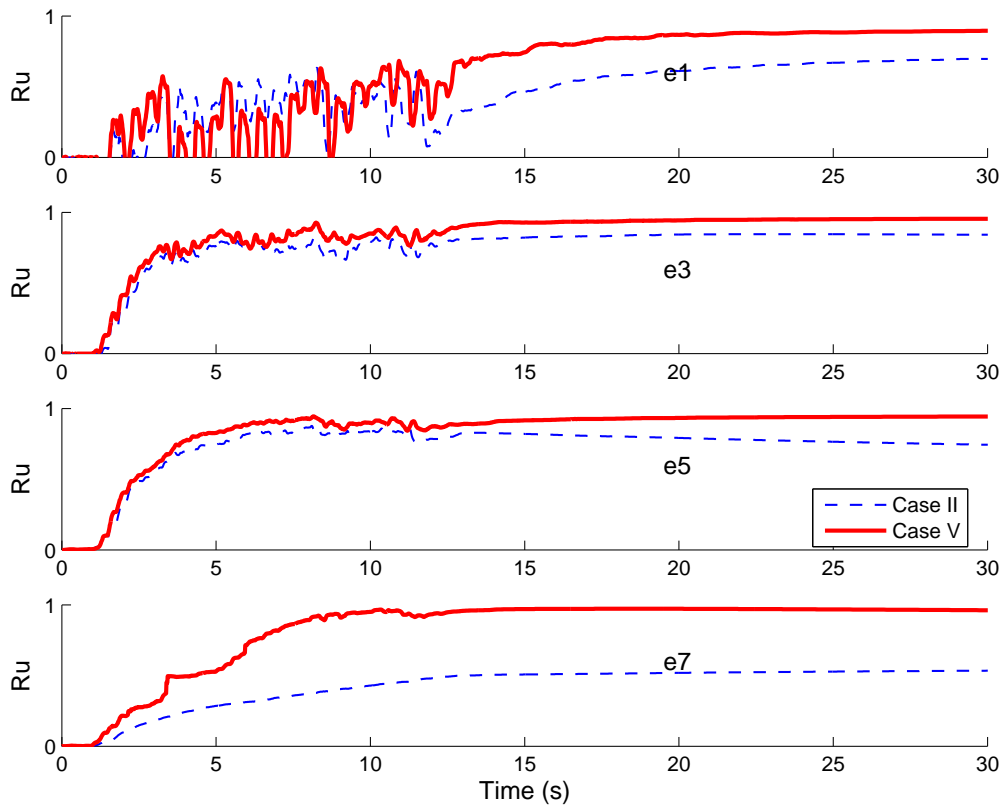


Figure 505.10: R_u times histories for elements e1, e3, e5, and e7 (upper Gauss point) for Cases II (level ground, with pile–column, free column head) and V (sloping ground, with pile–column, free column head).

in turn, results in a much larger and faster shearing of those lower loose soil layers. This significantly larger shearing results in a much higher R_u . Deformed shape, shown in Figure (505.12) for Case V, reinforces this explanation, showing much large shearing deformation in lower soil layers, below pile tip. Same observation can be made for Case VI, shown in Figure (505.12).

Observation similar to the above, for Cases II and V can be made for Cases III and VI, results for which are shown in Figure (505.11). One noticeable difference in R_u results between cases with free column head (Cases II and V) and cases with fixed rotation column head (Cases III and VI) is in significantly larger (and faster) development of R_u close to soil surface for a stiffer, no rotation column cases (Cases III and VI). This much larger R_u observed in a “stiffer” PCM system setup, is due to larger shearing deformation that develops in soils adjacent to the pile during shaking. The stiffer PCM system can displace less (because of additional no rotation condition on column top) while the soil beneath is undergoing shaking (same demand in all cases), thus resulting in larger relative shearing of soil, which then results in larger and faster pore pressure development close to the soil surface, where the column

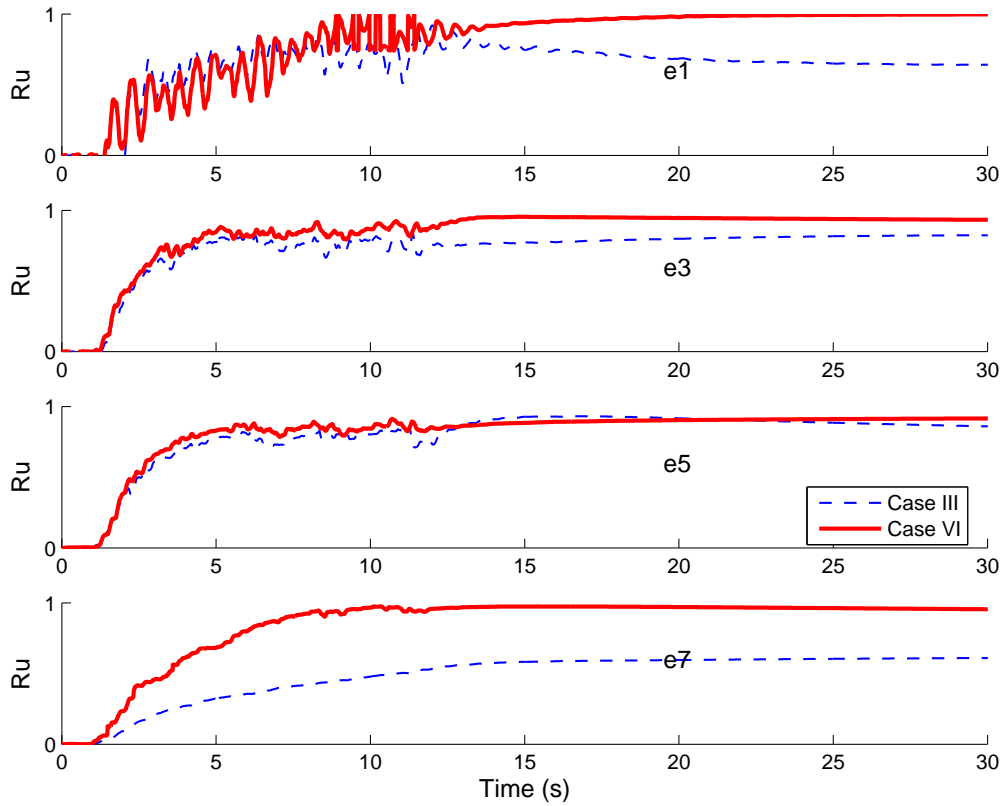


Figure 505.11: R_u times histories for elements e1, e3, e5, and e7 (upper Gauss point) for Cases III (level ground, with pile, no rotation of pile head) and VI (sloping ground, with pile-column, no rotation of column head).

no rotation effect is most pronounced.

505.5.2 Soil Skeleton Deformation

A number of deformation modes is observed for both level and sloping ground cases, with or without PCM system. Figure (505.12) shows deformation patterns and excess pore pressures in symmetry plane for all six cases over a period of eighty seconds. A number of observation can be made on both deformation patterns, excess pore fluid patterns and their close coupling.

Level Ground without Pile (Case I). Excess pore pressures and deformations in symmetry plane for level ground without a pile are shown in Figure (505.12) (I). At the very beginning (at $t = 2$ s) there is initial development of excess pore fluid pressure in the middle soil layers. This expected, as the self weight loading stage has densified lower soil layers enough so that their response is not initially contractive enough to produce excess pore pressure. Top soil layers, on the other hand, have a drainage boundary

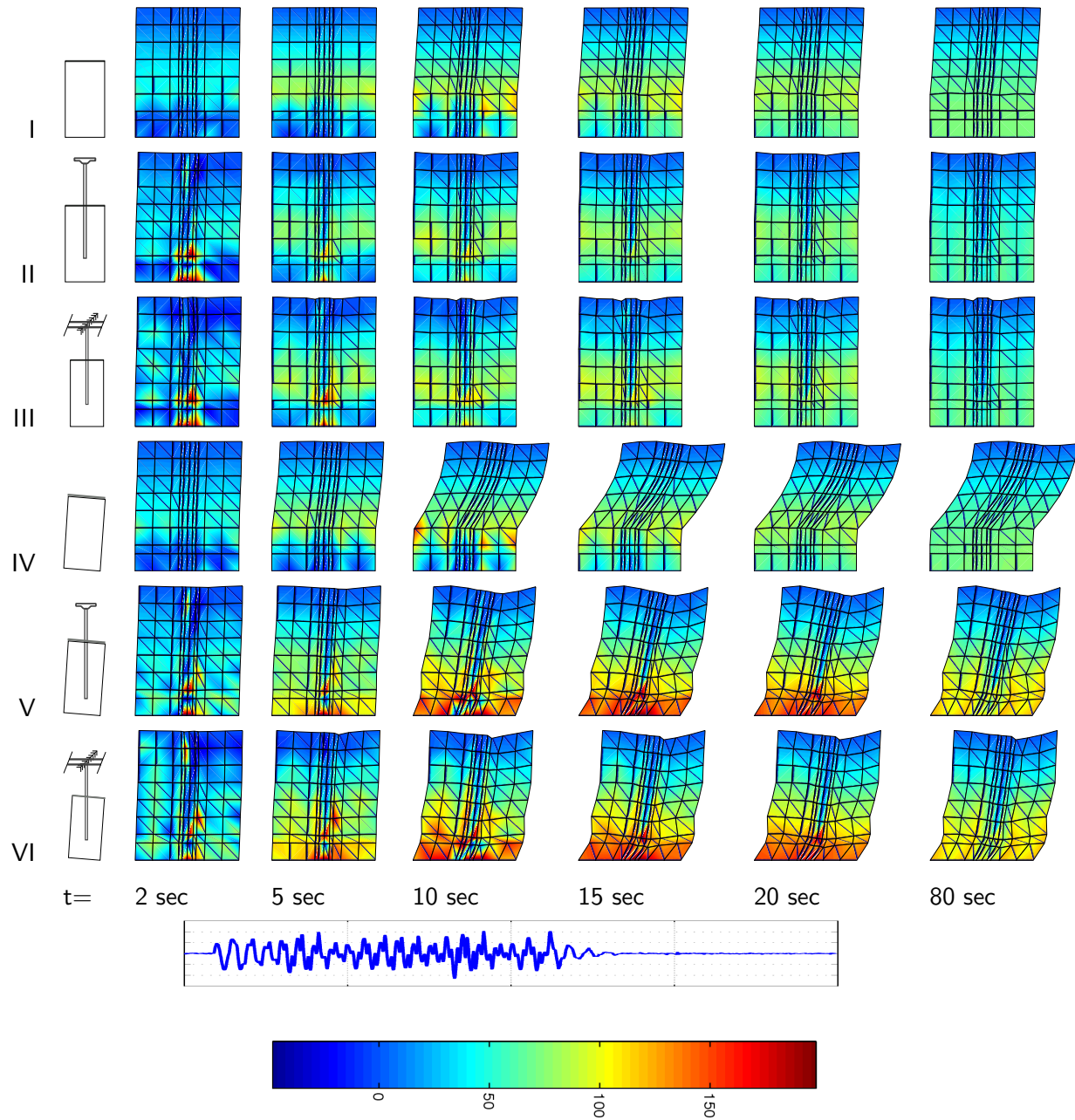


Figure 505.12: Time sequence of deformed shapes and excess pore pressure in symmetry plane of a soil system. Deformation is exaggerated 15 times; Color scale for excess pore pressures (above) is in kN/m^2 . Graph of ground motions used (also shown in Figure (505.8)) is placed below appropriate time snapshots and is matching for $t = 2, 5, 10, 15, 20$ seconds while at $t = 80$ seconds there is no seismic shaking.

(top surface) too close to develop any significant excess pore pressures. As seismic shaking progresses (for $t = 5, 10$ s), the excess pore pressure increases, and starts developing in lower soil layers as well. It should be noted that a small non-uniformity in results is present. For example, zones of variable, nonuniform excess pore pressures on the lower mid and right side for Case I at $t = 10$ s develop. Nonuniform mesh (many small, long elements in the middle, large elements outside this middle zone) may introduce small numerical errors in results which can be observed by slightly nonuniform results at $t = 10$ s and $t = 15$ s. It should be noted that results for excess pore pressure shown for first 13 seconds (during shaking) in Figure (505.12) (I) are transient in nature, that is, seismic waves are traveling throughout the domain (model) during shaking (first 13 seconds) and slight oscillations in vertical stresses are possible. This oscillations will contribute to the (small) non-uniformity of excess pore pressure results. After the shaking (after 15 seconds) resulting excess pore pressure field is quite uniform.

Level Ground with Pile (Cases II and III). Excess pore pressures and deformations in symmetry plane for models with PCM system and with two different boundary conditions at top of column (see model description in section 505.4.4) in level ground are shown in Figures (505.12) (II and III). One of the interesting observations is significant shearing and excess pore pressure generation adjacent to the pile tip. The reason for this is that pile is too short, that is, pile tip has significant horizontal displacements during shaking. Those pile tip displacements shear the soil, resulting in excess pore pressure generation. As soon as there is time for dissipation, this localized excess pore pressure dissipates to adjacent soil, and then, after shaking has ceased (at $t = 13$ s and later), it slowly dissipates upward. Addition of pile into the model (construction), with a highly impermeable elements (that mimic permeability of concrete) is apparent as there is a low excess pore pressure region in the middle of model, where pile is located.

Sloping Ground without Pile (Case IV). Excess pore pressures and deformation in symmetry plane for sloping ground without pile is shown in Figures (505.12) (IV). It is noted that initially the excess pore pressure starts developing in middle soil layers, similar to the Case I above. Bottom layers start developing excess pore pressure only after significant shear deformation occurs (at $t = 10$ s) at approximately 2/3 of the model depth. Lower layers have densified enough during self weight stage of loading that initial shaking is not strong enough to create excess pore water pressure, rather, those layers are fed by the excess pore pressure from above. Lower soil layers also do not develop much deformation, while middle and upper layers together develop excessive horizontal deformation.

Sloping Ground with Pile (Cases V and VI). Excess pore pressures and deformation in symmetry plane for sloping ground with PCM system are shown in Figures (505.12) (V and VI). Similar to the above cases

(II and III), pile is too short and there is again excessive shearing of soil at the pile tip, suggesting large movement of that pile tip. In addition to that, pile introduces significant stiffness to upper 12 meters of soil (along the length of pile) and helps reduce deformation of those upper soil layers. Down-slope gravity load is thus transferred to lower soil layers (below pile tip) which exhibit most of the deformation. It should be noted that soil in middle and upper layers (adjacent to pile) does deform, just not as much as the soil below pile tip. The predominant mode of deformation of middle soil layers is shearing in horizontal plane, around the pile. Deformation in horizontal plane is not significant as the pile is short in this examples (as mentioned above) and does not have enough horizontal support at the bottom. The deformation pattern of a soil – pile system is such that pile experiences significant rotation, and deforms with the soil that moves down-slope. If the pile was longer, and if it had significant horizontal support at the bottom, the middle and upper soil layers would have showed more significant flow around the pile in horizontal planes.

Upper layers undergo significant settlement, as seen in Figure (505.13). This settlement is mainly caused by the above mentioned rotation of pile–soil system, where soil in general settles (compacts) but also undergoes differential settlement, between left (up-slope from pile) and right (down-slope from pile) side of the model. As significant shearing with excess pore pressure generation develops in lower soil layers, below pile tip, those lower layers contribute to most of down-slope horizontal deformation. In a sense, all the demand from down-slope gravity forces and seismic shaking is now responded to by lower soil layers, which contribute to most of the excess pore pressure generation and consequently, to most of the soil deformation. Soil surface horizontal deformation is thus strongly influenced by significant shearing of the bottom layers and by rotation of the middle and upper soil layers with the pile. It is interesting to note that the largest settlement is observed just down-slope from pile for Cases V and VI.

505.5.3 Pile Response

Figure (505.14) shows bending moment envelops for pile–column–mass (PCM) system for all four cases (II, III, V and VI). It should be noted that bending moment diagrams are plotted on compression side of the beam–column. A number of observations can be made about bending moment envelopes. For cases with free pile head (shaking transverse to the bridge main axes, Cases II and V) the maximum moments are attained in soil, at depths of approximately $0.6D - 1.2D$, where D ($= 1.0\text{ m}$ in this case) is the pile diameter. Opposed to that are cases for PCM systems with restricted rotations at the pile top which (Cases III and VI), which, of course feature largest moment at the column top. Maximum bending moments for section of PCM system in soil (pile) in these two cases are now attained at the depth of approximately $1.8D - 2.0D$.

It is noted that bending moment envelopes are mostly symmetric. Slight non-symmetry is introduced

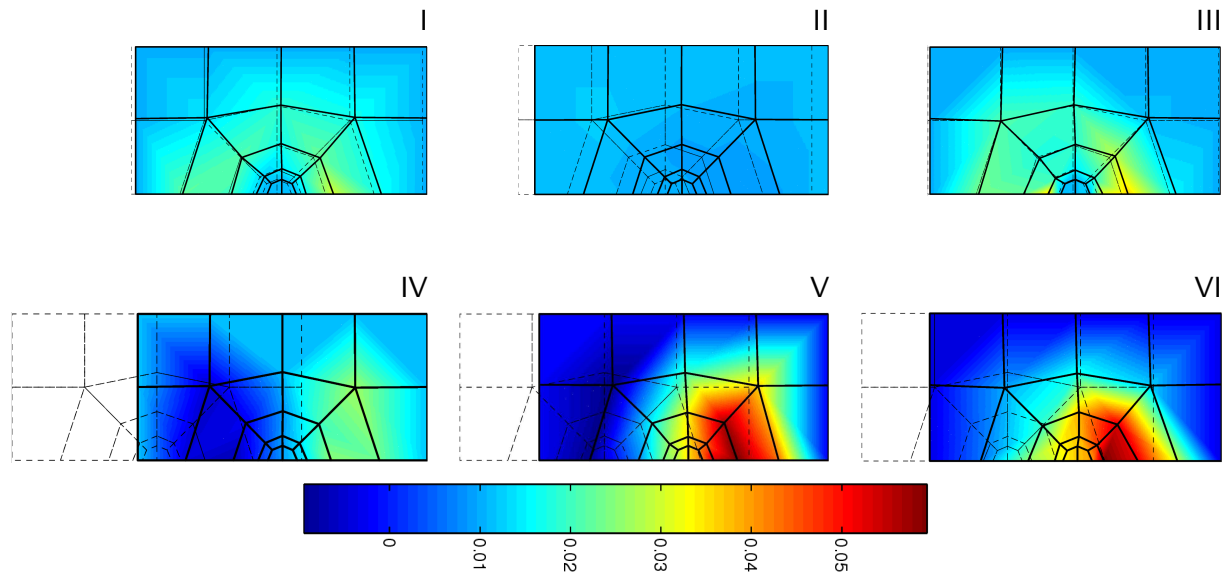


Figure 505.13: Soil surface settlements at 120 s for all six cases. Color scale given in meters

for cases on sloping ground (Case V and VI). It is also noted that moments do exist (are not zero) all the way to the bottom of the pile. Theoretically, moments should be zero at the pile tip, but since physical volume of the pile is considered (see note on that in section 505.4.2 and Figure (505.7)), differential pressure on pile bottom from soil will produce small (non-zero) moments even at the pile tip. More importantly, non-zero moments at the bottom and along the lower part of the pile show that pile is indeed too short, and thus changing curvatures are present along the whole length of the pile.

505.5.4 Pile Pinning Effects

Piles in sloping liquefying ground can also be used to resist movement of soil (all liquefied or liquefied with hard crust on top) down-slope. For models developed in this paper, pile pinning effect can be investigated for Cases IV, V and VI. In particular, deformation of sloping ground without the pile (Case IV) can be compared with either of the cases of piles in sloping ground, Cases V and VI. It is very important to note, again, that models developed here had relatively short pile, and that major soil shearing developed below the pile tip. This apparent shortcoming of a short pile results in reduced pile pinning capacity, thus reducing the down-slope movement by only approximately half, from 0.35 m (Case IV) to 0.22 m (Case V) and to 0.18 m (Case VI) as seen in Figure (505.15). It would have been expected that, had the pile been longer and had it penetrated in deeper, non-liquefiable layers, it would have reduced down-slope movement of the soil to a much larger extent. However, had the pile been longer and had it penetrated non-liquefiable layers, it would have had a much firmer horizontal support

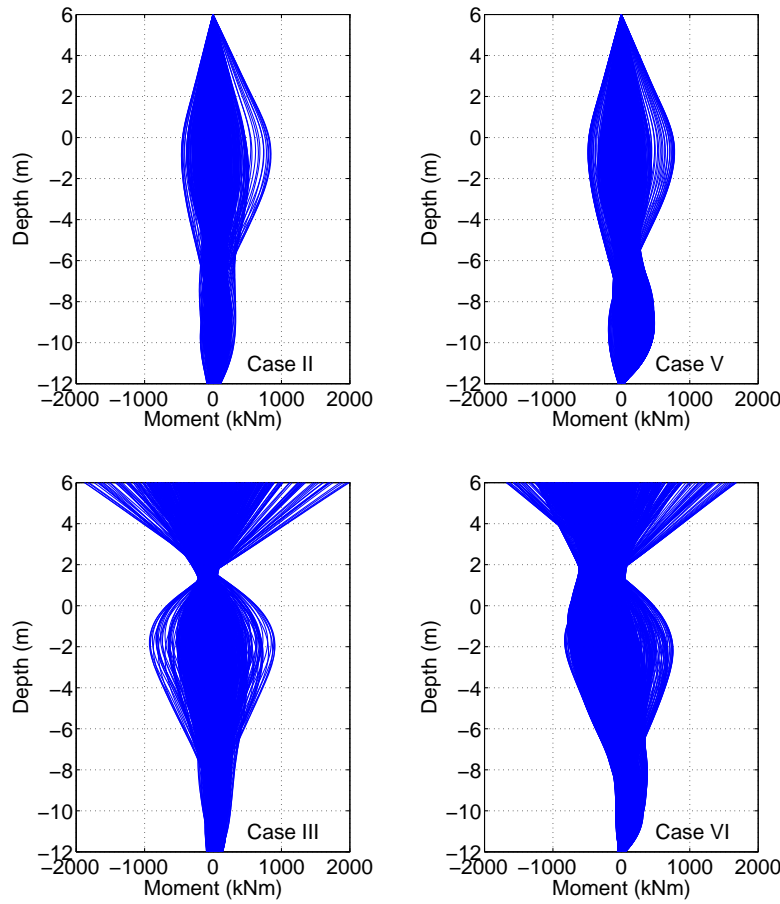


Figure 505.14: Envelope of bending moments for pile–column system for Cases II, III, V and VI.

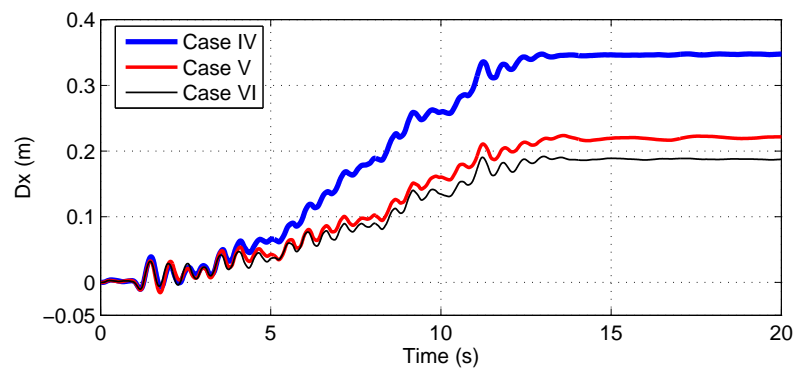


Figure 505.15: Down-slope movement at the ground surface (model center) for Cases IV (no pile), V and VI (with pile-mass system).

Chapter 506

Slope Stability in 2D and 3D

(1999-2010-)

(In collaboration with Dr. Nima Tafazzoli)

506.1 Chapter Summary and Highlights

506.2 Introduction

Presented here is a brief overview of a work on determining factors of safety for a 3D slope for one of the prominent dams in the midwest, for different saturation and water level conditions.

506.3 Dam Section Geometry

Figures 506.1 and 506.2 shows the satellite picture of location



Figure 506.1: Dam satellite picture. Upstream (south facing) three dimensional slope at connection of the embankment and concrete gravity dam is evaluated for potential stability problem.

Figure 506.3 shows the sonar data for water depth measurements at the location of a 3D slope in question.

An interesting topographical feature resembling a valley should be noted at the toe of (beginning of) wrap around section of upstream section of the embankment. That topographical feature is also apparent in a photo taken during Wold Creek Dam construction in 1948, show in Figure 506.4. Figure 506.5 shows rock surface under the embankment and alluvial fill, that serves as base rock foundation for both the alluvial fill and the embankment above. Figures 506.6, 506.7 and 506.8 show sections of the curved, 3D slope of the upstream embankment next to the concrete dam section. In particular, Figure 506.6 shows a dam section perpendicular to the dam axes. Note a significant extent of the alluvium that was left in place during dam construction. Similarly, the alluvium is present in both section inclined at 45° to dam axes (Figure 506.7) and a section parallel to the dam axes (Figure 506.8).

Analyzed 3D, curved section of the upstream embankment is also shown in a photograph in Figure 506.9, taken on morning of April 21st, 2010. Note a significant length/extent of the two sheet pile walls (one running along the length of work platform and the other one at the end of work platform, next to

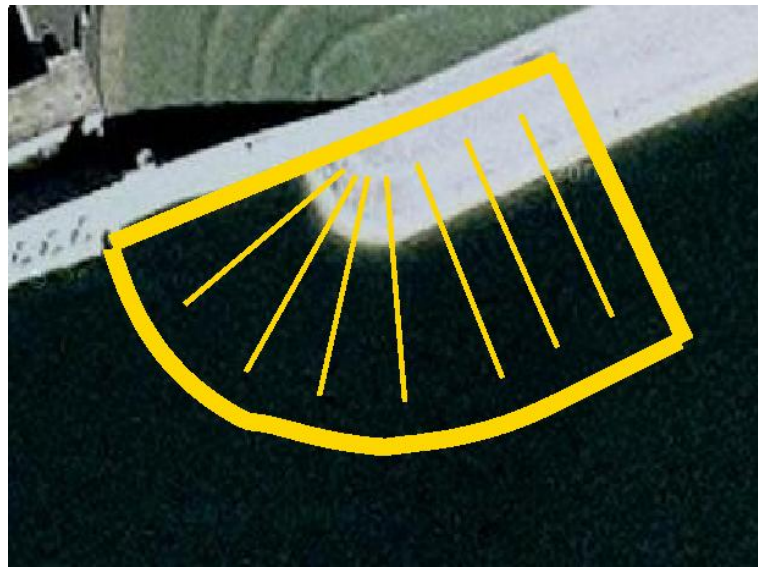


Figure 506.2: Dam satellite picture with location of 3D slope under consideration for potential stability problem.

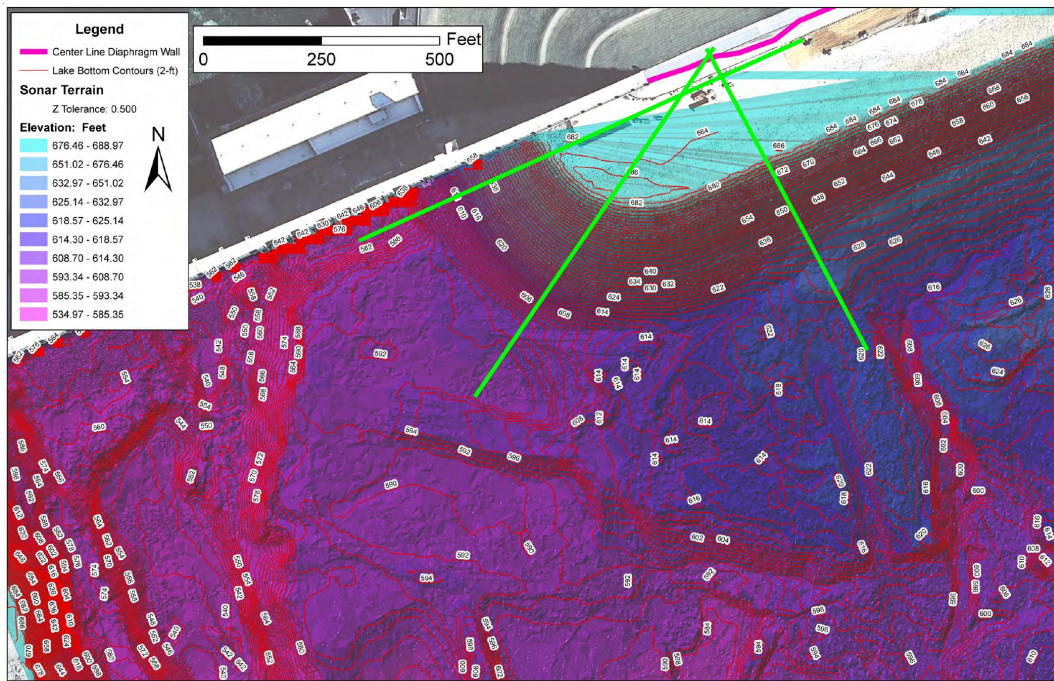


Figure 506.3: Dam sonar data for water depth for the analyzed 3D slope.

concrete dam section).

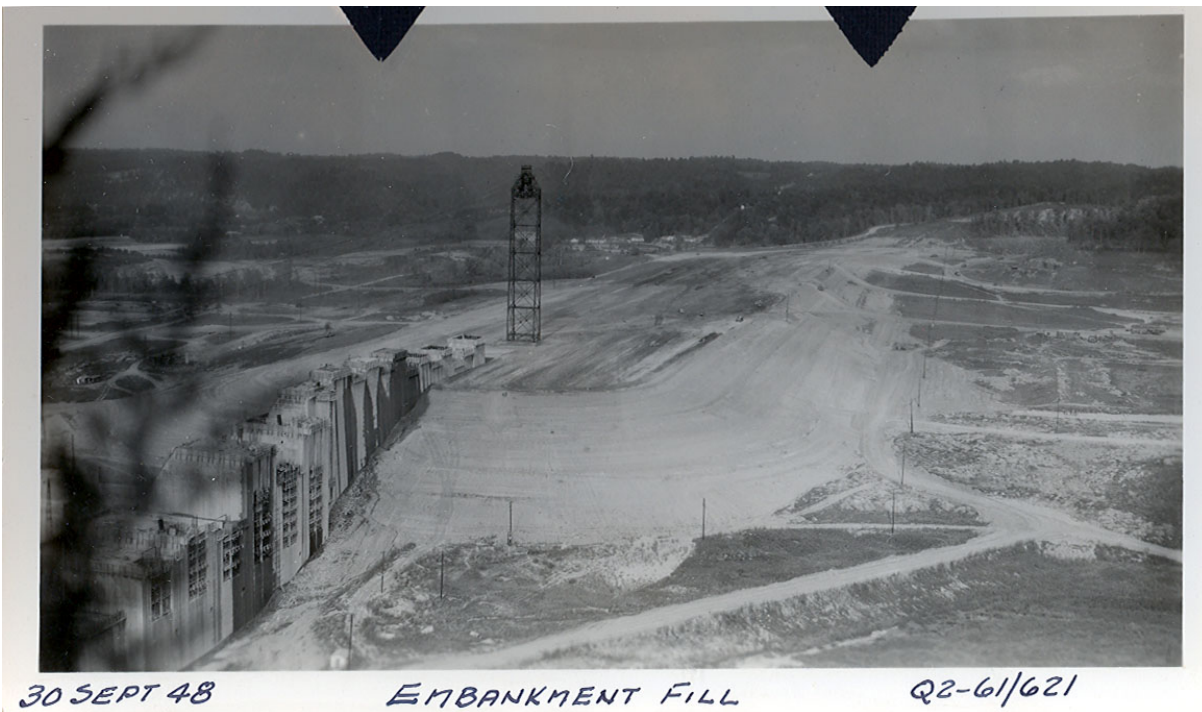


Figure 506.4: Dam during construction, 1948. View toward the upstream curved slope. Note shallow valley where the straight section of pole line ends, approximately at the end or straight slope, toward the beginning of curves slope section (Photo courtesy of Mike Zoccola, USACE).

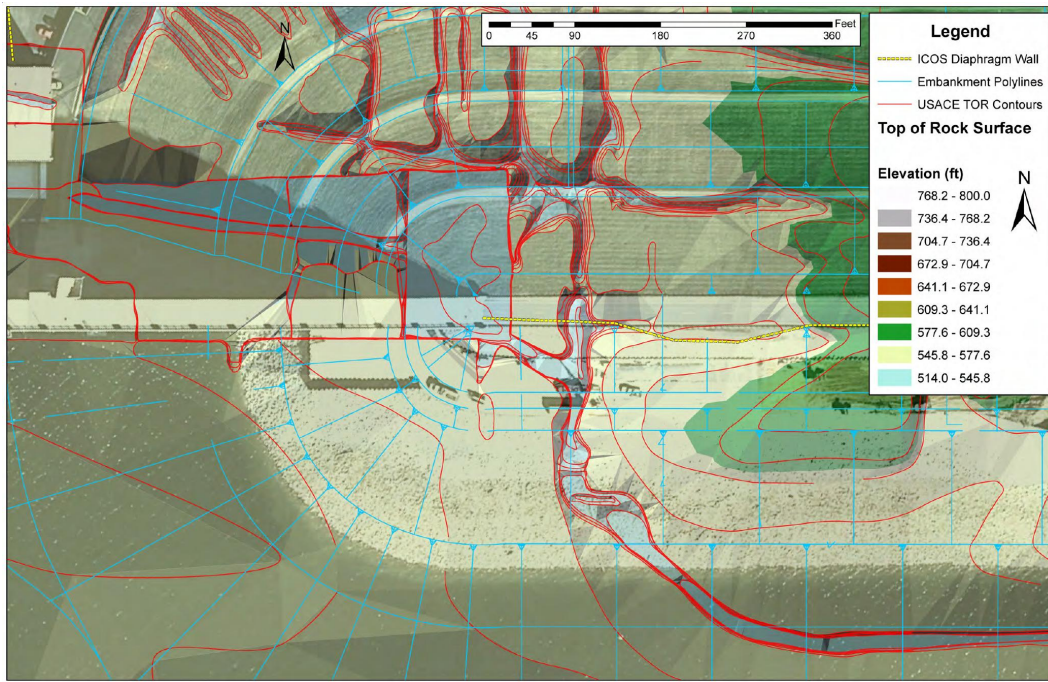


Figure 506.5: Dam rock surface data under the embankment and alluvial fill (under analyzed 3D slope), used for defining FEM model boundary conditions.

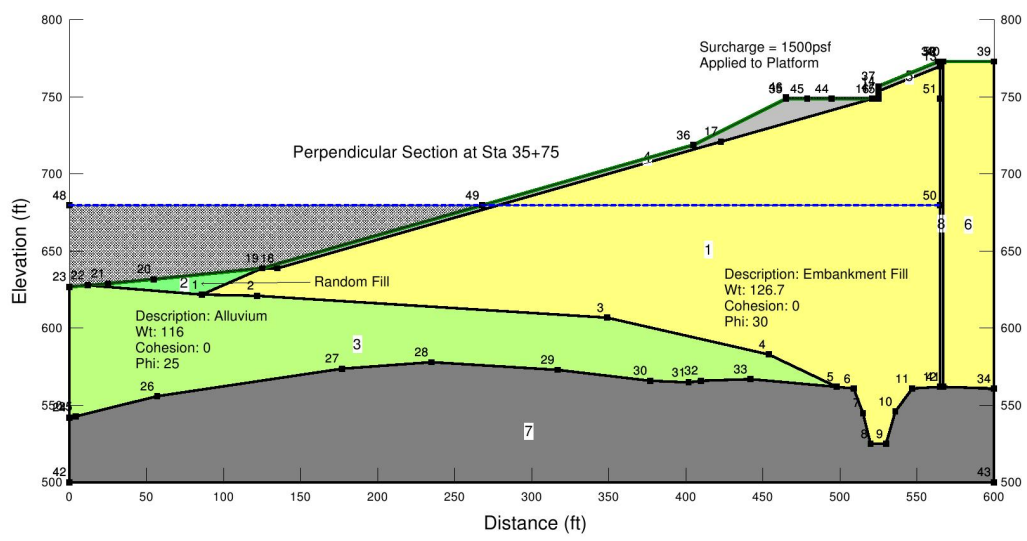


Figure 506.6: Dam section perpendicular to the dam axes for analyzed 3D slope.

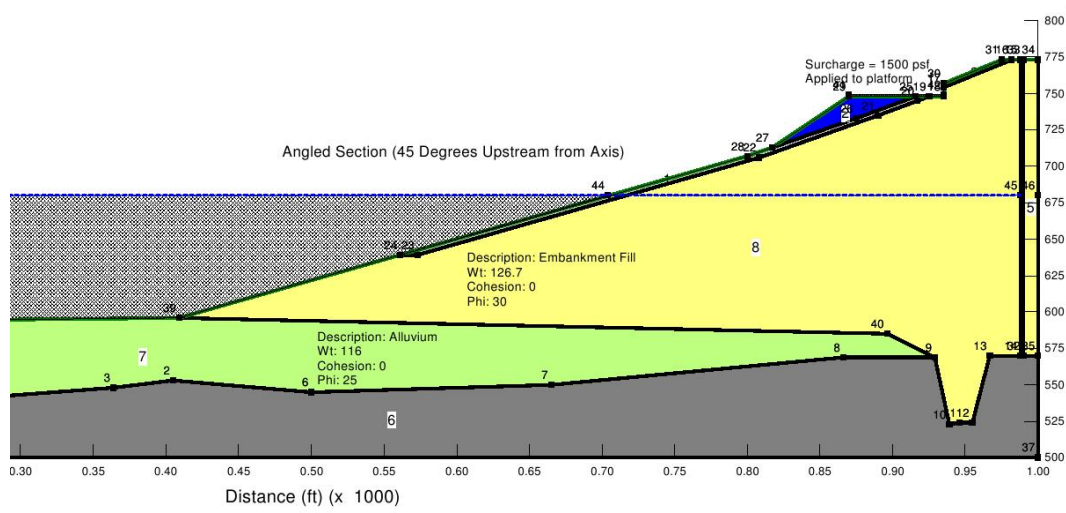


Figure 506.7: Dam section inclined at 45° to dam axes for analyzed 3D slope.

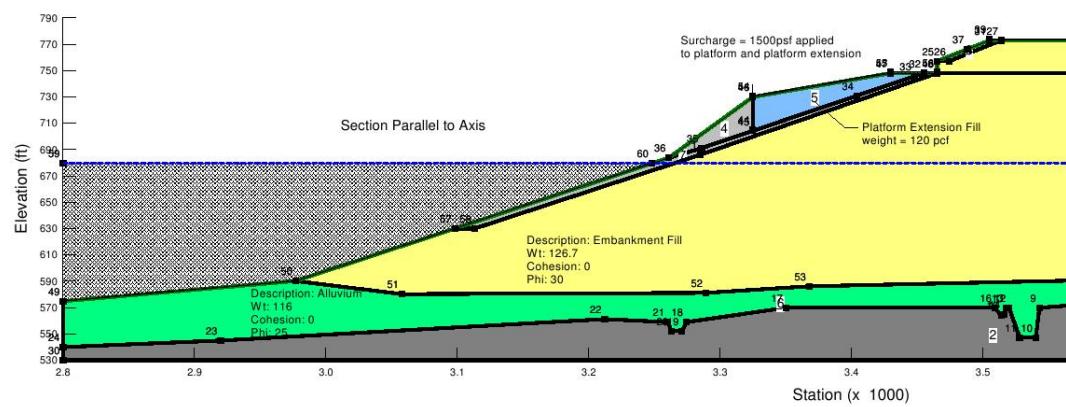


Figure 506.8: Dam section parallel to the dam axes for analyzed 3D slope.



Figure 506.9: Dam view toward the curved, "wrap" section, upstream side.

506.4 Finite Element Modeling

Analysis of 2D and 3D slope stability problem was performed using finite element method. In particular, the strength reduction method was used in conjunction with 2D and 3D finite element models to assess factors of safety. Main focus was on determining the difference between 2D and 3D factors of safety.

506.4.1 Material Models

During initial teleconference, in early April, it was decided to perform two dimensional and three dimensional analysis using finite element method for two limiting cases of material behavior:

- fully drained material behavior, with material defined by a friction angle and no cohesion,
- fully undrained material behavior, with material defined by an undrained shear strength.

Parameters for drained material modeling are given in table 506.1 below. In addition to that table

Table 506.1: Drained strength material parameters.

Material	Unit Weight [pcf]	ϕ [deg]	S_u [psf]
Embankment Fill	126.7	30	0
Alluvial Soil	116	25	0
Random Fill	120	20	0
Riprap	110	40	0
Shot Rock Fill	145	45	0
Platform Extension Fill	120	20	0

506.2 below, defines parameters for undrained material modeling. Those material parameters were agreed upon after few and a discussion. It should be noted that USACE has initiated a testing program that will determine material parameters of the embankment and the alluvium with higher certainty.

Two material models were used for analysis. For drained analysis, a Drucker Prager material model was used. This model is described in some detail in Section 3.5.7 of my lecture notes [Jeremić et al. \(1989-2025\)](#) (available online through my web site). It is important to note that single value of friction angle was used, thus rendering friction angle for both compression and extension the same. While there might be an influence of the difference of friction angle for compression and extension, such difference was not analyzed here. For undrained analysis a total stress, von Mises model was used. This model is also described in some details in Section 3.5.6 of my lecture notes [Jeremić et al. \(1989-2025\)](#). Both models used here feature perfectly plastic behavior after yielding, with associated plastic flow.

Table 506.2: Revised undrained strength material parameters.

Material	Unit Weight [pcf]	ϕ [deg]	S_u [psf]
Embankment Fill	126.7	0	2000
Alluvial Soil	116	0	1000-1500
Random Fill	120	0	500
Riprap	110	40	0
Shot Rock Fill	145	45	0
Platform Extension Fill	120	20	0

506.4.2 Two Dimensional Models

Three two dimensional (2D) models were developed in order to test the effects mesh size has on quality of simulations. Developed 2D mesh was based on perpendicular cross section, shown in Figure 506.6. Mesh for a 2D model, shown in Figure 506.10, represents a very coarse mesh, which, if higher order elements are used (with displacement interpolation higher than linear) might actually work quite well. However, with linear interpolating displacements, this mesh is clearly of low quality. However, this mesh was used as a first iteration, and to gain initial insight into 2D behavior.

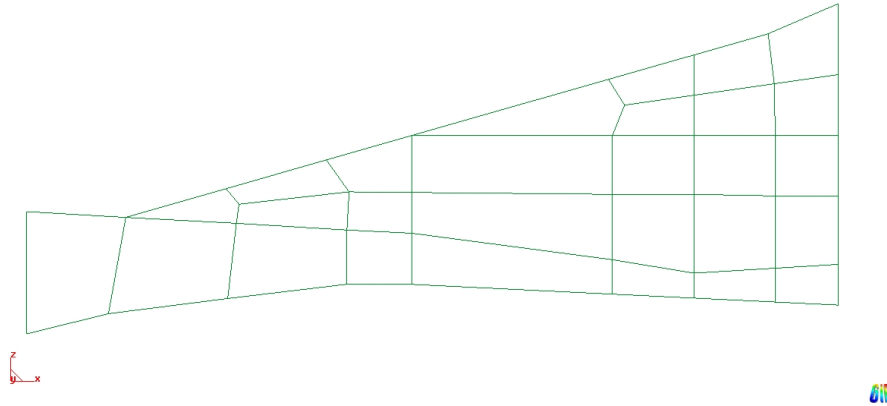


Figure 506.10: Coarse mesh model used for the 2D upstream section of the Dam.

Meshes shown in Figures 506.11 and 506.12, represent a refinement of the first mesh. Models using both meshes were tested for both drained and undrained material models. Results for both fine mesh (Fig. 506.11) and finest mesh (Fig. 506.12) were the same for all practical purposes (differences were negligible for the purpose of analysis), hence it was decided to use fine mesh (Fig. 506.11) for all

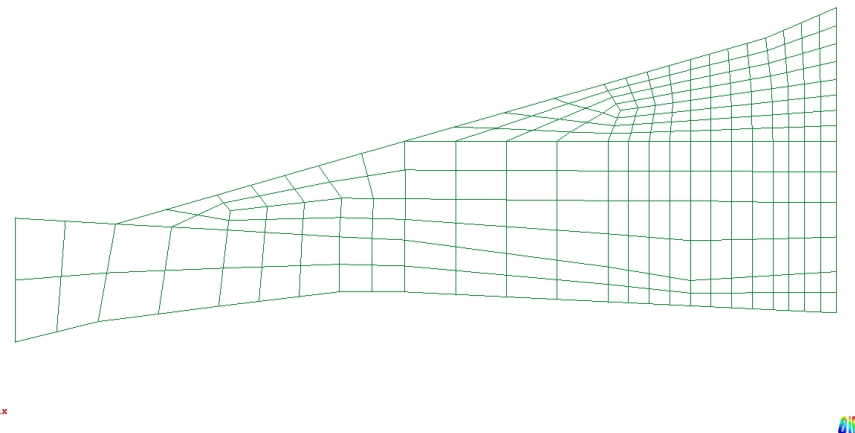


Figure 506.11: Fine mesh model used for the 2D upstream section of the Dam. This mesh was chosen as appropriate enough for all subsequent 2D analysis.

subsequent analysis in 2D.

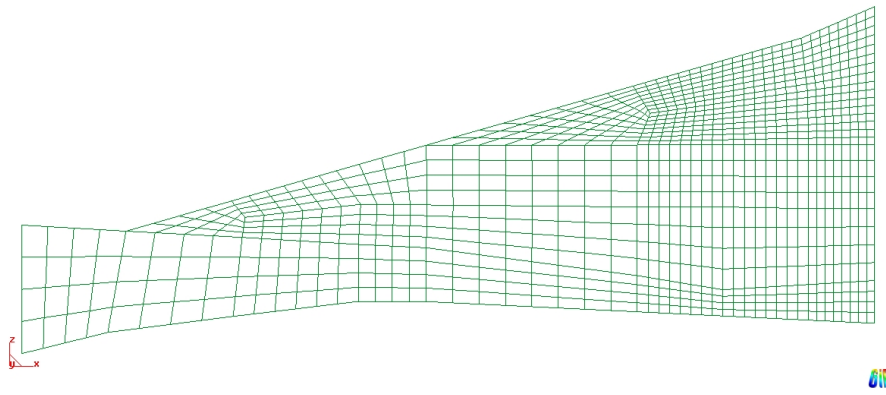


Figure 506.12: Much finer mesh model used for the 2D upstream section of Dam. Results obtained this mesh were the same as previous mesh (shown in Figure 506.11), leading to the choice of the previous mesh (Figure 506.11) for all 2D analysis.

It is important to note that all 2D meshes were actually developed using 3D, brick elements (in this case a linear interpolation, 8 node bricks). Appropriate boundary conditions were used to prevent out of plane displacements. While this approach uses extra resources (use of 3D element for a 2D problem) it allowed us to use the very same element and material models for both 2D and 3D problems, thus removing modeling uncertainty and emphasizing accuracy of determination of differences between 2D

and 3D slope stability. The finite element used for analysis in 2D (and later in 3D) was based on an eight node brick element, described in some more details in Section 2.3 of my lecture notes [Jeremić et al. \(1989-2025\)](#).

Mesh in Figure [506.11](#) has 250 brick finite elements while finest mesh in Figure [506.12](#) has 1000 brick finite elements. Boundary conditions for the 2D mesh were such that right vertical boundary (at the current Barrier wall) was allowed to move down but not horizontally. Lower mesh boundary (contact with base rock) was fully supported, while left vertical boundary (far into alluvium) was also allowed to move vertically but not horizontally. Work platform was modeled using loads, instead of extending the mesh to include the shape of the platform. This allowed for additional modeling flexibility, without the loss of accuracy. Loading tests with and without the work platform show that its influence on calculated factors of safety is negligible. Figure [506.13](#) shows a 2D model with location of work platform, water level at 680 ft, boundary conditions and the extent of alluvium layer.

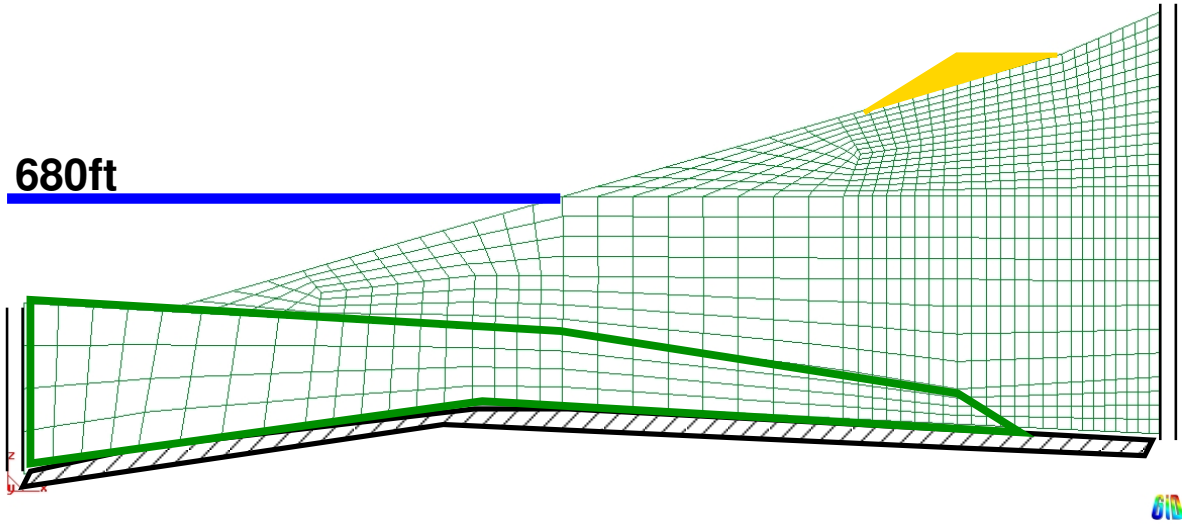


Figure 506.13: A 2D model with boundary conditions, water level at 680 ft and the work platform as load.

506.4.3 Three Dimensional Models

The Dam is a full three dimensional solid, consisting of foundation rock, concrete section and soil embankment section with barrier wall(s) (old and new one when finished). Ideally we would model the complete foundation-concrete-embankment-wall system with porous solid (soil skeleton), pore fluid

(water in fully and partially saturated pores), structural components (barrier walls) as well as solid concrete section.

Particular focus on assessing 2D versus 3D slope stability for the upstream, curved (wrap around) section, as well as the very short time frame for this project, dictated development of small part of the complete model. The most important feature of the 3D model was to use optimal model size (extent) so that all important features are properly captured. This was done by developing 3D model for upstream curved, wrap slope in two stages. First stage comprised development of the conical portion of mesh, which was then extended, using a straight second stage, extending the model into the embankment by 200 ft (60 meters).

Conical Section of a 3D Slope Three sections shown in Figures 506.6, 506.7 and 506.7 were used to develop three dimensional mesh. Conical wrap around part of the mesh features 1344 brick elements and is shown in Figure 506.14.

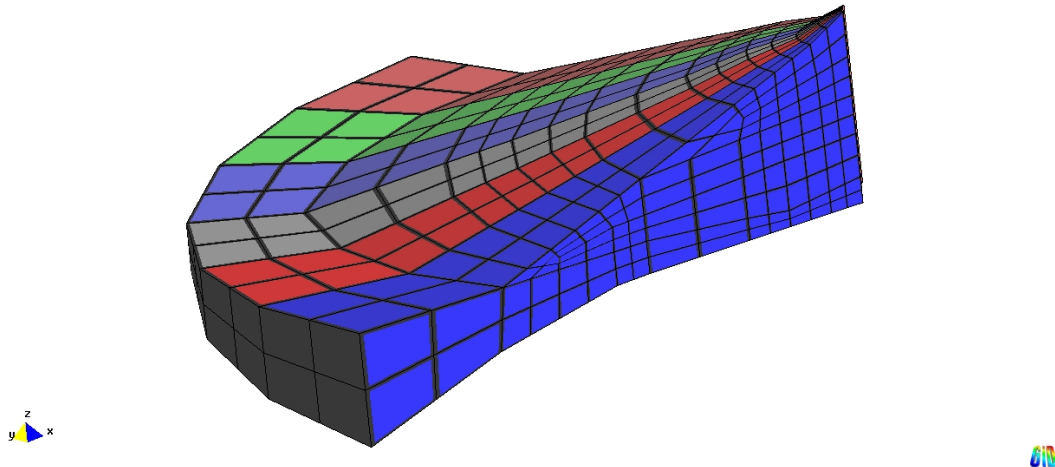


Figure 506.14: Conical section of the 3D upstream slope of the Dam, 3D mesh.

Boundary conditions are such that two vertical sections (one adjacent to the concrete monolith and the one adjacent to straight embankment sections have free vertical and in plane horizontal displacements while no out of plane displacement. A small quarter cylinder boundary was also developed at the top of the curved, wrap around section. This small part of boundary (radius of 2 meters) was necessary to properly mesh radial directions of the 3D model. Boundary conditions at that location are such that they prevent radial deformation while allowing vertical and tangential movement. This is achieved using short, stiff truss elements.

At the lower end of the model (well into alluvium), curved, radial section of the model is supported in such a way that radial deformation is prevented while vertical and horizontal tangential movement is allowed, again achieved using short, stiff truss elements.

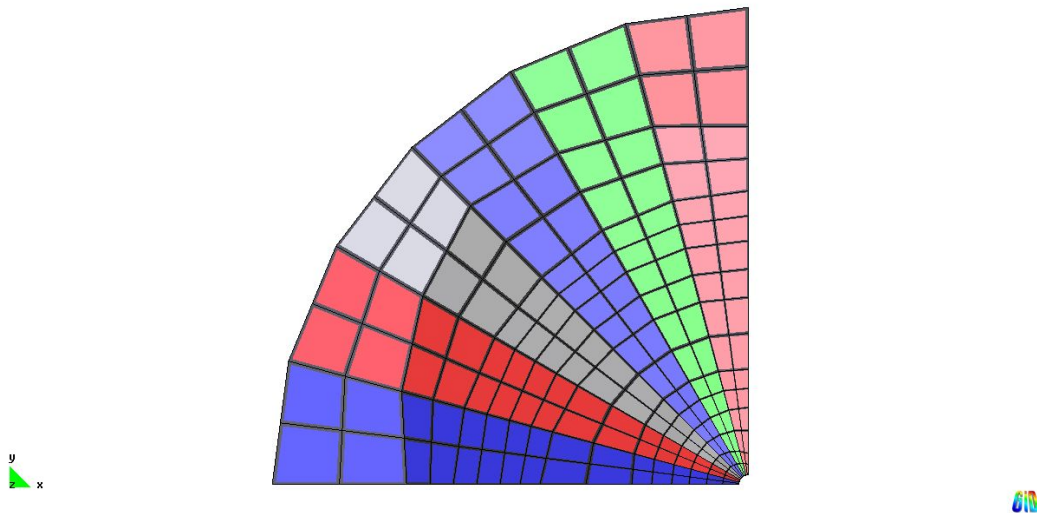


Figure 506.15: Curved section of the 3D upstream slope of the Dam, 3D mesh, top view. Note the difference in extent of the actual embankment (slightly different color of elements, alluvium is represented by last two layers of elements on the outskirts of model. Also note a small cylindrical section close to center of conical slope, that was used to control meshing.

Conical and Straight Section of a 3D Slope While conical section of the slope represent accurately the curved section of the dam, influence of the straight section cannot be neglected. A section (200 ft, 60 meters) of a straight embankment was added to a curved section in order to have a more realistic modeling of the complete upstream 3D embankment. Figures 506.16 and 506.17 show extended 3D mesh for curved and part of straight section of the upstream slope.

Boundary conditions were similar to the previous case for conical part of mesh, except where mesh extension was applied. Extended mesh was fully supported at the bottom, while vertical faces were supported in such a way not to have out of plane displacements while in plane (horizontal and vertical) displacements were left free. Loads from work platform and from water in the lake were applied as appropriate nodal forces.

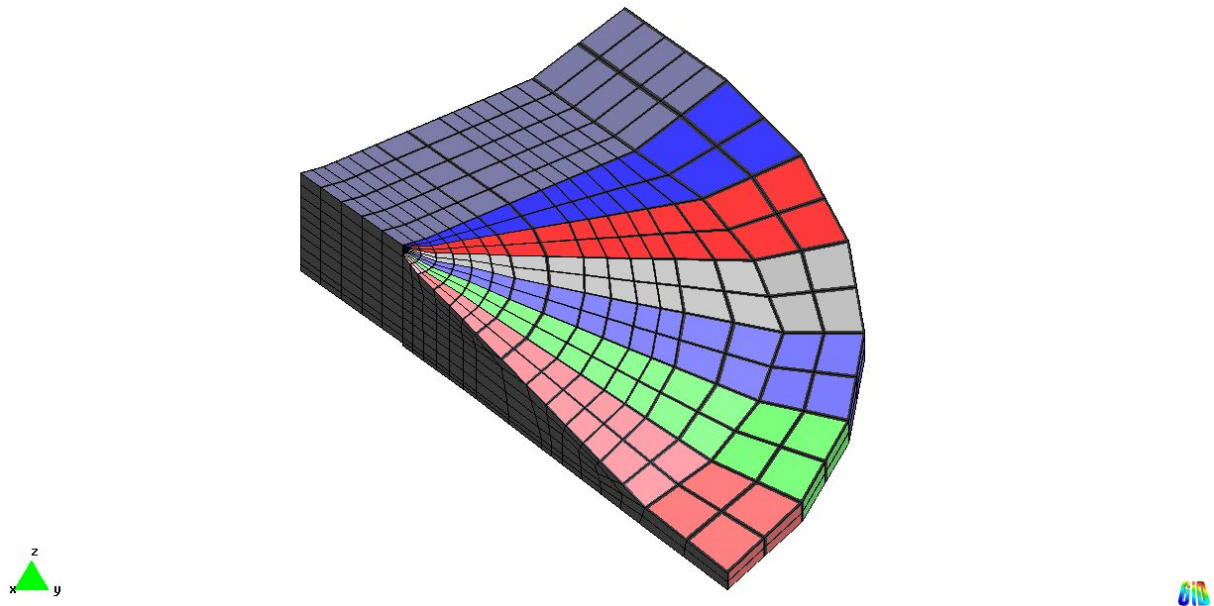


Figure 506.16: Curved and straight section of the 3D upstream slope of the Dam, 3D mesh.

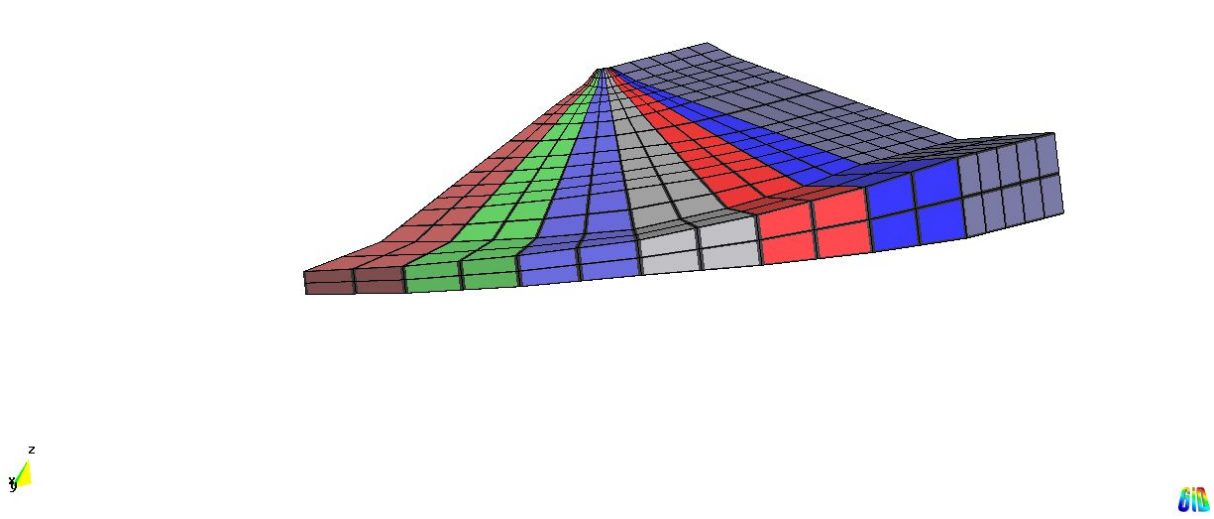


Figure 506.17: Curved and straight section of the 3D upstream slope of the Dam, 3D mesh.

506.4.4 Modeling Issues

Mesh Size Multiple mesh sizes were tested to alleviate any mesh dependency of the computed solution close to stability loss (close to but not into the development of localized deformation).

Following the Equilibrium Path Numerical integration of elastic-plastic constitutive equations was performed using both explicit and implicit algorithms (see [Jeremić et al. \(1989-2025\)](#), Sections 3.3 and 3.4). This was necessary in order to verify the solution accuracy. For explicit constitutive computations, explicit global solution scheme was used (see more detailed description of equilibrium following path algorithms in my lecture notes [Jeremić et al. \(1989-2025\)](#), Chapter 7). For implicit constitutive integrations, Newton method (cf. [Dennis and Schnabel \(1983\)](#), and [Jeremić et al. \(1989-2025\)](#), Chapter 7) was used on both constitutive and global solution levels. Global solution advancement was constrained using both load control (appropriate for factor of safety stability simulations) as well as displacement control (in order to validate load control solutions). Detailed discussion on both load and displacement control algorithms is given in lecture notes [Jeremić et al. \(1989-2025\)](#), Sections 7.3. and 7.4.

Strength Reduction Method Strength reduction method is often used with finite elements to assess factors of safety for slopes, foundations and other problems in geotechnical engineering where elastic-perfectly plastic failure is expected [Duncan \(1996\)](#) [Griffiths and Lane \(1999\)](#). Strength reduction method can be performed in two ways:

- Apply self weight to a model where strength parameters are reduced by Factor of Safety (FS). Perform analysis number of times for larger and larger FS, until the finite element system is not in equilibrium, that is external forces cannot be balanced by internal forces (see Section 7.1 in [Jeremić et al. \(1989-2025\)](#)). This approach has the benefit of not being mesh dependent, that is, for elastic – perfectly plastic material models (without softening), dependence of solution on mesh refinement does not become an issue ([Lu et al., 2009](#)). One potential drawback is that since there is no softening involved, deformation will not localize into localized zone, rather failure mode is somewhat diffuse, however still following proper displacement of blocks of material as system becomes unbalanced.
- Apply self weight to a model with full strength material parameters, and then gradually start softening the material parameters, by dividing them with FS. Perform reduction in parameters, until there is loss of equilibrium, that is until external forces cannot be balanced by internal forces (again see Section 7.1 in [Jeremić et al. \(1989-2025\)](#)). This approach might have a potential problem in that the mesh size/refinement will affect the solution, as material models involved are

softening, and different meshes will create different localization patterns and hence lead to different solutions. The benefit of this approach is that deformation will indeed localize in a very thin band, thus resembling the limit equilibrium approach that is popular for slope stability problems, however, such deformation patterns are mesh size/refinement dependent and thus not unique.

In this work, the first approach is used, that is self weight computations are performed for a number of models where strength parameters are reduced by FS, until such FS for which equilibrium between external and internal forces cannot be achieved.

Variable Water Levels Comparison of 2D vs 3D stability for two water elevation was originally suggested. Discussions during a meeting at a Dam site, further clarified conceptual problems with two water elevation, namely lake at 680 ft and water table in the embankment at 720 ft. For any water table that is above the lake level, there will exist a water flow (seepage) within the embankment toward the (lower level) lake water. Such seepage will create a seepage force $f_s = \gamma_w(dh)/(dl) = \gamma_w i$ where, γ_w is the unit weight of water, and $i = (dh)/(dl)$ is the hydraulic gradient. Clearly, with seepage from embankment toward the lake, such force destabilizes the embankment (slope). Finite Element formulation and tools that can model and simulate such fully coupled system (transient analysis of deforming porous soil with moving pore fluid) are available ([Cheng et al., 2007](#); [Jeremić et al., 2008](#); [Cheng and Jeremić, 2009a,b](#)), however material parameters for soil permeability as well as the extent of phreatic surface need to be determined. Due to unavailable test data for permeability of embankment soil and due to (high) uncertainty in the extent of phreatic surface (number of piezometric measurements placing the water table in the embankment at 720 ft were highly questionable, as discussed by the panel), only single phase soil (either effective stress or total stress) analysis were performed. This decision has no effect on analysis for cases where both lake and phreatic line in the embankment are at 680 ft. However, such decisions affects cases with different water levels (lake at 680 ft, phreatic line at):

- Fully undrained case with lake level at 680 ft, embankment phreatic level at 720 ft, was analyzed and in fact provides (based on theory of undrained soil behavior) the same factors of safety as no seepage case, that is, same water level in lake and embankment. This is due to the fact that for total stress analysis, pore fluid pressure does not influence the shear strength. In addition to that, with the assumption of fully undrained conditions, coefficient of permeability is nonexistent, there is no seepage, and hence there is no seepage force. In reality coefficient of permeability for soil is never really zero, however this case was treated as an extreme case, used purely for checking differences in factors of safety between 2D and 3D slope stability.
- Fully drained case with lake level at 680 ft, embankment phreatic level at 720 ft, was not analyzed

as neglecting seepage force would place calculated factors of safety on the *unsafe* side. While such analysis can be run using either buoyant weight approach (however somewhat inconsistent as noted by [Duncan \(1996\)](#)) or by mixing total stress and effective stress approach (more inconsistent) it was decided not to simulate this case.

506.5 Results: Factors of Safety

A large number of computations on a number of models were performed.

Factors of Safety for 2D Models

- Drained, Lake/Embankment at 680 ft,

$$FS_{2D} = 1.89$$

- Undrained, Lake/Embankment at 680 ft, alluvium weak of most likely ($S_u = 1000$ psf),

$$FS_{2D} = 2.22$$

- Undrained, Lake/Embankment at 680 ft, alluvium at most likely value ($S_u = 1500$ psf),

$$FS_{2D} = 2.50$$

Factors of Safety for Extended 3D Models

- Drained, Lake/Embankment at 680 ft,

$$FS_{3D} = 1.78$$

- Undrained, Lake/Embankment at 680 ft, (alluvium weak of most likely $S_u = 1000$ psf),

$$FS = 2.0$$

Comparison of 2D vs 3D Factors of Safety

- Drained, lake/water in embankment at 680 ft,

$$FS_{2D} = 1.89 \text{ vs } FS_{3D} = 1.78$$

FS reduced by 5.8 %.

- Undrained, Lake at 680 ft, embankment at 680 ft

(alluvium weak of most likely $S_u = 1000$ psf),

$$FS_{2D} = 2.22 \text{ vs } FS_{3D} = 2.00$$

FS reduced by 9.91 %.

- Undrained, Lake at 680 ft, embankment at 720 ft
(alluvium weak of most likely $S_u = 1000\text{psf}$),
 $FS_{2D} = 2.22$ vs $FS_{3D} = 2.00$
FS reduced by 9.91 %.

506.6 Uncertainty of Results

Full probabilistic analysis for large scale, elastic-plastic finite element models is currently within reach ([Sett et al., 2011a](#)) and will probably become a standard simulation tool within next 5 to 10 years. However, for such an analysis, a(n) (extensive) site characterization program is necessary, if probabilistic simulations are to be useful ([Sett and Jeremić, 2009](#)). Alternatively, one can use a simplified methodology, described in detail by [Duncan \(2000a\)](#), that can give sensible estimates of mean and standard deviation of common results obtained in soil mechanics. However, in view of lack of consistent material properties for the embankment further work on estimating uncertainty of factors of safety was discontinued. It is important to note that a program was initiated by the USACE to perform extensive testing of embankment soil and upon completion of that program, it will be possible to perform a simplified (and even a more accurate, full probabilistic analysis, as mentioned above) estimation of influence of material uncertainty on obtained factors of safety.

506.7 Conclusion

The main purpose of this study was to investigate changes in factors of safety for failure between 2D and 3D slope problems for curved part of the upstream section of a Dam embankment. Detailed models (both 2D and 3D) were developed for the upstream section of Wold Creek Dam and were analyzed. Strength reduction method was used to assess factors of safety in both 2D and 3D. It was shown that for a number of different cases (drained or undrained soil, lake at 680 ft and water table in the embankment either at 680 ft or at 720 ft for undrained case) the factor of safety is reduced in 3D when compared to 2D. Such reduction, however was not significant (up to approx. 10 %).

Of particular importance for this factor of safety comparison (2D vs 3D) was the robustness of simulations and a number of methods were used to ensure that obtained factors of safety, determined as failure to converge upon strength reduction, were due to loss of equilibrium, and not due to numerical problems leading to loss of convergence.

Appendix given below, contains two additional sections, describing numerical tool used in factor of safety computations (available in public domain) and deformation patterns close to failure for select

cases.

506.8 Displacement Patterns

Hypothetical displacement patterns are presented below in Figures 506.18, 506.19 and 506.20. It should be noted that displacements that results from simulations of stability by strength reduction method are not necessarily the failure modes, rather, they are just a side-product of simulation. However, it is instructive to inspect those displacements just before equilibrium is lost in order to gain a better understanding of potential failure patterns.

Figure 506.18 shows a 2D displacement pattern for a drained case with lake and embankment water level at 680 ft where $FS_{2D} = 1.89$. Noted is a clear rotating pattern of the slope just before loss of equilibrium.

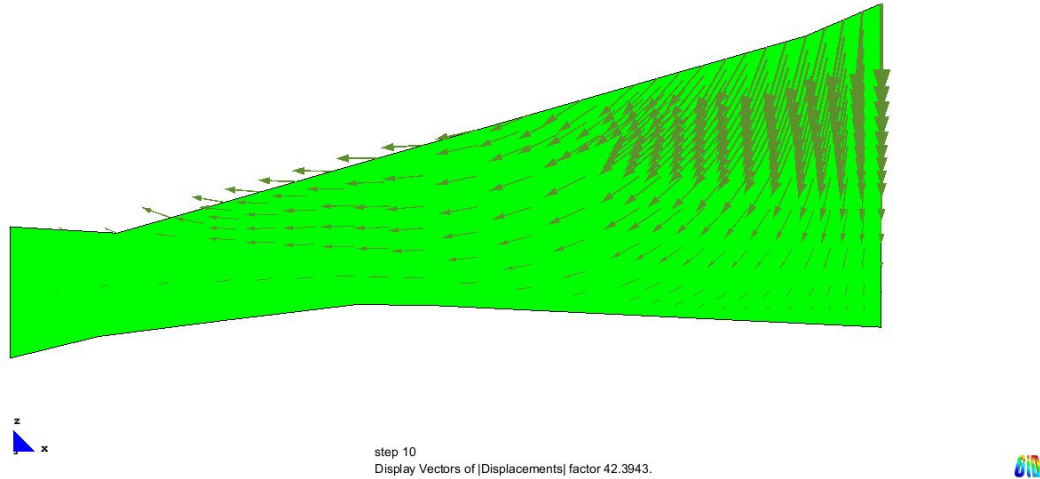


Figure 506.18: Drained case, lake and embankment water lever 680 ft, $FS_{2D} = 1.89$.

Figure 506.19 shows a 2D displacement pattern for an undrained case with more likely (stronger) alluvium ($S_u = 1000\text{psf}$). Note that while displacement pattern is somewhat similar to the previous case, the block movement on top of alluvium is much reduced, and main failure is through rotation mechanism.

Figure 506.20 shows a plan view of a 3D displacement pattern (vectors) for an undrained case with limiting weak alluvium and lake at 680 ft. Noted is the dominant 3D deformation pattern by which the curved and straight sections of the slope rotate around vertical axes and move toward the lake with direction biased toward dam axes. It is important to note that there is no single 2D section of the 3D

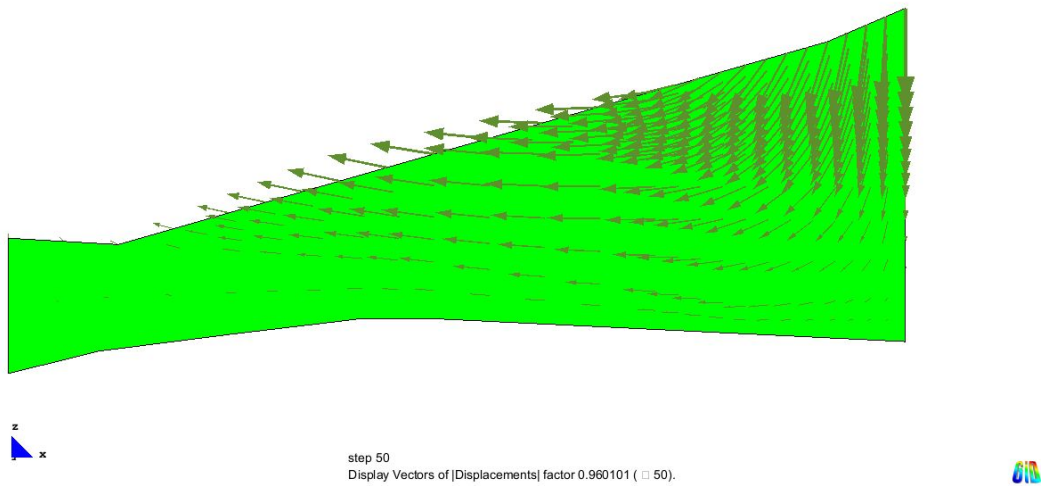


Figure 506.19: Undrained, L680 E680, Most Likely to Weak Alluvium, $FS_{2D} = 2.22$.

slope that can be used to model such failure as failure mode is fully three dimensional.

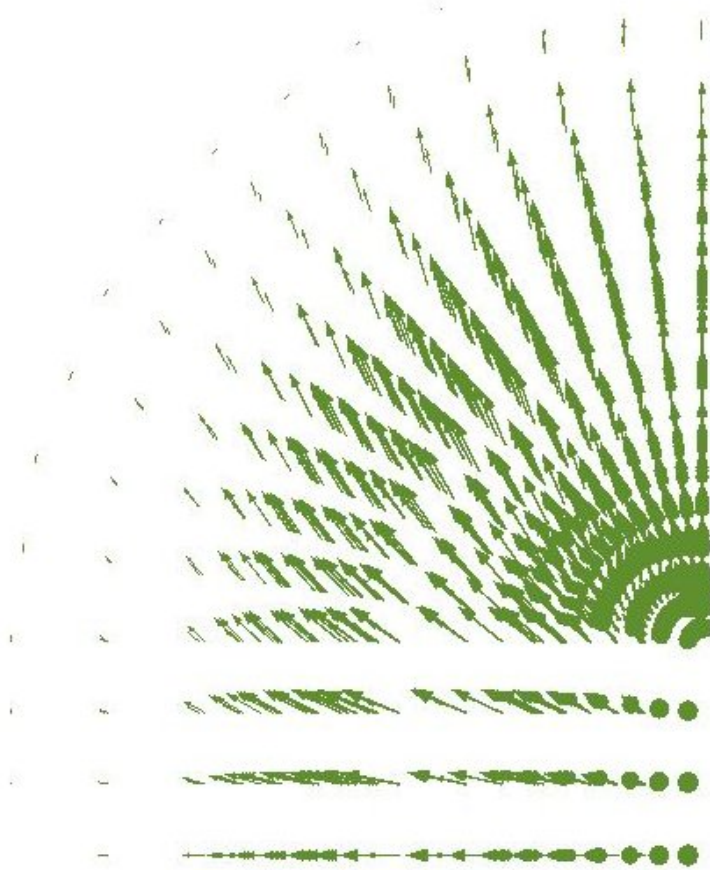


Figure 506.20: Plan view of a 3D undrained case, displacement vectors, lake and embankment at 680 ft, $FS_{3D} = 2.00$.

Chapter 507

Concrete Structures

(1989-2017-2018-2019-2020-2021-)

(In collaboration with Prof. Han Yang and Dr. Hexiang Wang)

507.1 Chapter Summary and Highlights

507.2 Concrete Wall/Membrane

507.2.1 Introduction

OECD organized project to investigate modeling of concrete walls that have alkali - silica reaction (ASR) has been going on for few years. Our modeling and simulation group, based at the University of California at Davis, in California, USA, and at the Lawrence Berkeley National Laboratory at Berkeley, in California, USA, has joined this effort only at the beginning of 2018. We have gotten project description and already existing reports from participants, in January/February of 2018. We managed to quickly make a model of the wall and to calibrate parameters for a concrete model that we use in our modeling and simulation program.

We rely on and used our program, called the Real-ESSI Simulator (Realistic Modeling and Simulation of Earthquakes, and Soils, and Structures and their Interaction), that is also known as the MS ESSI Simulator¹ (Jeremić et al., 1988-2025) (<http://real-essi.info/>). Real-ESSI Simulator is a software, hardware and documentation system for high fidelity, high performance, time domain, nonlinear/inelastic, deterministic or probabilistic, 3D, finite element modeling and simulation of (a) statics and dynamics of soil, (b) statics and dynamics of rock, (c) statics and dynamics of structures, (d) statics of soil-structure systems, and (e) dynamics of earthquake-soil-structure system interaction.

The Real-ESSI Simulator systems is used for the design and assessment of static and dynamic behavior of infrastructure objects, including buildings, bridges, dams, nuclear installations, tunnels, etc. For design, multiple linear elastic load cases can be combined and design quantities, sectional forces exported for design and cross section dimensioning. For assessment, realistic inelastic load staged analysis is performed, with all the inelastic components properly modeled, as listed below, and with all the simulation, algorithmic features available, as listed below. Analysis is performed in order to assess safety and economy of objects. The work on Real-ESSI Simulator is based on a philosophy that aims to develop modeling and simulations that inform and predict rather than (force) fit.

507.2.1.1 Motivation

The alkali - silica reaction (ASR), is a reaction that occurs over time in concrete, between the alkaline cement paste and the silica found in many common aggregates, triggered by the presence of moisture. The ASR does volumetric expansion of interface between cement paste and the aggregate, thus resulting

¹The Real-ESSI Simulator was developed in collaboration and with financial support from the US-DOE, US-NRC, US-NSF, CNSC-CCSN, Caltrans, etc.

in potentially damaging tensile stress within concrete. A comprehensive study of this effect on concrete properties has been done at University of Toronto, funded by Canadian Nuclear Safety Commission (CNSC). Five shear walls, two regular (REG A, REG B) and three ASR (ASR A1, ASR B1, ASR B2) along with their control specimens were tested as a part of Phase 1, Phase 2, and Phase 3 of the investigation program [ref Prof. Sheikh presentation].

It was proven that ASR causes changes in mechanical properties of the concrete, introducing inaccuracies if conventional analysis is used, without taking into account ASR. Beyond a certain age, modulus of elasticity and tensile strength of ASR concrete decrease, in contrast to regular concrete. Observed is degradation of the ductility in ASR specimens. While concrete expands, the bonding strength between concrete and rebars decreases causing drop in ductility. However, despite these changes in concrete, tested ASR shear wall showed higher peak shear strength compared to regular concrete.

This newly understood behavior of ASR concrete necessitates development of reliable numerical simulation, to be used for the design of new structures as well as to predict behavior of existing ones.

In order to model behavior of the examined wall specimens, Real-ESSI Simulator, ([Jeremić et al., 1988-2025](#)) was used.

Plane stress finite element with an inelastic plane stress material model for concrete was used for modeling of shear wall specimens. All inelastic material models and finite elements inside the Real-ESSI Simulator feature accurate energy dissipation modeling and calculation ([Yang et al., 2018, 2019a](#)).

Results from ASCET benchmark tests are used for validation of shear behavior for plane stress inelastic reinforced concrete wall tests.

507.2.2 Model Availability

The Real-ESSI input files for the ASR concrete wall example are available [HERE](#).

507.2.3 Model Development

507.2.3.1 Model Mesh

Finite element model includes all relevant parts of the experimental setup, as shown in Figures [507.3](#) and [507.2](#).

Beam slabs and steel plates are modeled using 27NodeBrick element, while steel bolt is represented as a single truss element. The shear wall is modeled using nonlinear layered plane stress elements. For the web part of the wall, the elements have a horizontal rebar layer, a vertical rebar layer, and an unconfined concrete layer. For the flanges (columns) of the shear wall, the elements have an additional layer of confined concrete. It is emphasized that the main wall is really made from unconfined concrete, and the

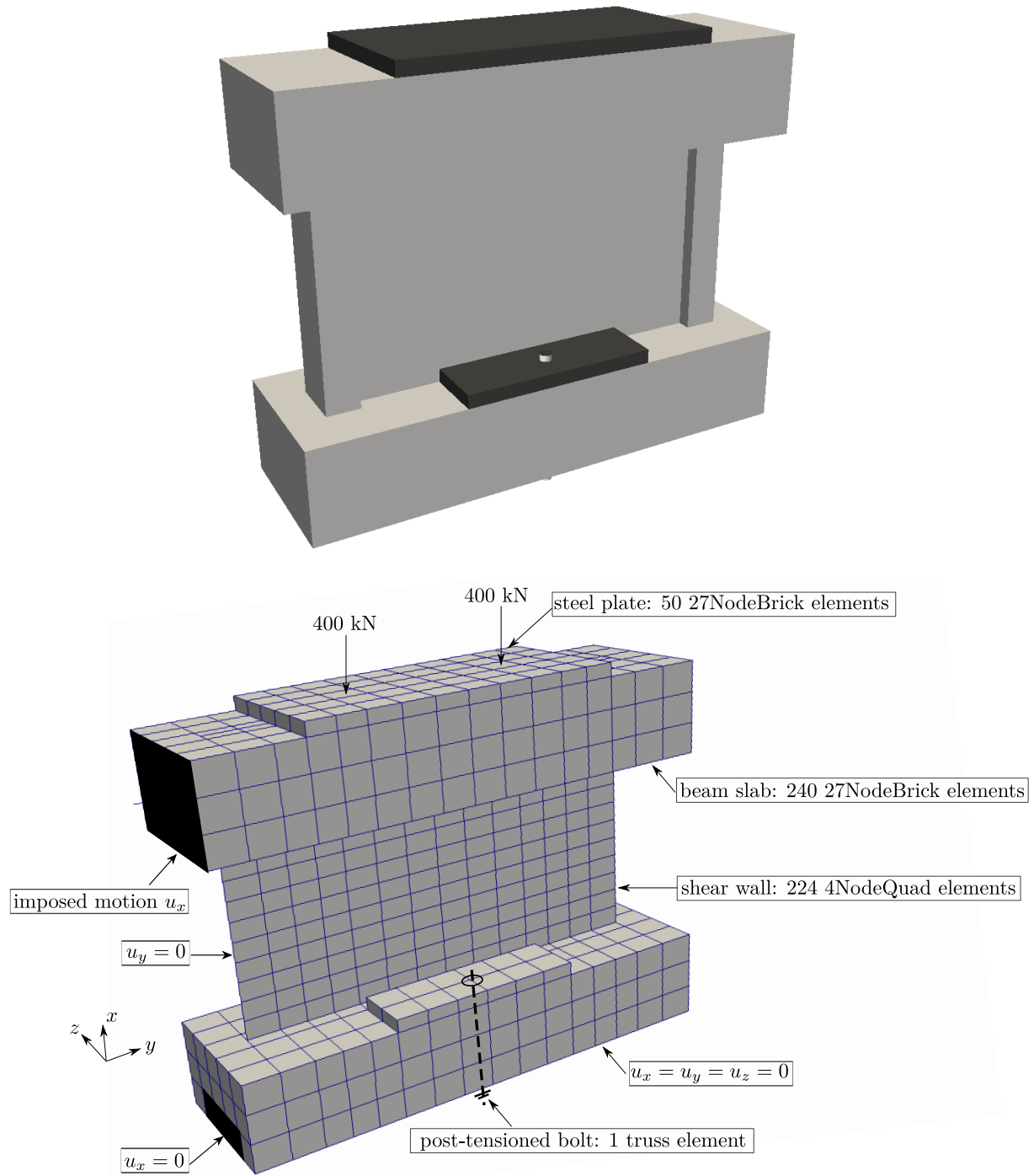


Figure 507.1: 3D rendered view and finite element mesh of the reinforced concrete shear wall model.

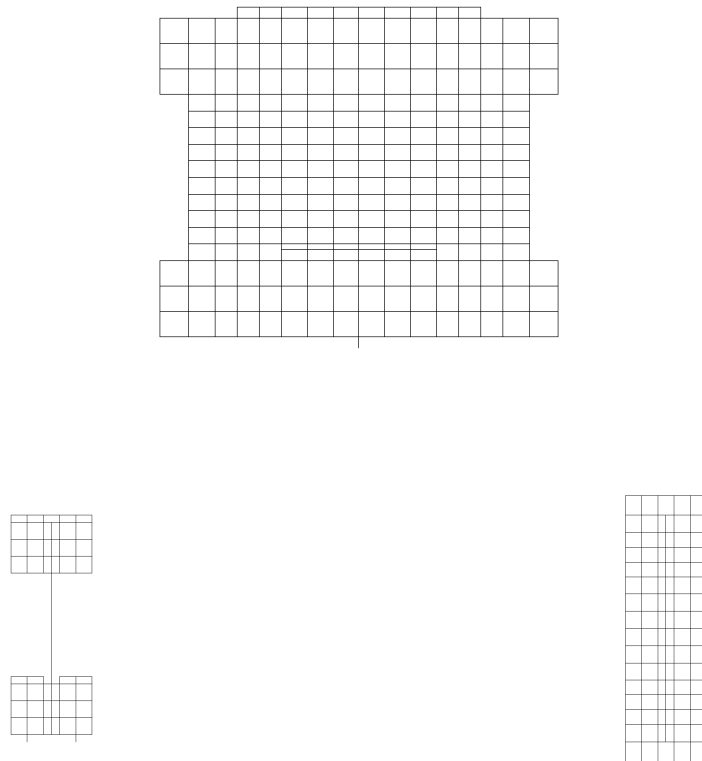


Figure 507.2: Different views of the finite element mesh.

only actually confined concrete is within concrete flanges. Detailed rebar plan and model dimensions are shown in Fig 507.3.

The bottom of the model is restrained in all directions, while the lateral sides of the bottom beam slab are restrained in direction of imposed motion. Since the shear wall consists of 2D plane stress elements the out-of plane displacement is also precluded. The sides of the top beam slab are also restrained to have the same displacement, which is important to represent the boundary conditions of the physical experiment. Initial model included inelastic contact/interface elements (stick-slip and gap open and close) at the bottom boundary. However it was concluded that there will be no slip and there is no gap opening so these elements were removed in order to speed up computations.

To correctly simulate the loading process of the experiment, four loading stages are applied:

1. Self-weight loading is applied to the whole model.
2. To represent post-tensioned force in the truss (bolt) element, the truss is stretched so that an adequate force is obtained and after that the bottom of the bolt is fixed.

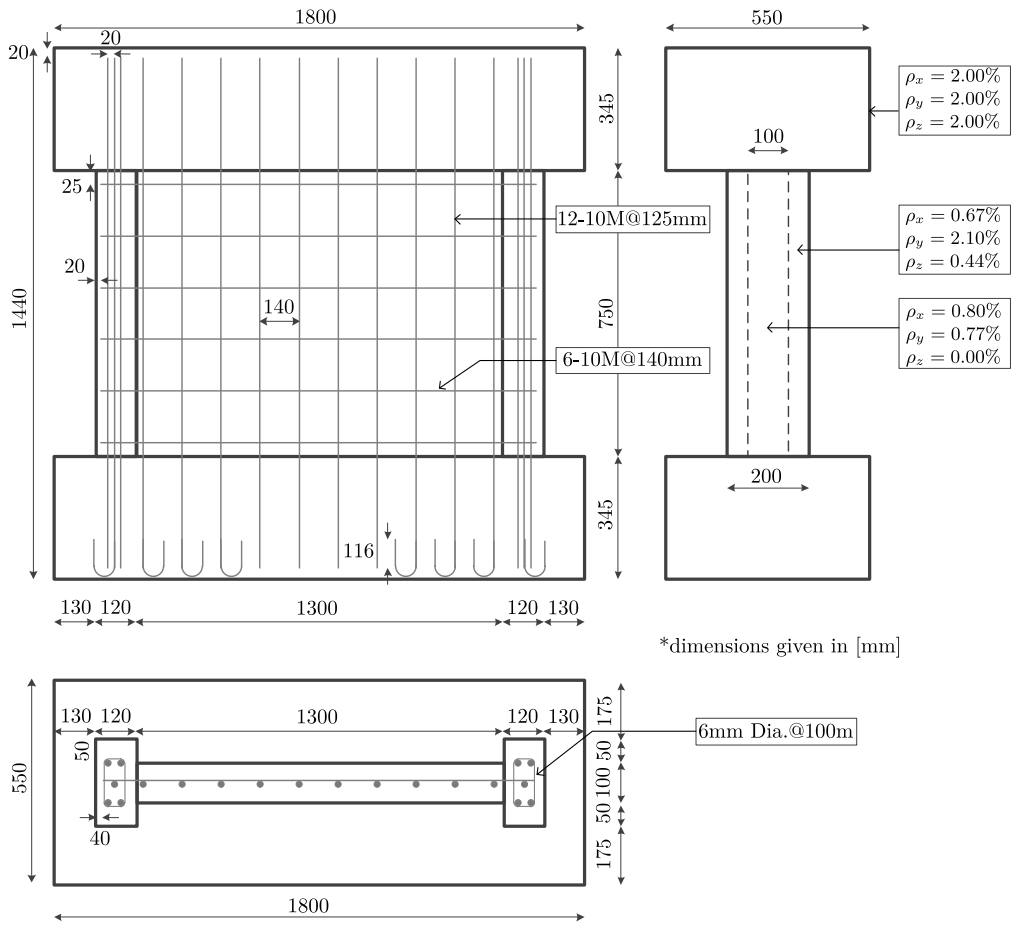


Figure 507.3: Schematics for the rebar plan of the shear wall model.

3. Two-point vertical loading is applied to the top steel plate.
4. Cyclic horizontal loading is applied (using displacement control) to the sides of the top beam slab.

507.2.3.2 Plastic Damage Concrete Material Model

Details for this model are given in Section 104.9.

507.2.3.3 Uniaxial Steel Material Model

Details for this model are given in Section 104.9.

507.2.3.4 Material Model Parameters

There are two approaches to determine the ASR affected concrete model parameters. The first choice is to obtain concrete samples directly from the existing structure. Those samples can be tested in the

laboratory to determine mechanical properties of the concrete material. This is a preferred way to obtain material properties.

In this project, the material properties for ASR affected concrete were obtained using laboratory, for concrete aged to 260, 610, and 995 days, as shown in Table 507.1. These values are used in the material models for finite element simulations.

Table 507.1: Mechanical properties for the ASR concrete at 260, 610, and 995 days.

Wall	Age (Days)	Compressive Strength (MPa)	Tensile Strength (MPa)	Elastic Modulus (MPa)	Expansion (%)
ASR A1	260	63.7	3.24	35750	0.190
ASR B1	610	67.1	N/A	32600	0.215
ASR B2	995	63.0	3.18	28100	0.223

The second approach is to estimate change of material properties, future material properties, based on currently measured material properties and empirical correlations. In what follows, it is demonstrated how to predict the mechanical properties of the ASR concrete at 610 and 995 days using the values at 260 days.

First, according to data provided for ASCET II workshop, the maximum ASR expansions of the concrete prisms in longitudinal and transverse directions are approximately 0.25% and 0.28%. For simplicity, an average value of 0.265% is chosen.

Estimations of ASR expansion rates at 260, 610, and 995 days are needed. According to various ASR models ([Charlwood et al., 1992](#); [Saouma and Perotti, 2006](#)), the rate of expansion after about 365 days is very small. So it is reasonable to use the maximum value of expansion (0.265%) for estimating mechanical properties of ASR concrete at 610 and 995 days. At 260 days, the expansion is estimated to be 0.23%.

The correlation between normalized mechanical properties of ASR concrete and rate of expansion/swelling from [Capra and Sellier \(2003\)](#) is used. At 0.265% swelling, at 365 days, the normalized compressive strength is 0.60 while the normalized tensile strength is 0.55. The normalized elastic modulus ranges from 0.60 to 0.70.

On the other hand, at 0.23% swelling, at 260 days, the normalized compressive strength is 0.65 while the normalized tensile strength is 0.60. The normalized elastic modulus is approximately 0.70. Therefore, from 260 days to 365 and consequently at 610 and 995 days, the compressive and tensile strengths both decrease approximately 92%. Similarly, the elastic modulus decreases approximately 85%.

Using these values, for ASR concrete older than 365 days, the compressive strength is 58.6MPa, the tensile strength is 2.98MPa, and elastic modulus 30387MPa. Note that these values match well with the experimental results shown in Table 507.1. It is important to note that concrete is a composite

material and that expansion of mass of concrete, within confines of reinforcing, can produce increase in confinement, which can have beneficial effects on concrete behavior.

507.2.4 Modeling of Energy Storage and Dissipation

Described in this section is modeling and calculation of energy storage and dissipation within concrete and steel. This section is based on recent work by Yang et al. (2018, 2019a).

507.2.4.1 Plastic Damage Concrete Material

The Helmholtz free energy potential postulated for the plastic damage concrete material has the form:

$$\psi(\epsilon_{ij}, \epsilon_{ij}^p, d^+, d^-) = (1 - d^+) \psi_0^+(\epsilon_{ij}, \epsilon_{ij}^p) + (1 - d^-) \psi_0^-(\epsilon_{ij}, \epsilon_{ij}^p) \quad (507.1)$$

where ψ_0^+ and ψ_0^- are tensile and compressive parts of the elastic free energy (strain energy), that are defined as:

$$\psi_0^+(\bar{\sigma}_{ij}(\epsilon_{ij}, \epsilon_{ij}^p)) = \frac{1}{2} \bar{\sigma}_{ij}^+ D_{ijkl}^{-1} \bar{\sigma}_{kl} = \frac{1}{2} \bar{\sigma}_{ij}^+ (\epsilon_{ij} - \epsilon_{ij}^p) \quad (507.2)$$

$$\psi_0^-(\bar{\sigma}_{ij}(\epsilon_{ij}, \epsilon_{ij}^p)) = \frac{1}{2} \bar{\sigma}_{ij}^- D_{ijkl}^{-1} \bar{\sigma}_{kl} = \frac{1}{2} \bar{\sigma}_{ij}^- (\epsilon_{ij} - \epsilon_{ij}^p) \quad (507.3)$$

The rate of strain energy can be calculated from:

$$\dot{E}_S = \dot{\psi}_0^+ + \dot{\psi}_0^- = \sigma_{ij}(\dot{\epsilon}_{ij} - \dot{\epsilon}_{ij}^p) \quad (507.4)$$

Taking the time derivative of Equation 507.1 gives the rate form of Helmholtz free energy:

$$\dot{\psi} = \frac{\partial \psi}{\partial \epsilon_{ij}} \dot{\epsilon}_{ij} + \frac{\partial \psi}{\partial \epsilon_{ij}^p} \dot{\epsilon}_{ij}^p + \frac{\partial \psi}{\partial d^+} \dot{d}^+ + \frac{\partial \psi}{\partial d^-} \dot{d}^- = (\sigma_{ij} \dot{\epsilon}_{ij} - \sigma_{ij} \dot{\epsilon}_{ij}^p) + (-\psi_0^+ \dot{d}^+ - \psi_0^- \dot{d}^-) \quad (507.5)$$

where the first term is the rate of strain energy given by Equation 507.4.

For a decoupled material model, the Helmholtz free energy can be decomposed into elastic and plastic parts (Collins and Houlsby, 1997). Subtracting the elastic part of the free energy (strain energy) from Equation 507.5 gives the rate form of the plastic free energy:

$$\dot{E}_P = \dot{\psi} - \dot{E}_S = -\psi_0^+ \dot{d}^+ - \psi_0^- \dot{d}^- = -\frac{1}{2} (\bar{\sigma}_{ij}^+ \dot{d}^+ + \bar{\sigma}_{ij}^- \dot{d}^-)(\epsilon_{ij} - \epsilon_{ij}^p) \quad (507.6)$$

The plastic energy dissipation D_P is defined as the difference between plastic work and plastic free energy (Farren and Taylor, 1925; Taylor and Quinney, 1934). The rate of plastic dissipation can be expressed as:

$$\dot{D}_P = \sigma_{ij} \dot{\epsilon}_{ij}^p - \dot{E}_P = \sigma_{ij} \dot{\epsilon}_{ij}^p + \frac{1}{2} (\bar{\sigma}_{ij}^+ \dot{d}^+ + \bar{\sigma}_{ij}^- \dot{d}^-)(\epsilon_{ij} - \epsilon_{ij}^p) \quad (507.7)$$

It can be proven that the rate of plastic dissipation given by Equation 507.7 is always non-negative. This means that the concrete material model used in this study satisfies the Clausius-Duhem inequality, which represents a form of the second law of thermodynamics.

Combining Equation 507.4, 507.6, and 507.7, the rate form of energy balance in this concrete material model is achieved:

$$\dot{E}_S + \dot{E}_P + \dot{D}_P = \sigma_{ij}\dot{\epsilon}_{ij} \quad (507.8)$$

507.2.5 Uniaxial Steel Material

The energy computation procedure for the uniaxial steel model is shown in Figure 507.4. Note that the only difference between the monotonic loading branch (Figure 507.4(a)) and the cyclic loading branch (Figure 507.4(b)) is that the strain reversal point c is at the origin o in the monotonic case. So the following explanation of the proposed energy computation method applies to both monotonic and cyclic loading scenarios.

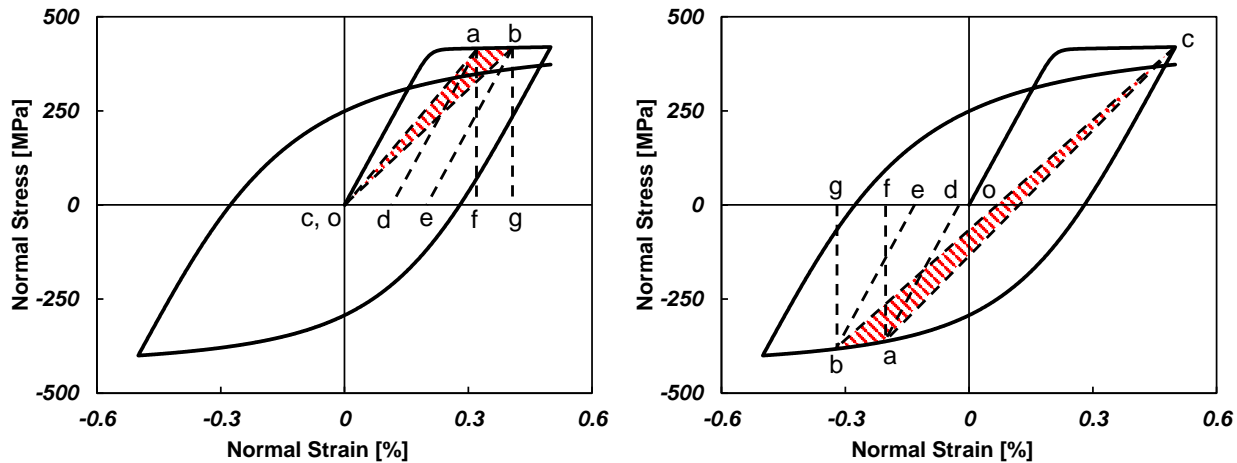


Figure 507.4: Energy computation of uniaxial steel fiber: (a) Monotonic loading branch; (b) Cyclic loading branch.

Firstly, the elastic strain energy density E_S is defined in accordance with the classic assumption that it is only a function of current stress state of the material, which yields:

$$E_S = E_S(\sigma) = \frac{1}{2E_0}\sigma^2 \quad (507.9)$$

where E_0 is the initial stiffness of the material.

Graphically, the elastic strain energy density of the material shown in Figure 507.4 at states a and b are the triangular areas afd and bge . Then the incremental form of Equation 507.9 is simply:

$$dE_S = \frac{1}{E_0}\sigma d\sigma \quad (507.10)$$

Next, the incremental plastic dissipation density D_P from state a to b is assumed to be the triangular area abc :

$$dD_P = \frac{1}{2}[(\sigma - \sigma_r)d\epsilon - (\epsilon - \epsilon_r)d\sigma] \quad (507.11)$$

This assumption ensures that the incremental plastic dissipation is non-negative, and that ensures that the second law of thermodynamics is satisfied.

For general case where the material does exhibit cyclic softening, plastic free energy density E_P is graphically described as the areas $adoc$ and $beoc$ at states a and b , respectively. The formulation for plastic free energy density E_P representing this assumption is given by:

$$E_P = \frac{1}{2} \left[\sigma \left(\epsilon - \frac{\sigma}{E_0} - \epsilon_r \right) + \sigma_r \epsilon \right] \quad (507.12)$$

The incremental form of Equation 507.12 is:

$$dE_P = \frac{1}{2} \left[(\sigma + \sigma_r) d\epsilon + \left(\epsilon - \frac{1}{E_0} \sigma - \epsilon_r \right) d\sigma \right] \quad (507.13)$$

Adding Equation 507.10, 507.11, and 507.13, the incremental form of energy balance is achieved:

$$dE_S + dE_P + dD_P = \sigma d\epsilon \quad (507.14)$$

where the increment of three energy components add up to the increment of stress power during any loading step.

507.2.6 Modeling and Simulation Results

In this chapter, the simulation results are presented and compared with corresponding experimental results. Three sets of FEM simulations (Reg A, Reg B, and ASR A1) using the Real-ESSI Simulator system ([Jeremić et al., 1988-2025](#)) (<http://real-essi.info/>) are performed. In the following sections, the force–displacement responses of these three sets of simulations are shown and discussed. The strain and stress distributions, that share similar pattern in all three simulations, are also presented. In order to investigate the level of damage in the shear wall, the evolution of concrete damage index as well as the plastic dissipation density are plotted and discussed.

507.2.6.1 Force–Displacement Response

Figures 507.5 and 507.6 present the force–displacement responses of the simulation and experiment results for regular concrete (Reg A and Reg B) and ASR concrete.

The ESSI simulation curves show good matching of experimental results. The differences in the envelopes of the cyclic loading curves, between the numerical and experimental results are within 10%.

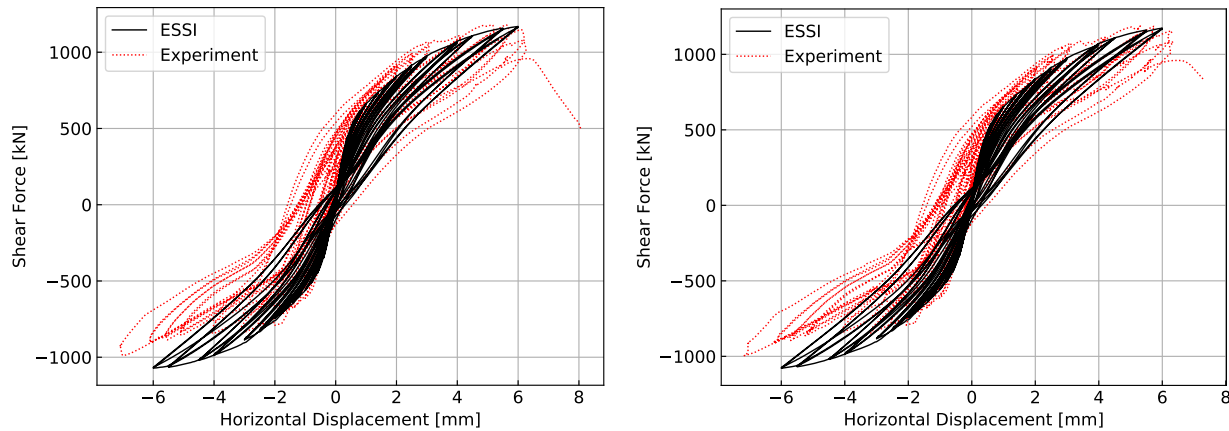


Figure 507.5: Force–Displacement responses of regular concrete tests: (a) Reg A; (b) Reg B.

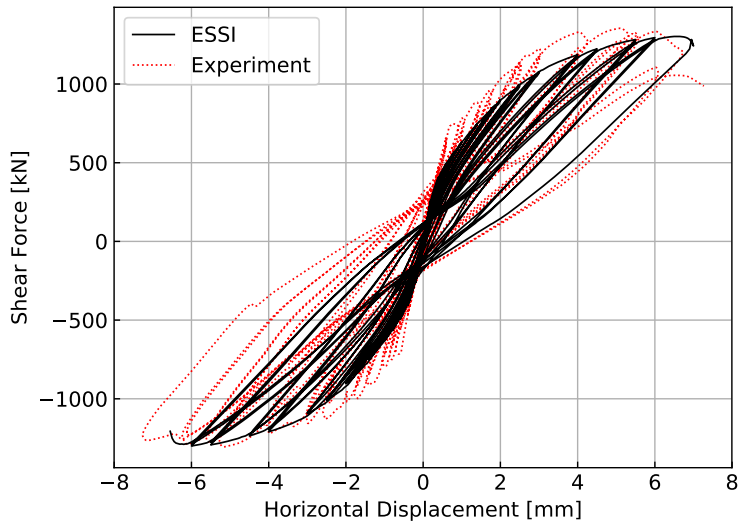


Figure 507.6: Force–Displacement response of ASR concrete test (ASR A1).

The shear strengths and failure loads/displacements given by ESSI simulations match well with the values determined by physical experiments. Note that this particular case with ASR concrete has a much larger unloading-reloading cyclic area, which means that ASR concrete has the capability of dissipating more input energy. It is important to note that this conclusion does not hold for other ASR concrete walls that were tested. This might indicate that for some structures with the ASR concrete, it is possible to dissipate more seismic energy if the structure is under earthquake cyclic loading. On the other hand, for some other structure with the ASR concrete, such conclusion might not hold as other test data suggests reduction of seismic energy dissipation capacity. This leads to the conclusion that variability of ASR concrete quality and material behavior can be significant.

507.2.6.2 Strain and Stress Distribution

Due to the fact that the stress, strain, and damage patterns in all three cases are very similar, only plots for the Reg A case is presented and discussed in the following sections.

Figure 507.7 shows the distribution of displacement components in the shear wall model at $u_y = 6$ mm. The vertical displacement distribution is almost symmetric. The left part of the shear wall is

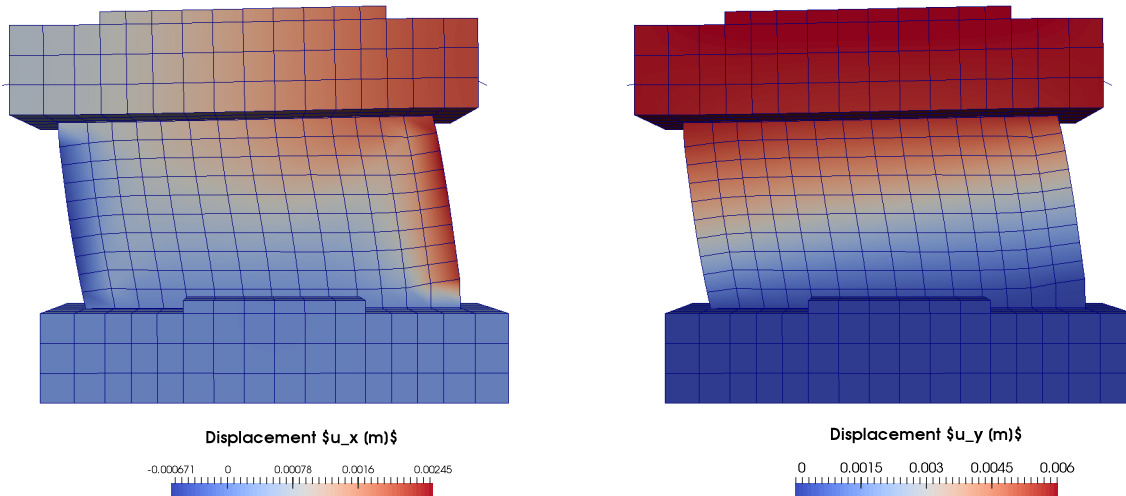


Figure 507.7: Distribution of displacement components in the shear wall model at $u_y = 6$ mm: (a) Vertical displacement u_x ; (b) Horizontal displacement u_y .

compressed down while the right part is extended up. It is noted that the upper support beam is thus not remaining horizontal, rather, it is applying bending load to the shear wall. The horizontal displacement in the top beam slab is almost uniform.

Figure 507.8 shows the distribution of strain components in the shear wall model at $u_y = 6$ mm. The dominant components of the strains are the vertical normal strain ϵ_{xx} due to the vertical loading, and the shear strain ϵ_{xy} due to the horizontal loading. As can be seen in the distribution of ϵ_{xx} , the maximum tensile strain is much larger than the maximum compressive strain. Tensile strain actually means that there is a crack that opened at the location. This is expected since the compressive strength of concrete is higher than the tensile strength.

A 45° shear zone can be observed in the shear wall, with significant amounts of tensile and shear strains. In addition, large tensile strains are developing around the top-left and bottom-right corners. As will be shown in the following section, the concrete in these areas is significantly damaged during the test.

Figure 507.9 shows the distribution of stress components in the shear wall model at $u_y = 6$ mm. To

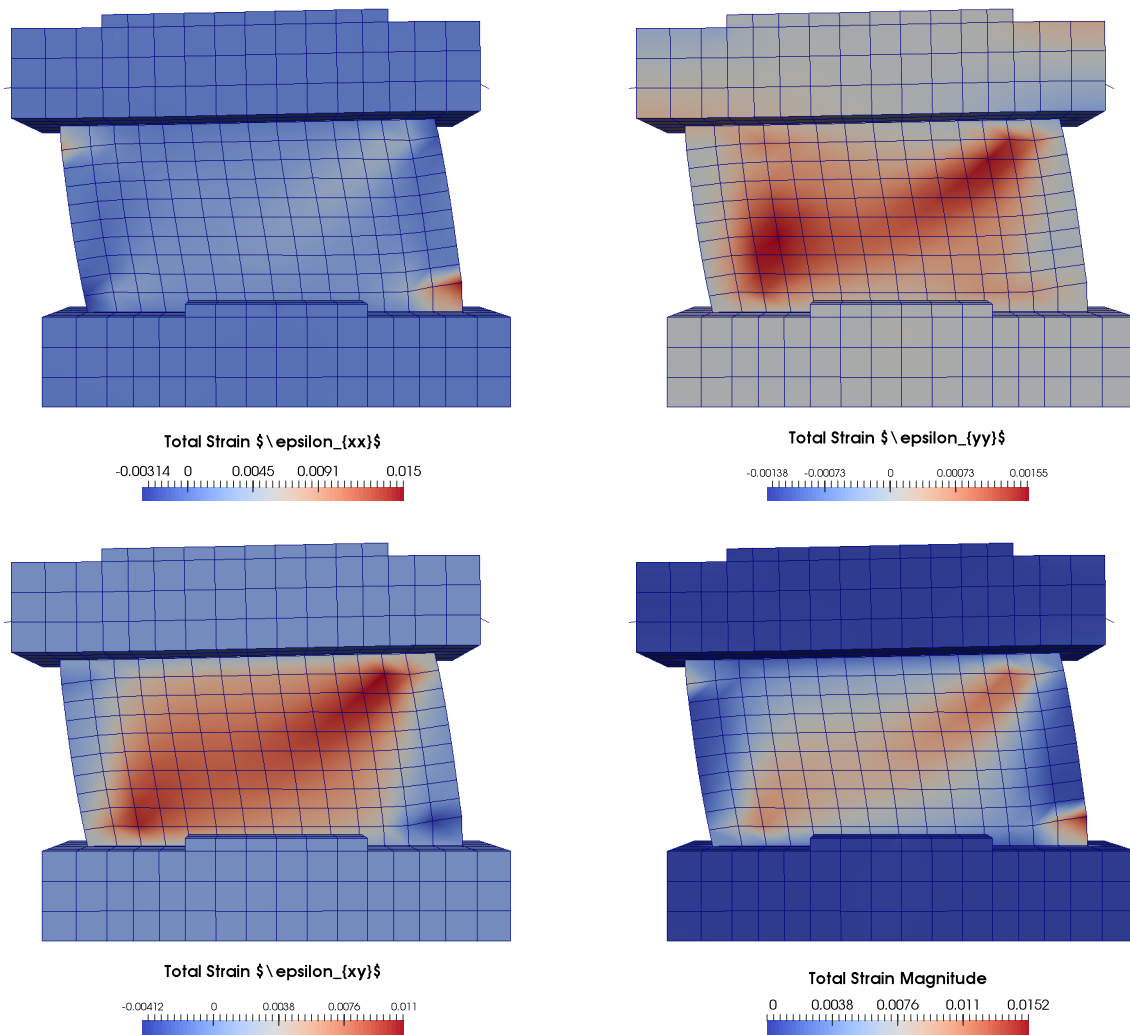


Figure 507.8: Distribution of strain components in the shear wall model at $u_y = 6 \text{ mm}$: (a) Vertical normal strain ϵ_{xx} ; (b) Horizontal normal strain ϵ_{yy} ; (c) Shear strain ϵ_{xy} ; (d) Strain magnitude $|\epsilon|$.

make the plots more clear, only stresses in the shear wall is plotted. Again, a 45° shear zone can be observed, that is consistent with the pattern in the strain plots.

Large compressive normal stresses are developed around the top-right and bottom-left corners, while large tensile normal stresses are observed around the top-left and bottom-right corners. The shear stresses at all four corners are significant.

Stress/force and strain/deformation distributions are not enough to directly quantify the level of damage in structures, especially in the case of cyclic loading. In order to analyze damage conditions, the concrete damage index and plastic energy dissipation are calculated and plotted, as shown in the next section.

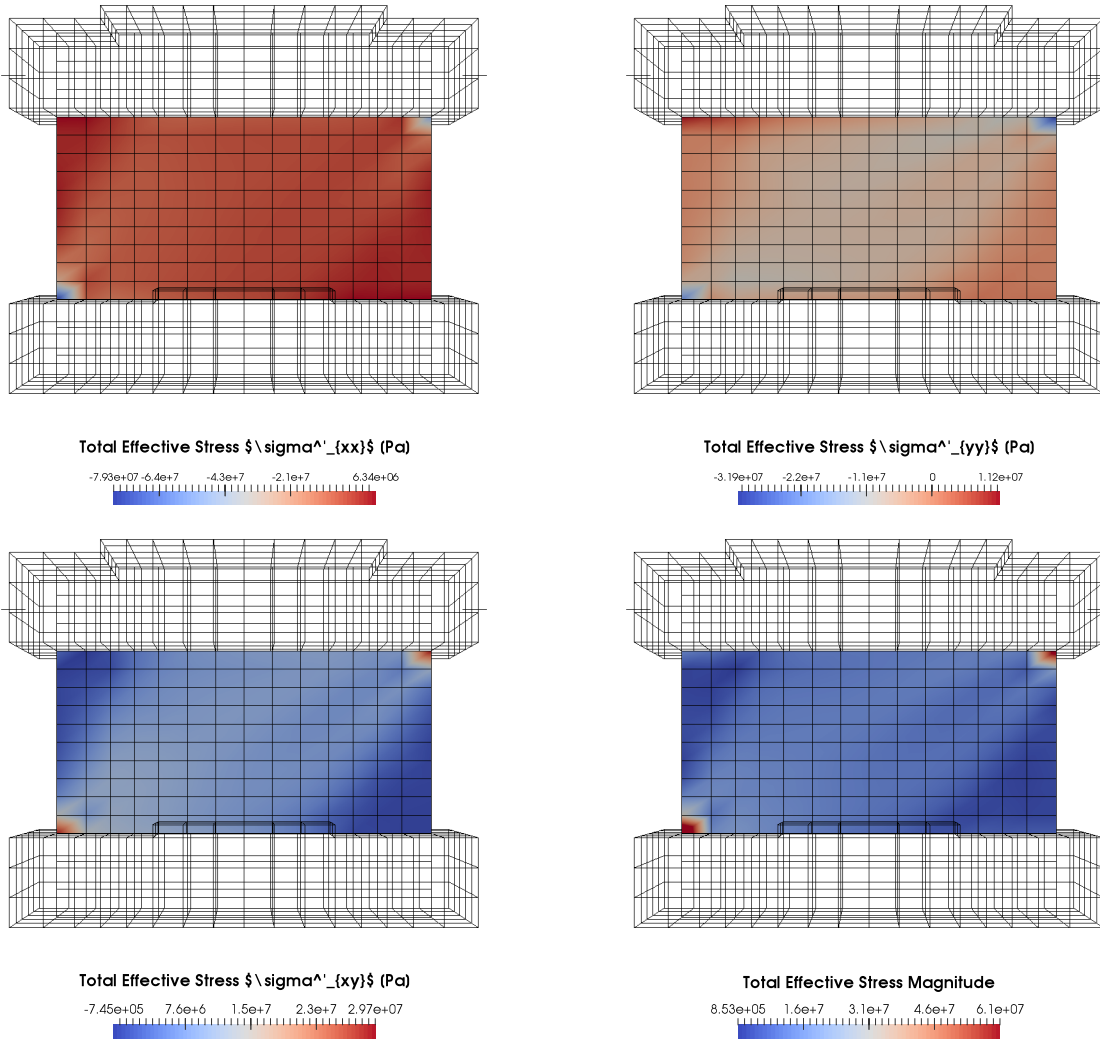


Figure 507.9: Distribution of stress components in the shear wall model at $u_y = 6$ mm: (a) Vertical normal stress σ_{xx} ; (b) Horizontal normal stress σ_{yy} ; (c) Shear stress σ_{xy} ; (d) Stress magnitude $|\sigma|$.

507.2.6.3 Concrete Damage and Energy Dissipation

Figure 507.10 shows the evolution of shear wall concrete damage index d^+ , defined in Equation 104.622, at different levels of deformation during cyclic loading. Only tensile damage index is presented in Figure 507.10 as no compressive damage occurs in the wall. It is noted that, according to damage evolution from Figure 507.10, three damage/cracks zones are observed in the wall for load/displacement cycles of $u_y = \pm 1.4\text{mm}$. Two 45° tensile/shear zones with opposite directions as well as a tensile failure zone along the bottom of the wall are developing. Note that the flanges experience damage at the bottom due to tension, which indicates that wall-flange system experiences bending, and not pure shear as intended.

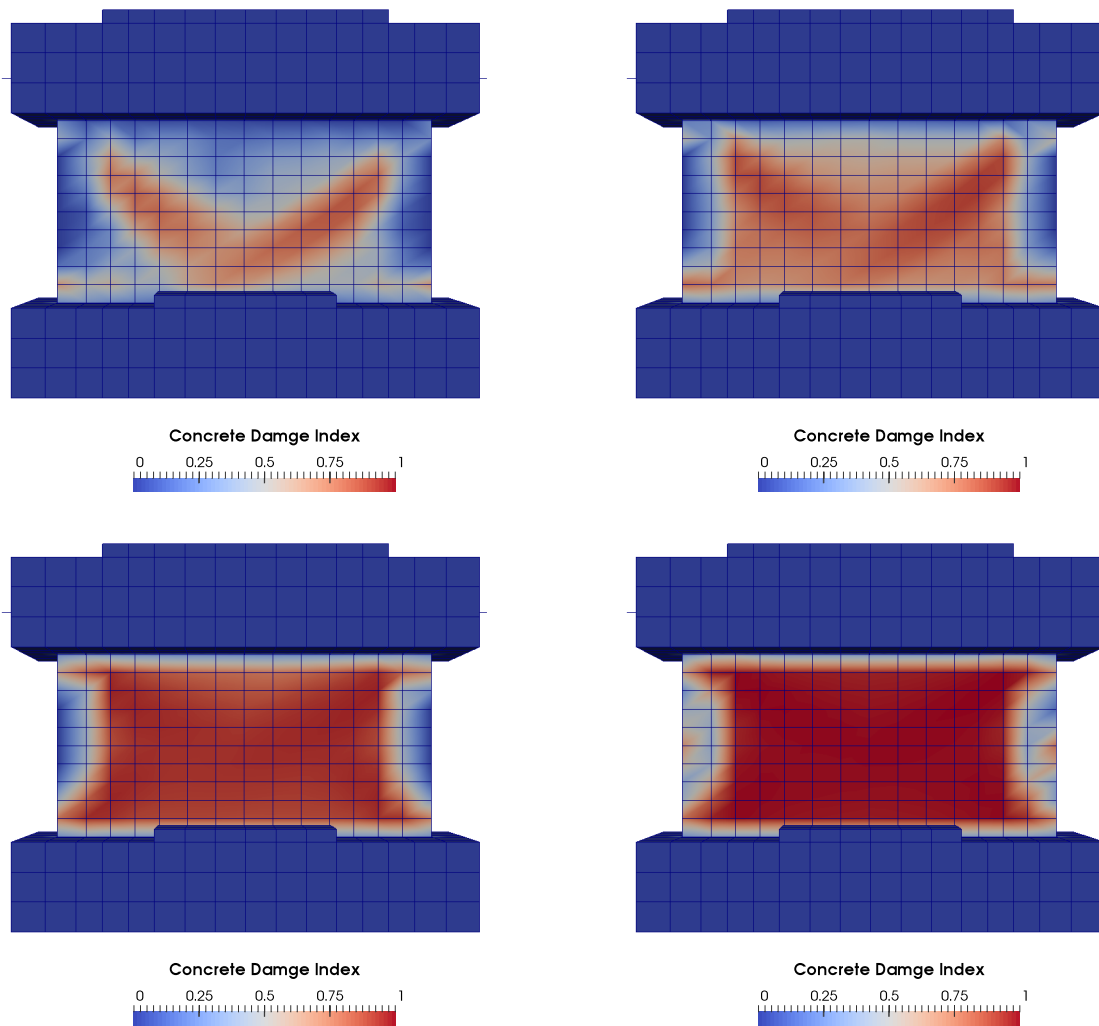


Figure 507.10: Evolution of concrete damage index in the shear wall model for different levels of cyclic loading: (a) At $u_y = \pm 1.4\text{mm}$; (b) At $u_y = \pm 1.8\text{mm}$; (c) At $u_y = \pm 3.0\text{mm}$; (d) At $u_y = \pm 5.0\text{mm}$.

As the loading/deformation cycles increase, the damage zones extends and the level of damage increases. At the end, the entire wall is damaged. In reality, due to variability of material properties, some wall regions will experience localization of deformation, as observed in experiments. Modeling of localization of deformation suffers from mesh dependency effects. It is noted that localization of deformation zones, as seen in Figures 507.10 and 507.11 are about the size of single finite element. It is likely that upon mesh refinement these zones would change (Lu et al., 2009), however this type of sensitivity study was not done here due to time constraints. We also note that a more sound approach to modeling localized deformation behavior would be through the use of Cosserat continuum (Cosserat, 1909; de Borst, 1987). Cosserat continuum finite element and micropolar elastic and elastic-plastic

models are available within the Real-ESSI Simulator, however calibration of material parameters for those models from current test results is beyond the scope and time frame of this study, and was not done.

Other than damage index, plastic energy dissipation density can also be used to illustrate damage in structures. The main difference between damage index and plastic energy dissipation is that the plastic energy dissipation increases even after an element is completely damaged, that is when $d^+ = 1.0$.²

Figure 507.11 shows the evolution of plastic energy dissipation density in the shear wall model at different stages of loading. At the beginning of the test, Figure 507.11(a), the distribution of plastic energy dissipation density is very similar to the distribution of a damage index (d^+). However, as the load cycles progress and displacement increase, Figure 507.11(b), significant amount of energy is dissipated at bottom corners of both flanges. Most of that plastic dissipation happens due to opening of gaps, tensile cracking, and some shear. Plastic dissipation due to tensile cracking can happen only once, as cracks will not "heal", hence there is a redistribution of loads and deformation within flange-wall system. Once flange cannot dissipate any more energy, only wall is left to pick up loads and dissipate energy due to tension and shear. It is noted again that there was no observed development of compression damage, hence there is no plastic dissipation in compressed concrete. Toward the end of simulation, Figure 507.11(c), a failure zone that is X shaped, with distinct 45° tensile plastic dissipation zones in the wall, and the plastic dissipation zone at the corners, bottom and top of flanges, is observed. At the end of the simulation, Figure 507.11(d), a failure zone due to tension and shear, encompasses flange corners and most of the wall.

Figure 507.12 shows animation of plastic dissipation development in the wall/membrane.

²Plastic dissipation is also very important for following seismic energy as it propagates through the soil structure system during earthquakes (Sinha et al., 2017; Wang et al., 2017). If seismic energy, and plastic dissipation can be accurately followed and its path even directed, during earthquake soil structure interaction (ESSI), soil structure systems can be optimized for safety and economy.

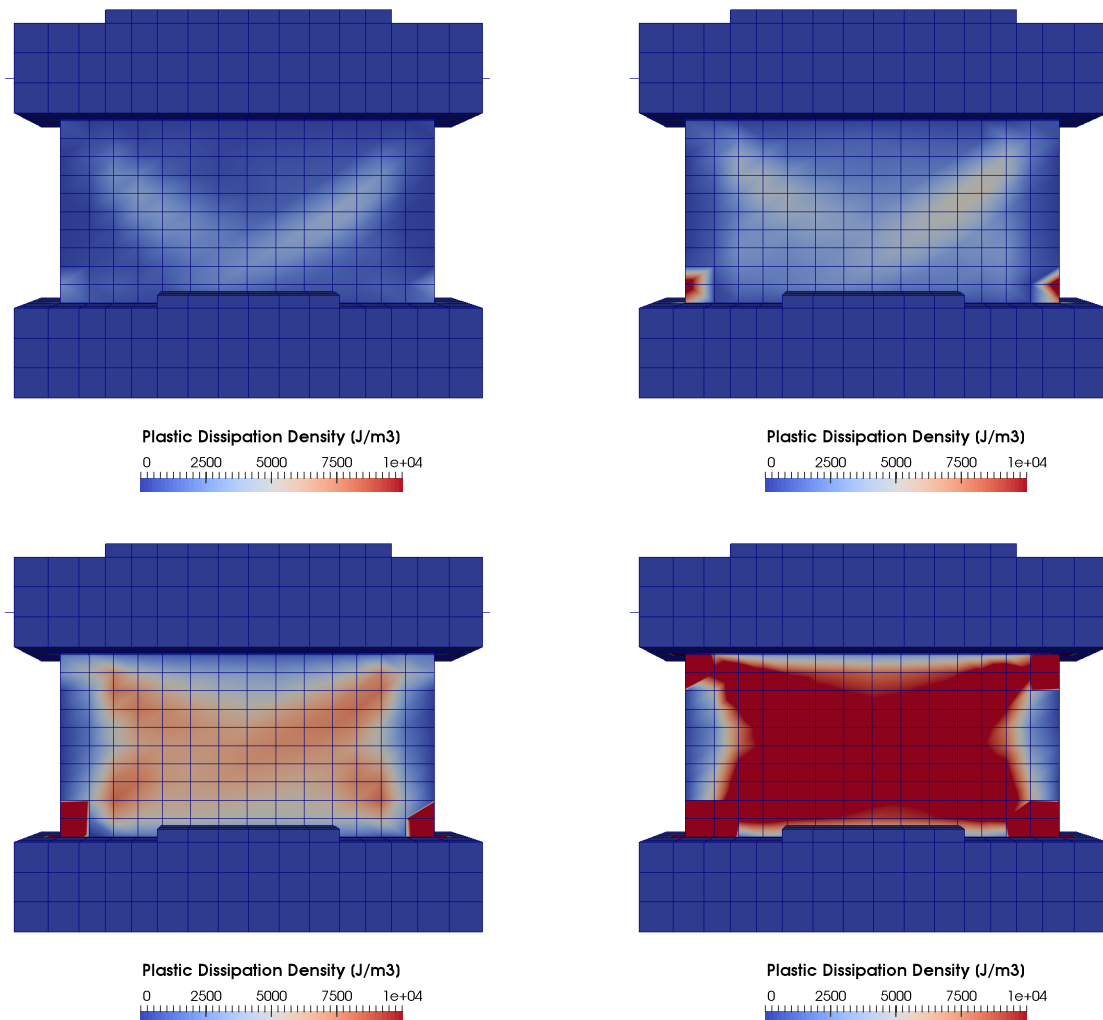


Figure 507.11: Evolution of plastic energy dissipation density in the shear wall model: (a) At $u_y = \pm 1.4\text{mm}$; (b) At $u_y = \pm 1.8\text{mm}$; (c) At $u_y = \pm 3.0\text{mm}$; (d) At $u_y = \pm 5.0\text{mm}$.

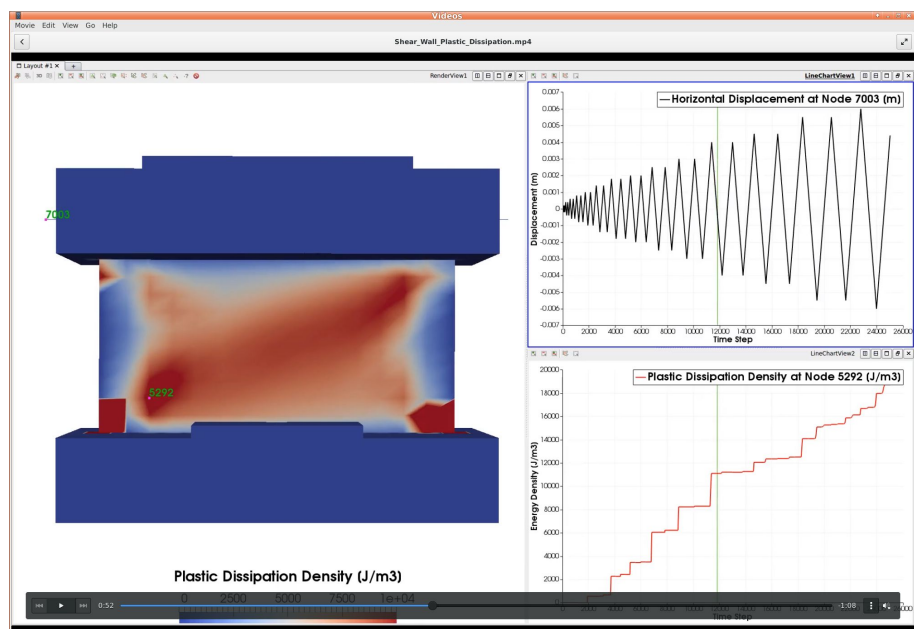


Figure 507.12: Animation of plastic dissipation in the wall/membrane.

Chapter 508

ESSI for Concrete Dams

(2019-2020-2021-)

(In collaboration with Prof. Han Yang and Dr. Hexiang Wang)

508.1 Chapter Summary and Highlights

508.2 Pine Flat Dam

Chapter 509

ESSI for Buildings

(2018-2019-2020-2021-)

(In collaboration with Prof. Han Yang, and Dr. Hexiang Wang)

509.1 2D Frame with Energy Dissipation

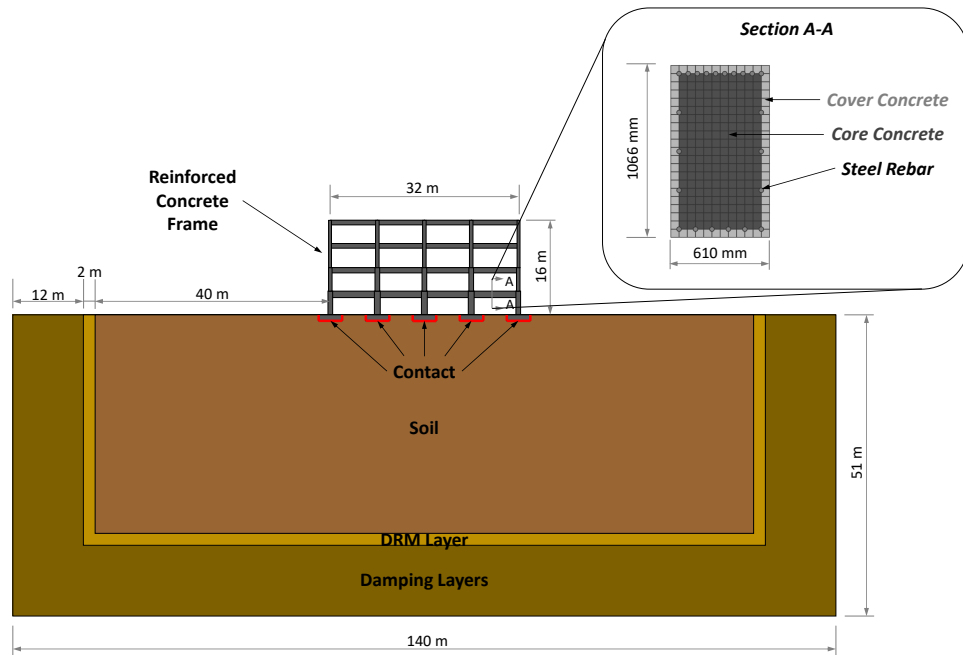


Figure 509.1: 2D frame model.

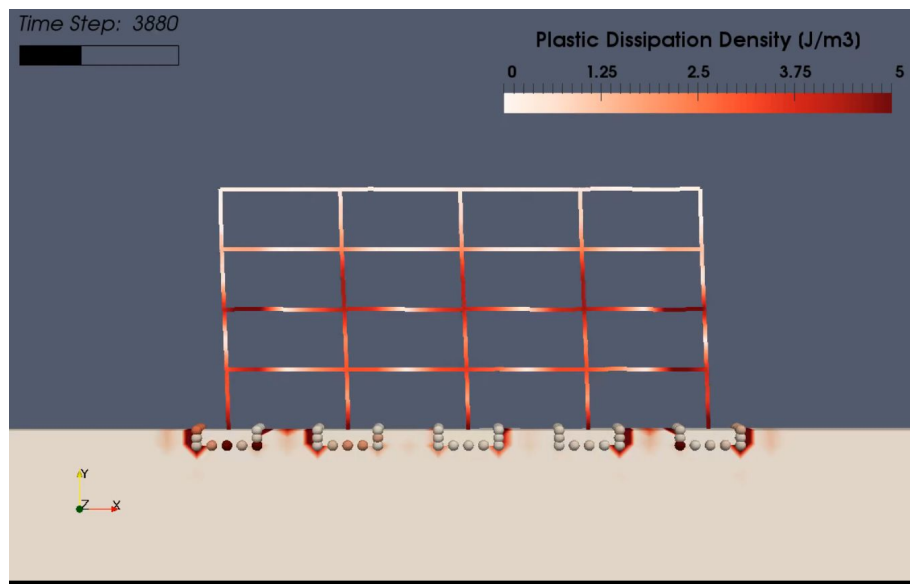


Figure 509.2: Energy Dissipation for a frame on spread foundations.

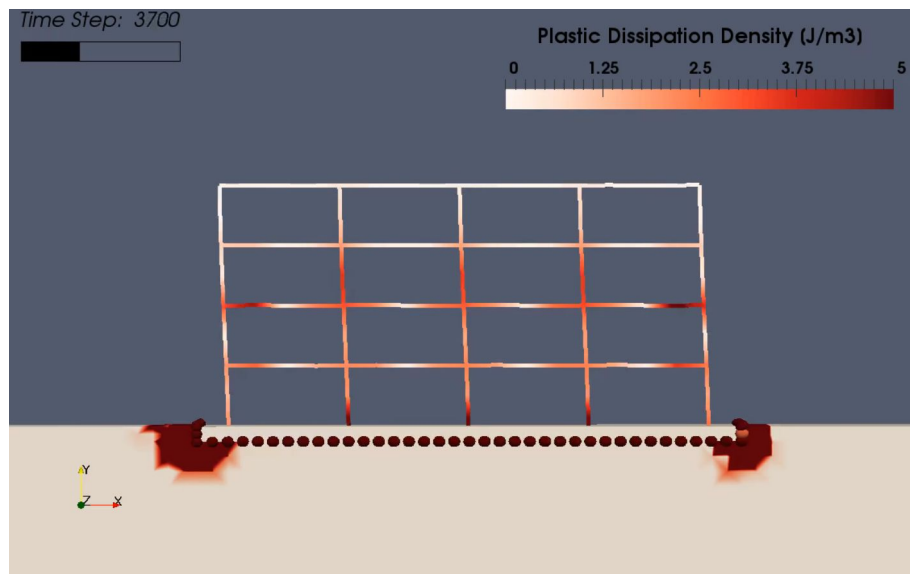


Figure 509.3: Energy Dissipation for a frame on slab foundation.

Finite element model, input files for the Real-ESSI simulator for Concrete Frame model are available:

- All model files, one by one,
- Model archive (tar xz)

For uncompressed and un-taring the model archive file, please use

```
tar -xvf Concrete_frame_PEER_model.txz.
```

509.2 Ventura Hotel

509.2.1 Finite Element Model

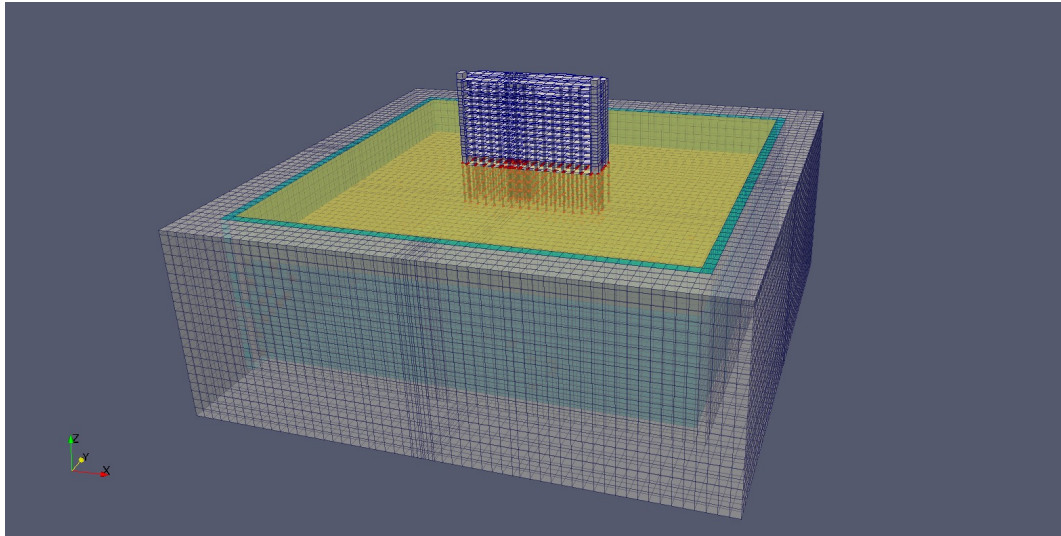


Figure 509.4: Ventura hotel model.

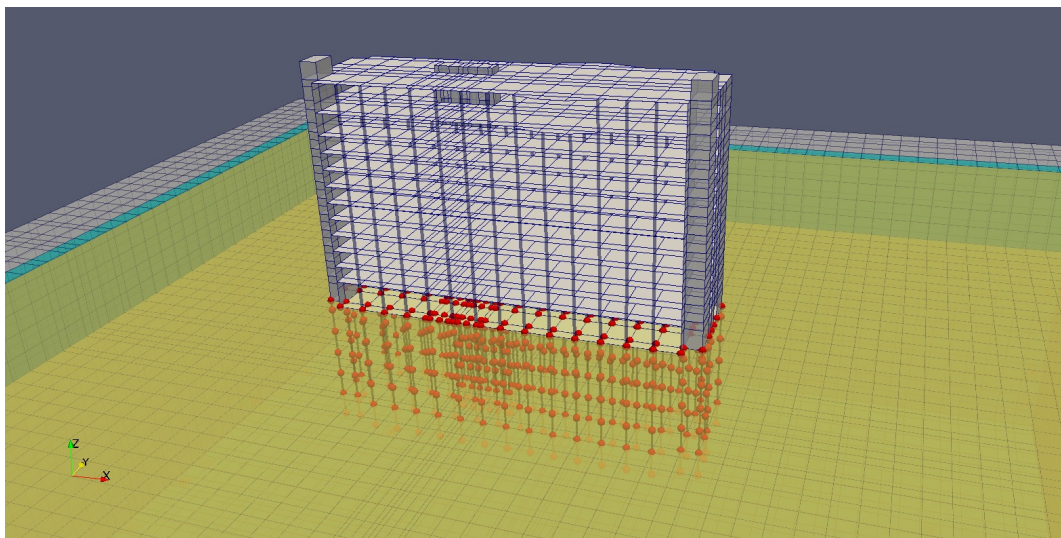


Figure 509.5: Ventura hotel model.

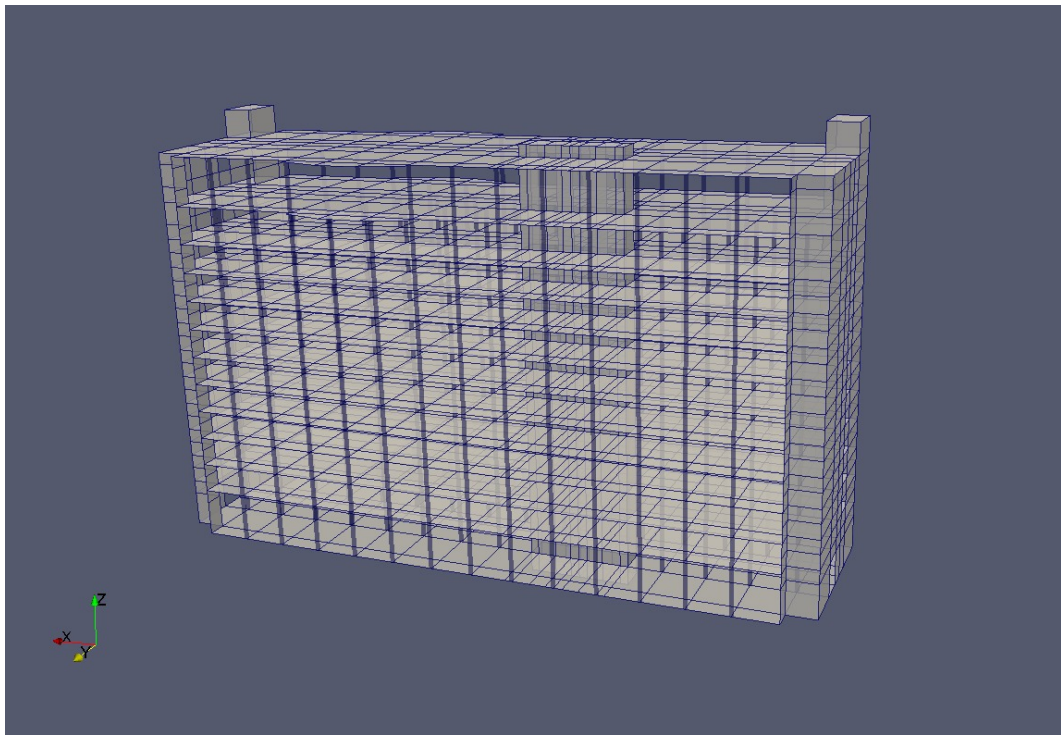


Figure 509.6: Ventura hotel model.

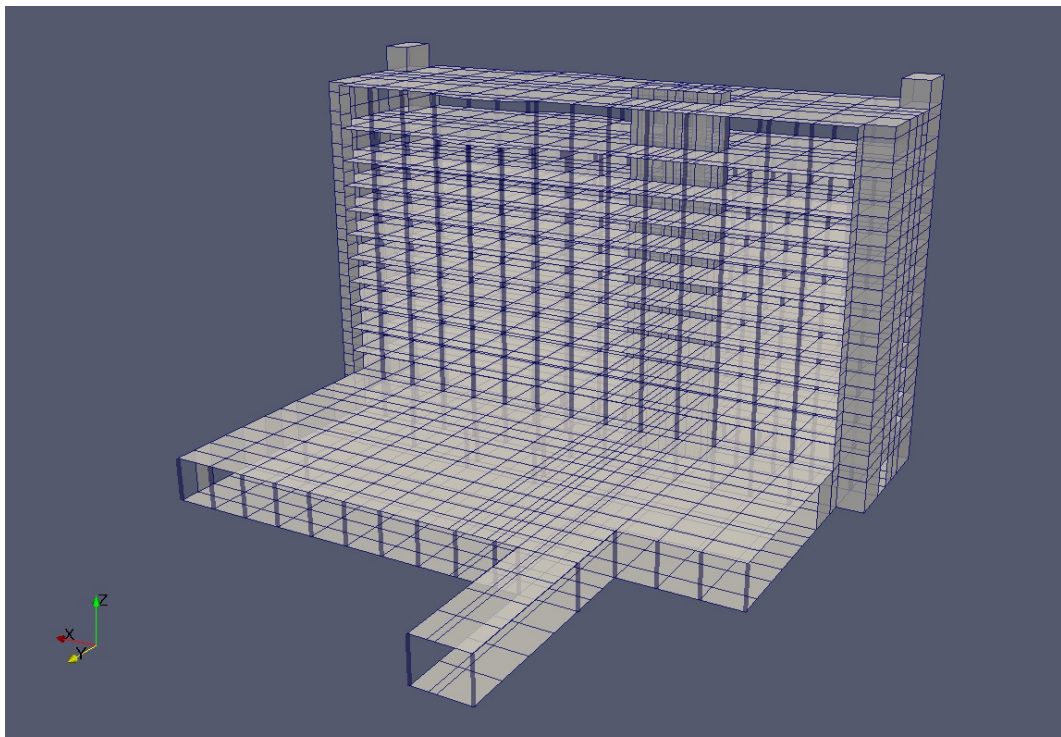


Figure 509.7: Ventura hotel model.

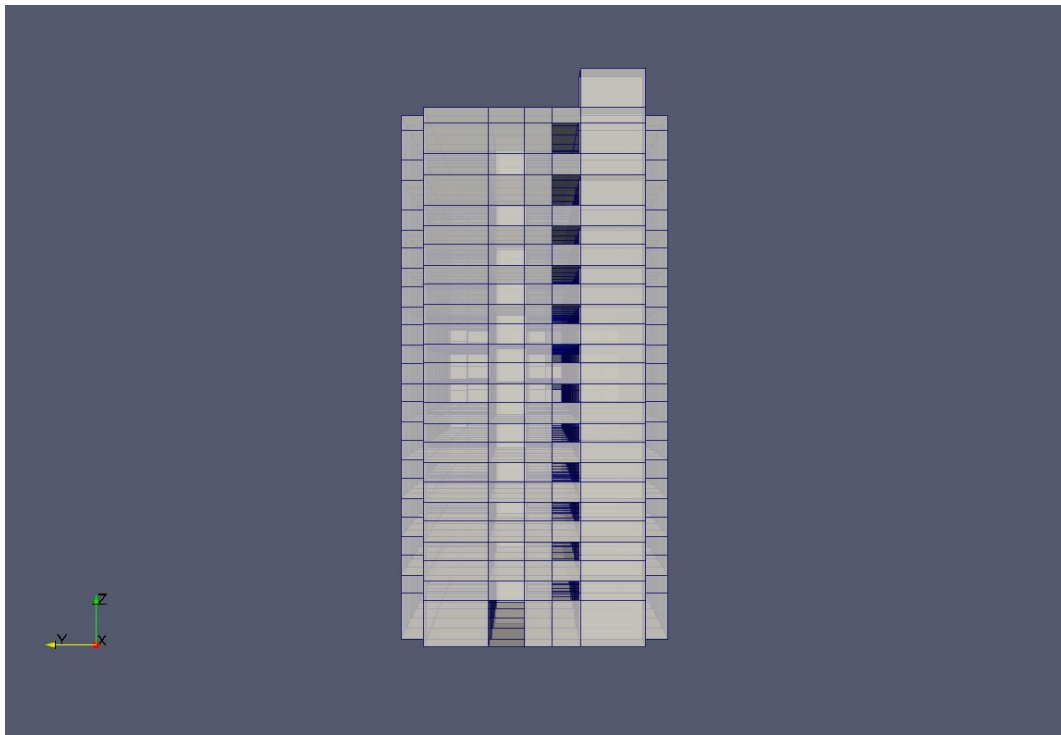


Figure 509.8: Ventura hotel model, view in X direction.

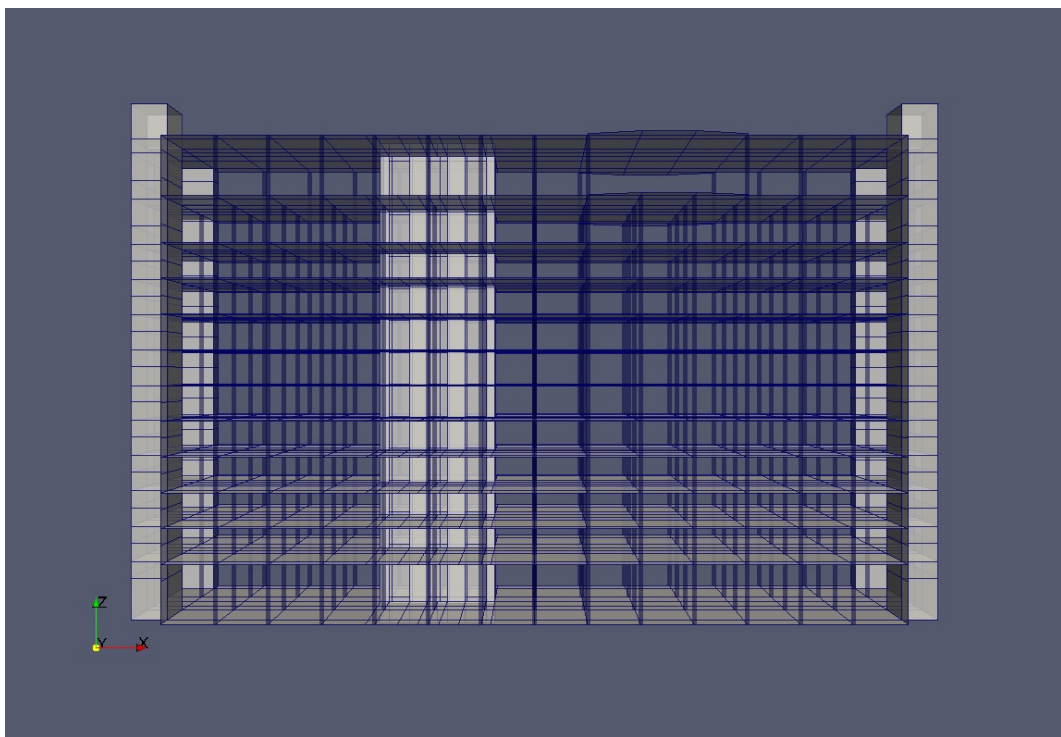


Figure 509.9: Ventura hotel model, view in Y direction.

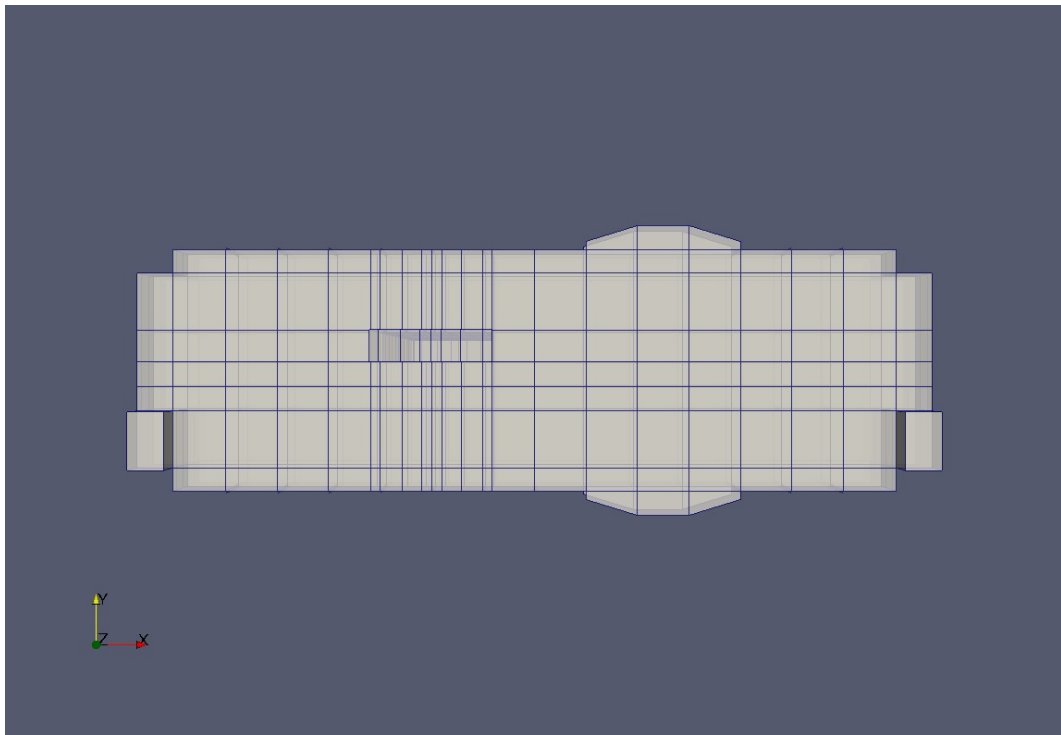


Figure 509.10: Ventura hotel model, view in Z direction.

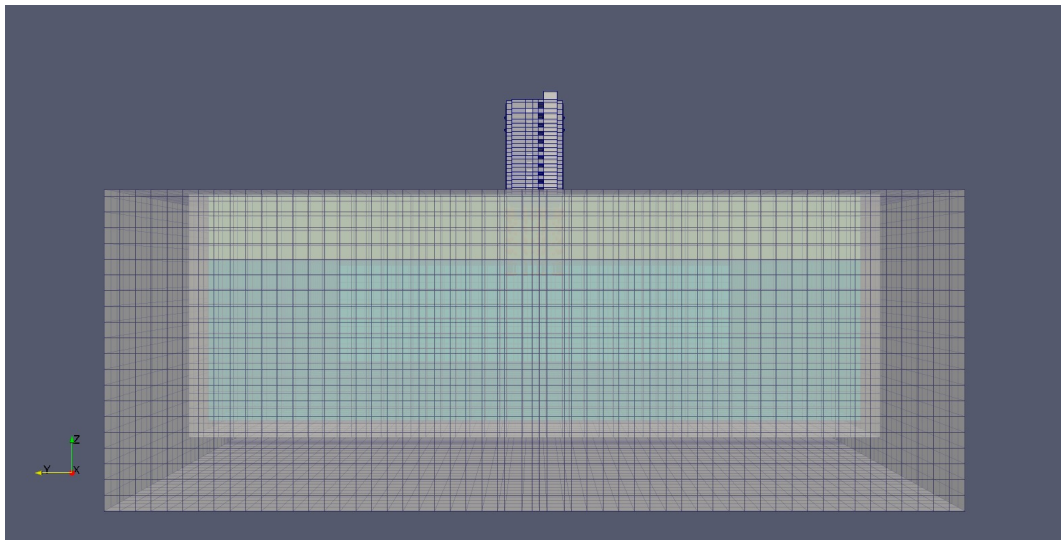


Figure 509.11: Ventura hotel model, view along X direction.

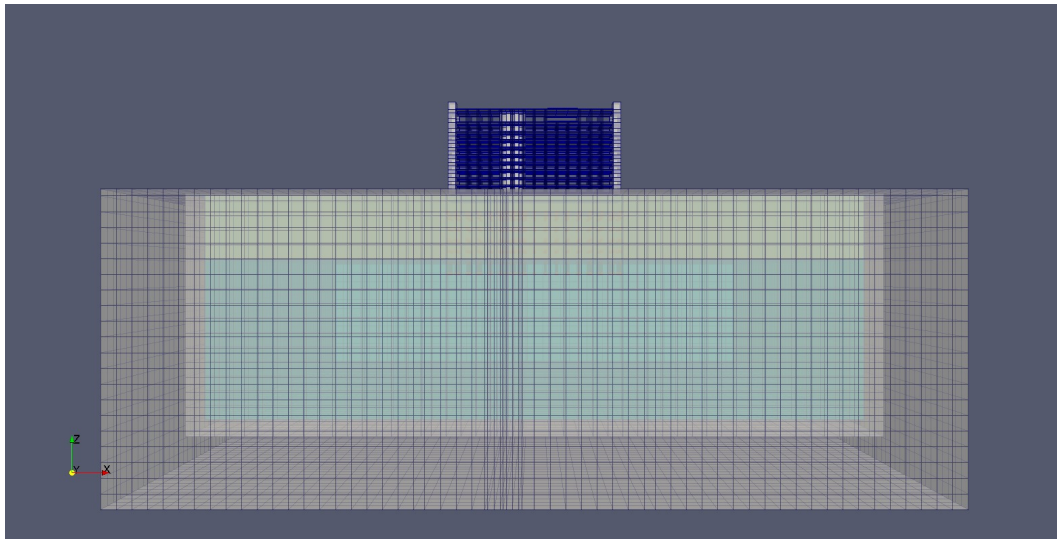


Figure 509.12: Ventura hotel model, view along Y direction.

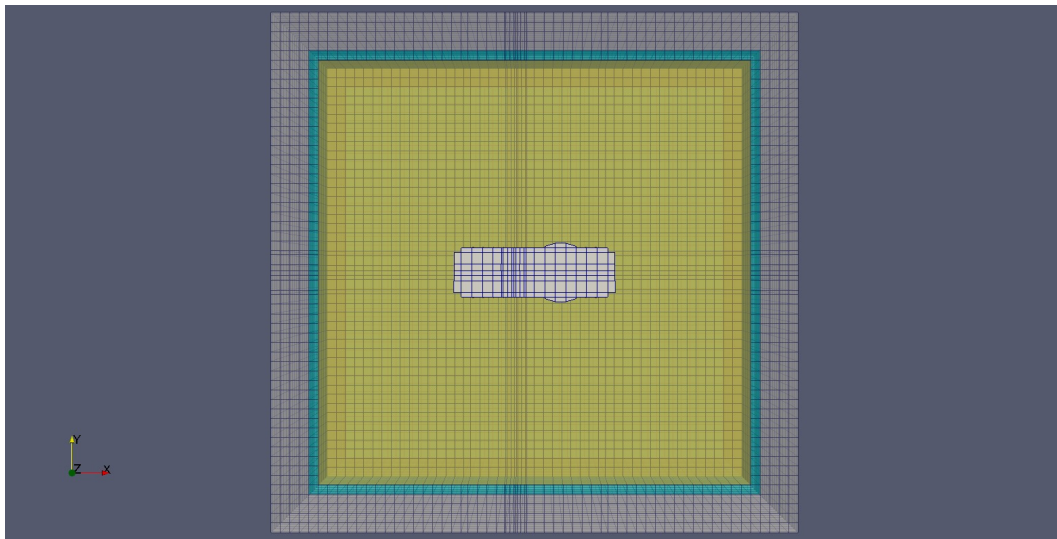


Figure 509.13: Ventura hotel model, view along Z direction.

Finite element model, input file for the Real-ESSI simulator for Ventura hotel model with and without SSI are available:

- [Full SSI model, \(7.8MB\)](#)
- [Structure only, non-SSI model, \(84kB\)](#)

NOTE: while full SSI model is only 11MB in compressed format, using xz compressor, fully uncompressed model files are over 3.7GB large, that is 3,770MB, or 3,868,356Kb.

For uncompressing and un-taring, please use

```
tar -xvf _Ventura_hotel_Full_SSI_Model_.tar.xz,
```

and

```
tar -xvf _Ventura_hotel_non_SSI_Model_.tar.xz.
```

509.3 Loma Linda Hospital

509.3.1 Finite Element Model

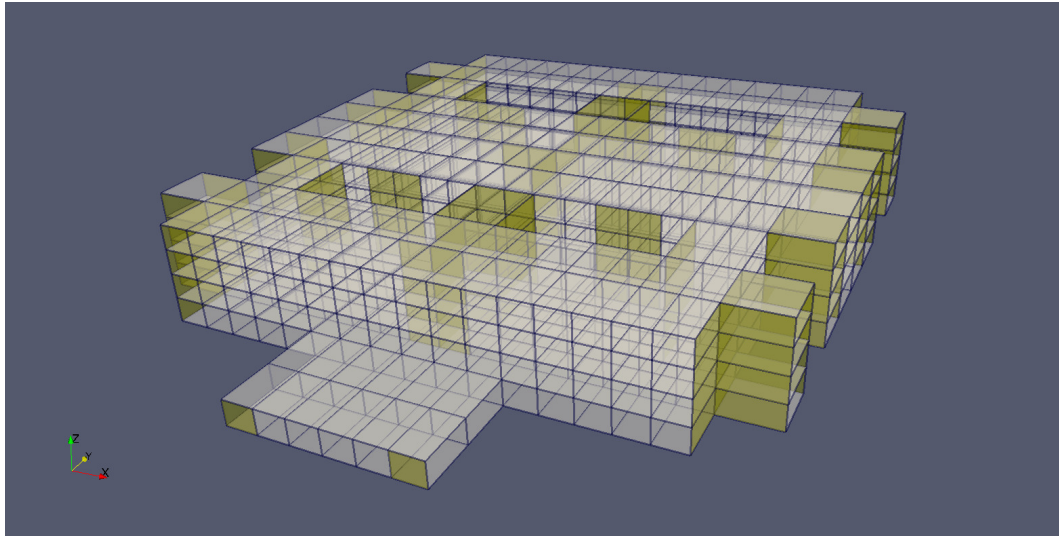


Figure 509.14: Loma Linda hospital 3D view.

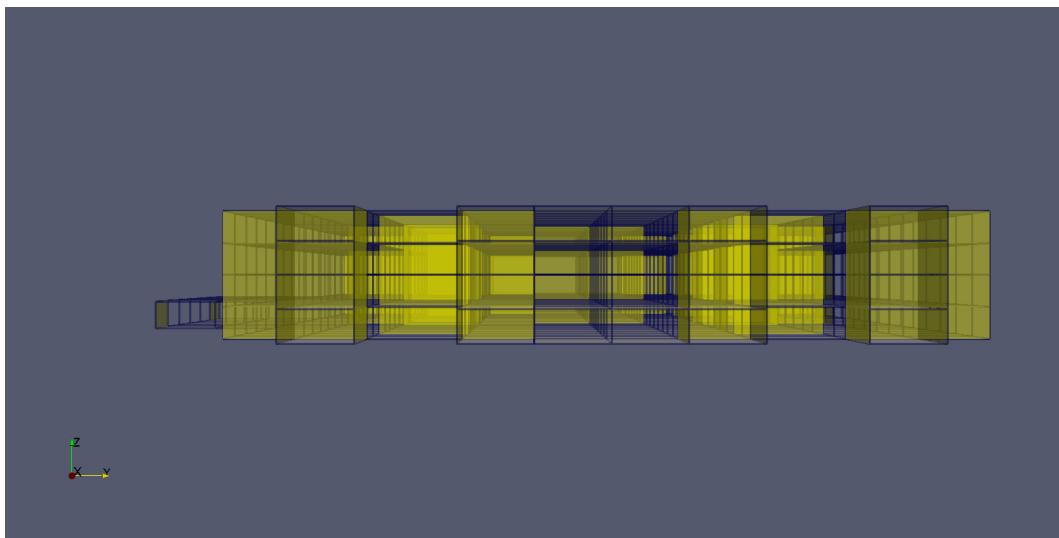


Figure 509.15: Loma Linda hospital view in X direction.

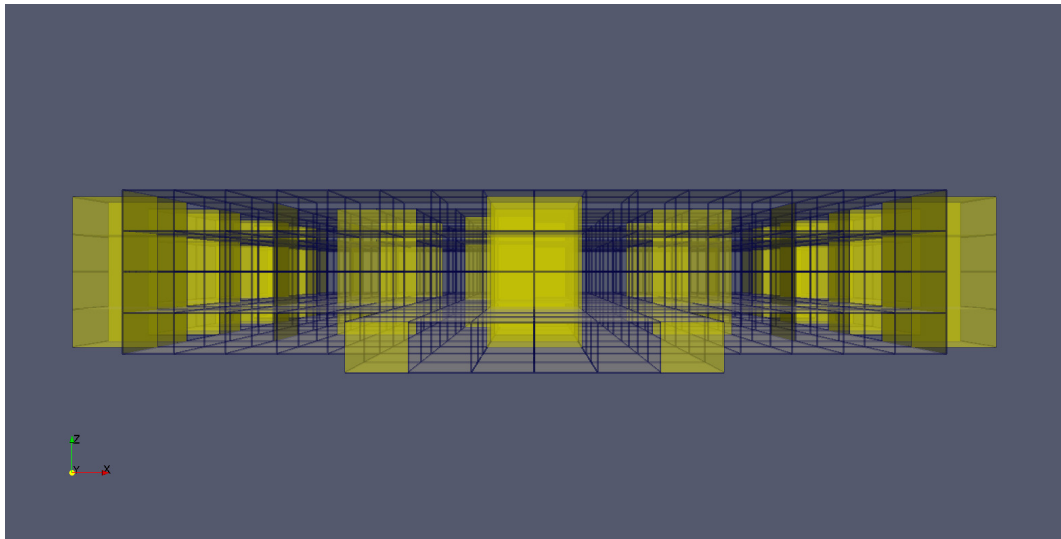


Figure 509.16: Loma Linda hospital view in Y direction.

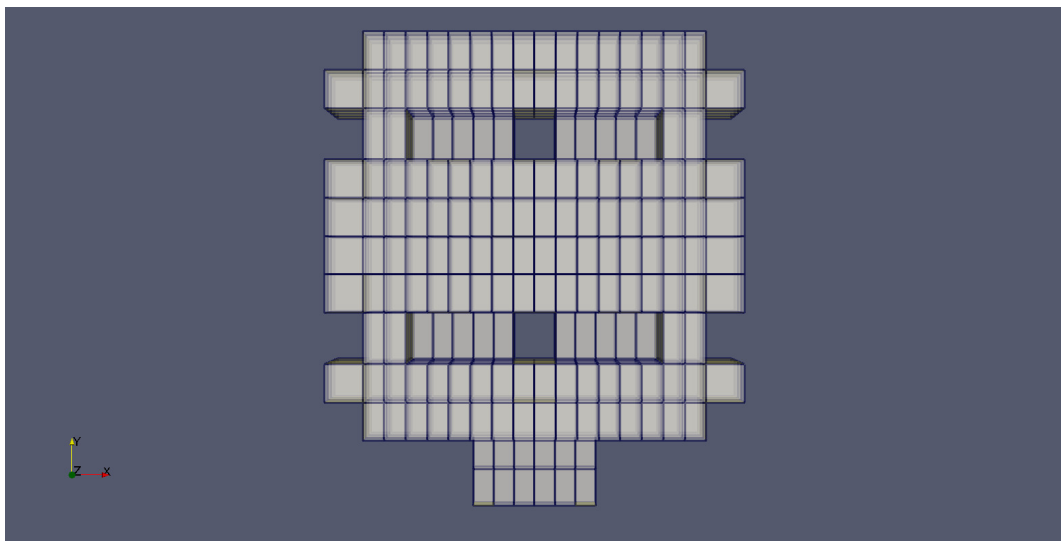


Figure 509.17: Loma Linda hospital view in Z direction.

509.4 ASCE-7 Model, Low, Steel Building

509.4.1 Finite Element Model

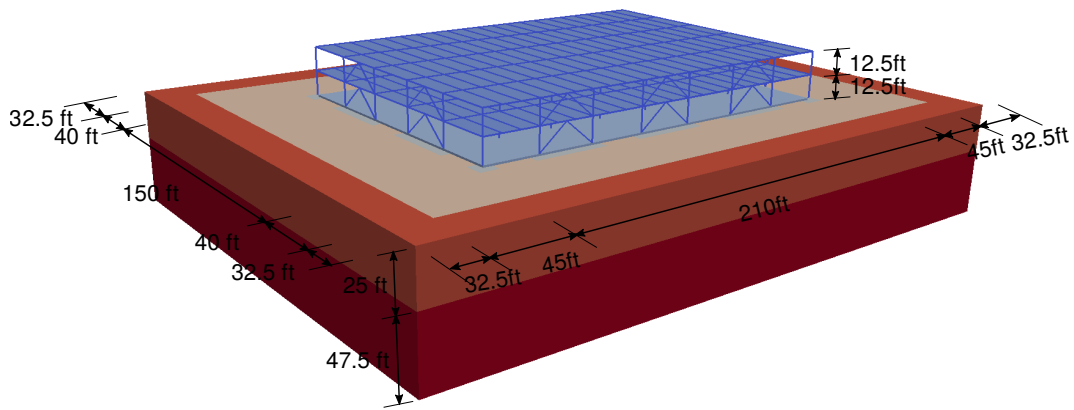


Figure 509.18: Low steel building model, 3D view.

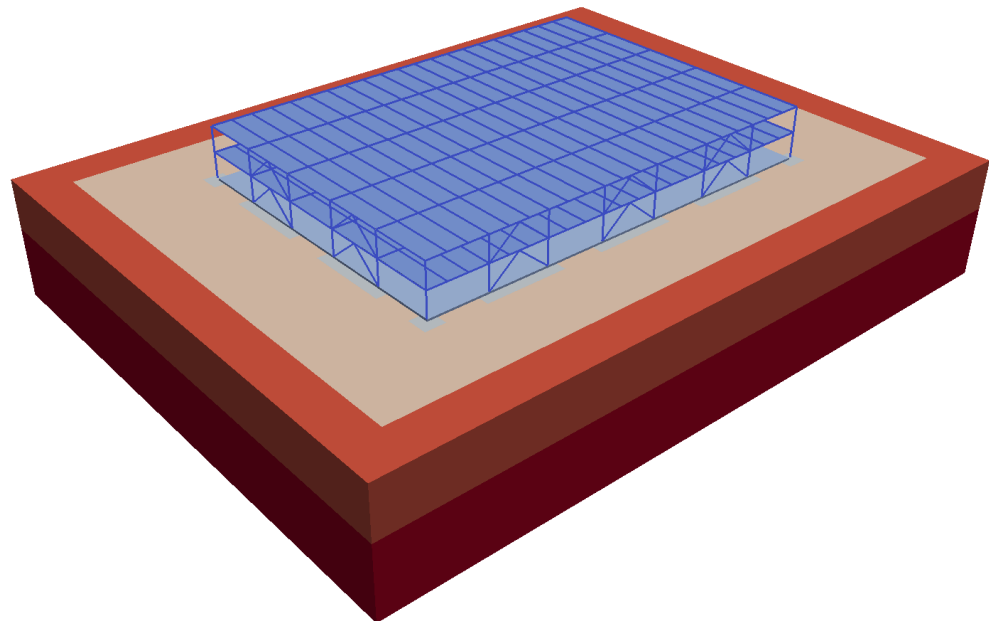


Figure 509.19: Low steel building model, 3D view.

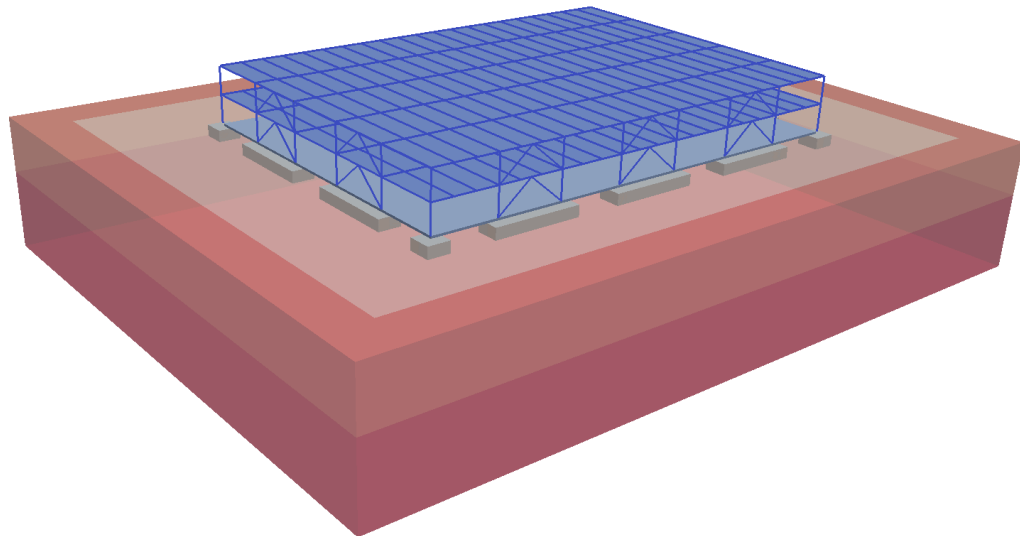


Figure 509.20: Low steel building model, 3D view.

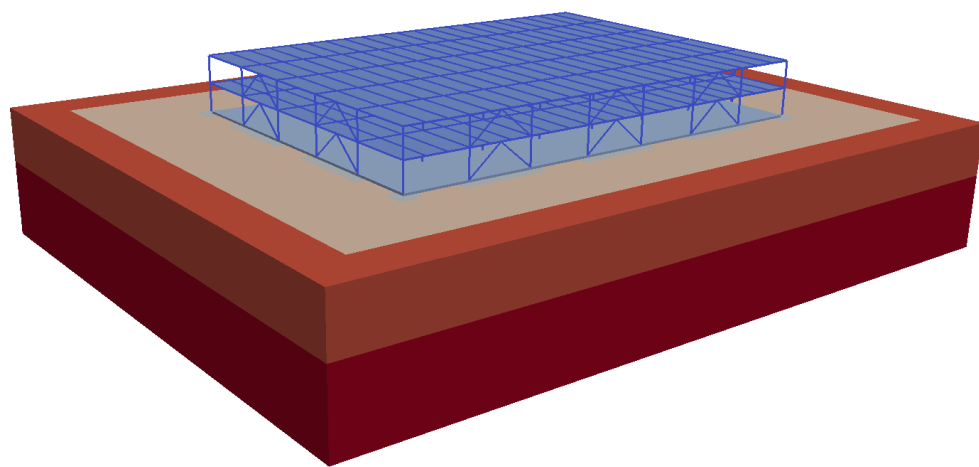


Figure 509.21: Low steel building model, 3D view.

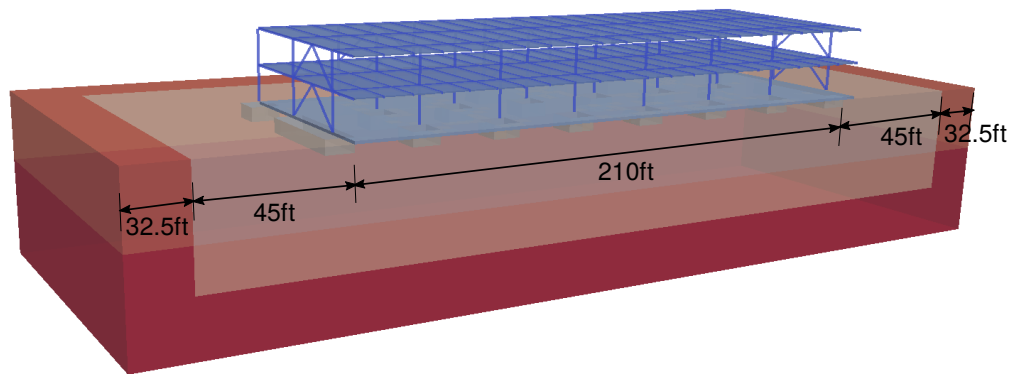


Figure 509.22: Low steel building model, 3D view.

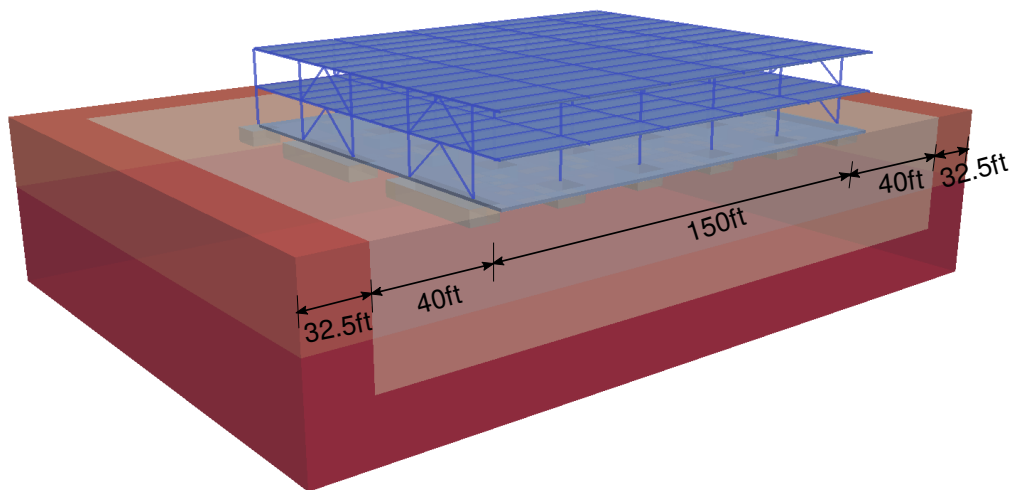


Figure 509.23: Low steel building model, 3D view.

Finite element model, input file for the Real-ESSI simulator for full SSI ASCE-7 model, low, steel building are available [HERE](#).

NOTE: This model is 1.1GB (1,102MB, 1,127,928Kb) in size even when compressed, due to large file describing incoherent motions. When uncompressed
(use

`tar -xvf _ASCE-7_low_steele_building_Model_.tar.xz`), models files grow to 3.0GB, that is 2,977MB, or 3,047,532Kb, so please be aware of disk space requirements for the model alone.

509.5 ASCE-7 Model, High, Concrete Building

509.5.1 Finite Element Model

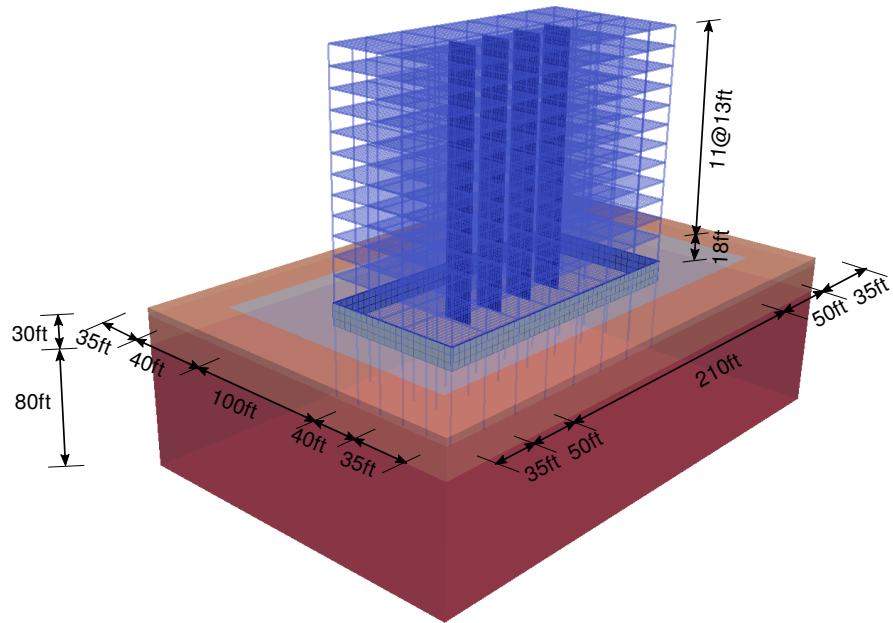


Figure 509.24: High concrete building model, 3D view.

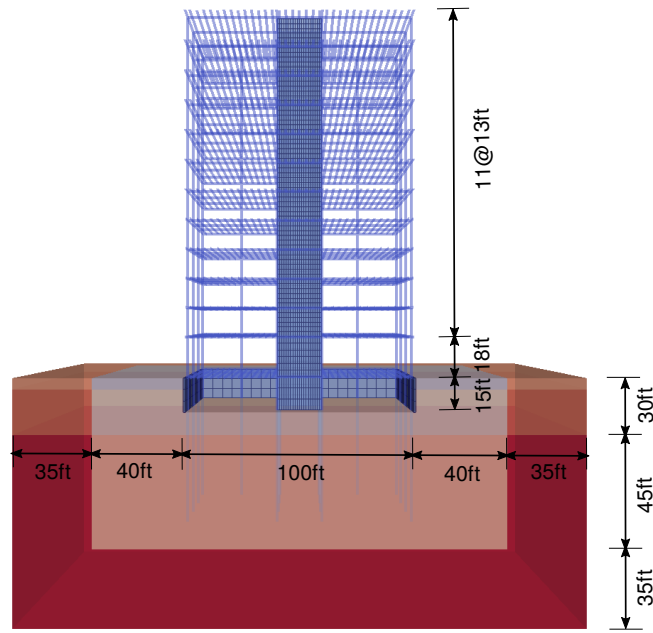


Figure 509.25: High concrete building model, XZ plane view.

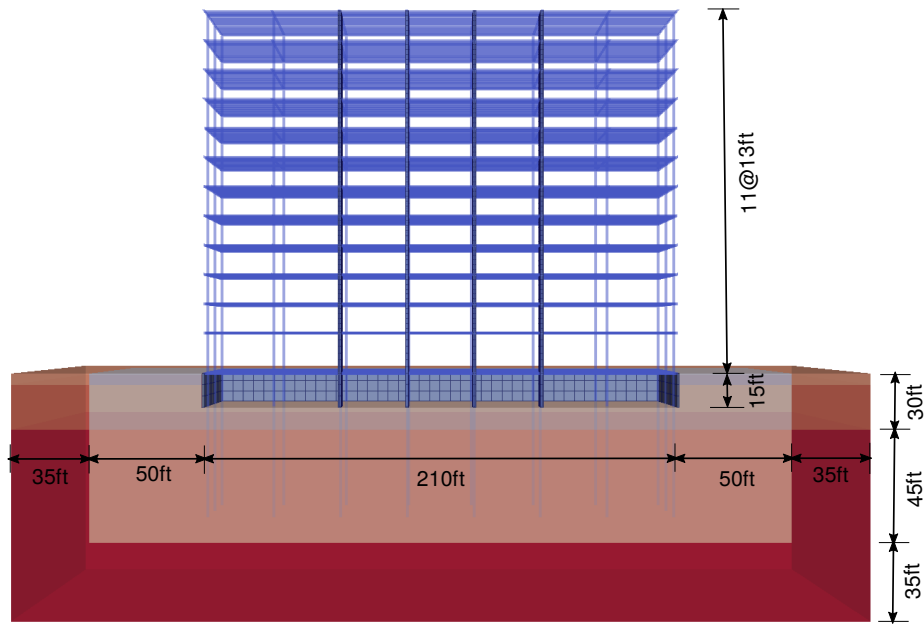


Figure 509.26: High concrete building model, YZ plane view.

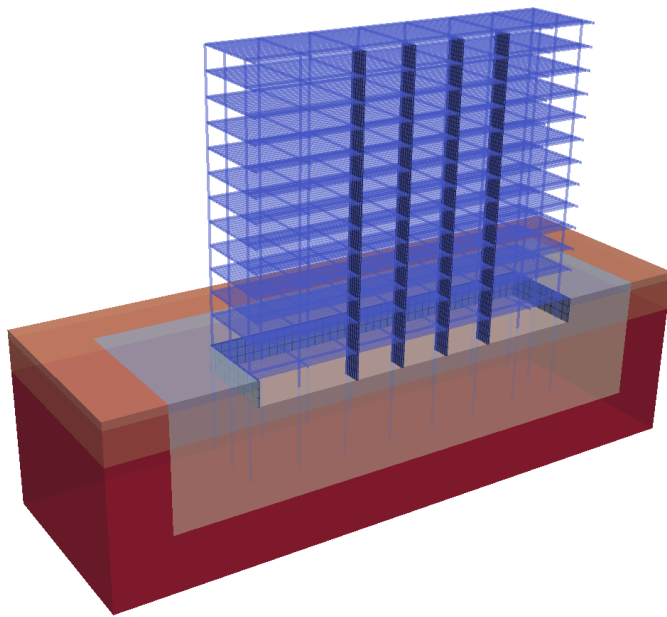


Figure 509.27: High concrete building model, cut through model view.

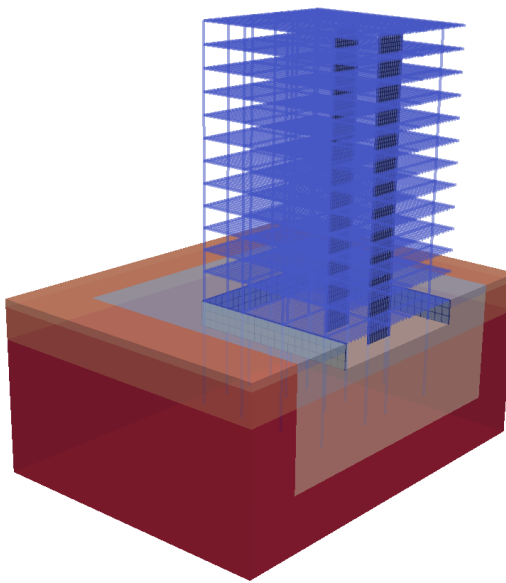


Figure 509.28: High concrete building model, cut through model view.

Finite element model, input file for the Real-ESSI simulator for full SSI ASCE-7 model, high concrete building are available [HERE](#).

NOTE: This model is only 11MB large when compressed. When uncompressed (use `tar -xvf _ASCE-7_tall_concrete_building_Model_.tar.xz`), models files grow to 1.9GB, that is 1,867MB, or 1,911,524Kb, so please be aware of disk space requirements for the model alone.

Chapter 510

Guidebook: Modeling and Simulation of Earthquake-Soil-Structure Interaction for Nuclear Energy Installations, Dams, Buildings, Bridges, Tunnels, &c.

(2016-2017-2018-2019-2020-2021-)

510.1 Motivation: Modeling and Simulation of Earthquake Soil Structure Interaction

Main motivation of this write-up (chapter, guidebook) is to provide a clear, practical, up to date guide on how to perform linear elastic and nonlinear, inelastic Earthquake Soil Structure Interaction (ESSI) modeling and simulations for infrastructure objects, including buildings, dams, bridges, nuclear installations, etc. This is particularly important at this time as a number of endeavors are underway to perform realistic ESSI analysis for a number of important soil, rock – structure systems, including dams, nuclear installations, bridges, buildings, etc.

This write-up is further motivated by the modeling and simulation challenges that are part of any soil, rock – structure system. These challenges are illustrated in Figure 510.1 for a number of soil, rock and soil/rock-structure systems.

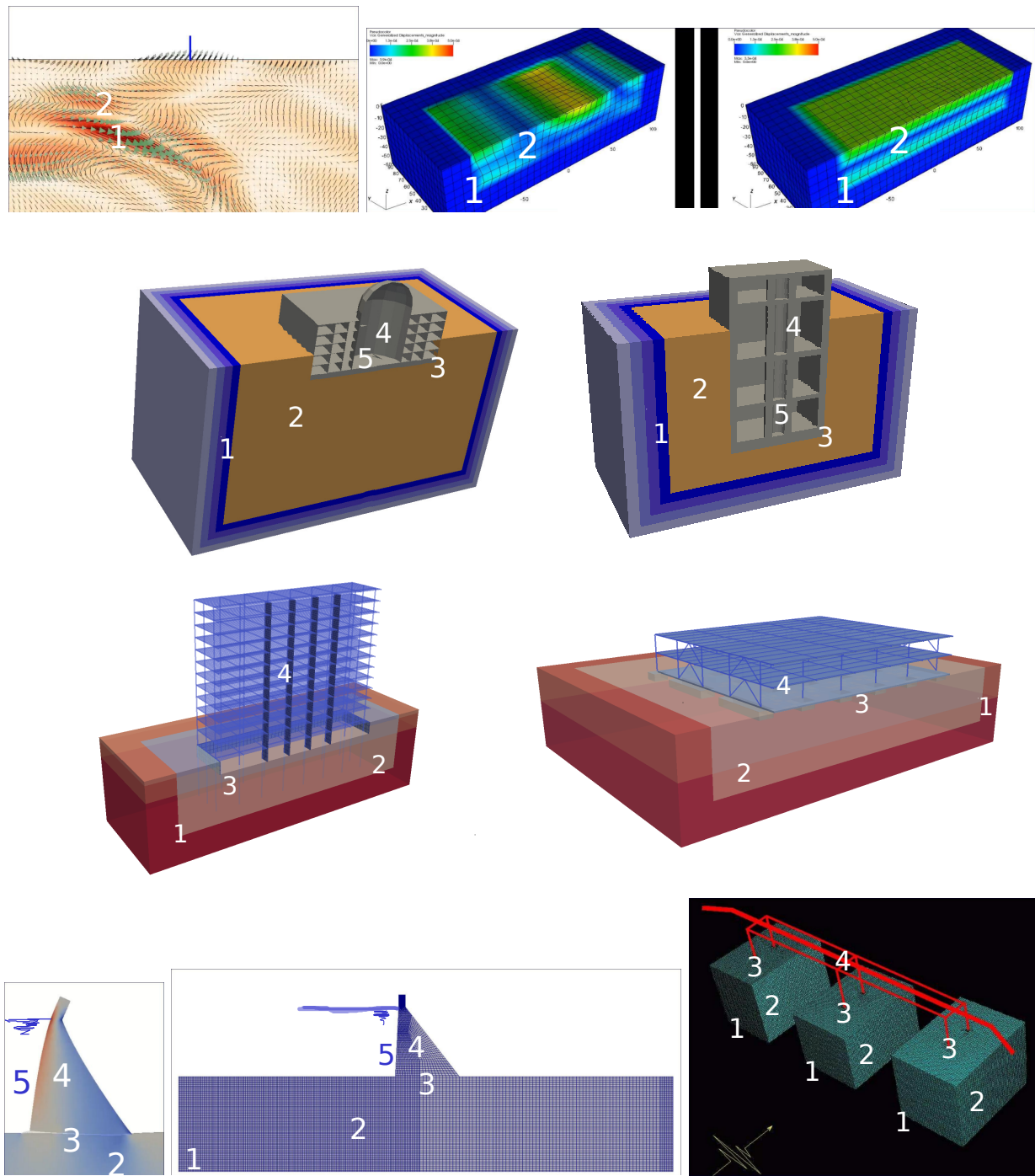


Figure 510.1: ESSI modeling and simulation challenges: Free field motions, 3C/6C vs $3 \times 1C$; Nuclear Power Plant structure – soil/rock system, Small Modular Reactor structure – soil/rock system; Low and High Building-foundation-soil system; Dam-Foundation-Fluid system; Bridge-soil system; Aspects of modeling: 1) Seismic motions, 2) Inelastic soil and rock, 3) Inelastic interface/contact/joints, foundation with soil/rock and interfaces/contacts/joints within structure, 4) Inelastic structure, systems and components, 5) Solid, Structure – Fluid interaction, external (reservoirs, fluid pools...) and internal (fully saturated and partially, (un-)saturated soil, rock and concrete).

Challenges for Modeling of Mechanics of Earthquake – Soil/Rock – Structure – Interaction. Presented are challenges related to the modeling of mechanics of ESSI problems.

- 1 Seismic motions: use of 1C, 3×1C and 3C motions, seismic motions input and radiation damping.
- 2 Inelastic, elastic plastic modeling of soil and rock, dry and/or partially or fully saturated, and energy dissipation in those soil/rock – structure components,
- 3 Inelastic, elastic plastic modeling of foundation concrete – soil/rock contacts/interfaces/joints that may be dry and/or partially or fully saturated, and energy dissipation in those parts of soil/rock – structure system,
- 4 Inelastic, elastic damage plastic modeling of structure, systems and components (SSCs). SSCs: beams, walls, plates, shell made of steel and reinforced concrete, base isolators and dissipators, systems and etc. and energy dissipation in those soil/rock – structure components,
- 5 Interaction of soil/rock – structure systems with internal, within structure or in pores of porous materials (soil, rock, concrete) and external fluids, reservoirs, pools, etc.

Challenges for Numerical Simulations of Earthquake – Soil/Rock – Structure – Interaction. Presented are challenges related to the numerical simulation of ESSI problems.

- A Inelastic simulations on constitutive level, stress-strain, constitutive problem solutions
- B Inelastic simulations on finite element level, nonlinear system of equations solutions
- C Time marching algorithms, numerical damping
- D High performance, parallel computing

510.2 Introduction

Focus is on modeling and simulation of linear elastic and nonlinear, inelastic, elastic-plastic behavior of soil/rock – structure systems during earthquakes.

It is assumed that earthquake motions, earthquake field is known. Earthquake motion or earthquake field, can be given as a simple 1C (1 Component) vertically propagating shear wave, that is obtained from a de-convolution of a given (1C) surface motion, using, for example SHAKE type analysis. Earthquake motion or earthquake field can also be given as a full 3C (3 Component) wave field that is obtained from analytic wave propagation solutions or from a regional geophysical model simulations, using, for example SW4 type analysis. In addition, earthquake motions can be defined in a probabilistic way...

510.3 Seismic Energy Input and Dissipation

Recorded lectures, together with slides, about these topics are available at

http://sokocalo.engr.ucdavis.edu/~jeremic/Real_ESSI_Simulator/OnlineLectures

More details about these topics are given in Section 109.2, on page 547 in Jeremić et al. (1989-2025).

510.3.1 Seismic Energy Input

Seismic energy input flux

510.3.2 Seismic Energy Dissipation

510.3.2.1 Seismic Energy Dissipation, Wave Reflection and Wave Radiation

Wave reflection and radiation damping

510.3.2.2 Seismic Energy Dissipation, Viscous Coupling

velocity proportional, viscous damping

510.3.2.3 Seismic Energy Dissipation, Material Inelasticity

Elastic-plastic energy dissipation of material, Displacement proportional

510.3.2.4 Seismic Energy Dissipation, Numerical, Algorithmic Positive and Negative Damping

510.4 Modeling: Seismic Motions

Recorded lectures, together with slides, about these topics are available at

http://sokocalo.engr.ucdavis.edu/~jeremic/Real_ESSI_Simulator/OnlineLectures

More details about these topics are given in Section 502.2, on page 2260 in Jeremić et al. (1989-2025).

510.4.1 Seismic Motions: Available Data

Details are given in Section 502.2.1, on page 2262 in Jeremić et al. (1989-2025).

510.4.2 Seismic Motion Development

Details are given in Section 502.2.3, on page 2266 in Jeremić et al. (1989-2025).

510.4.2.1 Seismic Motions from Empirical Models

Details are given in Section 109.2.3, on page 553 in Jeremić et al. (1989-2025).

510.4.2.2 Seismic Motions from Geophysical Models

Details are given in Section 109.2.6, on page 561 in Jeremić et al. (1989-2025).

Small Scale Geophysical Models.

Large Scale Regional Geophysical Models

510.4.2.3 Seismic Motions from 3D/3C Analytic Models

Details are given in Section 109.2.5, on page 557 in Jeremić et al. (1989-2025).

510.4.2.4 Seismic Motions from Full Waveform Inversion

This is based on recent work by Guidio (2020); Guidio et al. (2022b); Guidio and Jeong (2021); Guidio et al. (2022a).

510.4.3 6C vs 3C vs $3 \times 1C$ vs 1C Seismic Motions

Details are given in Section 504.4.1, on page 2504 in Jeremić et al. (1989-2025).

510.4.4 Incoherent Seismic Motions

Details are given in Section 109.2.8, on page 562 in Jeremić et al. (1989-2025).

510.4.5 Seismic Motion Input into FEM Models

Details are given in Section 109.4.1, on page 568 in Jeremić et al. (1989-2025).

510.5 Modeling: Inelastic, Nonlinear Material Modeling for Solids and Structures

Recorded lectures, together with slides, about these topics are available at

http://sokocalo.engr.ucdavis.edu/~jeremic/Real_ESSI_Simulator/OnlineLectures

510.5.1 Inelastic Material Modeling of Rock

Details are given in Section 104.8, on page 329 in Jeremić et al. (1989-2025).

510.5.1.1 Calibration of Inelastic Material Model Parameters for Rock

Details are given in Section 104.10, on page 368 in Jeremić et al. (1989-2025).

510.5.2 Inelastic Material Modeling of Soil

510.5.2.1 Dry Soil

Details are given in Section 104.6, on page 220 in Jeremić et al. (1989-2025).

510.5.2.2 Fully Saturated Soil

Details are given in Section 102.12, on page 137 in Jeremić et al. (1989-2025).

510.5.2.3 Partially Saturated, Unsaturated Soil

Details are given in Section 102.12.2, on page 152 in Jeremić et al. (1989-2025).

510.5.2.4 Calibration of Inelastic Material Model Parameters for Soil

Details are given in Section 104.10, on page 368 in Jeremić et al. (1989-2025).

510.5.3 Inelastic Material Modeling of Steel

Details are given in Section 104.9, on page 363 in Jeremić et al. (1989-2025).

510.5.3.1 Calibration of Inelastic Material Model Parameters for Steel

Details are given in Section 104.10, on page 368 in Jeremić et al. (1989-2025).